



## MODELLING OF CATALYTIC SYSTEMS TOWARDS GREEN FUELS

Jordi Morales Vidal

**ADVERTIMENT.** L'accés als continguts d'aquesta tesi doctoral i la seva utilització ha de respectar els drets de la persona autora. Pot ser utilitzada per a consulta o estudi personal, així com en activitats o materials d'investigació i docència en els termes establerts a l'art. 32 del Text Refós de la Llei de Propietat Intel·lectual (RDL 1/1996). Per altres utilitzacions es requereix l'autorització prèvia i expressa de la persona autora. En qualsevol cas, en la utilització dels seus continguts caldrà indicar de forma clara el nom i cognoms de la persona autora i el títol de la tesi doctoral. No s'autoritza la seva reproducció o altres formes d'explotació efectuades amb finalitats de lucre ni la seva comunicació pública des d'un lloc aliè al servei TDX. Tampoc s'autoritza la presentació del seu contingut en una finestra o marc aliè a TDX (framing). Aquesta reserva de drets afecta tant als continguts de la tesi com als seus resums i índexs.

**ADVERTENCIA.** El acceso a los contenidos de esta tesis doctoral y su utilización debe respetar los derechos de la persona autora. Puede ser utilizada para consulta o estudio personal, así como en actividades o materiales de investigación y docencia en los términos establecidos en el art. 32 del Texto Refundido de la Ley de Propiedad Intelectual (RDL 1/1996). Para otros usos se requiere la autorización previa y expresa de la persona autora. En cualquier caso, en la utilización de sus contenidos se deberá indicar de forma clara el nombre y apellidos de la persona autora y el título de la tesis doctoral. No se autoriza su reproducción u otras formas de explotación efectuadas con fines lucrativos ni su comunicación pública desde un sitio ajeno al servicio TDR. Tampoco se autoriza la presentación de su contenido en una ventana o marco ajeno a TDR (framing). Esta reserva de derechos afecta tanto al contenido de la tesis como a sus resúmenes e índices.

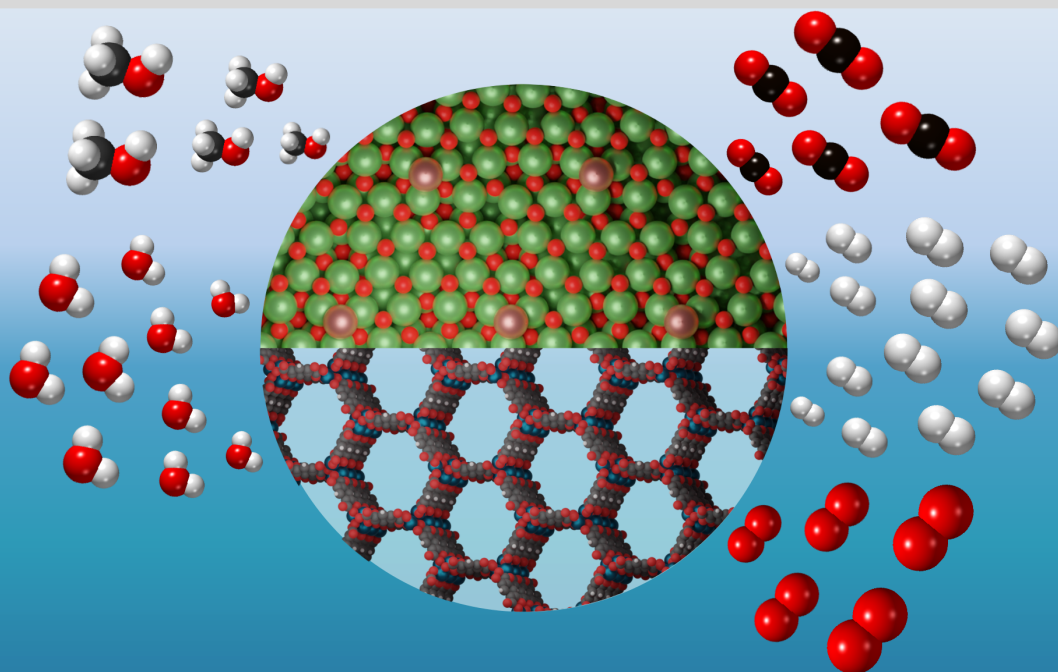
**WARNING.** Access to the contents of this doctoral thesis and its use must respect the rights of the author. It can be used for reference or private study, as well as research and learning activities or materials in the terms established by the 32nd article of the Spanish Consolidated Copyright Act (RDL 1/1996). Express and previous authorization of the author is required for any other uses. In any case, when using its content, full name of the author and title of the thesis must be clearly indicated. Reproduction or other forms of for profit use or public communication from outside TDX service is not allowed. Presentation of its content in a window or frame external to TDX (framing) is not authorized either. These rights affect both the content of the thesis and its abstracts and indexes.



# Modelling of catalytic systems towards green fuels

---

Jordi Morales Vidal



DOCTORAL THESIS  
2023

UNIVERSITAT ROVIRA I VIRGILI  
MODELLING OF CATALYTIC SYSTEMS TOWARDS GREEN FUELS  
Jordi Morales Vidal

UNIVERSITAT ROVIRA I VIRGILI  
MODELLING OF CATALYTIC SYSTEMS TOWARDS GREEN FUELS  
Jordi Morales Vidal

UNIVERSITAT ROVIRA I VIRGILI  
MODELLING OF CATALYTIC SYSTEMS TOWARDS GREEN FUELS  
Jordi Morales Vidal

**Jordi Morales Vidal**  
Modelling of catalytic systems  
towards green fuels

DOCTORAL THESIS

Supervised by  
Prof. Núria López Alonso and  
Dr. Manuel Ángel Ortuño Maqueda

Institute of Chemical Research of Catalonia (ICIQ)  
and Rovira i Virgili University (URV)



UNIVERSITAT ROVIRA I VIRGILI

Tarragona  
2023

UNIVERSITAT ROVIRA I VIRGILI  
MODELLING OF CATALYTIC SYSTEMS TOWARDS GREEN FUELS  
Jordi Morales Vidal



Institut Català d'Investigació Química  
Av. Països Catalans, 16  
43007 Tarragona. Spain

Prof. Núria López Alonso, group leader at the Institute of Chemical Research of Catalonia and Dr. Manuel Ángel Ortuño Maqueda, junior group leader at Centro Singular de Investigación en Química Biolóxica e Materiais Moleculares.

WE STATE that the present study, entitled “**Modelling of catalytic systems towards green fuels**”, presented by Jordi Morales Vidal for the award of the degree of Doctor in Chemical Science and Technology, has been carried out under our joint supervision at the Institute of Chemical Research of Catalonia and that it fulfills all the requirements to be eligible for the International Doctorate Award.

Tarragona, September 1<sup>st</sup>, 2023



Prof. Núria López Alonso



Dr. Manuel Ángel Ortuño Maqueda



UNIVERSITAT ROVIRA I VIRGILI  
MODELLING OF CATALYTIC SYSTEMS TOWARDS GREEN FUELS  
Jordi Morales Vidal

# Sponsors

The work presented in this Ph.D. thesis has been funded by the Institute of Chemical Research of Catalonia (ICIQ), member of the Barcelona Institute of Technology (BIST) and the Spanish Ministry of Science and Innovation (PRE2019-088791). The generous computer resources provided by the Barcelona Supercomputing Centre (MareNostrum) and the Spanish Supercomputing Network are also acknowledged.



UNIVERSITAT ROVIRA I VIRGILI





# Acknowledgements

No puc començar aquesta secció d'una altra manera que agraint a les tres persones que més m'han fet créixer, tant en la vessant científica com en la personal, desde que vaig arribar al ICIQ. Primer de tot gràcies Núria per donar-me l'oportunitat de començar al grup ara ja fa casi 6 anys com Summerfellow i poder allargar l'aventura durant el màster i el doctorat. El valor de tot el que après és incalculable, qui ho diria que aquell noi que va escriure a la carta de motivació que li agradava la química orgànica acabaria simulant sistemes ternaris amb òxids i metalls... Només puc donar les gràcies per tota la paciència que has tingut amb el meus dubtes i demostrar-me que sempre puc aconseguir molt més del que jo crec. La segunda persona es Manu, contigo empecé este largo camino y seguramente eres el responsable que lo tomara. Me siento muy afortunado de que mi carrera científica empezara bajo tu supervisión, no se me ocurre nadie mejor para ello. Siempre estaré agradecido por todo tu apoyo tanto cuando estabas en el grupo como en la distancia. Y en tercer lugar, pero no menos importante, Rodrigo. Tú me guiaste en la transición de los MOFs a los óxidos, en aprender a afrontar las intensas colaboraciones con nuestros colaboradores experimentales, y sobre todo a salir de mis colapsos. Además, todo esto en medio del COVID y pasando el tiempo que hiciera falta en las llamadas de Skype.

Then, I would also thank Gian-Marco to give me the opportunity to carry out my secondment in Louvain-la-Neuve. It was only for three months but it was enough to learn many new things and give me a bigger perspective of science. And of course, I would always be grateful to be able to meet all the people in the lab, which made me feel as I was at home.

I would also like to thank Prof. Javier Pérez-Ramírez for the fruitful

collaboration over the years with his group. Thaylan deserves a special mention here. We have shared many hectic times but we have always been able to achieve all the “impossible” deadlines.

I need to thank all the people in the computational lab, the actual members and a many former ones. It is supposed to be a working group but it is really more like a family. Especialment vull agrair tot el suport rebut per part de la Núria Vendrell i el Martin, estic segur que aquest laboratorí no podria funcionar ni un sol dia sense vosaltres.

Finalment, però no menys important, he d'agrair a la meva família, en especial als meus pares, i a tots els meus amics el suport incondicional que m'han donat sempre i en particular aquests últims anys. Sense ells, estic segur que no hagués estat possible arribar fins aquí.

# Contents

<b>Abstract</b>	<b>21</b>
<b>1 Introduction</b>	<b>23</b>
1.1 Global energy demand and CO <sub>2</sub> emissions . . . . .	24
1.2 Metal-organic frameworks for electrocatalysis . . . . .	26
1.3 CO <sub>2</sub> valorisation . . . . .	30
1.4 Synergies between experiments and modelling . . . . .	33
1.5 Objectives . . . . .	38
<b>2 Theoretical background</b>	<b>41</b>
2.1 Modelling at the atomic scale . . . . .	41
2.1.1 Schrödinger Equation . . . . .	42
2.1.2 Hohenberg-Kohn Theorems . . . . .	44
2.1.3 Kohn-Sham equations . . . . .	44
2.1.4 Exchange-correlation functionals . . . . .	46
2.1.5 Periodic systems . . . . .	50
2.1.6 Computation of Transition States . . . . .	54
2.2 Computational Hydrogen Electrode . . . . .	56
2.3 General computational details . . . . .	60
<b>3 Electrocatalytic sites of Earth-abundant MOF-74 for OER</b>	<b>63</b>
3.1 Methodology . . . . .	65
3.1.1 Computational details . . . . .	65

3.1.2	Thermodynamics of OER . . . . .	65
3.1.3	Fe-MOF-74 finite-size cluster . . . . .	68
3.2	Properties and catalytic activity of pristine <i>M</i> -MOF-74 . .	71
3.3	Models and catalytic activity of defective Fe-MOF-74 . . .	76
3.3.1	Structural and electronic properties . . . . .	76
3.3.2	Intermidates of OER . . . . .	78
3.3.3	Reversible linker reorganization . . . . .	81
3.4	Conclusions . . . . .	83
<b>4</b>	<b>Metal-promoted metal oxides for green methanol production</b>	<b>85</b>
4.1	Zn promotion of zirconia polymorphs . . . . .	88
4.1.1	Experimental insights in $ZnZrO_x$ . . . . .	89
4.1.2	Methodology . . . . .	92
4.1.3	Zn incorporation into $ZrO_2$ polymorphs . . . . .	96
4.1.4	Oxygen vacancies in $ZnZrO_x$ systems . . . . .	100
4.1.5	Reactivity of Zn-containing $ZrO_2$ polymorphs . . . . .	105
4.2	Metal promotional effects in $In_2O_3$ . . . . .	110
4.2.1	Experimental insights in <i>M</i> - $In_2O_3$ . . . . .	111
4.2.2	Methodology . . . . .	115
4.2.3	Incorporation and deposition of metals promoters on $In_2O_3$ . . . . .	118
4.2.4	Metal promoters speciation and active site formation	120
4.2.5	Mechanistic insights in <i>M</i> - $In_2O_3$ systems . . . . .	123
4.2.6	Promoters' speciation and catalytic activity . . . . .	126
4.3	Metal-metal oxide interactions in $Pd-In_2O_3/ZrO_2$ . . . . .	129
4.3.1	Experimental insights in $Pd-In_2O_3/ZrO_2$ . . . . .	130
4.3.2	Methodology . . . . .	133
4.3.3	Reaction-induced reconstruction of $Pd-In_2O_3/ZrO_2$ .	136
4.3.4	Identification of the active sites . . . . .	138
4.4	Conclusions . . . . .	142
<b>5</b>	<b>Conclusions and Outlook</b>	<b>147</b>

<b>6</b>	<b>Appendix</b>	<b>151</b>
6.1	Appendix A: Electrocatalytic sites of Earth-abundant MOF-74 for OER . . . . .	151
6.2	Appendix B: Zn promotion of zirconia polymorphs . . . . .	153
6.3	Appendix C: Metal promotional effects in $\text{In}_2\text{O}_3$ . . . . .	156
6.4	Appendix D: Metal-metal oxide interaction in $\text{Pd-In}_2\text{O}_3/\text{ZrO}_2$	164
	<b>Publications</b>	<b>195</b>





# Abbreviations

<b>STY</b>	Space-Time Yield
<b>AES</b>	Auger Electron Spectroscopy
<b>AFM</b>	Antiferromagnetic
<b>CHE</b>	Computational Hydrogen Electrode
<b>CI-NEB</b>	Climbing Image Nudged Elastic Band
<b>COP</b>	UN Climate Change Conference
<b>CP</b>	Coprecipitation
<b>DFT</b>	Density Functional Theory
<b>DOS</b>	Density of States
<b>eCO<sub>2</sub>RR</b>	Electrochemical CO <sub>2</sub> Reduction
<b>EDX</b>	Energy-Dispersive X-Ray Spectroscopy
<b>EELS</b>	Electron Energy-Loss Spectroscopy
<b>EPR</b>	Electron Paramagnetic Spectroscopy
<b>EXAFS</b>	Extended X-Ray Adsorption Fine Structure
<b>FM</b>	Ferromagnetic

<b>FSP</b>	Flame Spry Pyrolysis
<b>FS</b>	Final State
<b>GGA</b>	General Gradient Approximation
<b>HAADF</b>	High-Angle Annular Dark Field
<b>HER</b>	Hydrogen Evolution Reaction
<b>HRTEM</b>	High Resolution Transmission Microscopy
<b>IS</b>	Initial State
<b>LDA</b>	Local Density Approximation
<b>MEP</b>	Minimum Energy Path
<b>MOF</b>	Metal-Organic Framework
<b>NEB</b>	Nudged Elastic Band
<b>NP</b>	Nanoparticle
<b>NRR</b>	Nitrogen Reduction Reaction
<b>OER</b>	Oxygen Evolution Reaction
<b>ORR</b>	Oxygen Reduction Reaction
<b>PAW</b>	Projected-Augmented Wave
<b>PCET</b>	Proton-Coupled Electron Transfer
<b>PDS</b>	Potential Determining Step
<b>PES</b>	Potential Energy Surface
<b>RHE</b>	Reversal Hydrogen Electrode
<b>RWGS</b>	Reverse Water-Gas Shift Reaction

<b>SIE</b>	Self Interaction Error
<b>SMSI</b>	Strong Metal-Support Interaction
<b>STEM</b>	Scanning Transmission Electron Microscope
<b>TPR</b>	Temperature-Programmed Reduction
<b>TS</b>	Transition State
<b>VASP</b>	Vienna ab Initio Simulation Package
<b>WNA</b>	Water Nucleophilic Attack
<b>XANES</b>	X-Ray Adsorption Near-Edge Structure
<b>XAS</b>	X-Ray Adsorption Spectroscopy
<b>XPS</b>	X-Ray Photoelectron Spectroscopy
<b>XRD</b>	X-Ray Diffraction



# List of Publications

1. **Defects as catalytic sites for the oxygen evolution reaction in Earth-abundant MOF-74 revealed by DFT.** J. Morales-Vidal, R. García Muelas, M. A. Ortuño, Catal. Sci. Technol., **2021**, 11, 4, 1443-1450.
2. **Design of flame-made ZnZrOx catalysts for sustainable methanol synthesis from CO<sub>2</sub>.** T. P. Araújo, J. Morales-Vidal, T. Zou, M. Agrachev, S. Verstraeten, P. O. Willi, R. N. Grass, G. Jeschke, S. Mitchell, N. López, J. Pérez-Ramírez, Adv. Energy Mater., **2023**, 13, 14, 2204122.
3. **Flame spray pyrolysis as a synthesis platform to assess metal promotion in In<sub>2</sub>O<sub>3</sub>-catalyzed CO<sub>2</sub> hydrogenation.** T. P. Araújo, J. Morales-Vidal, T. Zou, R. García-Muelas, P. O. Willi, K. M. Engel, O. V. Safonova, D. F. Akl, F. Krumeich, R. N. Grass, C. Mondelli, N. López, J. Pérez-Ramírez, Adv. Energy Mater., **2022**, 12, 13, 2103707.
4. **Nanostructure of nickel-promoted indium oxide catalysts drives selectivity in CO<sub>2</sub> hydrogenation.** M. S. Frei, C. Mondelli, R. García-Muelas, J. Morales-Vidal, M. Philipp, O. V. Safonova, N. López, J. A. Stewart, D. Curulla Ferré, J. Pérez-Ramírez, Nat. Commun., **2021**, 12, 1, 1960.

5. **Reaction-induced metal-metal oxide interactions in Pd-In<sub>2</sub>O<sub>3</sub>/ZrO<sub>2</sub> catalysts drive selective and stable CO<sub>2</sub> hydrogenation to methanol.** T. P. Araújo, J. Morales-Vidal, G. Giannakakis, C. Mondelli, H. Eliasson. R. Erni. J. A. Stewart, S. Mitchell, N. López, J. Pérez-Ramírez, *Angew. Chem. Int. Ed.*, **2023**, e202306563.

The contributions of Jordi Morales Vidal to the previous publications are the following:

- He wrote the first draft and carried out all the DFT simulations in publication 1.
- He performed all DFT simulations, actively participated in the writing, produced DFT-related figures, and took part in the analysis and discussion of publications 2, 3, and 5.
- He did some of the DFT simulations and contributed to the design and production of some figure of publication 4.

Furthermore, Jordi Morales Vidal has contributed to the following publications:

1. **Computer simulations of porous materials: spectroscopic and catalytic properties.** J. Morales-Vidal, M. A. Ortuño, **2021**, 215-264.
2. **Chiral seeded growth of gold nanorods into fourfold twisted nanoparticles with plasmonic optical activity** B. Ni, M. Mychinko, S. Gómez-Graña, J. Morales-Vidal, M. Obelleiro-Liz, W. Heyvaert, D. Vila-Liarte, X. Zhuo, W. Albrecht, G. Zheng, G. González-Rubio, J. M. Taboada, F. Obelleiro, N. López, J. Pérez-Juste, I. Pastoriza-Santos, H. Cölfen, S. Bals, L. M. Liz-Marzán, *Adv. Mater.*, **2022**, 35, 1, 2208299.

3. **Selective hydrogenolysis of 5-hydroxymethylfurfural to 5-methylfurfural over Au/TiO<sub>2</sub>.** L. Dong, J. Morales-Vidal, L. Mu, L. Li, N. López, J. Pérez-Ramírez, Z. Chen, *Appl. Catal. B*, **2023**, 335, 122893.





# Abstract

With the current growth of the global population and the unsustainable increase of the energy demand and CO<sub>2</sub> emissions, we need to move forward to more environmentally friendly socioeconomic models to mitigate the effects of climate change. In this scenario, the development of technologies related to renewable energies and the valorisation of CO<sub>2</sub> are called to play a crucial role, which are the two central ideas of this thesis. In order to make these two processes affordable, I have employed density functional theory simulations and established tight synergies with experimental testing and characterization to contribute in the search and design of novel catalytic materials towards green fuels. I have assessed the electrocatalytic properties of earth-abundant based MOF-74 for oxygen evolution reaction, which is the bottleneck of green H<sub>2</sub> production *via* water splitting. Defective structures have been identified as the active sites of these materials. In reference to CO<sub>2</sub> valorisation, I have explored synthesis-structure-performance relationships of three metal-promoted metal oxides systems: ZnZrO<sub>x</sub>, metal-promoted In<sub>2</sub>O<sub>3</sub>, and the ternary Pd-In<sub>2</sub>O<sub>3</sub>/ZrO<sub>2</sub>. These systems have shown high stability and catalytic activity for the CO<sub>2</sub> hydrogenation with green H<sub>2</sub> to methanol, which is a vital commodity with a great potential as fuel. The proper combination of oxidic and metallic phases has been revealed as key for maximizing the catalytic properties of these systems and achieve high methanol productivity. Overall, the features that dictate the electrocatalytic activity of MOF-74 materials for oxygen evolution reaction and the thermocatalytic properties of metal-promoted metal oxides for CO<sub>2</sub> hydrogenation have been identified in this thesis. This paves the way to the rational design of novel catalytic materials for energy applications.

UNIVERSITAT ROVIRA I VIRGILI  
MODELLING OF CATALYTIC SYSTEMS TOWARDS GREEN FUELS  
Jordi Morales Vidal

# Chapter 1

## Introduction

The growth of the global population and economy is unequivocally correlated with an increase of the energy demand and CO<sub>2</sub> emissions.<sup>1-4</sup> The coupling of this unsustainable growth with our reliance on fossil fuels and geopolitical complexities, has led into an undeniable acceleration of the climate change and a global energy crisis.<sup>5-9</sup> As a result, an urgent and efficient transition into economies based in renewable energy sources and the valorisation of CO<sub>2</sub> are imperative to avoid the collapse of the humankind. This thesis revolves around these two preceding ideas, aimed at providing my humble contribution while acknowledging the intricate complexity of the scenario.

On the one hand, this thesis is centred in the modelling of metal-organic frameworks (MOFs) with Density Functional Theory (DFT) simulations to explore their electrocatalytic properties (**Chapter 3**).<sup>10</sup> Electrocatalysis represents a strategy to overcome the intermittent nature and inefficient storage of renewable energies.<sup>11</sup> Particularly, I assessed the catalytic activity of Earth abundant based MOF-74 systems towards oxygen evolution reaction (OER). This is the bottleneck of water splitting, which holds the potential for producing H<sub>2</sub> from water through a CO<sub>2</sub>-free path.<sup>12</sup>

On the other hand, I have used DFT simulations to unravel the architecture and the catalytic properties of metal-promoted metal oxides that have shown efficient methanol productivity *via* thermocatalytic CO<sub>2</sub> hydrogenation with green H<sub>2</sub> (**Chapter 4**).<sup>13-16</sup> This process represents a

## Chapter 1. Introduction

---

promising path for CO<sub>2</sub> valorisation by converting this greenhouse gas into methanol, a prospective energy carrier and a key chemical platform.<sup>17–26</sup>

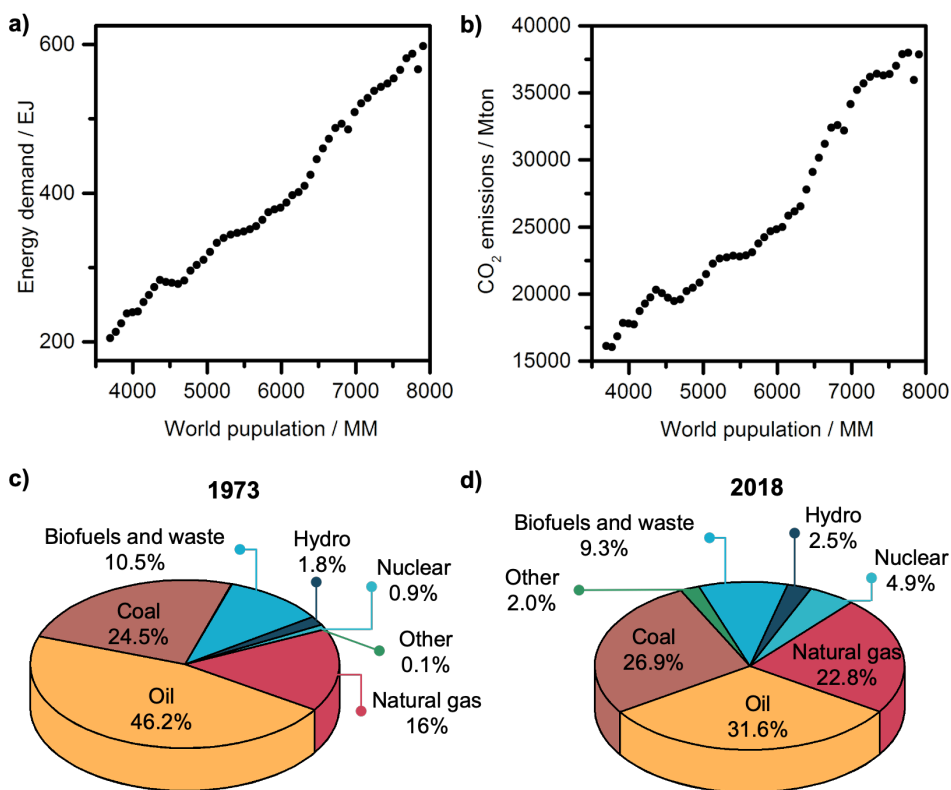
Finally, the other pivotal idea developed throughout this thesis is the need to establish tight synergies between experiments and DFT simulations. These synergies are crucial to obtain synthesis-structure-performance relationships and reveal key features of the materials under study due to their complex electronic and geometric properties.

### 1.1 Global energy demand and CO<sub>2</sub> emissions

The global energy demand is unsustainable increasing over the last years due to the growth of global population, which is accompanied with a higher degree of urbanization, economic development, industrialization, technological advancements, transportation, energy-intensive activities, and other factors linked to different aspects of modern life (**Figure 1.1**).<sup>1,2</sup> This situation puts a great strain on Earth and its natural resources, leading the planet to a point of almost no return. This is perfectly exemplified by the ever-earlier arrival of Earth Overshoot Day, which is the day within a calendar year when humanity's demand for ecological resources exceeds the Earth's capacity to regenerate them for that year.<sup>27</sup> Specifically, in 2023 we have alarmingly reached this point on August 22<sup>nd</sup>, which means that this year we would need 1.75 Earths to meet global natural resource demands. Moreover, the growth of the global population scales with a raise of anthropogenic greenhouse gasses emissions, in particular CO<sub>2</sub> (**Figure 1.1**).<sup>1,3,4</sup> This scenario is accelerating the climate change, which is bringing with it global warming, episodes of extreme weather, melting of polar ice caps, loss of biodiversity, ocean acidification and sea level rise.<sup>28–32</sup> Even the unequivocal signals from Earth calling for a change in our socioeconomic models, data comparing the global energy sources from 1973 and 2018 indicate that we are ignoring this call (**Figure 1.1**).<sup>4</sup> We have only increased a 1.4 % the contribution of renewable energies during this period. It is therefore clear that we need to urgently move forward to more sustainable life model by fostering the use of renewable energies and CO<sub>2</sub> valorisation,

### 1.1. Global energy demand and CO<sub>2</sub> emissions

which has been so far hindered by economic and political factors. In this regard, the contributions of the scientific community are pivotal to provide the technological advances to make this transition effective and affordable. Unfortunately, this would not be possible without a drastic change in the priorities and actions of the society, specially politicians and economic elites.



**Figure 1.1:** a) Global energy demand<sup>2</sup> and b) CO<sub>2</sub> emissions<sup>3</sup> vs world population<sup>2</sup> from 1970 to 2021. Energy sources for covering global energy demand at c) 1973 and d) 2018.<sup>4</sup>

## Chapter 1. Introduction

---

### 1.2 Metal-organic frameworks for electrocatalysis

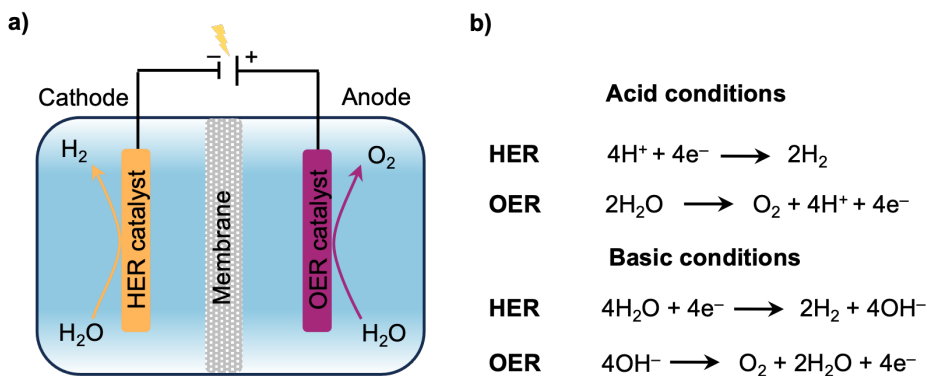
The most straightforward solution to decarbonize our energy sources relies on the use of renewable energies, such as solar, wind, or water. However, the intermittent character and the inefficient storage of these green energies may result in a disparity between energy supply and demand. In this scenario, the coupling of renewable energy sources with electrocatalysis arises as promising strategy to remediate the drawbacks of the former.<sup>11</sup> Particularly, the electricity obtained from environmentally friendly sources can be used to electrochemically convert simple and abundant molecules ( $\text{H}_2\text{O}$ ,  $\text{CO}_2$ , and  $\text{N}_2$ ) into higher value-products and store the energy in chemical bonds.<sup>33,34</sup> Nevertheless, such processes like OER, oxygen reduction reaction (ORR), electrochemical  $\text{CO}_2$  reduction (e $\text{CO}_2$ RR), or nitrogen reduction reaction (NRR), entail energy demanding reactions which are not favourable from a thermodynamic standpoint. Chapter 3 of this thesis focuses in OER, which together with hydrogen evolution reaction (HER) is involved in water splitting (**Equation 1.1**).<sup>35,36</sup> This represents a promising path to obtain green  $\text{H}_2$  which can be used as clean fuel, energy carrier and feedstock for a myriad of products.<sup>37</sup> Interestingly, green  $\text{H}_2$  can be employed in the thermocatalytic hydrogenation of  $\text{CO}_2$  to obtain methanol, which is the other catalytic process assessed in this thesis (**Chapter 4**).<sup>13-26</sup>



During water splitting in an electrocatalytic cell, HER and OER take place at the cathode and anode, respectively (**Figure 1.2**). HER is a two electron-proton transfer process that consists in the reduction of protons to form hydrogen gas, whereas OER involves the oxidation of water to produce oxygen gas through four proton-electron transfers. It should be noted that OER is considered the bottleneck of water splitting because of its higher energy requirements. Due to the sluggish kinetics of the OER, a high energy input is required to drive the reaction towards the products, the so-called overpotential.<sup>12</sup> This is determined by subtracting the standard potential, 1.23 V *vs* reversible hydrogen electrode (RHE), from the applied potential

## 1.2. Metal-organic frameworks for electrocatalysis

needed to attain a current density of 10 mA/cm<sup>2</sup>.<sup>38</sup>



**Figure 1.2:** a) Schematic representation of water splitting electrolyzer and b) reactions involved under acid and basic conditions.

Thus, the design and development of novel electrocatalysts that (i) allows the efficient oxidation of water at low overpotentials, (ii) based on Earth-abundant materials, and (iii) with high stability under reaction conditions, becomes crucial. The interplay between homogeneous and heterogeneous catalysis has emerged as a pivotal concept in this seek. Within this concept, metal-organic frameworks (MOFs) are ideal candidates for accomplishing the aforementioned requirements.

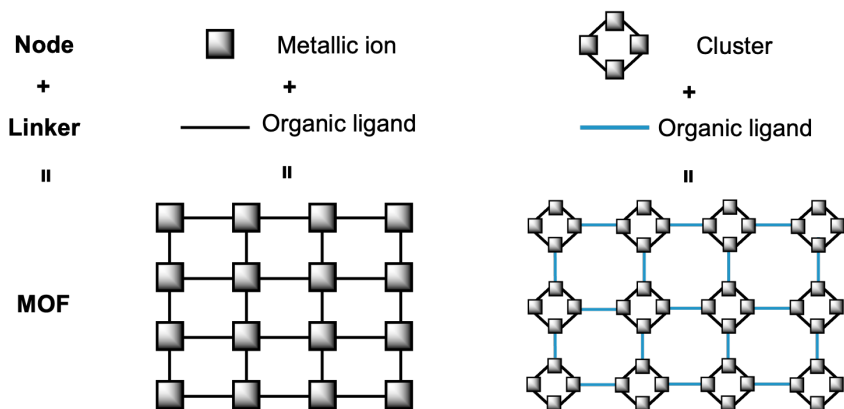
MOFs are crystalline porous materials that are built by nodes (metallic cations or clusters) connected by linkers (organic ligands), which could be arranged in different ways leading to a wide number of distinct topologies and pore sizes (**Figure 1.3**).<sup>39,40</sup> This hybrid structure renders materials with well-defined active sites easily tuneable, high surface areas, robustness, stability, reusability, and well-defined porosity where molecules can smoothly diffuse. In addition, these systems can be further tailored by post-synthetic modifications of the linkers and nodes by anchoring species or defect engineering.<sup>41–46</sup>

Thereby, MOFs combine the properties of homogeneous and



## Chapter 1. Introduction

---

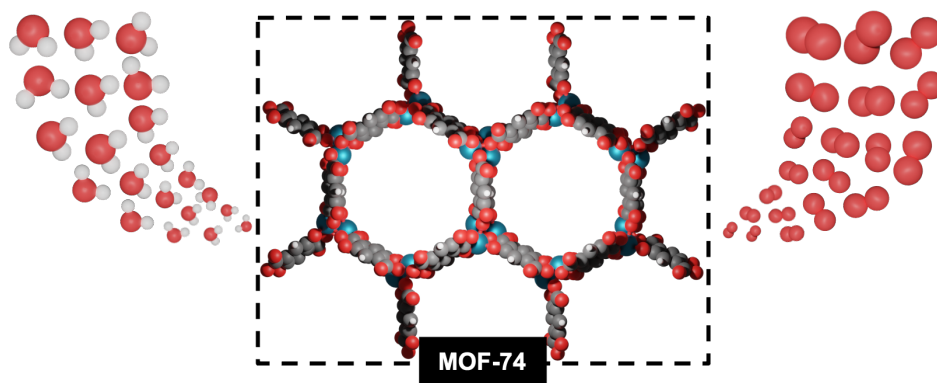


**Figure 1.3:** Schematic representations of the topology of MOFs.

heterogeneous catalysts and possesses the potential for rational design. Such versatility provides high applicability in a myriad of fields such as gas adsorption, gas separation, drug delivery, sensing and catalysis.<sup>47–55</sup> In reference to the last, MOFs have been successfully employed in thermocatalytic, photocatalytic and electrocatalytic processes. The application in electrocatalysis was initially hampered due to the intrinsic insulator character of these materials. However, several strategies (*i.e.* coupling to conductive materials, loading of nanoparticles (NPs) or guest species, or control over the film thickness of deposition) have been successfully developed to increase the conductivity of MOFs and enhance their properties as electrocatalysts.<sup>38,52,55–60</sup> Despite the high number of studies showing MOFs with promising electrocatalytic activity, the nature of their active sites remains elusive. Therefore, the integration of experimental information and computational approaches combined with the development of databases are called to play a crucial role to assess the electronic and structural properties of MOFs, explore their active sites and reaction mechanisms, and carry out high throughput screening coupled with artificial intelligence.<sup>40,61–68</sup> In this context, I have explored the catalytic activity of Co- and Fe-MOF-74 towards OER by means of DFT simulations in **Chapter 3 (Figure 1.4)**. These are

## 1.2. Metal-organic frameworks for electrocatalysis

Earth-abundant based materials that have shown promising electrocatalytic activities.<sup>69</sup> Thereby, I have employed computational approaches to elucidate the nature of the active sites and benchmark the methodology to reveal key aspects for the rational design of MOFs for electrocatalysis.<sup>10</sup>



**Figure 1.4:** Schematic representation of the process under study in **Chapter 3**, oxygen evolution reaction (OER) catalysed by MOF-74. Color code: O (red), H (white), C (dark gray), and metals (blue).

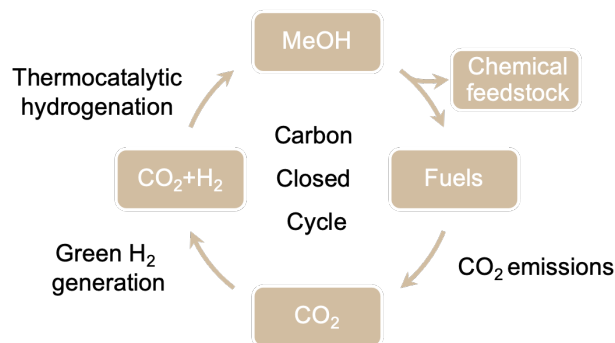
## Chapter 1. Introduction

---

### 1.3 CO<sub>2</sub> valorisation

The anthropogenic increase of the atmospheric concentration of greenhouse gases, specially CO<sub>2</sub>, is the main responsible of the exacerbated climate change and its every day more noticeable and undeniable consequences.<sup>70</sup> For this reason, in the context of the 21<sup>st</sup> UN Climate Change Conference (COP21) held in France in 2015, 195 parties signed a legally binding international treaty on climate change, the so-called Paris Agreement.<sup>71</sup> The long-term goal of this treaty is to hold the increase in the global average temperature to well below 2°C above pre-industrial levels with the aim to limit the increase to 1.5°C. In order to achieve this goal, greenhouse gas emissions must peak before 2025 at the latest, decline 43% by 2030, and become net-zero by 2050. COP21 marked a significant turning point in international climate negotiations and it is often considered a cornerstone in the series of UN Climate Change Conferences. Five more editions of these conference have been carried out in different cities since 2015 (COP22, COP23, COP24, COP25, and COP26). All of them focused in the implementation and assessment of the progress of the goals set in the Paris agreement in order to establish new guidelines and strategies. However, the achievement of these objectives is an enormous challenge due to our reliance in fossil fuels energy sources (**Figure 1.1**) and that CO<sub>2</sub> emitting technologies are the core of our society.<sup>21</sup> Thereby, on a short to medium term, one approach to mitigate the impact of CO<sub>2</sub> emissions is through its capture and valorisation. In such a way, the atmospheric concentration of this greenhouse gas would be reduced and it could be converted into valuable products. In this scenario, the thermocatalytic hydrogenation of CO<sub>2</sub> to methanol has become a hot topic in the scientific and industrial communities.<sup>8,17–26</sup>

Methanol is a versatile chemical feedstock employed to produce a myriad of products, such as acetic acid, formaldehyde, dimethyl ether, methylamine, olefins, aromatics, pharmaceutical products, and plastics among others.<sup>72–75</sup> Moreover, this C<sub>1</sub> alcohol is used as fuel or fuel additive, providing greener combustion than conventional fossil fuels.<sup>75,76</sup> Thereby, methanol is a vital commodity and its global demand has been duplicated in the last



**Figure 1.5:** Schematic representation of carbon close cycle based in the CO<sub>2</sub>-captured hydrogenation with green H<sub>2</sub> to methanol.

decade leading to an annual production of approximately 100 Mt at 2020.<sup>75</sup> Furthermore, projections indicate that the demand for this chemical will increase to 120 Mt by year at 2025 and further rise to 500 Mt by year at 2050.<sup>8</sup> Unfortunately, 99% of the global produced methanol is currently obtained from fossil fuels (coal and natural gas) and this represents *ca.* 5% of the chemical sector greenhouse gases emissions.<sup>75</sup> Therefore, only 1% of the global production is considered green methanol, which is obtained from biomass and renewable feedstocks. This huge disparity between green and fossil fuels-based methanol production is due to the difference on prices, being green methanol 1.3–2.6-fold more expensive.<sup>17</sup> However, with the aim of mitigating the effects of climate change and decrease the atmospheric CO<sub>2</sub> concentration, a transition to green methanol production is mandatory. In this context, the development of technologies able to make the thermocatalytic hydrogenation of captured CO<sub>2</sub> with green hydrogen viable is cornerstone to achieve a closed carbon cycle in methanol production (**Figure 1.5**).<sup>17</sup> Thus, different processes and materials must be further developed:

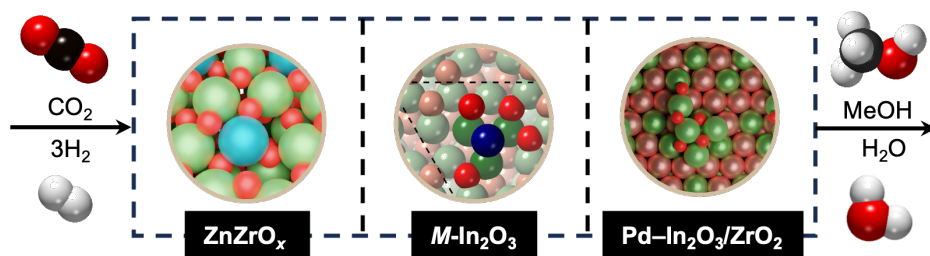
- Efficient electrocatalysts with low overpotentials towards water splitting to make green H<sub>2</sub> production feasible, as explained in previous

## Chapter 1. Introduction

---

sections and **Chapter 3** of this thesis.

- The current technologies employed for CO<sub>2</sub> capture must be improved to lower its cost.
- Design of novel catalysts based in Earth-abundant materials able to effectively activate CO<sub>2</sub><sup>19</sup> and its concomitant selective hydrogenation to methanol rendering high productivity. In this regard, **Chapter 4** of this thesis focuses in the seek of synthesis-structure-performance relationships in ZnZrO<sub>x</sub>, metal-promoted In<sub>2</sub>O<sub>3</sub>, and the ternary Pd-In<sub>2</sub>O<sub>3</sub>/ZrO<sub>2</sub> systems by means of DFT simulations and establishing tight synergies with experimental testing and characterization (**Figure 1.6**).<sup>13–16</sup> In particular, I have assessed in collaboration with the group of Prof. Javier Pérez-Ramírez (i) the influence of the synthetic method and the Zn speciation in the architecture and catalytic activity of ZnZrO<sub>x</sub> systems; (ii) the metal promotional effects of nine distinct metals introduced in In<sub>2</sub>O<sub>3</sub>; and (iii) the reaction-induced reconstructions observed under reaction conditions for the ternary Pd-In<sub>2</sub>O<sub>3</sub>/ZrO<sub>2</sub> system.



**Figure 1.6:** Schematic representation of the process under study in **Chapter 4**, CO<sub>2</sub> hydrogenation to methanol catalysed by metal-promoted metal oxides (ZnZrO<sub>x</sub>, M-In<sub>2</sub>O<sub>3</sub>, and Pd-In<sub>2</sub>O<sub>3</sub>/ZrO<sub>2</sub>). Color code: O (red), H (white), C (dark gray) Zr/In (green), Zn (light blue), Pd (light pink), and metal promoter (blue).

#### *1.4. Synergies between experiments and modelling*

---

## **1.4 Synergies between experiments and modelling**

The intersection between experiments and modelling would be pivotal for carry out fast, efficient, and rational search and design of novel materials and processes. This is crucial to move forward into sustainable socioeconomic models before the consequences of the climate change become irreversible. In the last years, the high degree of technological advancement and knowledge reached by the scientific community have enable us to have access to (i) experimental characterization techniques with unprecedented accuracy and resolution, and (ii) high computational power coupled with simulation methods with well balanced cost-accuracy ratio, such as DFT. These advances offer a comprehensive view of complex materials involved in intricate processes. In this regard, it is the synergy between experiments and modelling which leverages the strengths of both fields and is greater than the sum of its parts.

DFT simulations provides information of the materials and catalytic process at the atomic level of detail which is not possible to achieve with experimental characterization. However, the output and rationalization of the data obtained by DFT is highly dependent in the models employed. Therefore, the selection of such models should be strongly based in the experimental characterization insights. Moreover, it should be highlighted that the rationalization and elucidation of key factors ruling the catalytic activity of complex materials can not be revealed with a single DFT model or one characterization technique. Instead, a combination of different types of models and techniques, as well as assessment of the fresh, activated and used forms of the catalytic systems, are needed to obtain a comprehensive picture of the material and process under study. Once the key properties that drive the catalytic activity are elucidated by means of the synergy between experiments and DFT simulations, these "ingredients" can be employed to the rational design of novel systems. At this point, DFT simulations could be used as an effective tool to screen large pools of materials and select the best candidates to be tested in the laboratory. Overall, the cooperation between experiments and DFT should be understood as a feedback loop (**Figure 1.7**).

## Chapter 1. Introduction

---



**Figure 1.7:** Sketch of the feedback loop between experiments and simulations. Adapted from [77].

Thereby, this thesis revolves around the synergy between modelling and experiments, being the former the central point of the work. Furthermore, it should be mentioned that the synergy has been explored in two different ways. On the one hand, DFT simulations are employed in **Chapter 3** to elucidate the active sites of Earth-abundant based MOF-74, which have shown promising electrocatalytic activity towards OER in an already published experimental work.<sup>69</sup>

On the other hand, I have used DFT simulations in **Chapter 4** to reveal synthesis-structure-performance relationships of metal-promoted metal oxides ( $\text{ZnZrO}_x$ ,  $M\text{-In}_2\text{O}_3$ , and  $\text{Pd-In}_2\text{O}_3/\text{ZrO}_2$ ) with high activity and selectivity towards  $\text{CO}_2$  hydrogenation to methanol. In this case, the work has been carried out in tight collaboration with the group of Prof. Javier Pérez-Ramírez, who were in charge of the synthesis, experimental testing and in-depth characterization of the catalytic materials. The particular synergies established between the two fields, such as the implications of the experimental characterization for building the DFT models, are explained in detail in **Chapter 4**. The experimental techniques employed to characterize the fresh, activated and used catalysts were the following ones:

- High resolution transmission microscopy (HRTEM).<sup>78</sup>

#### 1.4. Synergies between experiments and modelling

---

- X-ray diffraction (XRD) and high-resolution-XRD (HR-XRD).<sup>78,79</sup>
- UV Raman.<sup>78,79</sup>
- High-angle annular dark-field scanning transmission electron microscopy coupled to energy-dispersive X-ray spectroscopy (HAADF-STEM-EDX).<sup>78-80</sup>
- HAADF-STEM coupled to electron energy-loss spectroscopy (HAADF-STEM-EELS).<sup>78-80</sup>
- X-ray photoelectron spectroscopy (XPS).<sup>79,80</sup>
- Two types of X-ray absorption spectroscopy (XAS): X-ray absorption near-edge structure (XANES) and extended X-ray adsorption fine structure (EXAFS).<sup>78-80</sup>
- Auger electron spectroscopy (AES).<sup>81</sup>
- Electron paramagnetic spectroscopy (EPR).<sup>79,82</sup>
- Temperature-programmed reduction with hydrogen (H<sub>2</sub>-TPR).<sup>83</sup>
- Volumetric CO and CO<sub>2</sub> adsorption ( $V_{CO}$  and  $V_{CO_2}$ , respectively).<sup>84</sup>

The fundamentals, the information that could be retrieved, and the limitations of these techniques are shown in **Tables 1.1** and **1.2**. It should be noted that information retrieved from the experimental techniques and the limitations depicted in **Tables 1.1** and **1.2** are focused in the systems under study of this thesis, but this list could be extended when characterizing other type of materials.



## Chapter 1. Introduction

**Table 1.1:** Fundamentals, retrieved insights, and limitations of the experimental characterization techniques employed in **Chapter 3**.

Technique	Fundamentals	Insights	Limitations
HRTEM	High-resolution images generated by the interaction of a focused electron beam transmitted through a thin material and the atoms of the sample.	Morphology of NPs. Lattice parameters. Crystal terminations. Identification of different polymorphs.	Complex sample preparation.
(HR)-XRD	Bragg's law and the interference of X-rays beam when interacting with the sample that produce a changing in the direction of the beam at some particular angle (diffraction angle). HR-XRD is based in the same principles but it provides higher sensibility and measurement must carried out at cyclotron facilities.	Morphology of NPs. Lattice parameters. Crystal terminations. Identification of different polymorphs.	Average of the whole material. NPs smaller than 4nm are not detected. High-crystalline samples needed.
UV-Raman	Spectroscopic technique that employs ultraviolet light as the excitation source and it is based in the inelastic scattering of photons (Raman scattering) when interacting with the sample.	Assessment of different particles' depth (from bulk to surface) by changing the wavelength of the laser source. Identification of different polymorphs.	Not suitable for fluorescent samples.
STEM-HAADF-EDX	STEM is an imaging technique based in the detection of the electrons transmitted by the sample when it is exposed to an electron beam. HAADF is a type of detector employed to increase the contrast with lighter elements. EDX is a spectroscopic technique based on the measurement of energies of the X-rays emitted by the sample when exposed to the electron beam, which are characteristic of each element.	Elemental composition. Degree of dispersion of selected elements. Atomic resolution.	Local region. The sensibility is function of the element under study. The signals between some elements are indistinguishable.
STEM-HAADF-EELS	EELS is a spectroscopic technique based on the measurement of the energy losses of electrons after interacting with the sample which are characteristic of each element.	Elemental composition. Degree of dispersion of selected elements. Atomic resolution.	Local region. The sensibility is function of the element under study. The signals between some elements are indistinguishable. Selection of the reference accounting for environmental effects. XPS O 1s: overlapping of different signals.
XPS	Spectroscopic technique based on the photoelectric effect where X-ray photons are used to eject electrons from the outermost energy levels of the atoms of the sample.	Surface-sensitive technique. Elemental composition. Chemical state. XPS O 1s: identification of different types of oxygen and oxygen vacancies.	

## 1.4. Synergies between experiments and modelling

**Table 1.2:** Fundamentals, retrieved insights, and limitations of the experimental characterization techniques employed in **Chapter 3**.

Technique	Fundamentals	Insights	Limitations
XANES	Synchrotron-based spectroscopic technique based on the photoabsorption of X-ray by the core level of the element under study followed by photoelectron emission and filling of the core hole by an electron in an other level. It covers a range of 30-50 eV above and below the adsorption edge. Synchrotron-based spectroscopic technique based in the same principle than XANES. It covers a range of 50-1500 eV above the adsorption edge. Spectroscopic technique based in the Auger effect. Detection of energetic electrons emitted after the filling of core holes originated by X-ray beam interacting with a particular element of the sample. Spectroscopic technique based in the change of the spin state of species of the sample with unpair electrons induced by the absorption of microwave radiation.	Element-specific. Chemical state.	Average of the whole material.
EXAFS		Element-specific. Coordination environment.	Average of the whole material. The signals between some elements are indistinguishable.
AES		Surface-sensitive. Element-specific.	Average of the whole material.
EPR		Identification of species related with different type of oxygen vacancies. Sensible to the amount of EPR active species.	Only species with unpair electrons are detected. Average of the whole material.
H <sub>2</sub> -TPR	Reduction of a material by being expose to hydrogen gas and gradually increase the temperature. The degree of reduction is determined by monitoring the amount of H <sub>2</sub> consumed or H <sub>2</sub> O.	At low temperature indicates the degree of surface reduction while at high temperatures depicts bulk reduction. Oxygen vacancy formation. H <sub>2</sub> adsorption properties of the sample. Ability of the sample to adsorb CO or CO <sub>2</sub> .	It cannot be carry out under particular reaction conditions. Average of the whole material.
V <sub>CO</sub> , CO <sub>2</sub>	Apply CO or CO <sub>2</sub> and measure the variations in the probe molecules pressure due to the adsorption and desorption process.		It cannot carry out under particular reaction conditions. Average of the whole material.

## Chapter 1. Introduction

---

### 1.5 Objectives

The general goal of this thesis is to provide my contribution to the design of catalytic systems towards green fuels to develop tools to enable the transition of our economic-social model into a more sustainable and environmentally friendly one. In particular, this thesis is focused in the assessment *via* DFT simulations of Earth-abundant based catalysts for OER and CO<sub>2</sub> hydrogenation to methanol. All the work presented has been carried out by establishing tight synergies with experimental testing and characterization. In addition, the FAIR principles have been followed, which means to make the results Findable, Accessible, Interpolable, and Reusable.<sup>85</sup> To this aim, all DFT data can be found online in the ioChem-BD repository.<sup>86,87</sup> Moreover, four of the five publications derived from this thesis were granted open access.<sup>13-16</sup> The particular objectives for each chapter are detailed in the following lines.

**Chapter 3** Electrocatalytic sites of Earth-abundant MOF-74 for OER. Rationalize *via* DFT simulations the electrocatalytic activity towards OER shown by Fe-MOF-74 in a previous experimental work<sup>69</sup>:

- Electronic and structural characterization of Fe-MOF-74.
- Elucidate the active sites of Fe-MOF-74 by computing the energy profiles associated with OER in different models.
- Benchmarking of the computational methodologies employed to evaluate their performance towards the assessment of electronic and structural properties of Fe-MOF-74, as well as its catalytic activity.
- Identification of key features of Fe-MOF-74 at the atomic level of detail to provide guidance for the rational design of other Earth-abundant based electrocatalytic materials.

**Chapter 4** Metal-promoted metal oxides for green methanol. production Uncover synthesis-structure-performance relationships of metal-promoted metal oxides for CO<sub>2</sub> thermocatalytic hydrogenation with green H<sub>2</sub> to methanol. With this aim, a tight collaboration between DFT simulations and experimental characterization and testing was carried out, being the former the main point of the chapter. The particular objectives of this chapter are divided in three subsections representing the three distinct catalytic systems under study (ZnZrO<sub>x</sub>, *M*-In<sub>2</sub>O<sub>3</sub>, and Pd-In<sub>2</sub>O<sub>3</sub>/ZrO<sub>2</sub>).

**Chapter 4.1** Zn promotion of zirconia polymorphs.

- Rationalize the Zn speciation, structural features and catalytic properties of the ZnZrO<sub>x</sub> catalysts prepared by two different synthetic methods, coprecipitation (CP) and flame spray pyrolysis (FSP).
- Assess the relative stability between *m*-, *t*-, and *c*-ZrO<sub>2</sub> polymorphs and the influence of Zn incorporation into different bulk, subsurface, and surface sites.
- Explore the formation of oxygen vacancies in Zn-doped and pure *m*-, *t*-, and *c*-ZrO<sub>2</sub> polymorphs.
- Compute the reaction energy profiles for CO<sub>2</sub> hydrogenation to methanol and CO on the most representative models of the three ZnZrO<sub>x</sub> polymorphs.
- Identify the key features that dictate the catalytic activity of ZnZrO<sub>x</sub> systems towards CO<sub>2</sub> hydrogenation.

**Chapter 4.2** Metal promotional effects in In<sub>2</sub>O<sub>3</sub>.

- Rationalize the speciation of nine different promoters introduced in In<sub>2</sub>O<sub>3</sub> with a standardized synthetic method (FSP).
- Reveal the activate sites of the nine *M*-In<sub>2</sub>O<sub>3</sub> systems towards CO<sub>2</sub> hydrogenation to methanol at the atomic level of detail.

## *Chapter 1. Introduction*

---

- Identify the key features that dictate metal promotional effects and thus the catalytic activity of the  $M\text{-In}_2\text{O}_3$  systems.

### **Chapter 4.3** Metal-metal oxide interactions in Pd-In<sub>2</sub>O<sub>3</sub>/ZrO<sub>2</sub>.

- Assess the reaction-induced reconstruction shown by the ternary Pd-In<sub>2</sub>O<sub>3</sub>/ZrO<sub>2</sub> catalytic system.
- Reveal the driving-force of the reconstruction by exploring the interactions of the different components of the catalyst at the atomic level of detail.
- Identify the active sites and the key features that dictate the catalytic activity of Pd-In<sub>2</sub>O<sub>3</sub>/ZrO<sub>2</sub> leading to higher methanol productivity compared with its binary counterparts.

## Chapter 2

# Theoretical background

Atomic-scale understanding of the catalytic systems studied in this thesis is key to elucidate their synthesis-structure-performance relationships. Therefore, I assessed from a computational standpoint the structural and electronic features of the materials, as well as the species involved in the chemical reactions of interest. This implies bond breaking and formation, which is not well defined in classical mechanics. For this reason, the majority of the work conducted in this thesis was carried out in the framework of quantum mechanics *via* Density Functional Theory (DFT) simulations.<sup>88</sup> Moreover, I also relied on the Computational Hydrogen Electrode (CHE)<sup>89</sup> approach to model electrochemical processes, such as OER. Thereby, the fundamentals of Density Functional Theory and the Computational Hydrogen Electrode are explained throughout this chapter.

### 2.1 Modelling at the atomic scale

DFT has become the state-of-the-art for rationalizing the properties of the matter at the atomic level of detail.<sup>90</sup> It is based on the principles of quantum mechanics and is an approach to solve the Schrödinger equation. The importance of DFT lies in a well balanced accuracy-efficiency, wide applicability, flexibility, and predictive capabilities.<sup>90</sup>

## Chapter 2. Theoretical background

---

### 2.1.1 Schrödinger Equation

Materials could be described as a collection of quantum particles, particularly electrons and nuclei. The Austrian physicists Erwin Schrödinger proposed that the behaviour of such particles is explained by means of wavefunctions with the time-independent Schrödinger equation (**Equation 2.1-2.2**).<sup>91</sup> This is an eigenvalues equation where  $\Psi$  is the state vector of the system and  $\hat{H}$  represents the Hamiltonian operator.  $\Psi_n$  are the solutions or eigenstates of  $\hat{H}$  and they have associated  $n$  eigenvalues ( $E_n$ ), which are real numbers. Finally, the position-space wavefunction is defined through the expansion in terms of the positions eigenvectors of the state vector (**Equation 2.3**).

$$|\hat{H}|\Psi\rangle = |E|\Psi\rangle \quad (2.1)$$

$$\hat{H}\Psi_n = E_n\Psi_n \quad (2.2)$$

$$\Psi(\mathbf{r}) = \langle\mathbf{r}|\Psi\rangle \quad (2.3)$$

The particular definition of the Hamiltonian is dependent of the system. In the case of chemical systems, such as atoms and molecules, we need to take into account some approximations due to their complexity. Each proton and neutron in the nuclei of the atoms are much more heavier than an individual electron (1800 times heavier). Thus, the respond of the electrons to changes is faster than the nuclei. Based on this fact, the Born-Oppenheimer approximation allows to decouple the nuclei and electrons into separate mathematical problems to found the ground state of the system (*i.e.* the lowest energy state).<sup>92</sup> Therefore, the Hamiltonian of a non-relativistic system with  $N$  electrons interacting with multiple nuclei is defined by the terms inside the brackets in (**Equation 2.4**). It is composed by the operators of the kinetic energy of each electron ( $\hat{K}$ ), the attraction between the nuclei and the electrons ( $\hat{V}$ ), and the repulsion between electrons ( $\hat{U}$ ).  $m_e$  and  $r$  stands for the mass and the position of the electrons, respectively.

## 2.1. Modelling at the atomic scale

$$\left[ \underbrace{-\frac{\hbar^2}{2m_e} \sum_{i=1}^N \nabla_i^2}_{\hat{K}} + \underbrace{\sum_{i=1}^N V(\mathbf{r}_i)}_{\hat{V}} + \underbrace{\sum_{i=1}^N \sum_{j<1} U(\mathbf{r}_i, \mathbf{r}_j)}_{\hat{U}} \right] \Psi = E\Psi \quad (2.4)$$

The wavefunction for a system of  $N$  electrons depends on the spatial coordinates of each electron and is written as **Equation 2.5**. It could be expressed as a product of single-electron wave functions ( $\psi_i(r)$ ) by means of the Hartree product (**Equation 2.6**). Even with this, the all-electron wavefunction of a simple CO<sub>2</sub> molecule, that contains 22 electrons, is a 66-dimensional function.<sup>93</sup> Considering a surface model of a Pt nanoparticle with 100 atoms leads to an all-electron wavefunction with more than 23,000 dimensions. Thus, is not possible to found the analytical solution of the Schrödinger equation for practical materials. In addition, the many-body nature of the equation makes this even more complicated. The single-electron wavefunctions ( $\psi_i(r)$ ) depend on the operator defining the electron-electron interaction ( $\hat{U}$ ). Simultaneously,  $\psi_i(r)$  are needed to be known to find the eigenvalues (solutions) of  $\hat{U}$ , therefore they dependent on their own solution.

$$\langle \mathbf{r} | \Psi \rangle = \Psi(\mathbf{r}_1, \dots, \mathbf{r}_N) \quad (2.5)$$

$$\Psi(\mathbf{r}_1, \dots, \mathbf{r}_N) = \Psi_1(\mathbf{r})\Psi_2(\mathbf{r}), \dots, \Psi_N(\mathbf{r}) \quad (2.6)$$

Finally, it is worth to mention that the all-electron wavefunction is not a physical observable and is function of  $3N$  coordinates. In contrast, the electronic density ( $n$ ) can be expressed as the sum over mono-electronic states (**Equation 2.7**) and describes the probability to find  $N$  electrons in a certain position of the space ( $\mathbf{r} = r_x, r_y, r_z$ ). Thus,  $n$  is an observable that only depends on three coordinates and the spin. It is therefore more convenient to solve the Schrödinger equation by means of the electron density than with the all-electron wavefunction.



## Chapter 2. Theoretical background

---

$$n(\mathbf{r}) = 2 \sum_i \Psi_i^*(\mathbf{r}) \Psi_i(\mathbf{r}) \quad (2.7)$$

### 2.1.2 Hohenberg-Kohn Theorems

In the context of the electron density, Hohenberg and Kohn postulated two fundamental mathematical theorems that are the pillars of DFT<sup>94</sup>:

*i)* The external potential ( $V(\mathbf{r})$ ) is a unique functional of the electronic density ( $n(\mathbf{r})$ ):  $V(\mathbf{r}) = F[n(\mathbf{r})]$ . As a consequence, the full many-body ground state is a unique functional of  $n(\mathbf{r})$  since the external potential defines the Hamiltonian of the system.

*ii)* The electron density that minimizes the energy of the overall functional  $F[n(\mathbf{r})]$  is the true electron density corresponding to the full solution of Schrödinger equation.

In other words, the first theorem shows that the lowest energy state ( $E$ ) of a system can be expressed as a functional of the electron density ( $E[n(\mathbf{r})]$ ), which gives the name to the density functional theory. Then, the second theorem depicts that if the exact form of the functional was known, the electron density could be optimized until reaching the minimized energy from the functional. In practice, the variational principle is employed with approximate forms of the functional through iterative processes to obtain the ground-state energy for the systems of interest.

### 2.1.3 Kohn-Sham equations

In order to provide a practical approach to iteratively minimize the  $F[n(\mathbf{r})]$ , Kohn-Sham equations were derived from the Hohenberg-Kohn Theorems.<sup>95</sup> First, the  $N$ -electron Schrödinger equation is simplified in  $N$  single-electron equations, as the full wavefunction can be expressed as product of single-electron wavefunctions (**Equation 2.6**). Thus, the resulting Schrödinger equation in function of the electron density is written as **Equation 2.8**.  $\hat{K}$  and  $\hat{V}_n$  are the operators for the kinetic energy of the electron (**Equation 2.9**) and the attractive interaction between the electron and the nuclei, respectively. Then,  $\hat{V}_H$  is the operator of the Hartree potential (**Equation**

## 2.1. Modelling at the atomic scale

---

**2.10)** that defines the interaction between a certain electron and the electron density ( $n(\mathbf{r})$ ). As the considered electron is also part of the  $n(\mathbf{r})$ , a non-physical interaction of the electron with itself arises which is an inherent inaccuracy of DFT, the so-called self-interaction error (SIE).<sup>96</sup>  $\hat{V}_{\text{XC}}$  describes the exchange and correlation contributions to the single-electron equations (**Equation 2.11**), as well as incorporates corrections for the self-interaction error. The exact form of the functional for  $\hat{V}_{\text{XC}}$  is unknown and different approximations has been therefore proposed to overcome this issue, as explained in the following section.

$$\left[ \hat{K} + \hat{V}_n(\mathbf{r}) + \hat{V}_\text{H}(\mathbf{r}) + \hat{V}_{\text{XC}}(\mathbf{r}) \right] \psi_i(\mathbf{r}) = e_i \psi_i(\mathbf{r}) \quad (2.8)$$

$$\hat{K} = -\frac{\hbar^2}{2m_e} \nabla_i^2 \quad (2.9)$$

$$\hat{V}_\text{H}(\mathbf{r}) = e^2 \int \frac{n(\mathbf{r}')}{|\mathbf{r} - \mathbf{r}'|} d^3\mathbf{r}' \quad (2.10)$$

$$\hat{V}_{\text{XC}}(\mathbf{r}) = \frac{\partial E_{\text{XC}}}{\partial n(\mathbf{r})} \quad (2.11)$$

Finally, the ground-state of a desired system is calculate *via* the following iterative process:

1. Define an initial electron density  $n_0(\mathbf{r})$ .
2. Solve Kohn-Sham equations with  $n_0(\mathbf{r})$  to find the single-electron wavefunction ( $\Psi_{i,0}(\mathbf{r})$ ).
3. Calculate a new electronic density  $n_1(\mathbf{r})$  with (**Equation 2.7**) and  $\Psi_{i,0}(\mathbf{r})$  from step 2.
4. If the difference between  $n_0(\mathbf{r})$  and  $n_1(\mathbf{r})$  is lower than a certain threshold,  $n_1(\mathbf{r})$  is considered the ground-state density. Otherwise,  $n_1(\mathbf{r})$  is updated and the cycle is repeated from step 2.

## Chapter 2. Theoretical background

---

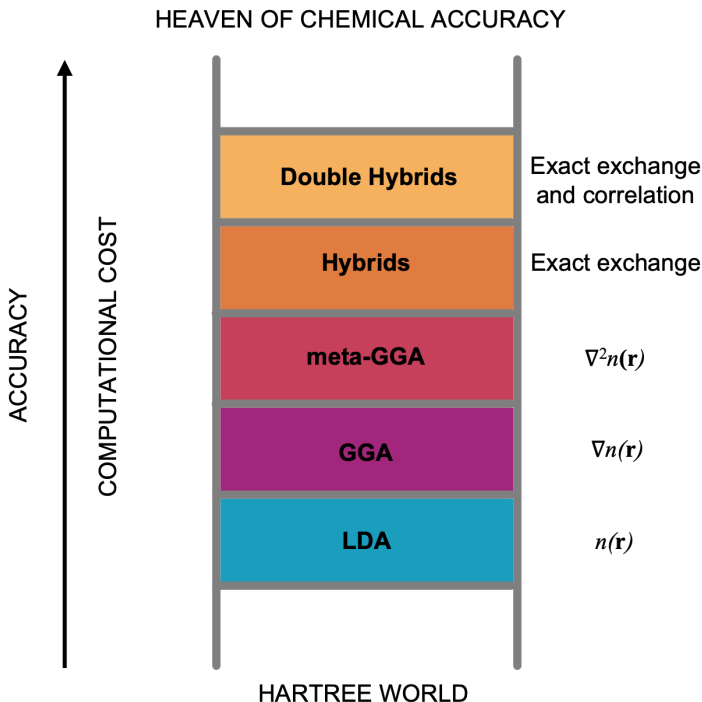
### 2.1.4 Exchange-correlation functionals

On the one hand, exchange is a quantum mechanical phenomenon that arises due to indistinguishable character of the electrons and it describes the energy required to interchange their positions. On the other hand, correlation could be dynamical and non-dynamical. The former defines how one electron is influenced by the movement of others and the last results from the near-degeneracy of different electronic states. It is worth to mention that exchange is typically one or two order of magnitude larger than correlation.<sup>97</sup> However, the exact functional for these two effects is not known and different approximations has been proposed to solve the Kohn-sham equations. They have been classified by John Perdew in terms of their accuracy/cost ratio in the so-called Jacob's ladder of DFT (**Figure 2.1**).<sup>93,98</sup>

**Local Density Approximation:** The simplest approach for the functional of the electronic density is the Local Density Approximation (LDA). The exchange-correlation energy depends only in the electronic density at each point of the space ( $n(\mathbf{r})$ ) and is approximated as the one of an homogeneous electron gas (**Equation 2.12**).<sup>95</sup> Therefore, exchange energy in the uniform density limit (*i.e.* the density has the same value at all positions) can be computed exactly. In reference to the correlation energy, there is not any exact form of a functional to describe it. Nevertheless, quantum Monte Carlo methods were used to obtain the correlation energy for different homogeneous electron gases with high accuracy and the values were interpolated to describe other systems.<sup>99</sup> Thereby, LDA correctly predicts properties of bulk solids or other materials with almost constant valence electron density. In contrast, it fails when describing systems where the electron density varies locally, such as molecular systems, leading to overestimated bonding energies.<sup>97</sup> In addition, it should be highlighted that when LDA is described separately for spin-up and spin-down densities, it is called the local spin-density approximation (LSDA).<sup>100</sup>

$$E_{\text{XC,LDA}}[n(\mathbf{r})] = \int n(\mathbf{r}) \epsilon_{\text{XC}}^{\text{homo}}(\mathbf{r}) d^3 \mathbf{r}' \quad (2.12)$$

2.1. Modelling at the atomic scale



**Figure 2.1:** Perdew’s ladder of DFT functionals. Adapted from [93].

**General Gradient Approximation:** The second rung in the Perdew’s ladder belongs to General Gradient Approximation (GGA).<sup>101</sup> These functionals account not only for the local electron density ( $n(\mathbf{r})$ ) but also for its gradient ( $\nabla n(\mathbf{r})$ ), as described in **Equation 2.13**. In such a way, local variations of the electron density are better described than with LDA.

$$E_{\text{XC,GGA}}[n(\mathbf{r})] = \int n(\mathbf{r})\epsilon_{\text{XC}}[n(\mathbf{r}), \nabla n(\mathbf{r})]d^3\mathbf{r}' \quad (2.13)$$

These functionals represent a well accuracy-cost trade-off and a wide range of them have been developed. They can be divided in empirical and non-empirical. In the first group we can find BLYP (Becke-Lee-Yang-

## Chapter 2. Theoretical background

---

Parr),<sup>102,103</sup> which is commonly used for molecular systems. In contrast, the non-empirical ones are mostly employed for periodic simulations of solids. Examples of this group are PW91 (Perdew-Wang),<sup>104</sup> RPBE (revised PBE),<sup>105</sup> PBEsol (PBE revised for solids),<sup>106</sup> and PBE (Perdew-Burke-Ernzerhof),<sup>107</sup> being the last one the most used along this thesis.

**meta-GGA:** The next rung in the ladder is represented by the meta-GGA functionals which include the Laplacian of the electron density ( $\nabla^2 n(\mathbf{r})$ ) and they are defined with **Equation 2.14**.

$$E_{XC,meta-GGA}[n(\mathbf{r})] = \int n(\mathbf{r})\epsilon_{XC}[n(\mathbf{r}), \nabla n(\mathbf{r}), \nabla^2 n(\mathbf{r})]d^3\mathbf{r}' \quad (2.14)$$

These kind of functionals do not provide a clearly better accuracy-cost ratio compared to GGA. However, there are some examples that are gaining popularity lately: TPPS (Tao-Perdew-Staroverov-Scuseria),<sup>108</sup> SCAN (Strongly Constrained and Appropriately Normed),<sup>109</sup> Minnesota M06-L,<sup>110</sup> and Minnesota M11-L.<sup>111,112</sup>

**Hybrid Functionals:** One step up in Perdew's ladder lead to Hybrid Functionals. **Equation 2.15** shows how this approach describes the exchange-correlation energy ( $E_{XC}^{hybrid}$ ) as a combination of (i) a fraction ( $\alpha$ ) of non-local Hartree-Fock exact exchange ( $E_X^{HF}$ ) and (ii) one of the aforementioned approximations of exchange-correlation functional ( $E_X^{DFT}$  and  $E_C^{DFT}$ ).

$$E_{XC}^{hybrid} = \underbrace{\alpha E_X^{HF}}_{\text{exact HF exchange}} + \underbrace{(1 - \alpha) E_X^{DFT}}_{\text{DFT exchange}} + \underbrace{E_C^{DFT}}_{\text{DFT correlation}} \quad (2.15)$$

In the field of molecular chemistry and homogeneous catalysis, B3LYP has become the gold-standard functional.<sup>103,113</sup> However, it is not suitable for periodic solid systems as it fails in accurately describe long-range effects. In this scenario, PBE0 was proposed, which is the hybrid version of PBE but is unfortunately prone to convergence errors.<sup>114</sup> Therefore, Heyd, Scuseria, and Ernzerhof formulated the range-separated HSE functionals based on

## 2.1. Modelling at the atomic scale

PBE0 (**Equation 2.16**).<sup>115</sup> In this approach, exchange is divided in short- and long-range by the adjustable parameter  $\omega$ . Thus, HSE is equivalent to PBE0 for  $\omega = 0$  while is equivalent to PBE when  $\omega$  tends to infinity. HSE03 and HSE06 are the most popular hybrid functionals in the field of heterogeneous catalysis and they differ one to each other by the parameter  $\omega$ .<sup>115–117</sup>

$$\begin{aligned}
 E_{XC}^{\text{HSE}} = & \underbrace{\alpha E_X^{\text{HF,SR}}(\omega)}_{\text{short-range HF exchange}} + \underbrace{(1 - \alpha) E_X^{\text{PBE,SR}}}_{\text{short-range PBE exchange}} + \\
 & \underbrace{E_X^{\text{PBE,LR}}}_{\text{long-range PBE exchange}} + \underbrace{E_C^{\text{PBE}}}_{\text{PBE correlation}}
 \end{aligned} \tag{2.16}$$

The importance of the hybrid functionals relies in the fact that they are able to mitigate the self-interaction error (SIE) inherent to DFT.<sup>96</sup> In simulations of materials for catalysis, especially in systems with highly correlated  $d$  and  $f$  electrons, is crucial to minimize the effect of this error. LSDA, GGA, and meta-GGA functionals tend to unphysical delocalize valence electrons and overstabilize metallic states. This derives in a systematic underestimation of band gaps which cannot be neglected when assessing catalytic properties. Unfortunately, in contrast to simulations conducted with codes that employs localized basis set, the use of hybrid functionals with plane-wave based calculations (mostly employed in this thesis) are prohibitively expensive to carry out routine simulations. The differences in computational cost between PBE and HSE simulations could reach two orders of magnitude. In this scenario, DFT+U approach has appeared as a cheaper, although probably less reliable solution to mitigate the SIE in plane-wave based codes.

**DFT+U:** The Hubbard model is employed in this approach to capture the effects of strong on-site electron correlations.<sup>118</sup> It was introduced in DFT by Anisimov and later simplified by Dudarev.<sup>119–121</sup> The last, combined the on-site Coulomb  $U$  and exchange  $J$  interaction terms in the effective  $U$  parameter ( $U^{\text{eff}}$ ).  $U^{\text{eff}}$  can be understood as an energy penalty applied to enforce the localization of electrons in partially occupied strongly correlated

## Chapter 2. Theoretical background

---

orbitals, such as  $d$  and  $f$  states, while the other electrons are treated at the DFT level. The energy of a systems described with DFT+U can be expressed with **Equation 2.17**, where  $n_m^\sigma$  represents the occupation of the atomic orbitals that are corrected by  $U^{eff}$ ,  $n$  is the number of electrons,  $m$  the quantum number, and  $\sigma$  the spin.

$$E_{\text{DFT+U}} = E_{\text{DFT}} + \frac{(U - J)}{2} \sum_m^\sigma (n_m^\sigma - (n_m^\sigma)^2) \quad (2.17)$$

The DFT+U approach provides a computationally cheap way to mitigate the SIE in plane-wave based codes and to obtain accurate results compared to hybrid functionals.<sup>122,123</sup> The major drawback of this methodology is the selection of the  $U^{eff}$ . It can be empirically fitted to a known experimental measured quantity, such as band gap, reaction energies, or formation enthalpies or alternatively it can be obtained by linear response theory.<sup>124–126</sup> However,  $U^{eff}$  is totally lack of transferability and is very sensitive to the element, the structural and electronic environment, and even to the implementation of the plane-wave code employed for the simulations.<sup>67</sup>

**Dispersion interactions:** The aforementioned DFT approaches fail in correctly describing dispersion interactions, in particular long-range interactions arising from fluctuating charge distributions (*i.e.* London dispersion forces).<sup>127</sup> These interactions cannot be neglected in many systems such as materials that contain organic linkers with aromatic-aromatic interactions (as it is the case of the MOFs studied in this thesis), layered materials, or to describe the physisorption of aromatic molecules, among other examples.<sup>67</sup> Therefore, different approaches has been proposed to mitigate this issue, being the most popular the semi-empirical correction developed by Grimme and the first-principles approach based in the electron density density of Tkatchenko-Scheffler.<sup>128–132</sup>

### 2.1.5 Periodic systems

Heterogeneous catalysts are usually solids, such as metals, metal oxides, or MOFs, which can be defined within periodic boundary conditions.

## 2.1. Modelling at the atomic scale

---

These systems are typically crystalline structures built by ordered periodic arrangement of atoms in the three dimensions of the space. The periodicity and symmetry of the crystal is described by the Bravais lattice. Then, the unit cell is the fundamental building block of the crystal structure. It is characterized by three lattice vectors ( $n_1$ ,  $n_2$ , and  $n_3$ ), which determine its shape and size and represent the translations that generate the entire lattice. Therefore, the position of each atom inside the lattice can be determined with **Equation 2.18** for any integer  $n_1$ ,  $n_2$ , and  $n_3$ . Additionally, the primitive cell is the smallest unit cell that can be used to built the whole crystal lattice.

$$\mathbf{r} = n_1\mathbf{a}_1 + n_2\mathbf{a}_2 + n_3\mathbf{a}_3 \quad (2.18)$$

We can also define the reciprocal lattice, which is more convenient to carry out simulations with plane-wave based codes. It is described with the reciprocal vectors  $b_1$ ,  $b_2$ , and  $b_3$  obtained from **Equation 2.19**. The combination of these lattice vectors leads to the reciprocal space (**Equation 2.20**), where  $v_1$ ,  $v_2$ , and  $v_3$  are integers. In this context, a reciprocal lattice of particular interest is called the Brillouin Zone, which is a primitive cell in the reciprocal space.<sup>93</sup>

$$\begin{aligned} \mathbf{b}_1 &= 2\pi \frac{\mathbf{a}_2 \times \mathbf{a}_3}{\mathbf{a}_1 \cdot \mathbf{a}_2 \times \mathbf{a}_3} \\ \mathbf{b}_2 &= 2\pi \frac{\mathbf{a}_3 \times \mathbf{a}_1}{\mathbf{a}_1 \cdot \mathbf{a}_2 \times \mathbf{a}_3} \\ \mathbf{b}_3 &= 2\pi \frac{\mathbf{a}_1 \times \mathbf{a}_2}{\mathbf{a}_1 \cdot \mathbf{a}_2 \times \mathbf{a}_3} \end{aligned} \quad (2.19)$$

$$\mathbf{G} = v_1\mathbf{b}_1 + v_2\mathbf{b}_2 + v_3\mathbf{b}_3 \quad (2.20)$$

**Blöch's theorem** Different basis sets can be used to solve the single-electron Schrödinger equation. For simulations of molecular systems is convenient to employ localised atom-centered wave functions, such as Slater or Gaussian orbitals.<sup>97</sup> In contrast, plane waves are more suitable to study solids.<sup>93</sup> Such plane waves take advantage of the periodicity of the systems in the framework of the Bloch's theorem to decrease the computational



## Chapter 2. Theoretical background

---

cost.<sup>133</sup> The theorem states that the wavefunction of an electron in a crystal can be expressed with **Equation 2.21**. This is the product of a periodic function ( $u_{\mathbf{k}}(\mathbf{r})$ ) and a plane-wave dependent of the vectors  $\mathbf{k}$ , which are defined in the reciprocal space ( $k$  space). The  $u_{\mathbf{k}}(\mathbf{r})$  has the same periodicity as the crystal lattice and can be expanded as a set of plane waves according to **Equation 2.22**. Thus, it is possible to solve Kohn-Sham equations independently for each value of  $\mathbf{k}$ .<sup>93</sup>

$$\phi_{\mathbf{k}}(\mathbf{r}) = u_{\mathbf{k}}(\mathbf{r})e^{i\mathbf{k}\mathbf{r}} \quad (2.21)$$

$$u_{\mathbf{k}}(\mathbf{r}) = \sum_{\mathbf{G}} c_{\mathbf{G}}e^{i\mathbf{G}\mathbf{r}} \quad (2.22)$$

By combining the previous two equations we get **Equation 2.23**. According to this expression, a summation over an infinite number of plane waves is required to evaluate the solution in a single point of the  $k$  space. However, this could be simplified because the plane waves with low kinetic energies, which represent the states that dictate the electronic properties of the materials, are more physically important than the ones associated with high energies. Therefore, when simulating periodic systems, the number of plane waves is truncated by setting a kinetic energy cut-off.<sup>93</sup>

$$\phi_{\mathbf{k}}(\mathbf{r}) = \sum_{\mathbf{G}} c_{\mathbf{K}+\mathbf{G}}e^{i(\mathbf{K}+\mathbf{G})\mathbf{r}} \quad (2.23)$$

Additionally, an important concept in plane-wave based simulations is the  $k$ -point grid employed to sample the  $k$  space, in particular the Brillouin Zone. The  $k$ -points represent specific values of the wave vector  $\mathbf{k}$ . By computing the wavefunctions and energies at various of these  $k$ -points, we can obtain a description of the electronic structure of the crystal. Thus, the selection of an appropriate  $k$ -point grid is crucial to accurately represent the electronic features of a material. Increasing the density of the grid leads to more accurate results in expense of computational cost. There are methods, such as the Monkhorst-Pack,<sup>134</sup> that efficiently generate a  $k$ -point grid by taking into account the symmetry of the crystal lattice under study. Overall,

---

## 2.1. Modelling at the atomic scale

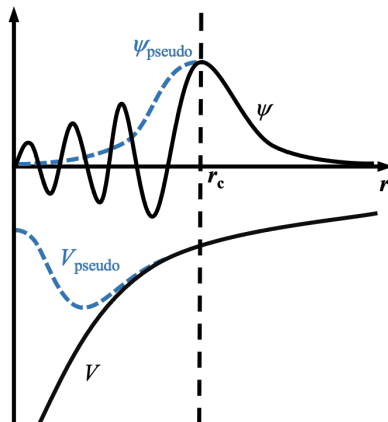
---

a proper selection of the energy cut-off and  $k$ -points grid is required to obtain a well-balanced ratio of accuracy and cost. However, there is a third point that is crucial to carry out efficient plane-wave based simulations, the use of pseudopotentials.

**Pseudopotentials** A large set of plane waves would be required to account for all electrons of the atoms included in the crystal unit cell. Thus, even with an efficient energy cut-off and  $k$ -points, the simulations would be extremely computationally expensive. This is because a large number of wavefunctions is required to describe the core electrons and the rapid oscillations of the valence electrons wavefunction in the regions close to the nuclei.<sup>135</sup> In addition, most physical properties of solids depend only in the valence electrons, as they are more influenced by their chemical environment. Therefore, the pseudopotential approach consists in describing the core electrons and their strong ionic interaction with the nuclei with a weaker effective potential ( $V_{\text{pseudo}}$ ) based in a set of pseudo wavefunctions ( $\psi_{\text{pseudo}}$ ). Thus, only valence electrons are computed explicitly when solving the Kohn-Sham equations. It should also be mentioned that there is a certain cut-off radius ( $r_c$ ) where pseudopotential and all electron wavefunction overlap (**Figure 2.2**). The perfect pseudopotential must be soft and transferable. A soft pseudopotential implies that the pseudo wavefunctions are expanded with a small number of plane waves. The concept transferable means that the properties of the atom are well-described independently of the chemical environment. A decrease in the  $r_c$  implies an increase of the transferability in detriment of the softness, and the other way around. The most employed groups of pseudopotentials are the Vanderbilt ultrasoft (US-PP)<sup>136</sup> and the Projector-Augmented Wave (PAW)<sup>137,138</sup> pseudopotentials. The second group was selected to carry out the simulations of this thesis due to their better ability to describe transition, alkali, and alkali-earth metals.<sup>138</sup>

## Chapter 2. Theoretical background

---



**Figure 2.2:** Schematic representations of pseudoelectron (dotted blue line) and all electron (black line) wave functions, and their corresponding potentials.  $r_c$  is the cut-off radius where the all electron wavefunctions and pseudopotentials overlap. Adapted from Ref. [135].

### 2.1.6 Computation of Transition States

In the previous sections of this chapter, different methods and approaches to efficiently and accurately compute the ground-state energy of solids and molecules has been explained. This is paramount to rationalize the structural and electronic properties of heterogeneous catalysts, which are needed to identify synthesis-structural-performance relationships. However, we also need to explore the adsorption of molecules and the formation/breaking of bonds on the surface of the catalysts. From the thermodynamic standpoint, we explore the different intermediates involved in the transformation of molecules to obtain the desired products. Then, from the kinetics point of view, we need to locate transition states (TS) that connects the different intermediates. Mathematically, the intermediates of the reactions are local minima of the potential energy surface (PES) while TS are saddle points. Both intermediates and TS are critical points of the PES (the gradient of potential energy is 0). However, the second derivatives of the potential

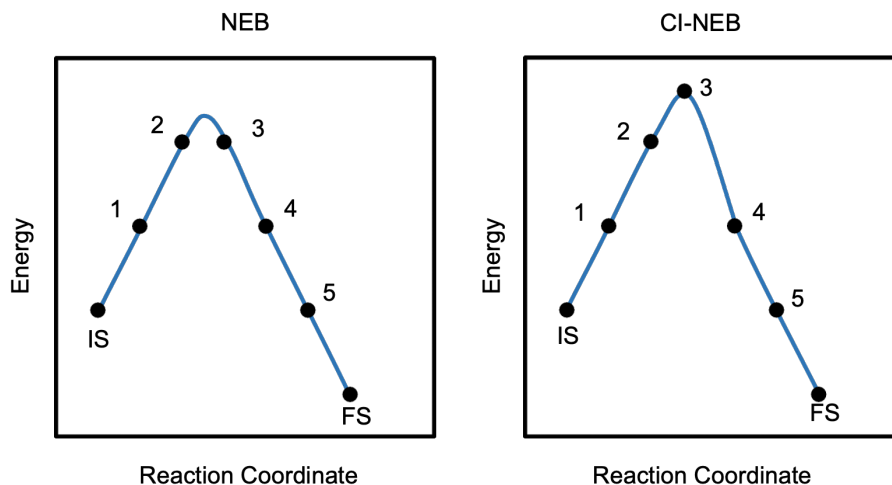
## 2.1. Modelling at the atomic scale

---

energy are all positive for the intermediates, while TS present a negative second derivative. Therefore, the numerical approaches employed to allocate the intermediates are different from the ones used for TS.

The Nudged Elastic Band (NEB) method is the most used in heterogeneous catalysis.<sup>139,140</sup> It consists in looking for the minimum energy path (MEP) between two intermediates, which are minima of the PES and we can label as initial state (IS) and final state (FS). First,  $n$  interpolated structures (images) between the IS and FS are generated. Then, a constrained optimization of the images is carry out as an elastic band. Spring forces are introduced between the band connecting the images and the force resulting from the potential perpendicular to the band is projected out. Conceptually, each image is optimized taking into account the neighbouring images and maintaining equal spacing. However, any of the constrained-optimized images describes exactly the transition state. For this reason, a modification of the NEB method was introduced to find the exact TS, the so-called climbing image (CI-NEB).<sup>141</sup> In this approach, the image with the highest energy does not feel the spring forces along the band and its true force along the tangent is inverted. Thus, the energy of this image is minimized in all directions but maximized along the band. In this way, the highest image is driven up to the saddle point and their spacing with the neighbours images is not equal. **Figure 2.3** shows a comparison between NEB and CI-NEB.

## Chapter 2. Theoretical background



**Figure 2.3:** Schematic representations of NEB (left) and CI-NEB (right) with the minimum energy path (MEP) and images shown as blue lines and black dots, respectively. The numbers depict the different constrained-optimised images, while IS and FS stands for the initial and final states, respectively.

## 2.2 Computational Hydrogen Electrode

The catalytic properties at atomic level of detail of the *M*-MOF-74 systems explored in **Chapter 3** were assessed from a thermodynamical standpoint by computing the Gibbs energy profiles for OER on different models. Gibbs free energies of the different intermediates can be computed as a function of pressure and temperature as defined by **Equation 2.24**, where  $H$  and  $S$  represents the enthalpy and entropy, respectively. Accordingly,  $G$  for each intermediate involved was calculated with **Equation 2.25**. The enthalpy was estimated by incorporating vibrational energy corrections ( $E_{\text{vib}}$ ) into the electronic DFT energy ( $E_{\text{DFT}}$ ).  $E_{\text{vib}}$  was obtained from the normal modes of vibration ( $K$ ), as expressed in **Equation 2.26**, where  $k_b$  and  $\theta$  represent

## 2.2. Computational Hydrogen Electrode

the Boltzmann's constant and the characteristic vibrational temperature, respectively. The last can be written as **Equation 2.27** which includes the vibrational frequency for each normal mode ( $\nu_K$ ) and the Planck's constant ( $h$ ). Finally, the entropic term ( $S$ ) was calculated as the vibrational entropy (**Equation 2.28**) for all intermediates but for  $\text{H}_2$  and  $\text{H}_2\text{O}$  was obtained from tabulated values.<sup>142</sup>

$$G(T, p) = H(T, p) - TS(T, p) \quad (2.24)$$

$$G = E_{\text{DFT}} + E_{\text{vib}} - TS \quad (2.25)$$

$$E_{\text{vib}} = k_B \sum_K \frac{1}{2} \theta_{\nu, K} \quad (2.26)$$

$$\theta = \frac{h\nu_K}{k_B} \quad (2.27)$$

$$S = k_B \sum_K \left( \frac{\frac{\theta_{\nu, K}}{T}}{e^{\frac{\theta_{\nu, K}}{T}} - 1} - \ln \left( 1 - e^{-\frac{\theta_{\nu, K}}{T}} \right) \right) \quad (2.28)$$

However, when modeling electrochemical reactions, we need to take into account some other phenomena, such as electron transfer, pH, and electric potential. In this context, J. K. Nørskov and co-workers formulated the Computational Hydrogen Electrode (CHE) to model the free-energy landscape of the Oxygen Reduction Reaction (ORR) on Pt(111).<sup>89</sup> In addition, this formalism has been applied for other electrochemical process, for example  $\text{CO}_2$  reduction (e $\text{CO}_2$ R), Hydrogen Evolution Reaction (HER), and Oxygen Evolution Reaction (OER) among others.<sup>143–145</sup> Therefore, we have employed this approach in the modelling of OER on *M*-MOF-74 in **Chapter 3** of this thesis and the procedure can be described with the 6 following steps:

1. At standard conditions (pH = 0,  $p = 1 \text{ H}_2 \text{ bar}$ ,  $T = 298.15 \text{ K}$ ) and an electrode potential ( $U$ ) of 0 V vs the Standard Hydrogen Electrode

## Chapter 2. Theoretical background

---

(SHE), the chemical potential of a proton in the reaction of a proton-coupled electron transfer ( $\text{H}^+ + \text{e}^-$ ) is equal to one-half of  $\text{H}_2$  Gibbs free energy (**Equation 2.29**).

$$G_{\text{H}^+} = \frac{1}{2}G_{\text{H}_2,\text{DFT}} \quad (2.29)$$

2. DFT electronic energy of the reaction intermediates are corrected with the vibrational energy ( $E_{\text{vib}}$ ) and entropic contributions ( $S$ ) as expressed in **Equation 2.25**.
3. In order to account for the electrode potential, the Gibbs free energy of the intermediates which involves a electron transfer is shifted by  $-eU$ , where  $e$  is the charge of the electron and  $U$  is the electrode potential .
4. Contributions of the interaction of the molecules and the electric field that arises from the electrochemical double layer (EDL) on the surface of the electrode can be added through  $p \cdot E_{\text{EDL}}$ , where  $p$  stands for the dipole moment of the molecule. However, this effect was neglected in this thesis.
5. Inclusion of solvation contributions. The Gibbs energy of liquid water was calculated by adding a solvation correction computed with the implicit solvation model VASP-MGCM,<sup>146</sup> as elaborated in detail later on.
6. The free energy of protons is linearly corrected at pH different from 0 according to **Equation 2.30**.

$$G(\text{pH}) = -k_b T \ln[\text{H}^+] = k_b T \ln(10) \cdot \text{pH} \quad (2.30)$$

With all the aforementioned considerations at hand, the reaction energies ( $\Delta G$ ) for the OER are generalised in **Equation 2.31**.

$$\Delta G = \Delta E_{\text{DFT}} - \Delta E_{\text{vib}} - T \Delta S - k_b T \ln(10) \cdot \text{pH} - eU \quad (2.31)$$

## 2.2. Computational Hydrogen Electrode

---

Particular details of the procedure to compute the Gibbs energy of  $\text{H}^+$ ,  $\text{H}_2\text{O}$ , and  $\text{O}_2$  molecules should be highlighted.  $G_{\text{H}_2}$  was calculated according to **Equation 2.32**, where  $S_{\text{H}_2(\text{g})}$  is the experimental entropy of  $\text{H}_2$  in gas phase at standard conditions reported in the literature.<sup>142</sup>

$$G_{\text{H}_2(\text{g})} = E_{\text{H}_2(\text{g}),\text{DFT}} + E_{\text{H}_2(\text{g}),\text{vib}} - TS_{\text{H}_2(\text{g})} \quad (2.32)$$

I employed **Equation 2.33** to calculate the Gibbs energy of liquid water ( $G_{\text{H}_2\text{O}(\text{l})}$ ). A water molecule was optimized in gas phase ( $E_{\text{H}_2\text{O}}$ ) and a solvation correction was added *via* the implicit model VASP-MGCM.<sup>146</sup> Similarly to  $\text{H}_2$ , the value of  $S_{\text{H}_2\text{O}(\text{l})}$  was taken from the literature.<sup>142</sup>

$$G_{\text{H}_2\text{O}(\text{l})} = E_{\text{H}_2\text{O}(\text{l}),\text{DFT}} + E_{\text{H}_2\text{O}(\text{l}),\text{vib}} - TS_{\text{H}_2\text{O}(\text{l})} \quad (2.33)$$

Finally,  $G_{\text{O}_2}$  was derived from the computed values of  $G_{\text{H}_2(\text{g})}$  and  $G_{\text{H}_2\text{O}(\text{l})}$  and the experimental Gibbs energy of the water splitting as described in **Equations 2.34-2.36**.



$$4.92\text{eV} = 2G_{\text{H}_2(\text{g})} + G_{\text{O}_2(\text{g})} - 2G_{\text{H}_2\text{O}(\text{l})} \quad (2.35)$$

$$G_{\text{O}_2(\text{g})} = 4.92\text{eV} + 2G_{\text{H}_2\text{O}(\text{l})} - 2G_{\text{H}_2(\text{g})} \quad (2.36)$$



## Chapter 2. Theoretical background

---

### 2.3 General computational details

Two different catalytic processes have been assessed in this thesis, in particular the electrocatalytic OER and thermocatalytic CO<sub>2</sub> hydrogenation. Therefore, distinct catalytic materials have been explored, such as MOFs, metal oxides, metals, and combinations between them. Thus, different methodologies and models are required to properly represent and simulate them. Nevertheless, the general approaches used along the thesis are going to be depicted in this section.

All periodic calculations were conducted with Vienna ab initio simulation package (VASP)<sup>147,148</sup> at DFT level employing the PBE exchange-correlation functional.<sup>107</sup> The density functional was complemented when needed by (i) Grimme's D3 approach<sup>130</sup> to account for the long-range dispersion interactions and (ii) the Hubbard correction,<sup>118</sup> by means of the Dudarev approach,<sup>121</sup> to mitigate the SIE<sup>96</sup> for the electrons in high correlated orbitals (*d* and *f*). Core electrons were described by projector augmented-wave (PAW) pseudopotentials<sup>137,138</sup> and valence electrons were represented with plane waves with a kinetic energy cut-off of 450-500 eV. The Monkhorst pack method<sup>134</sup> was used to sample the Brillouin zone with a  $\Gamma$ -centered sufficiently narrow reciprocal grid size to converge the simulations in terms of *k*-points. Spin polarization was included when needed.

Bulk lattice parameters for all the modelled materials were optimized with higher energy cut-off (600-800 eV) to avoid the Pulay stress.<sup>93</sup> This could arise from the incompleteness of the basis set when changing the size of the unit cell. With the optimized parameters at hand, slab models were built to represent the surface of metal-oxides and metals, where the catalytic processes usually takes place. The most stable termination or the one identified in the experimental characterization were modelled with enough atomic layers. The number of atomic layers depends in the nature and degree of openness of the surface and the property of interest. In general, some layers were kept fixed to mimic bulk positions while the outermost were allowed to relax. A dipole correction was applied along the *z*-axes to account for the asymmetry in the relaxations,<sup>149</sup> and a vacuum region of at least 12 Å was added between slabs.

### 2.3. *General computational details*

---

Numerical frequencies were computed with a step size of  $\pm 0.015$  Å to calculate vibrational partition functions, as well as to confirm the nature of the transition states, which were located with the climbing image nudged elastic band (CI-NEB) approach.<sup>141</sup> Only selected atoms of the models, which were preserved along the reaction paths, were allowed to move.

All computational and structural details for the DFT simulations discussed in this thesis can be found online in the ioChem-BD repository.<sup>86,87</sup> The particular links associated with each chapter will be displayed thorough the thesis.

## *Chapter 2. Theoretical background*

---

## Chapter 3

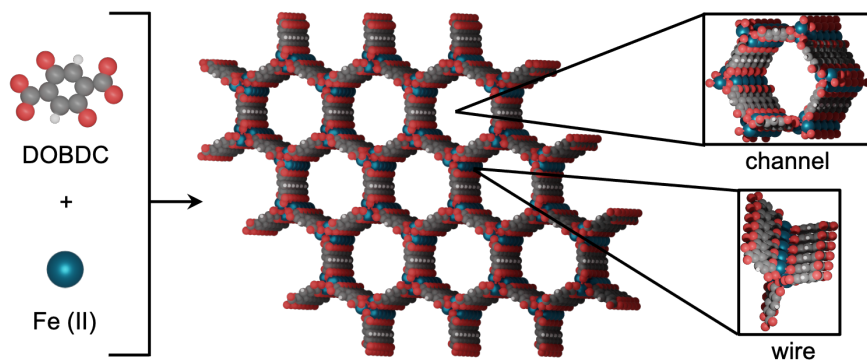
# Electrocatalytic sites of Earth-abundant MOF-74 for Oxygen Evolution Reaction

Electrocatalysis has emerged as promising field to overcome the intermittent character of renewable energies and convert abundant and simple molecules ( $\text{H}_2\text{O}$ ,  $\text{CO}_2$ , and  $\text{O}_2$ ) into high-value products. In this context, water splitting is expected to play a crucial role in the development of a sustainable hydrogen economy. However, great efforts are required to find efficient electrocatalysts for OER. This is the bottleneck of water splitting since it involves four electron-proton transfers and it requires high overpotentials.<sup>12</sup> Currently, the most effective electrocatalysts for OER are noble-metal based oxides, specifically  $\text{RuO}_2$  and  $\text{IrO}_2$ .<sup>150</sup> However, the scarcity of these materials hinders their widespread commercialization. Therefore, Earth-abundant based alternatives are key to turning water splitting into an affordable process. In this scenario, MOFs have shown great potential as electrocatalysts.<sup>38,52,53</sup> The hybrid nature and the versatility of these crystalline porous materials make ideal candidates for bridging the gap between homogeneous and heterogeneous catalysis.<sup>39,40</sup> Indeed, catalytic activity towards OER have been already proven in several Co/Fe based MOFs, such as  $\text{Fe}_3\text{-Co}_2$ ,<sup>151</sup> A/B-MOF-Co/Fe,<sup>152</sup> NNU-21-24,<sup>153</sup> Co-Fe-B,<sup>154</sup>

### Chapter 3. Electrocatalytic sites of Earth-abundant MOF-74 for OER

CoFe-PYZ,<sup>155</sup> CoFe-MOF<sup>156</sup>, and 2D Fe/Co-THT.<sup>157</sup>

In this chapter, I assess from a computational standpoint the work of Xu and co-workers,<sup>69</sup> who have demonstrated the potential of Earth-abundant based MOFs of the well-known MOF-74 family as electrocatalysts towards OER.<sup>158,159</sup> MOFs belonging to this family are composed by coordinately unsaturated divalent cations  $M(\text{II})$  connected by 2,5-dihydroxybenzene-1,4-dicarboxylate (DOBDC) organic linkers (**Figure 3.1**). The combination of such nodes and linkers leads to a three-dimensional honeycomb structure with hexagonal channels and one-dimensional metallic wires. Low overpotentials (0.3-0.4 eV) and high Faradaic efficiency (90%) were achieved in Co- and Fe-MOF-74.<sup>69</sup> However, the true nature of the active sites remains unclear. Therefore, I have carried out DFT simulations to elucidate the catalytic properties of such systems at the atomic scale and guide the rational design of new electrocatalysts.<sup>10</sup>



**Figure 3.1:** Building units and periodic structure of Fe-MOF-74. Color code: O (red), H (white), C (dark gray), and Fe (blue).

## 3.1 Methodology

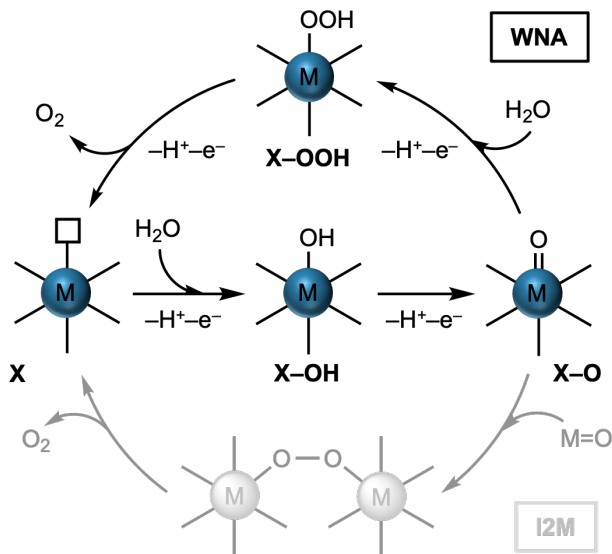
### 3.1.1 Computational details

All periodic simulations were carried out with PBE functional<sup>107</sup> supplemented with D3 dispersion approach<sup>130</sup> and  $U^{eff}$  correction<sup>121</sup> for the  $d$  orbitals of Co and Fe. We employed  $U^{eff}$  values of 5.3 eV and 6.5 eV, for Co and Fe, respectively. These  $U^{eff}$  values were suggested by linear response for  $M$ -MOF-74 systems and they led to excellent agreement with experiments, in terms of lattice parameters and CO<sub>2</sub> adsorption energies.<sup>160</sup> The periodic models for Co(II)- and Fe(II)-MOF-74, which are isostructural, were obtained by optimizing the unit cell (with a energy cut-off of 600 eV) of the dehydrated Co(II)-MOF-74 X-ray crystal structure.<sup>158</sup> The computed lattice parameters are in line with the experimental values with a relative error smaller than 1%. We employed a  $1 \times 1 \times 1 \times 2$   $k$ -point mesh for sampling the Brillouin zone of the pristine models ( $a = b = 26.129$  Å and  $c = 6.821$  Å), while  $\Gamma$ -point was used for the defective material due to the use of a supercell ( $a = b = 26.129$  Å and  $c = 13.642$  Å).

### 3.1.2 Thermodynamics of OER

Four proton-coupled electron transfer (PCET) steps are involved in OER to convert water in oxygen. **Figure 3.2** shows the two main reaction mechanism that have been proposed, the water nucleophilic attack (WNA) and the oxo coupling (I2M).<sup>145</sup> The first two steps are common in both mechanism. A water molecule is adsorbed on the active site (**X**, representing a coordinately unsaturated metal of  $M$ -MOF-74) with the release of a proton and electron leading to the hydroxo intermediate (**X-OH**). Then, **X-OH** is oxidised in a second PCET to form the metal-oxo moiety (**X-O**). Reached this point, the two mechanism diverge. In the I2M, two **X-O** intermediates interact to form the O<sub>2</sub> molecule. In contrast, in the WNA mechanism, a hydroperoxo intermediate (**X-OOH**) is formed by the nucleophilic attack of a water molecule to **X-O** with the release of an electron and proton. Finally, the last PCET entails the formation of the oxygen molecule from **X-OOH** and recovery of the active site.

Chapter 3. Electrocatalytic sites of Earth-abundant MOF-74 for OER



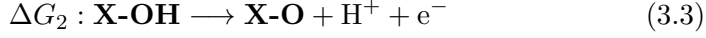
**Figure 3.2:** WNA and I2M reaction mechanisms for OER. I2M is shown in gray since it was not considered in this work.

We only considered the WNA mechanism because two consecutive coordinately unsaturated metal sites on a wire of the *M*-MOF-74 are always pointing to different channels. Thus, the interaction of two **X-O** intermediates, as described in the I2M mechanism, is not feasible. Therefore, we computed the Gibbs energy profiles for WNA (**Equations 3.1-3.8**) within the framework of the CHE<sup>89</sup> as detailed **Chapter 2**. It should be noted that kinetic energy barriers were neglected because the ones associated with the PCET were previously calculated to be around 0.2 eV and thus surmountable at room temperature.<sup>161</sup>

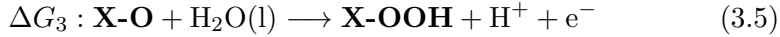


$$\Delta G_1 = G_{\mathbf{X-OH}} + \frac{1}{2}G_{\text{H}_2(\text{g})} - G_{\mathbf{X}} - G_{\text{H}_2\text{O}(l)} - k_b T \ln(10) \cdot \text{pH} - eU \quad (3.2)$$

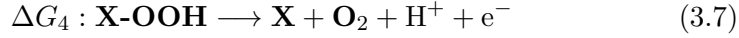
### 3.1. Methodology



$$\Delta G_2 = G_{\mathbf{X-O}} + \frac{1}{2}G_{\mathbf{H_2(g)}} - G_{\mathbf{X-OH}} - k_b T \ln(10) \cdot \text{pH} - eU \quad (3.4)$$



$$\Delta G_3 = G_{\mathbf{X-OOH}} + \frac{1}{2}G_{\mathbf{H_2(g)}} - G_{\mathbf{X-O}} - G_{\mathbf{H_2O(l)}} - k_b T \ln(10) \cdot \text{pH} - eU \quad (3.6)$$



$$\Delta G_4 = G_{\mathbf{X}} + G_{\mathbf{O_2}} + \frac{1}{2}G_{\mathbf{H_2(g)}} - G_{\mathbf{X-OOH}} - k_b T \ln(10) \cdot \text{pH} - eU \quad (3.8)$$

The catalytic activity shown by for Co- and Fe-based MOF-74 systems in the experimental testing<sup>69</sup> was linked to the simulations by means of the overpotential ( $\eta$ ). In the case of simulations, the theoretical overpotential ( $\eta_{\text{theor}}$ ) was obtained with **Equation 3.9**.  $\Delta G_{\text{PDS}}$  represents the Gibbs energy of the potential determining step (PDS), which is the step with highest  $\Delta G$ .

$$\eta_{\text{theor}} = \left( \frac{\Delta G_{\text{PDS}}}{e} \right) - 1.23 \text{ V} \quad (3.9)$$

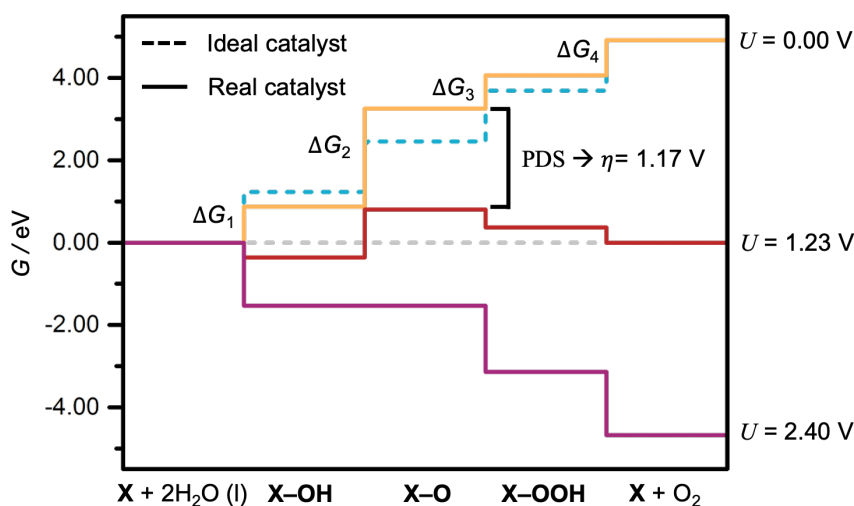
We assessed the free energies and the overpotentials at standard conditions (pH = 0 and  $T = 298.15 \text{ K}$ ). This is possible because the calculated free energies using **Equations 3.1 -3.8** exhibit a constant variation with pH and the external potential ( $U$ ). Thus, the theoretical overpotential is independent of the pH and  $U$ .<sup>162</sup>

**Figure 3.3** graphically depicts the concepts of overpotential and PDS. The energy profile for an ideal electrocatalyst towards OER would imply that the four steps in the WNA mechanism have the same Gibbs free energy



*Chapter 3. Electrocatalytic sites of Earth-abundant MOF-74 for OER*

( $4.92 \text{ eV}/4 = 1.23 \text{ eV}$ ) at standard conditions (dashed blue). In such a way, when applying the OER standard potential of  $1.23 \text{ V}$  all steps would become downhill (dashed gray). However, real catalysts do not show this behaviour and their energy profiles involves at least one step with  $\Delta G$  higher than  $1.23 \text{ eV}$  (solid orange). Therefore, these steps remain uphill when applying  $U = 1.23 \text{ eV}$  (solid red). It is required to apply an overpotential to make all the steps downhill (solid purple), which is thus associated with the PDS.



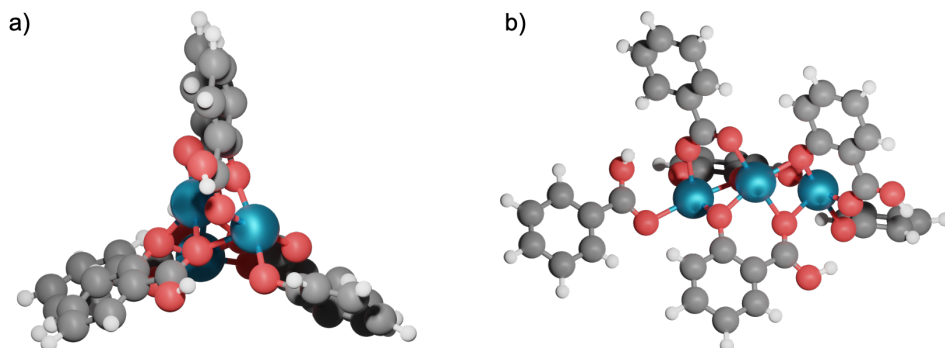
**Figure 3.3:** Schematic Gibbs energy profiles for ideal and real catalysts at different potentials.

### 3.1.3 Fe-MOF-74 finite-size cluster

We built a finite-size 88-atom cluster model of Fe-MOF-74<sup>163</sup> to benchmark the computational approach used in the DFT+ $U$  periodic simulations with respect to higher level methods, such as hybrid and meta-GGA density functionals. These kind of functionals were previously used to successfully study molecular systems,<sup>164</sup> solids,<sup>165,166</sup> and related materials.<sup>167</sup> Therefore, we built a finite-size 88-atom cluster model of Fe-MOF-74.<sup>163</sup> We employed

### 3.1. Methodology

as starting point the optimized periodic structure from PBE+ $U$ . We cleaved a cluster model containing a metal wire with three five-coordinate Fe(II) cations and six DOBDC linkers. With the aim of ensuring the neutrality of the system, we used hydrogen atoms to (i) cap the three carboxylate functional groups ( $\text{COO}^-$ ) coordinated to Fe cations and replace (ii) the oxido ( $\text{O}^-$ ) and  $\text{COO}^-$  groups of the negatively charged linkers that are non-coordinated to metal wire. Thus, the cluster model contains a central Fe with exactly the same chemical environment to the metals of the extended periodic structure and two peripheral metals with slightly modified coordination (**Figure 3.4**).



**Figure 3.4:** Top (a) and side (b) views of the finite-size 88-atom cluster model of Fe-MOF-74. Color code: O (red), H (white), C (dark gray), and Fe (blue).

Moreover, all carbon atoms of the DOBDC linker but the ones belonging to carboxylate groups were kept frozen during the optimization of the intermediates to reproduce the mechanical constraint of the Fe-MOF-74 crystal structure. The simulations of the OER intermediates within the cluster model were conducted with Gaussian09<sup>168</sup> with an ultrafine grid and different exchange-correlation density functionals. Particularly, PBE density functional based in the GGA approximation,<sup>107</sup> one meta-GGA (M06-L),<sup>110</sup> and five hybrids with different percentage of nonlocal Hartree–Fock exchange

### *Chapter 3. Electrocatalytic sites of Earth-abundant MOF-74 for OER*

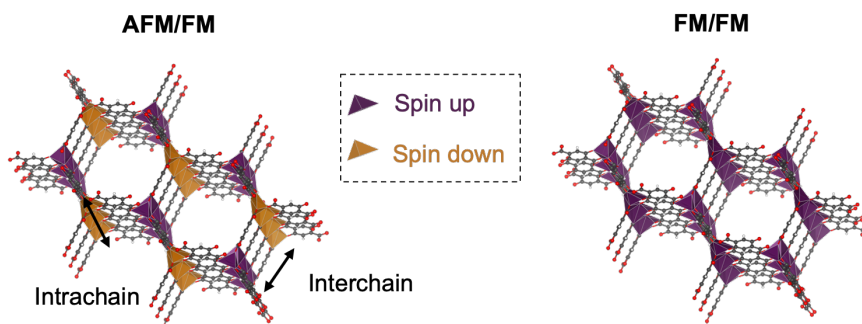
---

(PBE0,<sup>114</sup> HSE03,<sup>115</sup> HSE03-13,<sup>169</sup> B3LYP,<sup>103,113</sup> and B3LYP-15<sup>170</sup>). D3 approach<sup>130</sup> was used to account for dispersion interactions in all simulations but the ones performed with M06-L density functional. We employed the 6-31G (*d*, *p*) basis sets and diffusion was included for oxygen atoms.<sup>171–173</sup> The scalar-relativistic Stuttgart–Dresden SDD pseudopotential was used to represent the core electrons of Fe atoms while the outer ones were described with its associated double- $\zeta$  basis set.<sup>174</sup> All geometry optimizations were carried out in gas phase but H<sub>2</sub>O molecule was computed with the SMD model to account for solvation effects.<sup>175</sup> Finally, we computed analytical vibrational frequencies (i) to confirm that the OER intermediates are minima in the potential energy surface and (ii) to obtain their corresponding Gibbs energies. Additional assumptions for computing the thermodynamics of OER were applied in the framework of CHE method as explained in the previous section and **Chapter 2**.

3.2. Properties and catalytic activity of pristine *M*-MOF-74

### 3.2 Properties and catalytic activity of pristine *M*-MOF-74

Periodic models of Co- and Fe-MOF-74 were used to assess the catalytic properties of the pristine materials. Their unit cells are composed by 18 transition metals (II) cations distributed along 6 wires connected with DOBDC linkers (**Figure 3.1**). In line with previous experimental and theoretical works, we considered high spin configurations for Co and Fe.<sup>176–179</sup> Indeed, this is the configuration that one would expect by means of Crystal Field Theory due to the nature and coordination environment of the cations and the weak field character of the linkers.

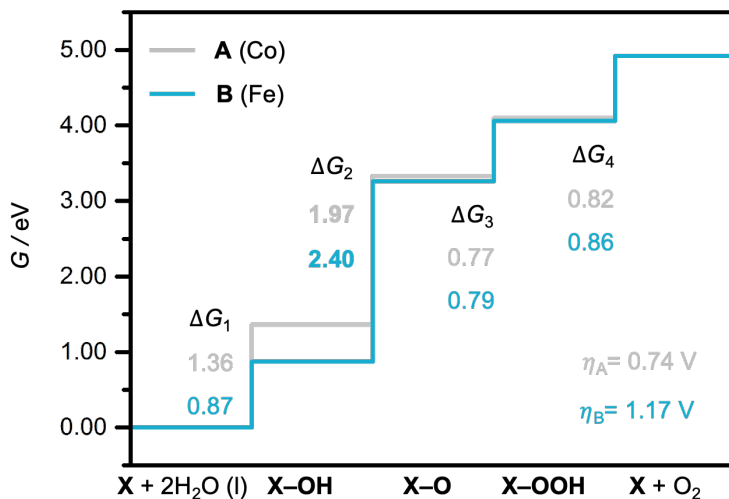


**Figure 3.5:** Models for *M*-MOF-74 with (left) antiferromagnetic (AFM) interchain and ferromagnetic (FM) intrachain couplings and (right) ferromagnetic intra- and interchain interactions. Color code: C (dark gray), O (red), spin up *M* (purple polyhedra), and spin down *M* (orange polyhedra).

In reference to magnetic properties, we explored the couplings between wires (interwire) and within the same wire (intrawire) (**Figure 3.5**). Previous experimental studies indicated that intrawire interactions presents always a ferromagnetic character (FM). In contrast, interwire interactions are antiferromagnetic (AFM) but FM coupling was also observed when applying a magnetic field or temperature.<sup>158</sup> Therefore, we computed the two kind

Chapter 3. Electrocatalytic sites of Earth-abundant MOF-74 for OER

of interwire interactions for Co- and Fe-MOF-74 models. We obtained isoenergetic structures within 0.02 eV, in agreement with previous theoretical studies.<sup>178</sup> Then, we computed the Gibbs energy profiles of the OER to assess the catalytic activity of the homometallic pristine Co-MOF-74 (**A**) and Fe-MOF-74 (**B**) models with interwire AFM interactions (**Figure 3.6**). The formation of **X-OOH** ( $\Delta G_3$ ) and **O<sub>2</sub>** ( $\Delta G_4$ ) leads to very similar values for both models **A** and **B**. In contrast, the two first PCET involving the formation of **X-OH** ( $\Delta G_1$ ) and **X-O** ( $\Delta G_2$ ) intermediates differ in *ca.* 0.5 eV. Spin densities (**Appendix A, Table 6.2**) and structural features of the **B-OH** and **B-O** are in line with previous theoretical works. [180, 181] In addition, analogous results were obtained for models with interwire FM coupling (**Appendix A, Table 6.1**).



**Figure 3.6:** OER Gibbs energy profiles for models **A** and **B** at pH = 0,  $T = 298.15$  K, and zero potential ( $U = 0$  V).

Previous literature point to a scaling relationship of 3.2 eV (*i.e.* a constant Gibbs energy difference) between **X-OH** and **X-OOH** intermediates in

### 3.2. Properties and catalytic activity of pristine M-MOF-74

metals and metal oxides,<sup>162,182</sup> as well as for molecular catalysts.<sup>164</sup> Besides, similar values (between 2.5 and 3.2 eV) were reported for several MOF catalysts.<sup>153,155</sup> Indeed, we obtained Gibbs free energies differences of 2.74 and 3.19 eV, for **A** and **B**, respectively.

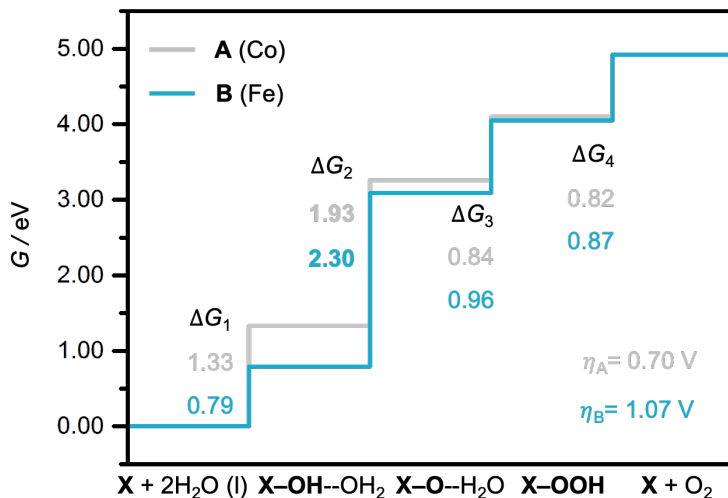
Then, we compared the obtained theoretical overpotentials ( $\eta_{\text{theor}}$ ) with the experimental overpotentials values by analysing the most energetically demanding steps (PDS) for systems **A** and **B**. In both cases, the PDS is represented by the oxidation of **X-OH** to **X-O** intermediate ( $\Delta G_2$ ), which render  $\eta_{\text{theor}}$  of 0.74 and 1.17 eV for **A** and **B**, respectively. Thus, although the computed Gibbs energy profiles are in agreement with previous theoretical works,  $\eta_{\text{theor}}$  are higher than those reported in the experiments (*ca.* 0.4 eV).<sup>69</sup> In view of such discrepancy, we computed the Gibbs free energy profiles for some models mixing Co and Fe sites in the same wire. The results were analogs to the ones obtained for the homometallic pristine models **A** and **B** (**Table 3.1**). Therefore, we performed additional simulations to validate our computational approach, in particular, the influence of local effects of the solvent and the methodology.

**Table 3.1:** Gibbs free energies ( $\Delta G$ , in eV) and theoretical overpotentials ( $\eta_{\text{theor}}$ , in V). Values in bold indicate the PDS.

Model	Site	$\Delta G_1$	$\Delta G_2$	$\Delta G_3$	$\Delta G_4$	$\eta_{\text{theor}}$
Co <sub>17</sub> -Fe-MOF-74	Co	1.38	<b>1.98</b>	0.77	0.78	0.75
	Fe	0.83	<b>2.40</b>	0.80	0.90	1.17
Co <sub>16</sub> -Fe <sub>2</sub> -MOF-74	Co	1.43	<b>1.98</b>	0.76	0.76	0.75
	Fe	0.85	<b>2.41</b>	0.79	0.88	1.18

**Solvation** We assessed the effect of including one explicit water molecule in the simulation of the intermediates involved in the PDS (**X-OH** and **X-O**). Thus, these intermediates could be stabilized by the formation of hydrogen bonds. However, the Gibbs energy profiles and the computed theoretical overpotentials did not change significantly, being 0.70 and 1.07 eV for **A** and **B**, respectively (**Figure 3.7**).

Chapter 3. Electrocatalytic sites of Earth-abundant MOF-74 for OER



**Figure 3.7:** OER Gibbs energy profiles for models **A** and **B** considering a explicit water molecule at pH = 0,  $T = 298.15$  K, and zero potential ( $U = 0$  V).

**Benchmark** We evaluated the impact of the methodology by benchmarking the results obtained with PBE+U with periodic models of Fe-MOF-74 with meta-GGA and hybrid density functionals in finite-size clusters.<sup>163</sup> The Gibbs energies and the overpotential obtained for the cluster model and different density functionals follow the same trends that the ones observed in the periodic models (**Table 3.2**). Density functionals with *ca.* 15% of Hartree-Fock exact exchange present lower overpotentials, but they are still higher than the experimental values. Moreover, the variations in the exact numbers of  $\Delta G_{1-4}$  observed along **Table 3.2** were expected since Corminbouef and co-workers previously reported about density functional sensitivity in molecular OER catalysts.<sup>183</sup> Moreover, the spin densities obtained at the periodic PBE+U level are similar to those observed for hybrid functionals ((**Appendix A, Table 6.3**)). Thereby, these benchmark calculations support the reliability of periodic PBE+U for the systems under study.

3.2. *Properties and catalytic activity of pristine M-MOF-74*

**Table 3.2:** Gibbs free energies ( $\Delta G$ , in eV) and theoretical overpotentials ( $\eta_{\text{theor}}$ , in V) obtained with the finite-size 88-atom cluster model of Fe-MOF-74 and different density functionals (DF). Values in bold indicates the PDS.

DF	$\chi^a$	$\Delta G_1$	$\Delta G_2$	$\Delta G_3$	$\Delta G_4$	$\eta_{\text{theor}}$
PBE	0	0.20	1.30	<b>1.85</b>	1.57	0.62
M06-L	0	0.22	<b>1.80</b>	1.48	1.42	0.57
HSE03-13	13	0.57	<b>1.84</b>	1.50	1.01	0.61
B3LYP-15	15	0.54	<b>1.82</b>	1.51	1.05	0.59
B3LYP	20	0.66	<b>2.03</b>	1.36	0.87	0.80
HSE03	25	0.80	<b>2.35</b>	1.16	0.61	1.12
PBE0	25	0.82	<b>2.38</b>	1.13	0.59	1.15

<sup>a</sup> Percentage of nonlocal Hartree-Fock exchange.

Overall, the simulations of OER intermediates and the associated overpotentials obtained with periodic PBE+ $U$  for the models of pristine Co- and Fe-MOF-74, together with the calculations to validate the computational approach, point to the under coordinate metal sites of these systems are not the active catalytic sites.



*Chapter 3. Electrocatalytic sites of Earth-abundant MOF-74 for OER*

---

### 3.3 Models and catalytic activity of defective Fe-MOF-74

The high theoretical overpotentials rendered by the pristine models **A** and **B** of *M*-MOF-74 led us to explore new catalytic sites by considering defective analogs, particularly structures with missing linkers.<sup>184,185</sup> We focused in Fe-MOF-74 with the aim of building models to represent an internal defect within the framework, as well as the external surface of a MOF nanoparticles or film.

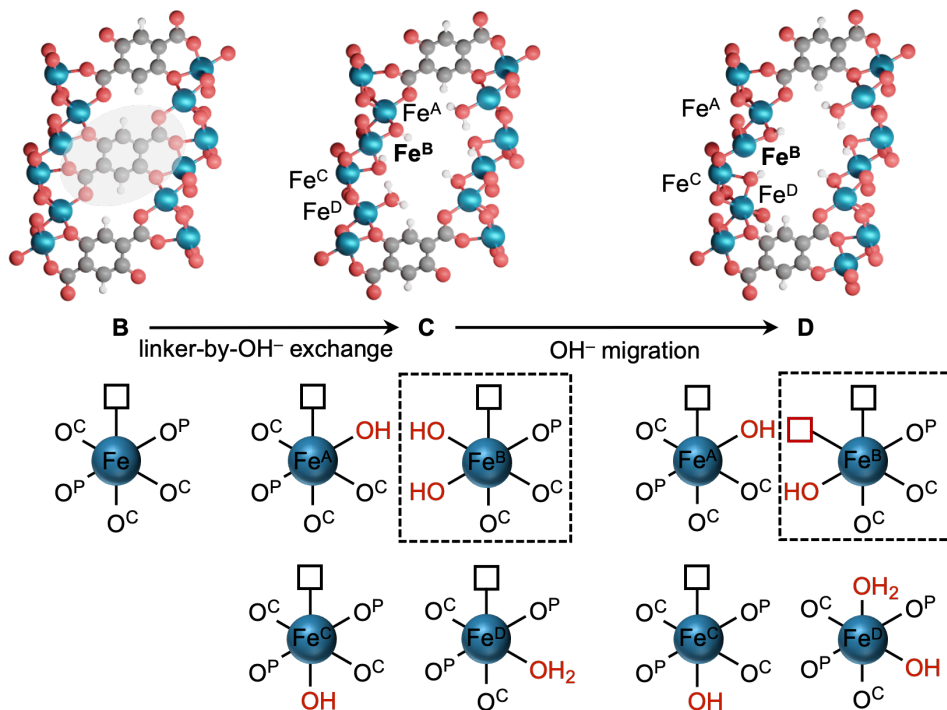
#### 3.3.1 Structural and electronic properties

Fe-MOF-74 defective structures were built and explored by removing a DOBDC linker of pristine model **B** and being subject to the following three considerations to ensure the reliability of the models:

1. The lattice parameter *c* of the pristine model **B** was doubled (from 6.821 to 13.642 Å) to prevent an excessive concentration of defects that could compromise the stability of the MOF.
2. We replaced one tetra-anionic six-coordinated linker (DOBDC) by two H<sub>2</sub>O and two hydroxides (OH<sup>-</sup>) to maintain the neutral character of the system and balance the coordination sites.<sup>186,187</sup>
3. Systematic exploration of different potential active sites.

There are different ways to replace one DOBDC linker by water molecules and hydroxides which lead to different Fe-MOF-74 defective structures. Therefore, the particular procedures to obtain two defective models (**C** and **D**) from pristine MOF structure **B** are explained in the following lines and shown in **Figure 3.8**.

### 3.3. Models and catalytic activity of defective Fe-MOF-74



**Figure 3.8:** Fe-MOF-74 pristine (**B**) and defective models (**C** and **D**) with the local coordination of their Fe centres. The dotted-squared Fe sites depict the centres discussed in detail along the text. Color code: O (red), H (white), C (dark gray), and Fe (blue).

Each DOBDC linker in **B** contains six oxygen atoms that belong to a carboxylate moiety ( $O^C$ ) or to a phenolate group ( $O^P$ ). In addition, the removal of such a linker renders two defective wires since each linker is connected to two wires. In the case of model **C**, we obtained two equally-modified wires by (i) eliminating one DOBDC, (ii) replacing the bi-coordinated  $O^P$  and  $O^C$  groups by four  $OH^-$ , and (iii) saturating the mono-coordinated  $O^C$  sites with two  $H_2O$ . The coordination mode of the hydroxides and water molecule in the defective model **C** resemble the one of

### Chapter 3. *Electrocatalytic sites of Earth-abundant MOF-74 for OER*

---

the oxygen atoms of DOBDC in the pristine model **B**. Thereby, the Fe atoms in the defective wires of **C** (labeled Fe<sup>A-D</sup>) are five-coordinated octahedra as those in **B** but with a different ligand environment. Besides, the constraints imposed by the linker in **B** are eliminated in **C** leading to ligands with higher mobility. Regarding the defective model **D**, it was built from **C** by leaving one entire defective wire unmodified and changing the coordination pattern of one OH<sup>-</sup>. In this case, Fe<sup>A</sup> and Fe<sup>C</sup> are five-coordinated sites with the same ligand environment as those of **C**, while Fe<sup>B</sup> is four-coordinated and Fe<sup>D</sup> is six-coordinated. Structure **C** is 0.16 eV more stable than **D**. This small difference indicates that **D** is thermally accessible and it could be relevant for catalytic purposes. The optimization of alternative defective structures to further explore the configurational space evolved to structures equivalent to **C** and **D**.

We also computed the band gap of **B**, **C**, and **D** to compare their electronic properties. We obtained a band gap of 1.86, 1.75, and 1.64 eV for **B**, **C**, and **D**, respectively. This indicates that the missing linker does not alter significantly the electronic properties of Fe-MOF-74, which is in agreement with previous theoretical studies of UiO-66 MOF.<sup>188</sup>

#### 3.3.2 Intermediates of OER

In analogy to pristine models, we computed the Gibbs energy profiles to identify the PDS and the associated  $\eta_{\text{theor}}$  on the defective models. However, in contrast to pristine models that contains only one type of coordinately unsaturated metal, different potential active sites were originated due to the linker removal in the defective models. Thus, the thermodynamics of OER were explored in several Fe centres of **C** and **D**.

First, we computed the Gibbs energy associated with the four intermediates of the OER on **C** (**Table 3.3**). **C** contains four Fe centres with the same coordination number as pristine model **B** but different ligand environment (Fe<sup>A-C</sup>). Therefore, we computed the first PCET leading to the formation of hydroxo intermediates ( $\Delta G_1$ ) on the four centres (**C<sup>A-C</sup>-OH**). The second step ( $\Delta G_2$ ) entails the formation of the oxo moiety (**C<sup>A-C</sup>-O**), which could take place in a terminal (**t**) or in a bridge (**b**) site. Then, the

### 3.3. Models and catalytic activity of defective Fe-MOF-74

reaction proceeds with the water nucleophilic attack ( $\Delta G_3$ ) to the oxo group leading to hydroperoxo intermediate ( $\mathbf{C}^{\mathbf{A-C}}\text{-OOH}$ ). Finally, the last PCET ( $\Delta G_4$ ) yields to  $\text{O}_2$  molecule and the recovery of the coordinately unsaturated metal  $\mathbf{C}^{\mathbf{A-C}}$ . The results for the four  $\mathbf{C}^{\mathbf{A-C}}$  sites, considering both the formation of terminal and bridge oxo moieties, do not depict significant differences between Fe centres (**Table 3.3**).

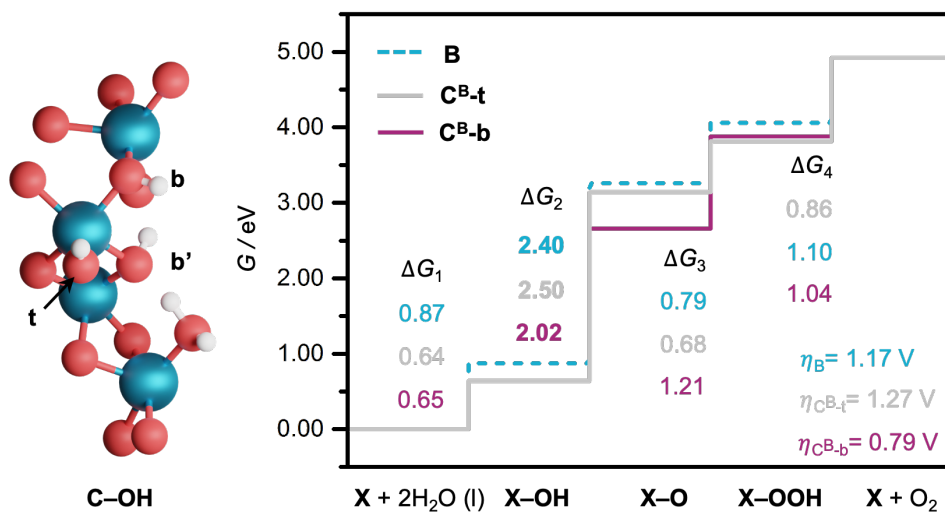
**Table 3.3:** Gibbs free energies ( $\Delta G$ , in eV) and theoretical overpotentials ( $\eta_{\text{theor}}$ , in V) associated with different Fe centres in defective model **C**. Values in bold indicate the PDS.

Model	$\Delta G_1$	$\Delta G_2$	$\Delta G_3$	$\Delta G_4$	$\eta_{\text{theor}}$
$\mathbf{C}^{\mathbf{A-t}}$	0.63	<b>2.39</b>	0.78	1.12	1.16
$\mathbf{C}^{\mathbf{A-b}}$	0.63	<b>2.00</b>	1.33	0.96	0.77
$\mathbf{C}^{\mathbf{C-t}}$	0.78	<b>2.44</b>	0.78	0.92	1.21
$\mathbf{C}^{\mathbf{C-b}}$	0.80	<b>2.27</b>	1.04	0.81	1.04
$\mathbf{C}^{\mathbf{D-t}}$	0.85	<b>2.43</b>	0.74	0.90	1.20
$\mathbf{C}^{\mathbf{D-b}}$	0.84	<b>2.25</b>	0.98	0.85	1.02

Hence, for the sake of relevance, we focused in the Gibbs energy profiles of  $\mathbf{C}^{\mathbf{B}}$ , namely **C** from now on, and compared to pristine **B** (**Figure 3.9**). Minor differences are observed in  $\Delta G_1$  between the pristine and defective models. Then, the oxidation of  $\mathbf{C-OH}$  to  $\mathbf{C-O}$  represents the PDS in terminal ( $\mathbf{C-O-t}$ ) and bridge positions ( $\mathbf{C-O-b}$  and  $\mathbf{C-O-b'}$ ) as it was observed for **B**. The values associated with  $\mathbf{C-O-t}$  are very similar to  $\mathbf{B-O}$ , while the process is favoured in  $\mathbf{C-O-b}$  due to the stabilization of the oxo group by two Fe centres. The alternative bridge position ( $\mathbf{C-O-b'}$ ) was discarded because a spontaneous proton transfer from the water ligand was identified rendering the formation of two hydroxo groups. Moreover, some differences can be observed for  $\Delta G_3$  and  $\Delta G_4$  along the different models but they can be neglected because the catalytic activity is dictated by the PDS ( $\Delta G_2$ ). The  $\eta_{\text{theor}}$  associated with  $\mathbf{C-O-t}$  is very similar to the pristine analogue  $\mathbf{B-O}$ , 1.27 and 1.17 eV, respectively. In contrast, the bridge site in the defective model  $\mathbf{C-O-b}$  present a lower overpotential of 0.79 V. However,

Chapter 3. Electrocatalytic sites of Earth-abundant MOF-74 for OER

this value is still high compared to the experimental overpotential (ca. 0.4 V).

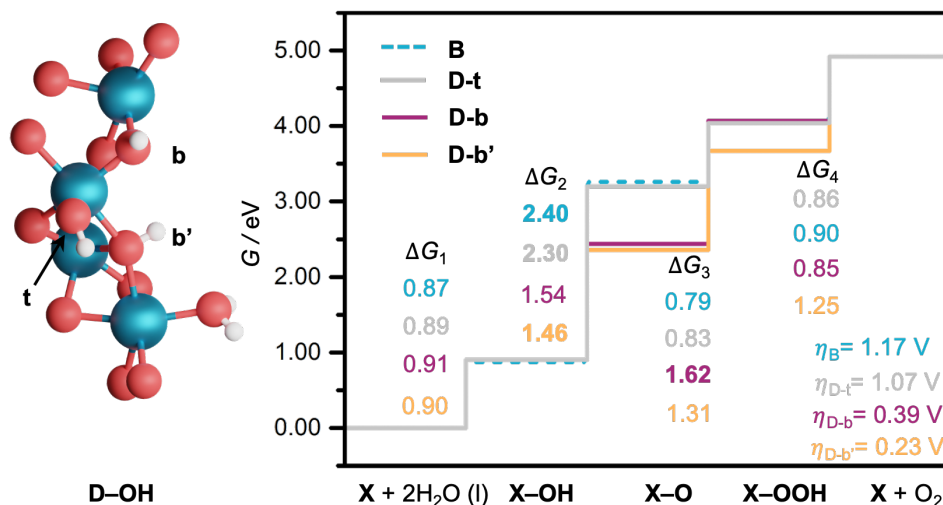


**Figure 3.9:** Simplified C-OH structure and OER Gibbs energy profiles for models B and C at pH = 0,  $T = 298.15$  K, and zero potential ( $U = 0$  V).

Then, we computed the OER Gibbs energy profiles on defective model **D** (Figure 3.10). This model contains four different Fe centres (**D<sup>A-C</sup>**). **D<sup>A</sup>** and **D<sup>C</sup>** are five-coordinated centres analogues to the ones assessed in **C**. **D<sup>D</sup>** is a six-coordinated centre which does not represent an open metal site suitable for carry out the reactivity. Therefore, we only explored the formation of **D-OH** in **D<sup>B</sup>**, namely **D** from now on. In line with **C**, the first PCET is very similar to that obtained for pristine **B**. Next, the removal of one  $H^+/e^-$  was assessed in a terminal and two bridge sites, leading to three different oxo intermediates (**B-O**, **B-O-b**, and **B-O-b'**). In analogy to **B** and **C**,  $\Delta G_2$  represents the PDS in the terminal site with an associated  $\eta_{\text{theor}}$  of 1.07 V. In contrast, the stabilization of the oxo group in the bridge positions lead to a relevant decrease of  $\Delta G_2$ . Indeed, the formation of **D-O-b'** still represent the PDS while  $\Delta G_3$  becomes the PDS in the **D-O-b**

### 3.3. Models and catalytic activity of defective Fe-MOF-74

path. Thereby, we obtained lower  $\eta_{\text{theor}}$  than in previous models and closer to the reported experimental overpotentials. In particular, we found  $\eta_{\text{theor}}$  of 0.39 and 0.23 V for **D-b'** and **D-b**, respectively.



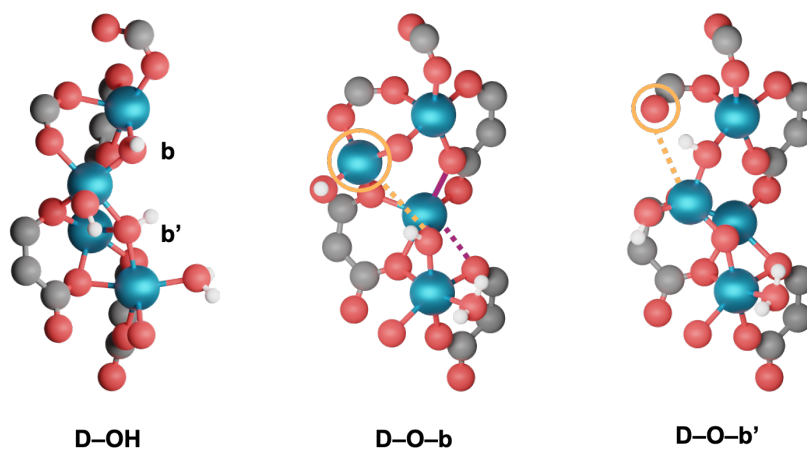
**Figure 3.10:** Simplified **D-OH** structure and OER Gibbs energy profiles for models **B** and **D** at pH = 0,  $T = 298.15$  K, and zero potential ( $U = 0$  V).

#### 3.3.3 Reversible linker reorganization

The stabilization of the oxo intermediates in bridge positions in defective models (**C** and **D**) is key to rationalize the catalytic activity of Fe-MOF-74. In particular, the low theoretical overpotentials obtained for **D**, led us to explore in further detail this structure. We identified a reversible linker reorganization associated with the formation of **D-O-b** and **D-O-b'** (**Figure 3.11**). This is in line with previous studies that attributed enhanced catalytic activity to bond-forming and bond-breaking processes within MOFs structures.<sup>189</sup> The oxidation of **D-OH** into **D-O-b** involves the breaking of a Fe-OH bond (dotted orange) and the formation of an

*Chapter 3. Electrocatalytic sites of Earth-abundant MOF-74 for OER*

oxo moiety bonded to a four-coordinated tetrahedral Fe centre (orange).<sup>190</sup> Besides, another reorganisation takes place in a neighbour Fe centre where a new Fe-O bond (purple) is formed while another one is broken (dotted purple). Regarding the formation of **D-O-b'**, it also renders an oxo group bonded to a four-coordinated tetrahedral Fe centre (orange) because of the breaking of a Fe-O bond (dotted orange). Remarkably, the octahedral coordination environment exhibited by the Fe centres in **D-OH** is recovered with the formation of the hydroperoxo intermediate **D-OOH** from **D-O-b** and **D-O-b'**.



**Figure 3.11:** Simplified structures for the computed **D-OH**, **D-O-b**, and **D-O-b'** intermediates. Dotted and solid purple lines indicate bond-breaking and bond-forming processes, respectively. Four-coordinate Fe centres are highlighted in orange. Color code: O (red), H (white), C (dark gray), and Fe (blue).

## 3.4 Conclusions

In this chapter, I have employed DFT+ $U$  periodic simulations to explore the structural and electronic features of the homometallic pristine Co(II)- and Fe(II)-MOF-74, as well as their catalytic activity towards OER. We have demonstrated that (i) the coordinately unsaturated sites of these pristine materials lead to high overpotentials and can not explain the catalytic activity observed in the experiments, and (ii) the reliability of our computational approach by carrying out benchmarks against high-level theory methods. Besides, we have systematically assessed different defective structures of Fe-MOF-74 and their catalytic properties. We have revealed that these defective sites are key to rationalize their catalytic activity. Indeed, the theoretical overpotentials yielded by Fe-MOF-74 with missing linkers are comparable to experimental data. This is possible because the defective structures (i) make feasible the formation of bridge oxo intermediates and (ii) introduce flexibility within the framework that allows reversible linkers reorganizations.

Overall, we point to defects as the active sites of Fe-MOF-74 towards OER and we highlight the importance of dynamic reorganization of the framework under reaction conditions. Therefore, this study paves the way to understand the true nature of the active sites in MOFs for electrochemical applications. Furthermore, it encourages to invest efforts towards defects engineering on MOFs for catalytic applications.



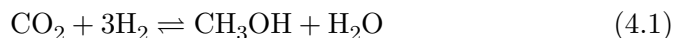
*Chapter 3. Electrocatalytic sites of Earth-abundant MOF-74 for OER*

---

## Chapter 4

# Metal-promoted metal oxides for green methanol production

The thermocatalytic hydrogenation of CO<sub>2</sub> to methanol (**Equation 4.1**) is envisaged to play a key role in the global efforts to tackle the climate change.<sup>8,17-26</sup> In this context, the design of Earth-abundant based catalysts able to suppress CO formation, which occurs through the reverse water-gas shift reaction (RWGS, **Equation 4.2**), is pivotal to ensure the effective production of methanol at industrial scale.



Metal-promoted metal oxides have shown promising potential due to the inherent features of these two types of materials.<sup>13-15,191-203</sup> CO<sub>2</sub> hydrogenation requires the activation of CO<sub>2</sub> and H<sub>2</sub>, followed by hydride-proton transfers leading to methanol (**Figure 4.1**). In this regard, metal oxides exhibit ideal acid-base properties to activate CO<sub>2</sub> on their basic oxygen atoms of the surface and to favour the protonation of key intermediates.

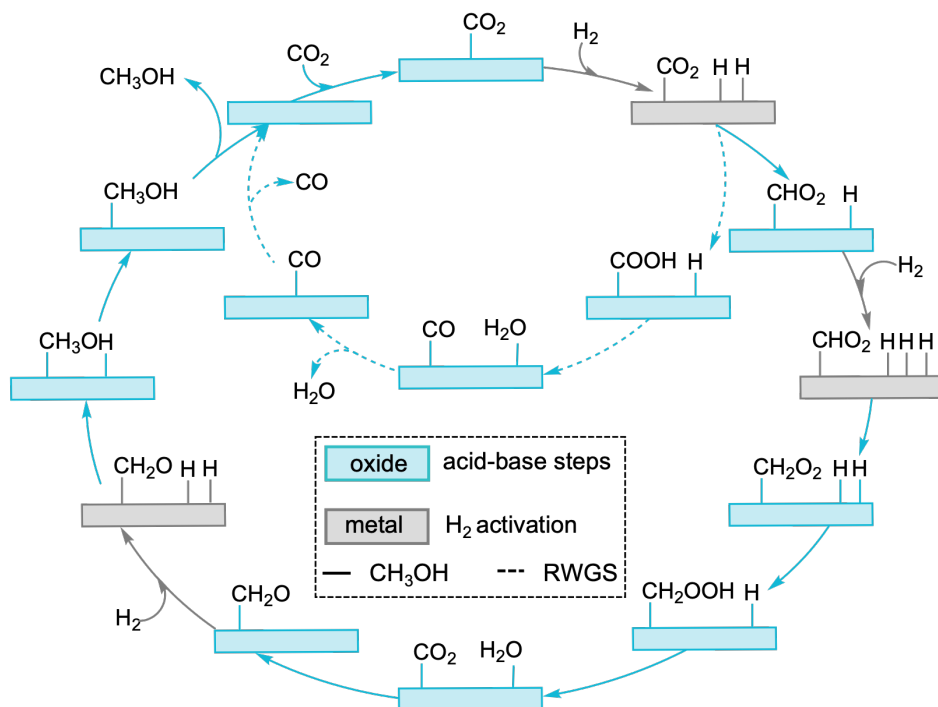
## *Chapter 4. Metal-promoted metal oxides for green methanol production*

---

Despite metal oxides present high selectivity to methanol, they do not possess optimal catalytic activity. This is because these materials have limited ability to activate  $\text{H}_2$  through heterolytic splitting leading to protons ( $\text{H}^+$ ) and hydrides ( $\text{H}^-$ ). In contrast, metal surfaces are able to activate hydrogen with low energy process *via* homolytic dissociation rendering neutral hydrogen atoms ( $\text{H}$ ). Nevertheless, an excess of  $\text{H}$  fosters both  $\text{MeOH}$  and  $\text{CO}$  formation.<sup>14,191</sup> Yet, metal surfaces are not able to effectively activate  $\text{CO}_2$  nor favour protonation steps. Thereby, a tight cooperation between the metal promoters and metal oxides is key to achieve high methanol productivity. However, the rational design of efficient multicomponent catalysts is hampered because of (i) the complex structural and electronic properties inherent to metal oxides, and (ii) the intricate interaction between the metal promoters and metal oxides, which modify the intrinsic properties of the two phases.

In this chapter, I present the systematic exploration *via* DFT simulations of  $\text{ZnZrO}_x$ ,<sup>13</sup> metal-promoted  $\text{In}_2\text{O}_3$ ,<sup>14,15</sup> and  $\text{Pd-In}_2\text{O}_3/\text{ZrO}_2$ <sup>16</sup> catalytic systems. This has been carried out in close cooperation with our experimental collaborators from the group of Prof. Pérez-Ramírez at ETH Zürich. Synthesis-structure-performance relationships were revealed by (i) comparing different synthetic methods, (ii) carrying out in deep experimental characterization and (iii) assessing the speciation and reactivity of the catalytic systems at the atomic level by means of DFT simulations. In particular, I focus in the modelling of these catalytic systems while highlighting the strong synergies established with experiments that were key to shed light to the properties of these convoluted materials. I have given special attention to show how the results of different experimental characterization techniques are combined and interpreted to build robust and rational models of the catalytic materials for DFT simulations. The fundamentals of the different experimental techniques are depicted in **Tables 1.1 and 1.1**, while particular insights associated with different systems provided by the analysis of the results and the implications rendered for the rational modelling are shown along this chapter. Moreover, I have assessed the architecture of the active sites at the atomic level of detail to reveal the key geometric and electronic features dictating the performance of the

different systems under study.



**Figure 4.1:** Reaction mechanism for CO<sub>2</sub> hydrogenation to methanol and the side RWGS reaction. Acid-base steps favoured on metal-oxides and H<sub>2</sub> activation favoured on metallic surfaces are depicted in blue and gray, respectively. The formate pathway was selected as it was identified as the dominant path in previous works of metal oxides.<sup>191,199,204–206</sup>

## *Chapter 4. Metal-promoted metal oxides for green methanol production*

---

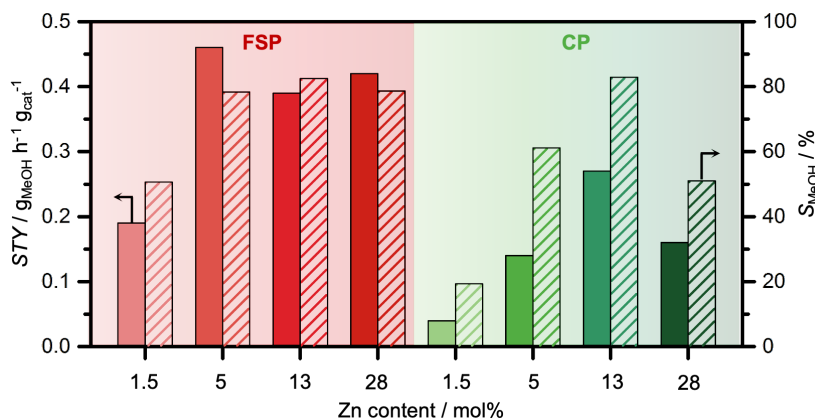
### **4.1 Zn promotion of zirconia polymorphs**

Zinc-zirconia ( $\text{ZnZrO}_x$ ) has emerged as promising Earth-abundant based and cost-effective material for  $\text{CO}_2$  hydrogenation to methanol. Indeed, this mixed reducible oxide has shown high selectivity and stability.<sup>199–202</sup> Previous works indicate that incorporation of Zn as single sites into the  $\text{ZrO}_2$  lattice (*i.e.* formation of solid solutions) is crucial to effectively activate  $\text{CO}_2$  and  $\text{H}_2$  to obtain  $\text{CH}_3\text{OH}$  while suppressing the RWGS.<sup>199,201,202,207</sup> Therefore, the common method to prepare  $\text{ZnZrO}_x$  catalysts is the coprecipitation (CP), since it favours the formation of the desired solid solutions. However, CP induces the incorporation of Zn into surface sites as well as bulk position. The last is detrimental for the catalytic properties because it leads to materials with low specific surface area and less efficient utilization of Zn.<sup>199–201,208,209</sup> Additionally, there are not systematically studies that explored in detail the architecture of the catalyst, such as the impact of zirconia polymorph or the Zn speciation. Therefore, the descriptors ruling the reactivity and stability of  $\text{ZnZrO}_x$  are still unclear. This, together with higher productivity requirements, hamper the use of these catalysts at the industrial scale. In this context, our collaborators from the group of Prof. Pérez-Ramírez employed flame spray pyrolysis (FSP) to prepare a broad range of  $\text{ZnZrO}_x$  catalysts with different amount of Zn. FSP was selected since is a one step and scalable method that offers effective control over the nanostructure of the catalyst, such as the crystal size morphology and surface area, rendering high stable and pure well-defined multicomponent materials.<sup>15,210–217</sup> The catalytic activity of such flame-made  $\text{ZnZrO}_x$  catalysts platform was tested and compared with CP-made analogs. Then, synthesis-structure-performance relationships were explored by in-depth experimental characterization and DFT simulations, which are the main theme of this section of the thesis.<sup>13</sup>

#### 4.1. Zn promotion of zirconia polymorphs

##### 4.1.1 Experimental insights in $\text{ZnZrO}_x$

The catalytic activity of FSP- and CP-made  $\text{ZnZrO}_x$  catalysts with 1.5-28 mol% Zn towards  $\text{CO}_2$  hydrogenation to  $\text{CH}_3\text{OH}$  was compared by means of space-time yield ( $STY$ ), which are the grams of  $\text{CH}_3\text{OH}$  produced by hour and gram of catalyst. **Figure 4.2** shows that coprecipitated materials present a typical volcano shape.  $STY$  increases when increasing the amount of Zn but it decreases after 13 mol%. In contrast, catalysts prepared by FSP exhibit a plateau at 5 mol%. The best FSP-made catalyst renders a *ca.* twofold  $STY$  with a significant smaller amount of Zn content (5 mol%) compared to the most active CP system (13 mol%). The trends exhibited by FSP- and CP-made  $\text{ZnZrO}_x$  catalysts in terms of selectivity to methanol are analogs to the catalytic activity. Interestingly, the best CP system exhibits the same selectivity as the FSP materials, which indicates that the two families of catalysts present similar active sites. These catalytic results led our experimental colleagues to explore the architecture of the catalysts in detail.



**Figure 4.2:** Methanol space-time yield ( $STY$ ) and selectivity ( $S_{\text{MeOH}}$ ) towards  $\text{CO}_2$  hydrogenation of FSP- and CP-made catalysts with different Zn content. Reaction conditions:  $T = 593 \text{ K}$ ,  $P = 5 \text{ MPa}$ ,  $GHSV = 24000 \text{ cm}^3 \text{ h}^{-1} \text{ g}_{\text{cat}}^{-1}$ .

#### *Chapter 4. Metal-promoted metal oxides for green methanol production*

---

Thereby, several characterization techniques were employed to assess the structural properties of the fresh and used catalysts. The insights provided by each characterization technique and the implications derived for the modelling of  $\text{ZnZrO}_x$  catalytic systems are shown in **Table 4.1**. Moreover, the catalytic activity of the different catalysts was tested under  $\text{CO}_2:\text{CO}$  feeds to explore their stability in the presence of carbon monoxide. The associated spectra and detailed data for the experimental characterization of the different systems can be found in [13].

In-depth experimental characterization shows that the best catalysts (CP and FSP with 13 and 5 mol% Zn, respectively) contains high dispersed Zn species incorporated into  $\text{ZrO}_2$  lattice. However, while the *t*- $\text{ZrO}_2$  is the dominant phase in CP-made catalysts and favours the Zn incorporation into bulk sites, FSP-made systems contains mixtures of *m*-, *t*-, and *c*- $\text{ZrO}_2$  phases with single sites of Zn incorporated into surface positions. Additionally, the amount of *m*- $\text{ZrO}_2$  at the surface of the FSP systems increases under reaction conditions. Thus, from the modelling standpoint, we needed to assess bulk and slab models of the three polymorphs to elucidate the Zn speciation and the catalytic properties of the  $\text{ZnZrO}_x$  systems.

## 4.1. Zn promotion of zirconia polymorphs

**Table 4.1:** Experimental insights provided by in-depth experimental characterization and their implications in the design of rational DFT models.

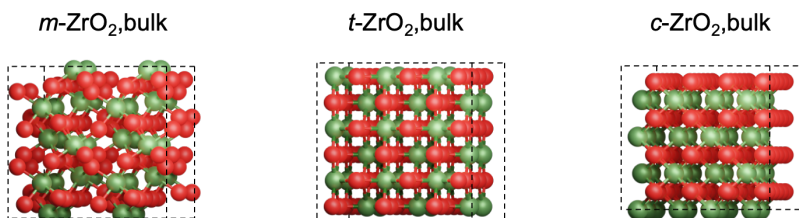
Technique	Experimental insights	Modelling implications
HRTEM and XRD	<p>CFP-made catalysts  <math>t</math>-ZrO<sub>2</sub> with some <math>m</math>-ZrO<sub>2</sub> and ZnO at low and high Zn contents, respectively.</p> <p>FSP-made catalysts                      Mixture of <math>t</math>-, <math>c</math>-, and <math>m</math>-ZrO<sub>2</sub>. The amount of <math>m</math>-ZrO<sub>2</sub> increases upon reaction.</p>	<p>Models of the three ZrO<sub>2</sub> polymorphs.</p>
XPS	<p>Significant Zn content in bulk sites.</p> <p>Zn located at surface sites.</p>	<p>Asses the incorporation of Zn into bulk and surface sites.</p>
UV Raman	<p>The fluorescent character of the samples does not allow the acquisition of Raman spectra.</p> <p>The surface of catalyst with low Zn content (1.5 and 5 mol%) transforms from <math>t</math>- to <math>m</math>-ZrO<sub>2</sub> upon reaction.</p> <p><math>c</math>-ZrO<sub>2</sub> is the dominant phase at higher Zn contents (13 and 28 mol%) and some <math>m</math>-ZrO<sub>2</sub> signals are also detected.</p>	<p>Slab models of the three ZrO<sub>2</sub> polymorphs.</p>
HAADF-STEM-EDX	<p>High Zn dispersion in the fresh catalysts.</p> <p>Some degree of sintering in the used samples.</p> <p>Phase segregation observed at high Zn contents (28 mol%).</p>	<p>Explore the catalytic activity in models with single sites of Zn incorporated into surface sites of the three ZrO<sub>2</sub> polymorphs.</p> <p>Deposition of Zn with metallic character on ZrO<sub>2</sub> discarded.</p>
XANES	<p>Atomically dispersed Zn species up to 5 mol%.</p> <p>Some segregation observed at higher Zn contents with non-detrimental effects in their catalytic activity.</p> <p>Oxidized Zn in used catalysts with 5 and 13 Zn mol%.</p>	
EXAFS	<p>Zn-O and Zn-Zn contributions in used catalyst with 13 Zn mol%.</p> <p>Zn-O contributions in used catalyst with 5 Zn mol%.</p> <p>Linear correlation between CO<sub>2</sub> uptake and STY up to 5 mol% of Zn.</p>	
Volumetric chemisorption	<p>Absence of metallic Zn.</p> <p>Different signals and intensities in function of conditions (further explained in the text).</p>	<p>Explore different type of oxygen vacancies and their influence in the speciation and catalytic activity.</p>
Zn LMM Auger	<p>Different signals and intensities in function of conditions (further explained in the text).</p> <p>Stable catalytic activity.</p>	<p>Discard the formation of MeOH through the CO path.</p>
EPR		
Catalytic testing under CO <sub>2</sub> :CO feeds		



## Chapter 4. Metal-promoted metal oxides for green methanol production

### 4.1.2 Methodology

DFT simulations were performed with the PBE<sup>107</sup> density functional and particular structures were assessed with the hybrid functional HSE03 with 13% of non-local Hartree-Fock exchange.<sup>169</sup> Core electrons were described with PAW pseudopotentials<sup>137,138</sup> and valence electrons were represented with plane-waves with a kinetic cut-off energy of 500 eV. We used a  $\Gamma$ -centered mesh with a reciprocal grid size narrower than  $0.037 \text{ \AA}^{-1}$  to sample the Brillouin zone.  $m$ -,  $t$ -, and  $c$ -ZrO<sub>2</sub> belong to  $P2_1/C$ ,  $P4_2/nmc$ , and  $Fm-3m$  space groups, respectively. Their lattice parameters were optimized with a kinetic energy cut-off of 700 eV and they were in line with experiments and previous theoretical works.<sup>13,218-221</sup> We employed  $2 \times 2 \times 2$  (monoclinic and cubic) and  $2 \times 2 \times 3$  (tetragonal) supercells to assess the incorporation of Zn in bulk sites (by replacing one Zr atom), as well as to explore the oxygen vacancy formation in undoped and Zn-doped ZrO<sub>2</sub> systems (**Figure 4.3**).

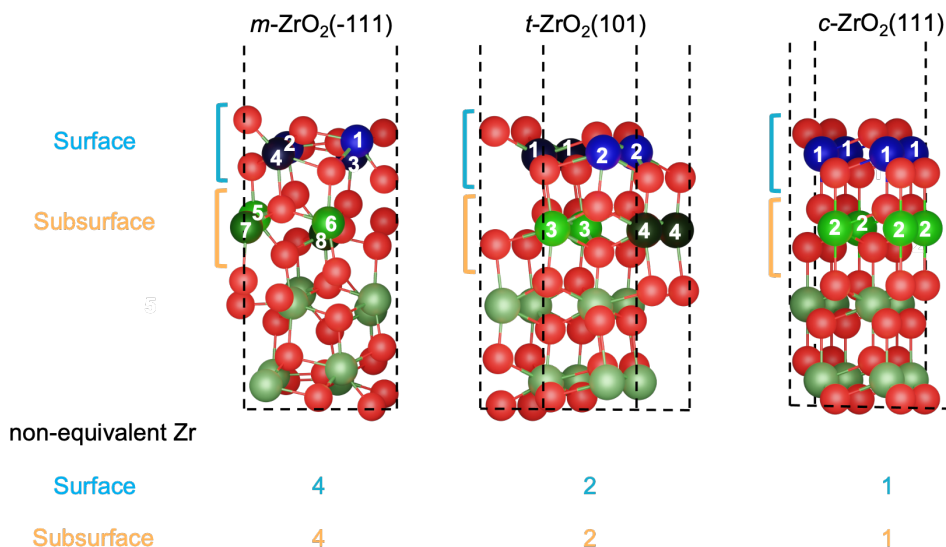


**Figure 4.3:** Supercells of  $m$ -,  $t$ -, and  $c$ -ZrO<sub>2</sub> polymorphs used to assess the properties of bulk sites. Color code: Zr (green) and O (red).

From the optimized lattice parameters we built slab models of the most stable oxygen terminated surface of each polymorph.<sup>222,223</sup> Thereby, we used  $p(1 \times 1)$  ( $-111$ ),  $p(1 \times 2)$  ( $101$ ), and  $p(2 \times 2)$  ( $111$ ) slab models for  $m$ -,  $t$ -, and  $c$ -ZrO<sub>2</sub>, respectively. In all cases, the slabs contain four layers being the two outermost allowed to relax while the inner two layers were kept fix mimicking bulk positions. Although the ZrO<sub>2</sub> motifs are different for the three polymorphs, the three models contain the same number of ZrO<sub>2</sub>

#### 4.1. Zn promotion of zirconia polymorphs

formula units and equal ratio of relaxed/fixed atoms.

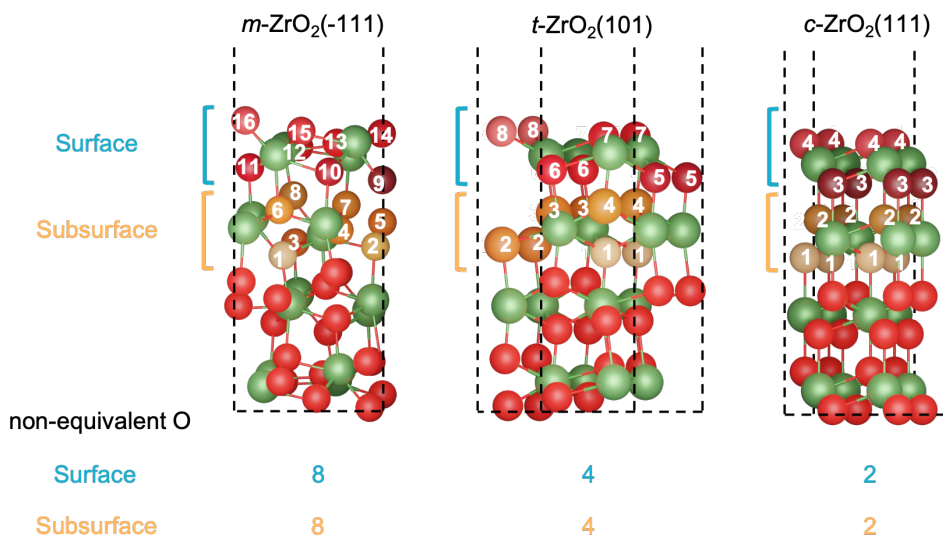


**Figure 4.4:** Slab models of  $m$ -,  $t$ -, and  $c$ - $\text{ZrO}_2$  polymorphs used to assess the properties of all non-equivalent surface (shades of blue) and subsurface (shades of green) sites. O atoms are depicted in red and Zr atoms in bulk sites are represented in green.

With these slab models at hand, we assessed the incorporation of Zn by replacing each of non-equivalent Zr atoms of the surface and subsurface  $m$ -,  $t$ -, and  $c$ - $\text{ZrO}_2$  sites (**Figure 4.4**). We also studied the formation of oxygen vacancies in the undoped and Zn-doped  $\text{ZrO}_2$  slab models (**Figure 4.5**). Additional details about Zn-Zr replacements and the assessment of the vacancy formation in the three  $\text{ZrO}_2$  polymorphs can be found in [13]. Moreover, energy profiles for  $\text{CO}_2$  hydrogenation to methanol and the competitive RWGS were computed on  $\text{ZnZrO}_x$  slab models with one oxygen vacancy of the three polymorphs. These surfaces,  $\text{CO}_2$ ,  $\text{H}_2$ , and  $\text{H}_2\text{O}$  were used as thermodynamic sinks. Furthermore, all input and outputs of the simulations can be accessed at <http://doi.org/10.19061/>

Chapter 4. Metal-promoted metal oxides for green methanol production

iochem-bd-1-259.



**Figure 4.5:** Slab models of  $m$ -,  $t$ -, and  $c$ - $\text{ZrO}_2$  polymorphs used to assess the formation of oxygen vacancies in all non-equivalent surface (shades of red) and subsurface (shades of orange) positions. Zr atoms are depicted in green and O atoms at bulk positions are represented in red.

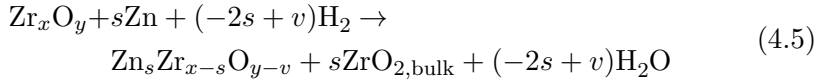
The equations employed to evaluate the relative energy between  $\text{ZrO}_2$  polymorphs, as well as to assess Zn-doped and oxygen defective structures are explained in the following lines. I used **Equations 4.3-4.4** to calculate the formation energy ( $E_f$ ) of  $m$ -,  $t$ -, and  $c$ - $\text{ZrO}_2$  and compare their relative stability. Metallic Zr bulk ( $E_{\text{Zr,bulk}}^{\text{DFT}}$ ) and molecular  $\text{O}_2$  ( $E_{\text{O}_2,\text{gas}}^{\text{DFT}}$ ) were employed as references.



$$E_f = E_{\text{ZrO}_2,\text{bulk}}^{\text{DFT}} - E_{\text{Zr,bulk}}^{\text{DFT}} - E_{\text{O}_2,\text{gas}}^{\text{DFT}} \quad (4.4)$$

#### 4.1. Zn promotion of zirconia polymorphs

I assessed the tendency of Zn to incorporate into  $\text{ZrO}_2$  lattice (bulk, surface, and subsurface sites) and the formation of oxygen vacancies by computing the associated potential energy ( $E$ ) of each structure with **Equations 4.5-4.6**. The formula unit of each bulk polymorph ( $E_{\text{ZrO}_2,\text{bulk}}^{\text{DFT}}$ ), Zn metal ( $E_{\text{Zn,bulk}}^{\text{DFT}}$ ), hydrogen ( $E_{\text{H}_2,\text{gas}}^{\text{DFT}}$ ) and water ( $E_{\text{H}_2\text{O,gas}}^{\text{DFT}}$ ) were used as energy references.  $\text{Zr}_x\text{O}_y$  stands for the undoped bulk supercells or the slab model of each polymorph, the parameter  $s$  represents the number of Zr atoms replaced by Zn, and  $v$  is the number of oxygen vacancies.



$$E = E_{\text{Zn}_s\text{Zr}_{x-s}\text{O}_{y-v}}^{\text{DFT}} + sE_{\text{ZrO}_{2,\text{bulk}}}^{\text{DFT}} + (-2s + v)E_{\text{H}_2\text{O,gas}}^{\text{DFT}} - E_{\text{Zr}_x\text{O}_y}^{\text{DFT}} - sE_{\text{Zn,bulk}}^{\text{DFT}} - (-2s + v)E_{\text{H}_2,\text{gas}}^{\text{DFT}} \quad (4.6)$$

Segregation energies ( $E_{\text{seg}}$ ) were calculated with **Equation 4.7** to analyse the tendency of the incorporated Zn atoms to move from bulk sites to subsurface and surface sites.

$$E_{\text{seg}} = E_{\text{Zn@surface/subsurface}} - E_{\text{Zn@bulk}} \quad (4.7)$$

Finally, oxygen vacancy formation energy ( $E_{\text{vac}}$ ) was calculated following **Equation 4.8**.

$$E_{\text{vac}} = E_{\text{Zn}_s\text{Zr}_{x-s}\text{O}_{y-v+1}}^{\text{DFT}} + E_{\text{H}_2\text{O,gas}}^{\text{DFT}} - E_{\text{Zn}_s\text{Zr}_{x-s}\text{O}_{y-v}}^{\text{DFT}} - E_{\text{H}_2,\text{gas}}^{\text{DFT}} \quad (4.8)$$

## Chapter 4. Metal-promoted metal oxides for green methanol production

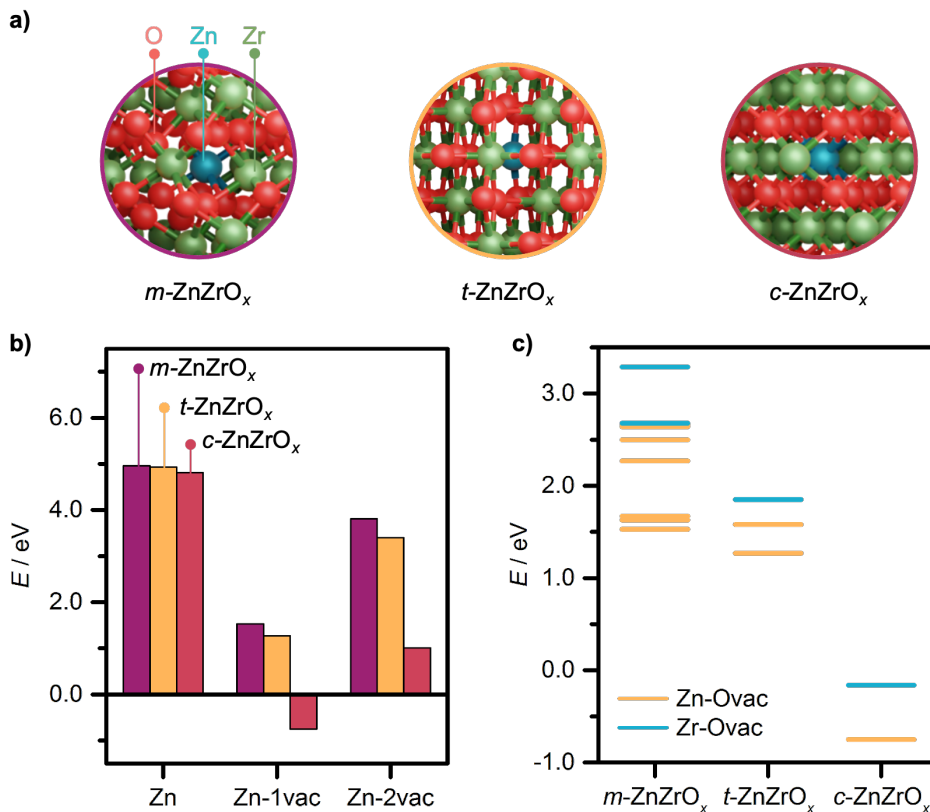
---

### 4.1.3 Zn incorporation into $\text{ZrO}_2$ polymorphs

Experimental characterization point to FSP-made catalysts are formed by a combination of *m*-, *t*-, and *c*- $\text{ZrO}_2$ . In contrast, *t*- $\text{ZrO}_2$  is the dominant phase in CP-made materials and *c*- $\text{ZrO}_2$  can not be disregarded as these two polymorphs are indistinguishable by XRD. Previous studies indicate that the three polymorphs exist at ambient pressure with different stability as a function of temperature.<sup>224</sup> *m*- $\text{ZrO}_2$  is the most stable polymorph at room temperature. However, when raising the temperature up to 1480 and 2650 K, it transforms into *t*- $\text{ZrO}_2$  and *c*- $\text{ZrO}_2$ , respectively. We computed the formation energy ( $E_f$ , **Equations 4.3-4.4**) of the three polymorphs. *m*- $\text{ZrO}_2$  is the most stable polymorph, being *t*- and *c*- $\text{ZrO}_2$  0.11 and 0.21 eV per formula unit less stable, respectively. Therefore, we employed supercells of the three bulks to assess the influence of Zn incorporation and the formation of oxygen vacancies in their relative stability (**Figure 4.3-4.6a**). The energies associated with the most stable structures with Zn incorporated into the lattice (Zn) and the formation of one (Zn-1vac) and two (Zn-2vac) oxygen vacancies are shown **Figure 4.6b**. It indicates that Zn incorporation is slightly favoured in *t*- and *c*- $\text{ZrO}_2$  structures. The incorporation is fostered by the formation of oxygen vacancies, in particular for *t*- and *c*- $\text{ZrO}_2$  polymorphs, which exhibits a higher stabilization compared to *m*- $\text{ZrO}_2$ . This explains the high content of Zn in bulk sites observed in the experimental characterization for CP-made catalysts and the presence of *t*- $\text{ZrO}_2$  although is less stable than its *m*- $\text{ZrO}_2$  counterparts. Going in further detail in the formation of oxygen vacancies, they are favoured in sites situated next to Zn (**Figure 4.6c**). Analogous results were obtained for the formation of a second oxygen vacancy (**Appendix B, Figure 6.1a**). However, although these structures are favoured over their non-defective counterparts, they are less stable than those with one vacancy.

Moving on to Zn incorporation and formation of oxygen vacancies in surface and subsurface sites, **Figure 4.7** depicts the results of the most stable structures. The results are analogous to those obtained for bulk sites and the incorporation of Zn into surface sites is fostered by the formation of oxygen vacancies. However, the incorporation of Zn is favoured in *m*- and *t*- $\text{ZrO}_2$

#### 4.1. Zn promotion of zirconia polymorphs



**Figure 4.6:** a) Models and b) potential energies ( $E$ ) of the most stable structures with one incorporated zinc atom (Zn) and one (Zn-1vac) and two (Zn-2vac) oxygen vacancies in bulk sites of  $m$ -,  $t$ -, and  $c$ -ZrO<sub>2</sub> polymorphs. c)  $E$  associated with bulk ZnZrO<sub>x</sub> models with one oxygen vacancy next to Zn(Zn-Ovac) or Zr(Zr-Ovac).

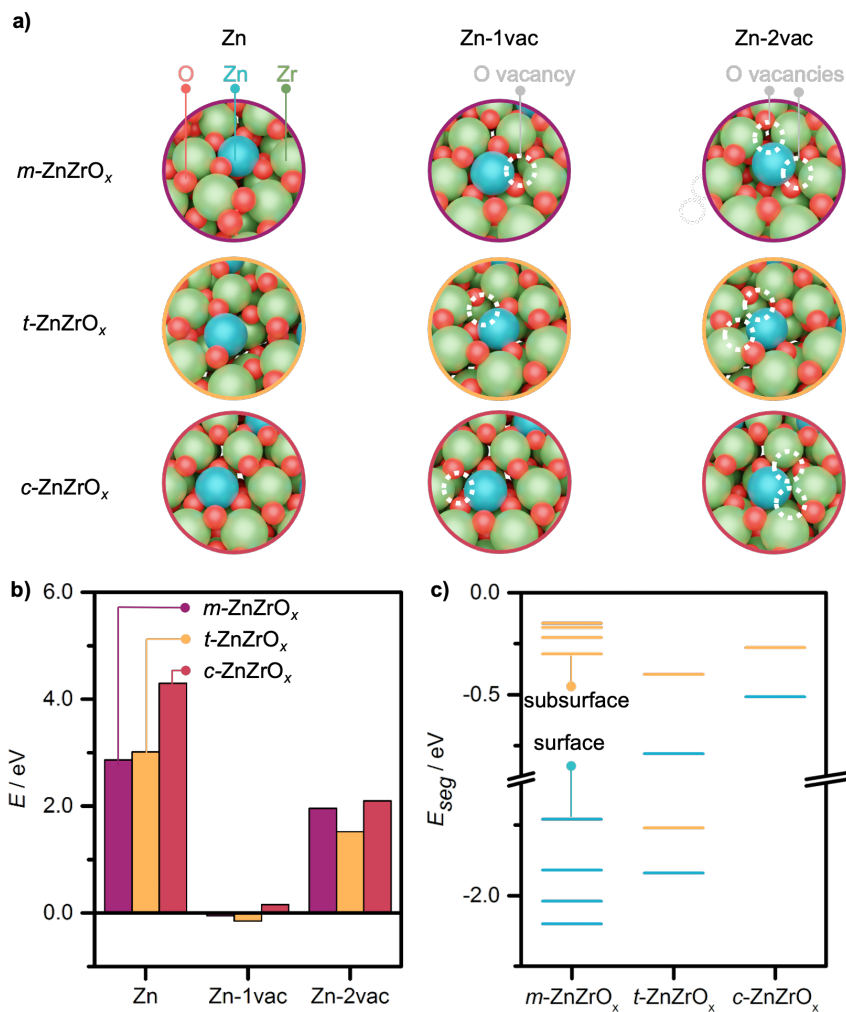
over  $c$ -ZrO<sub>2</sub> structures. These results are in line with UV-Raman spectra that indicates the coexistence of the three phases in the surface of FSP-made catalysts. Moreover, it should be highlighted that Zn incorporation and oxygen vacancies are favoured in surface over subsurface sites and just as

#### *Chapter 4. Metal-promoted metal oxides for green methanol production*

---

for bulk sites, structures with two vacancies are less stable than those with one vacancy (**Appendix B, Figures 6.1b-6.2**). Then, we assessed the tendency of Zn incorporated to bulk sites to move to subsurface and surface positions by means of segregation energies ( $E_{\text{seg}}$ , **Equation 4.7**). The results obtained for  $E_{\text{seg}}$  point to surface sites as the most stable positions from a thermodynamic standpoint and the ability of FSP to reach these sites (**Figure 4.6c**). Finally, segregation is more favoured in *m*- and *t*-ZrO<sub>2</sub> over *c*-ZrO<sub>2</sub> structures, which is in line with UV-Raman spectra of the FSP-made catalyst since *c*-ZrO<sub>2</sub> phase is only detected in the surface at high Zn contents.

#### 4.1. Zn promotion of zirconia polymorphs



**Figure 4.7:** a) Models and b) potential energies ( $E$ ) of the most stable structures with one incorporated zinc atom (Zn) and one (Zn-1vac) and two (Zn-2vac) oxygen vacancies at surface sites of  $m$ -,  $t$ -, and  $c$ -ZrO<sub>2</sub> polymorphs. c) Segregation energies ( $E_{seg}$ ) for a zinc atom to move from bulk to surface and subsurface sites in the three ZrO<sub>2</sub> polymorphs.



## Chapter 4. Metal-promoted metal oxides for green methanol production

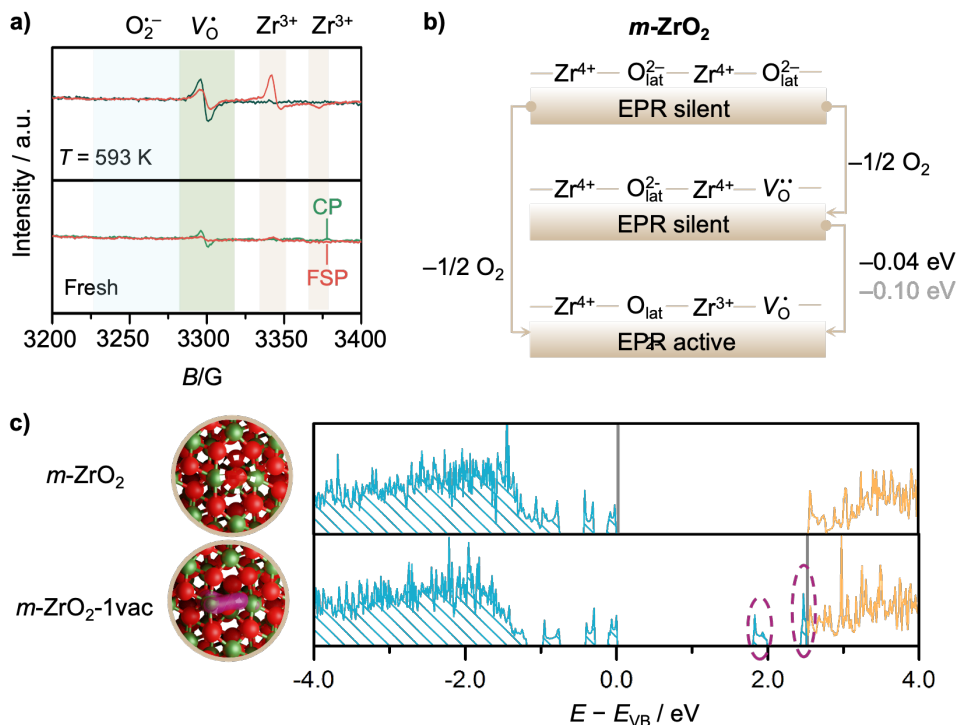
---

### 4.1.4 Oxygen vacancies in $\text{ZnZrO}_x$ systems

Previous studies indicated that the catalytic activity towards  $\text{CO}_2$  hydrogenation to methanol of other metal oxides systems, such as  $\text{In}_2\text{O}_3$ ,<sup>204</sup>  $\text{In}_2\text{O}_3\text{-ZrO}_2$ ,<sup>208</sup> and  $\text{Pd-In}_2\text{O}_3\text{-ZrO}_2$ ,<sup>210</sup> is dictated by the presence of oxygen vacancies. Additionally, previous works also point to the importance of these defects in the catalytic activity of  $\text{ZnZrO}_x$  systems, but there is a lack of fundamental understanding.<sup>203</sup> Thus, we combined paramagnetic spectroscopy (EPR) spectra and DFT simulations to provide insights in the oxygen vacancy formation mechanism in the most active FSP- and CP-made  $\text{ZnZrO}_x$  catalysts.

First, it should be noted that in metal oxides the formation oxygen vacancy ( $V_{\text{O}}$ ) leads to the presence of two excess electrons that could be accommodated in different ways as a function of the reducible character of system.<sup>13</sup> In the case of non-reducible oxides (*i.e.*  $\text{MgO}$ ), the two electrons are trapped in the vacancy site ( $V_{\text{O}}^{\bullet\bullet}$ ) which is EPR silent. In contrast, in reducible oxides, such as  $\text{CeO}_2$  and  $\text{TiO}_2$ , two cations are reduced to  $\text{Ce}^{3+}$  and  $\text{Ti}^{3+}$ , respectively, which would be EPR active. Midway between these two behaviours, one electron could be trapped in the vacancy site ( $V_{\text{O}}^{\bullet}$ ) and the other could be able to reduce a metal cation, which also could lead to EPR active species. The EPR spectrum of the fresh FSP catalyst depicts a weak signal related with  $V_{\text{O}}^{\bullet}$  (**Figure 4.8a**). This signal becomes stronger and accompanied by the formation of Zr cations with one unpaired  $d$  electron ( $\text{Zr}^{3+}$ ) under thermal treatment, which is not observed for the CP catalyst. DFT simulations show that the formation of the EPR active species ( $V_{\text{O}}^{\bullet}$  and  $\text{Zr}^{3+}$ ) in  $m\text{-ZrO}_2$  structures is favoured by 0.4 eV over EPR silent species ( $V_{\text{O}}^{\bullet\bullet}$ ), and further corroborated with simulations with the hybrid functional HSE03 with 13% of non-local Hartree-Fock exchange (**Figure 4.8b**). Therefore, the behaviour of  $m\text{-ZrO}_2$  relies in the midway between non-reducible and reducible oxides **Figure 4.8c**. Additionally, the formation of  $\text{Zr}^{3+}$  was not identified by DFT simulations in  $t\text{-ZrO}_2$  and  $c\text{-ZrO}_2$  surfaces, which is in line with the absence of this signal in the CP catalyst.

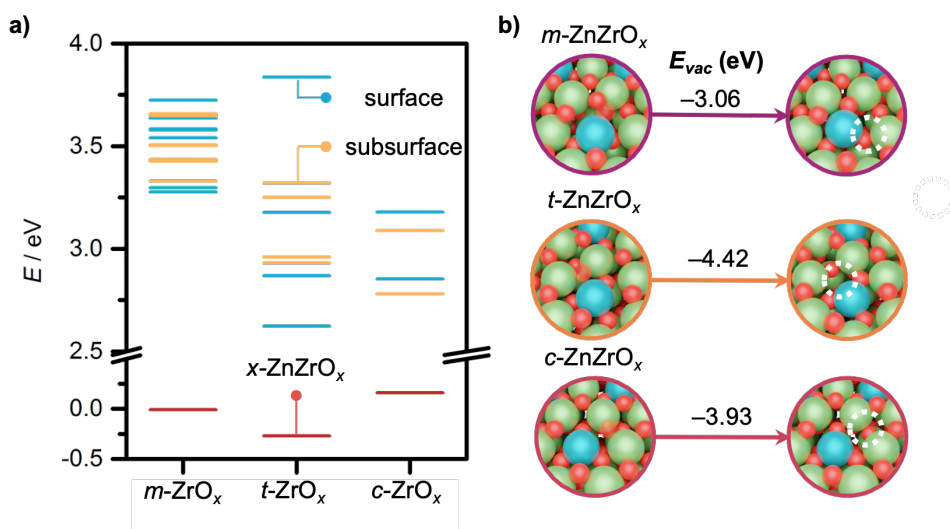
4.1. Zn promotion of zirconia polymorphs



**Figure 4.8:** **a)** EPR spectra of the best fresh and activated ( $T = 593$  K,  $P = 0.1$  MPa, and Ar flow of  $20 \text{ cm}^3 \text{ min}^{-1}$ ) FSP- and CP-made ZnZrOx. **b)** Oxygen vacancy formation mechanism of  $m\text{-ZrO}_2$  EPR active and silent structures obtained *via* DFT simulations. The values in black and gray were obtained with PBE and HSE03 functionals, respectively. **c)** DFT models and Density of States (DOS) for pristine and oxygen defective  $m\text{-ZrO}_2$ . DOS are aligned *vs* the valence band of the pristine surface. Color code for DOS: Unoccupied and occupied bands (blue and orange, respectively), top of the valence band (gray line), and states arising from reduction of the metal oxide (highlighted with dotted magenta lines). Color code for the models: O (red), O vacancy site (dotted white lines), H (white), Zr (green). Partial electron density of the highest occupied states originated upon vacancy formation is depicted in magenta.

Chapter 4. Metal-promoted metal oxides for green methanol production

Interestingly, as the incorporation of Zn promotes the formation of oxygen vacancies, the appearance of these defective sites is favoured near Zn positions over undoped sites (**Figure 4.9a**). Indeed, the formation of oxygen-defective  $\text{ZnZrO}_x$  structures is very exothermic (**Figure 4.9b**). Therefore, these structures are particularly relevant for the catalytic properties, but they are EPR silent. Nevertheless, the  $\text{Zr}^{3+}$  signal associated with undoped  $m\text{-ZrO}_2$  could be used as a proxy of the formation of defective  $\text{ZnZrO}_x$  ensembles, since the former would be only generated once the oxygen vacancies are formed near Zn sites.



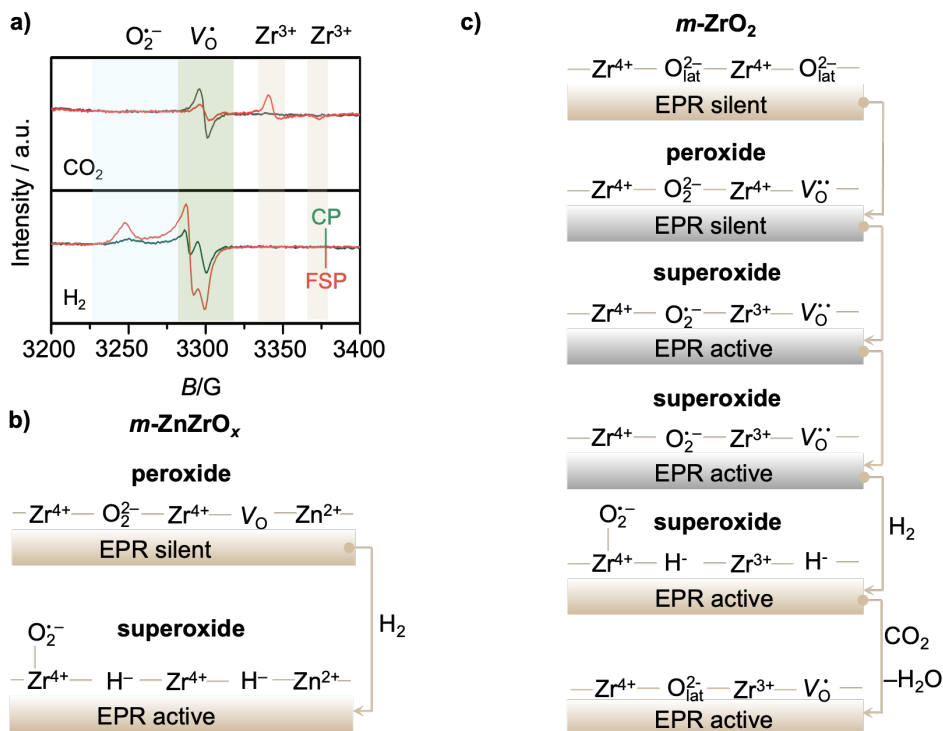
**Figure 4.9:** **a)** Potential energy ( $E$ ) associated with undoped  $m$ -,  $t$ - and  $c$   $\text{ZrO}_2$  models with one oxygen vacancy at different surface and subsurface sites. The values for the most stable  $\text{ZnZrO}_x$  defective structures are also shown ( $x\text{-ZnZrO}_x$ ). **b)** Vacancy formation energy ( $E_{vac}$ ) obtained from **Equation 4.8**, and required to form the  $x\text{-ZnZrO}_x$  systems, which were employed to compute energy profiles for  $\text{CO}_2$  hydrogenation to methanol and carbon monoxide. Color code: O (red), O vacancy site (shaded red and dotted white lines), H (white), Zr (green), and Zn (blue).

---

#### 4.1. Zn promotion of zirconia polymorphs

Furthermore, EPR measurements under H<sub>2</sub> feeds indicated the appearance of superoxide species (O<sub>2</sub><sup>•-</sup>) in FSP and CP catalysts, being the signal stronger in FSP systems and depicting a higher amount of oxygen vacancies **Figure 4.10a**. Furthermore, DFT simulations provides additional insights to this fact (**Figure 4.10b,c**). We found that the formation of O<sub>2</sub><sup>•-</sup> is stabilized by the incorporation of hydrogen to vacancy sites, both in undoped and Zn doped *m*-ZrO<sub>2</sub> systems. Finally, after exposing the samples to CO<sub>2</sub>, the V<sub>O</sub><sup>•</sup>-Zr<sup>3+</sup> signals are recovered due to H<sub>2</sub>O formation. Overall, the strong synergies between EPR spectra and DFT simulations gave us insights about the vacancy formation mechanism in ZnZrO<sub>x</sub> systems.

Chapter 4. Metal-promoted metal oxides for green methanol production



**Figure 4.10:** a) EPR spectra of the best fresh and activated under flowing  $\text{H}_2$  and  $\text{CO}_2$  flows ( $T = 593 \text{ K}$ ,  $P = 0.1 \text{ MPa}$ , and flow of  $20 \text{ cm}^3 \text{ min}^{-1}$ ) FSP- and CP-made  $\text{ZnZrO}_x$  catalysts. Proposed mechanisms obtained *via* DFT simulations for b) peroxides evolution to superoxides species stabilized by  $\text{H}_2$  in  $m\text{-ZnZrO}_x$ ; and c) superoxide formation and stabilization by the presence of  $\text{H}_2$  and recovery of  $\text{V}_\text{O}^\bullet\text{-Zr}^{3+}$  moieties under  $\text{CO}_2$  flows due to  $\text{H}_2\text{O}$  formation in  $m\text{-ZrO}_2$ . All the attempts to obtain the structures in gray boxes *via* DFT led to alternative structures.

---

#### 4.1. Zn promotion of zirconia polymorphs

##### 4.1.5 Reactivity of Zn-containing ZrO<sub>2</sub> polymorphs

With the in detail analysis of the structure of the catalysis carried out by experimental characterization and DFT simulations, we moved on to shed light on the catalytic properties. We computed the reaction energy profiles of the CO<sub>2</sub> hydrogenation to methanol and the RWGS competitive reaction on the Zn-doped and oxygen vacancy-containing surfaces of the three polymorphs (**Figure 4.11** and **Appendix B, Figure 6.3**). This particular models were selected because they were found as the most dominant in our DFT speciation studies and they are in line with the experimental characterization. Previous computational studies on ZnZrO<sub>x</sub><sup>199,203</sup> and other related metal oxides (In<sub>2</sub>O<sub>3</sub><sup>204</sup> and metal-doped In<sub>2</sub>O<sub>3</sub><sup>191,205,206</sup>) pointed to the formate pathway as the most favoured route for CO<sub>2</sub> hydrogenation to methanol (**Figure 4.1**). Thus, this pathway was employed to compare the reaction energy profiles on the three Zn-containing ZrO<sub>2</sub> polymorph with one oxygen vacancy due to the structural similarities with the aforementioned metal oxide systems. Additionally, the results of the catalytic testing under CO<sub>2</sub>:CO feeds discard the formation of methanol through CO path.

The process starts with the activation of CO<sub>2</sub> and H<sub>2</sub>. Carbon dioxide is adsorbed in an oxygen of the lattice as a carbonate with two oxygen interacting with open metal sites (Zr),<sup>225</sup> while H<sub>2</sub> is heterolytically dissociated leading to ZnH+OH. At this point, the paths for RWGS and methanol diverge. In the first case, a proton is transferred to CO<sub>2</sub> leading to a carboxylate (COOH). Then, COOH is protonated and dehydrated rendering carbon monoxide and water. In contrast, if CO<sub>2</sub> is hydrogenated leading to formate (HCOO), we enter in the methanol path. This is followed by the heterolytic activation of another H<sub>2</sub> molecule in a Zn-O pair. Then, HCOO is further hydrogenated to CH<sub>2</sub>O<sub>2</sub>, which is subsequently protonated to form CH<sub>2</sub>OOH. The last, is further protonated and dehydrated to form CH<sub>2</sub>O, which after another hydrogen heterolytic dissociation, it is hydrogenated to obtain the methoxy intermediate (CH<sub>3</sub>O). Finally, CH<sub>3</sub>OH is formed as result of the protonation of CH<sub>3</sub>O.

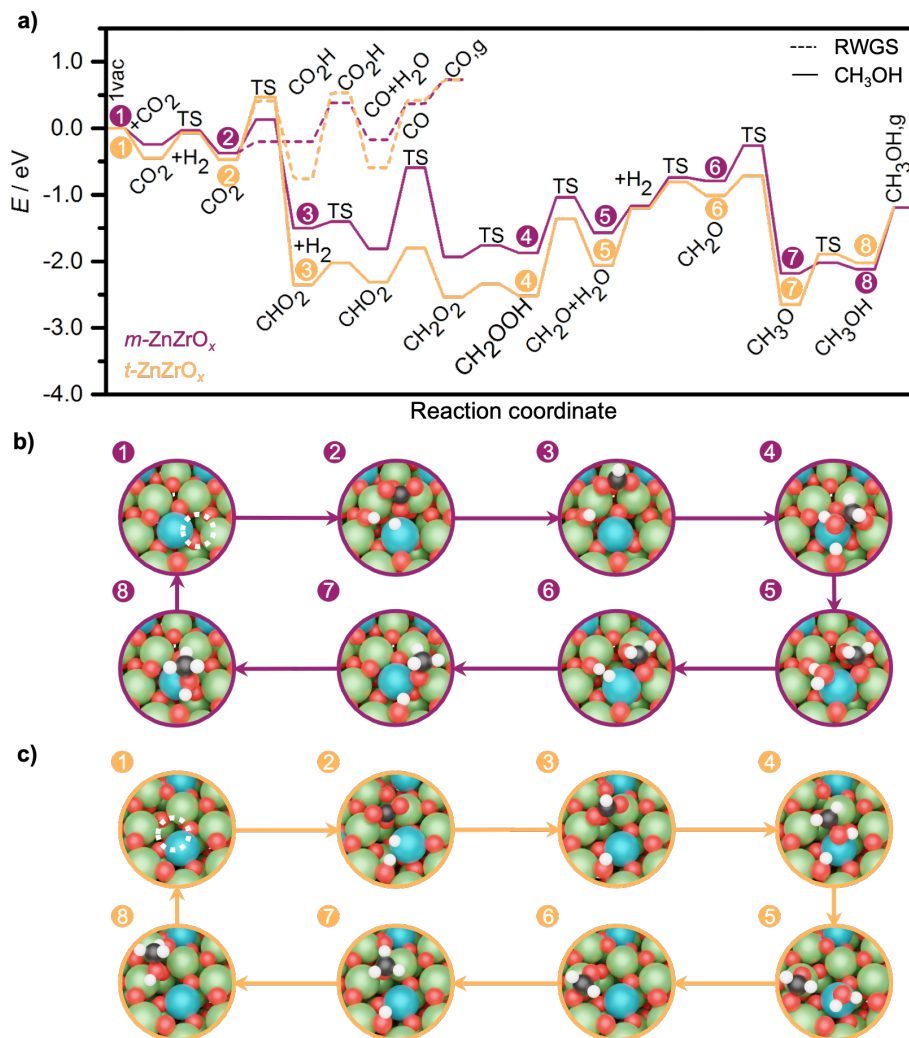
The reaction energy profiles for the *m*-, *t*-, and *c*-ZnZrO<sub>x</sub> surfaces indicated that the three of them are selective to methanol (**Figure**

*Chapter 4. Metal-promoted metal oxides for green methanol production*

---

**4.11 and Appendix B, Figure 6.3**). However, significant differences should be highlighted between *m*-ZnZrO<sub>x</sub> and the other polymorphs. Key intermediates, such as CHO<sub>2</sub>, CH<sub>2</sub>O<sub>2</sub>, CH<sub>2</sub>OOH, and CH<sub>3</sub>O, are overstabilized on *t*- and *c*-ZnZrO<sub>x</sub> surfaces. This points to *m*-ZnZrO<sub>x</sub> as the most active polymorph, which is in line with the detection of this phase by UV-Raman on the surface of the most active catalyst (FSP-made ZnZrO<sub>x</sub> catalyst with 5 mol% Zn).

4.1. Zn promotion of zirconia polymorphs



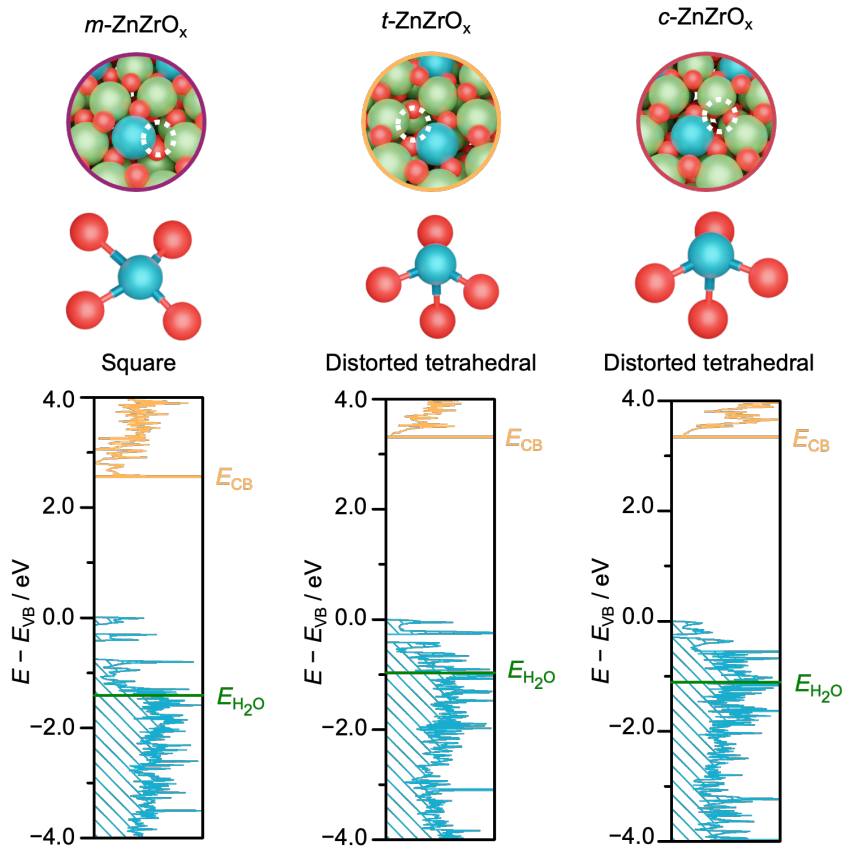
**Figure 4.11:** a) Reaction energy profiles for CO<sub>2</sub> hydrogenation to methanol and RWGS on *m*-, and *t*-ZnZrO<sub>x</sub> models with one oxygen vacancy. Snapshots of relevant intermediates associated with the labels in a) for b) *m*-ZnZrO<sub>x</sub> and c) *t*-ZnZrO<sub>x</sub>. Color code: Zr (green), Zn (blue), O (red), C (dark gray), H (white), and oxygen vacancy (dotted white circles). Adapted from [13].



#### Chapter 4. Metal-promoted metal oxides for green methanol production

We attribute the overstabilization of these intermediates to structural and electronic features. Particularly, the coordination environment of Zn and the acidity of the Zr cations. Zn presents a distorted tetrahedral coordination in *t*- and *c*-ZnZrO<sub>*x*</sub>, which resembles the one exhibited by Zn in bulk ZnO. In contrast, Zn in *m*-ZnZrO<sub>*x*</sub> exhibits a square coordination (**Figure 4.12**). The overstabilized key intermediates on *t*- and *c*-ZnZrO<sub>*x*</sub> interact through oxygen with the Zr cations of the three ZnZrO<sub>*x*</sub> polymorph surfaces. Thus, we assessed the acidity of these cations. We compared the relative position of the bottom of the conduction band ( $E_{CB}$ ) of the three ZnZrO<sub>*x*</sub> surfaces with respect to the highest occupied state of a water molecule ( $E_{H_2O}$ ).  $E_{CB}$  was selected as it represents the unoccupied states with the lowest energy and it could be related with the ability to accept electron density (*i.e.* acidity). Moreover,  $E_{H_2O}$  was used as a reference and it was obtained from a water molecule that was not interacting with the surfaces. Interestingly, the smallest difference between  $E_{CB}$  and  $E_{H_2O}$  was found for *m*-ZnZrO<sub>*x*</sub> (**Figure 4.12**). Thereby, the interaction of the oxygen of the key intermediates increases with the acidity of the Zr cations, which could be related with a higher position of the  $E_{CB}$ .

4.1. Zn promotion of zirconia polymorphs



**Figure 4.12:** Models of  $m$ -,  $t$ -, and  $c$ - $\text{ZnZrO}_x$  with one oxygen vacancy (top). Local coordination of Zn in the three models (centre). Associated DOS with one  $\text{H}_2\text{O}$  molecule placed in the vacuum region of the unit cell avoiding the interaction with the surface (bottom). DOS are aligned *vs* the valence band of each surface. Unoccupied and occupied bands are depicted in orange and blue, respectively. Bottom of the conduction band ( $E_{\text{CB}}$ ) is indicated with an orange line while the highest occupied state of water molecule ( $E_{\text{H}_2\text{O}}$ ) is highlighted with a green line. Color code: Zr (green), Zn (blue), O (red), and oxygen vacancy (dotted white circles).

## *Chapter 4. Metal-promoted metal oxides for green methanol production*

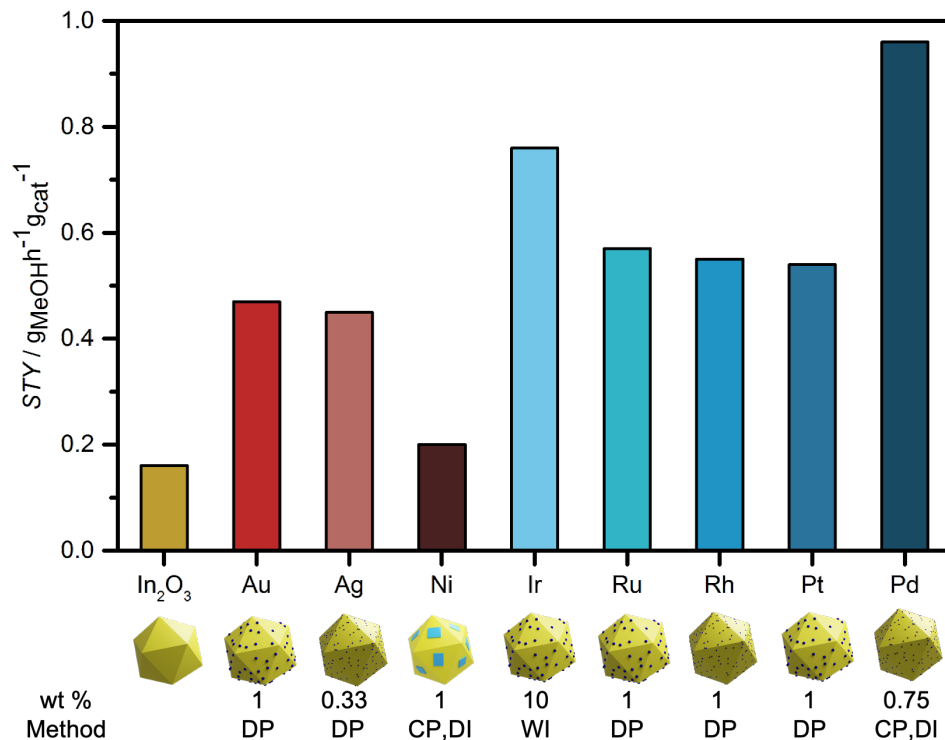
---

### **4.2 Metal promotional effects in $\text{In}_2\text{O}_3$**

In analogy to  $\text{ZnZrO}_x$  catalysts,  $\text{In}_2\text{O}_3$  has shown high selectivity and stability towards  $\text{CO}_2$  hydrogenation to methanol.<sup>226</sup> The groups of Prof. Javier Pérez-Ramírez and Prof. Núria López joint their efforts to rationalize the promising  $\text{In}_2\text{O}_3$  catalytic activity by combining experiments and DFT simulations.<sup>204</sup> It was demonstrated that oxygen vacancies are formed on the anisotropic surface of indium oxide rendering a particular  $\text{In}_3\text{O}_5$  ensemble, which is selective to methanol by suppressing the RWGS side reaction. Nevertheless, the methanol productivity over  $\text{In}_2\text{O}_3$  is limited and a plethora of metal promoters have been proposed in the literature to enhance the activation of  $\text{H}_2$  on this system. Indeed, the formation of high-dispersed Pd,<sup>191</sup> Pt,<sup>192</sup> Ir,<sup>193</sup> Rh,<sup>194</sup> Ag,<sup>195</sup> Ru,<sup>196</sup> and Au species,<sup>197</sup> in the form of low nuclearity-clusters or small metal nanoparticles (NPs), have shown higher *STY* compared with pure  $\text{In}_2\text{O}_3$ . Similarly, layered  $\text{InNi}_3$  alloys supported on  $\text{In}_2\text{O}_3$  and Co NPs decorated with indium oxide, exhibited beneficial effects in terms of methanol productivity.<sup>14,198</sup> However, the synthetic method, metal loading, reaction conditions, and architectures of these  $M\text{-In}_2\text{O}_3$  catalysts are different (**Figure 4.13**). Thus, a direct and reliable comparison between systems is not possible which hampers the elucidation of the promotional effects and the design of optimal catalysts.

For this reason, our experimental colleagues in the group of Prof. Javier Pérez-Ramírez employed FSP as standardized synthetic method to introduce nine different metal promoters (Pd, Pt, Ir, Rh, Ru, Ni, Co, Ag, Au) at 0.5 wt %. This method was selected due to its superior performance over other methods as mentioned in the previous section. Similarly to the  $\text{ZnZrO}_x$  study, catalytic testing of the nine  $M\text{-In}_2\text{O}_3$  catalysts was followed by in-depth experimental characterization and DFT simulations, being the last the central focus of this section.

## 4.2. Metal promotional effects in $\text{In}_2\text{O}_3$



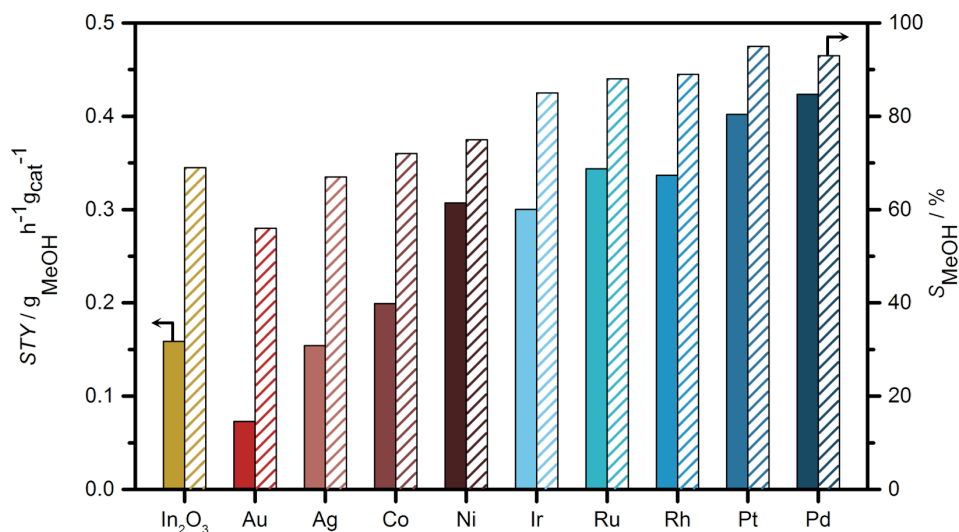
**Figure 4.13:** Methanol  $STY$  for undoped and metal-promoted  $\text{In}_2\text{O}_3$  systems reported in the literature prepared with different synthetic methods and amount of metals (wt %) leading to different catalytic architectures as depicted in the schemes. CP, DP, DI, and WI stand for coprecipitation, deposition precipitation, dry impregnation and wet impregnation, respectively.

### 4.2.1 Experimental insights in $M\text{-In}_2\text{O}_3$

The catalytic data obtained by our experimental colleagues for the FSP-made  $\text{In}_2\text{O}_3$  and  $M\text{-In}_2\text{O}_3$  systems is shown in **Figure 4.14**. Methanol  $STY$  results indicate that all doped systems improve the catalytic activity

Chapter 4. Metal-promoted metal oxides for green methanol production

exhibited by the undoped indium oxide but Ag- and Au-In<sub>2</sub>O<sub>3</sub>. In reference to the selectivity, we can classify the catalysts in three families: (i) Pd, Pt, Rh, Ru, and Ir markedly increase the methanol selectivity with values between 85 and 95 %, compared to the 68% displayed by undoped In<sub>2</sub>O<sub>3</sub>; (ii) Co and Ni render a moderate improvement (72 and 75%, respectively); and (iii) Au and Ag exhibit 56 and 67%  $S_{MeOH}$ , which are lower/similar values to those obtained for the undoped catalyst.



**Figure 4.14:** Methanol  $STY$  (colored bars) and  $S_{MeOH}$  (striped bars) towards CO<sub>2</sub> hydrogenation over undoped In<sub>2</sub>O<sub>3</sub> and  $M$ -In<sub>2</sub>O<sub>3</sub> catalysts. Reaction conditions:  $T = 553$  K,  $P = 5$  MPa,  $GHSV = 24000$  cm<sup>3</sup> h<sup>-1</sup> g<sub>cat</sub><sup>-1</sup> and  $H_2/CO_2 = 4$ .

With this catalytic results at hand, a battery of experimental characterization techniques were conducted over fresh, activated (2h under reaction conditions), and used catalysts (24h). Similar techniques to the ones presented for ZnZrO<sub>x</sub> systems were employed. However, additional ones such as temperature-programmed reduction with hydrogen (H<sub>2</sub>-TPR) and XPS O 1s spectra were used to provide additional insights in the oxygen

---

#### 4.2. *Metal promotional effects in $\text{In}_2\text{O}_3$*

vacancy formation over  $\text{In}_2\text{O}_3$  surface. The main insights provided by the experimental characterizations and the implications in the models and properties assessed by DFT are summarized in **Table 4.2**. The associated spectra and further detailed information for the FSP-made undoped and metal-promoted  $\text{In}_2\text{O}_3$  systems can be found in [15].

The detailed experimental characterization indicated that the metals promoters present different speciation which has a strong impact in the catalytic activity. Crystalline  $\text{In}_2\text{O}_3(111)$  faces are preserved in all catalytic systems with the promoters exhibiting different degree of dispersion and clustering. Particularly, the dopants are found to be deposited or incorporated into  $\text{In}_2\text{O}_3$  lattice, or to segregate into metal NPs of different sizes. Thus, different models were employed in the DFT simulations to assess the factors dictating the different speciation of the promoters at the atomic level of detail. Then, we used the most relevant models based in the experimental characterization and DFT results to explore the formation of oxygen vacancies and identify the catalytic sites for the different systems. Overall, we explored the synergy between experiments and simulations to shed light to the promotional effects exhibited by the FSP-made  $M\text{-In}_2\text{O}_3$  catalysts.

Chapter 4. Metal-promoted metal oxides for green methanol production

**Table 4.2:** Experimental insights provided by in-depth experimental characterization and their implications in the design of rational DFT models.

Technique	Experimental insights	Modelling implications
XRD	Crystalline $\text{In}_2\text{O}_3$ and absence of big metal NPs.	Slab models of $\text{In}_2\text{O}_3(111)$ surfaces for all systems.
HRTEM	$\text{In}_2\text{O}_3(111)$ termination in all catalysts. Detection of Au and Ag NPs with (111) termination.	Slab models of $\text{In}_2\text{O}_3(111)$ surfaces for all systems. Consider reactivity of Au(111) and Ag(111) surfaces.
HAADF-STEM-EDX	Pd, Pt, Ir, Ru, and Rh: High-dispersed and low-nuclearity species. Co and Ni: Some degree of clustering. Au and Ag: Segregation into NPs.	Different models are needed to consider the distinct degrees of clustering exhibited by the metal promoters.
XANES	All promoters reduced to metallic species but Co and Rh exhibited oxidic character.	Assess the tendency of the metal promoters to be incorporated into $\text{In}_2\text{O}_3$ lattice or to be deposited on the surface.
EXAFS	High interaction of all promoters with $\text{In}_2\text{O}_3$ . Pd, Pt, Ir, Ru, Rh, Ag, and Au: M-In contributions. Au and Ag: M-M contributions (non-discardable for Pd and Rh). Rh and Co: M-O and M-O-In contributions.	Consider different models for different metal promoter speciation to study the catalytic activity of the different systems.
XPS	All promoters present at the surface and Co bulk incorporation.	Explore the ability of the metal promoters to occupy bulk and surface sites.
$\text{H}_2$ -TPR	Features associated with surface oxygen vacancies for all systems.	Asses the formation of oxygen vacancies and their influence in the speciation and catalytic properties.
XPS O 1s	The portion of oxygen defects is similar in all catalysts but a higher amount in Pd- $\text{In}_2\text{O}_3$ .	
In MNN Auger testing	Absence of over-reduction of $\text{In}_2\text{O}_3$ to metallic In.	Discard metallic In.
Catalytic testing under $\text{CO}_2$ :CO feeds	In general the catalytic activity of all M- $\text{In}_2\text{O}_3$ decrease in CO presence.	Discard the formation of MeOH through the CO path.

---

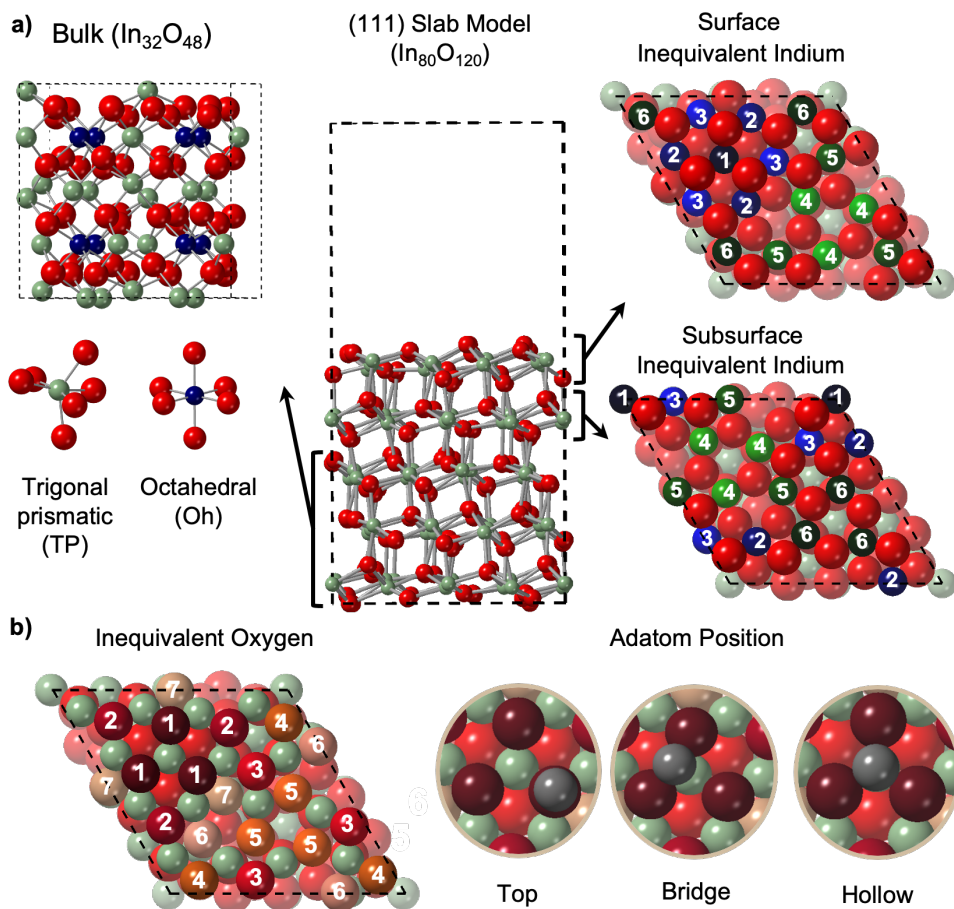
## 4.2. Metal promotional effects in $\text{In}_2\text{O}_3$

### 4.2.2 Methodology

DFT simulations were conducted with the PBE density functional.<sup>107</sup> Valence electrons were represented with plane-waves with a kinetic cut-off energy of 500 eV and core electrons were described with PAW pseudopotentials<sup>137,138</sup>. We used a  $\Gamma$ -centered mesh with a reciprocal grid size narrower than  $0.021 \text{ \AA}^{-1}$  to sample the Brillouin zone. The bulk of  $\text{In}_2\text{O}_3$  was represented with the cubic bixbyite structure optimized in previous studies with a kinetic cut-off energy of 800 eV.<sup>227</sup> Then, a slab model of the  $\text{In}_2\text{O}_3$  (111) surface was built, which is the most stable surface and it was identified by XRD and HRTEM in the systems under study.<sup>204,227,228</sup> We employed a  $p(1 \times 1)$  expansion with five O-In-O trilayers. The three bottommost layers were kept fixed mimicking bulk positions whereas the others were allowed to relax (**Figure 4.15**). I computed the potential energy ( $E$ ) of  $M\text{-In}_2\text{O}_3$  in order to assess the tendency of the metal promoters to be incorporated into bulk, subsurface, and surface sites of  $\text{In}_2\text{O}_3$  lattice (14 sites) or to be deposited on the surface (26 sites), as depicted in **Figure 4.15**. Moreover, energy profiles for oxygen vacancy formation,  $\text{CO}_2$  hydrogenation to methanol, and the competitive RWGS were computed on the most relevant models of  $M\text{-In}_2\text{O}_3$  according to experimental characterization and DFT simulations.  $M\text{-In}_2\text{O}_3$ ,  $\text{CO}_2$ ,  $\text{H}_2$ , and  $\text{H}_2\text{O}$  were used as thermodynamic sinks. DFT data associated with all structures shown in this section can be found online at <http://dx.doi.org/10.19061/iochem-bd-1-219>.



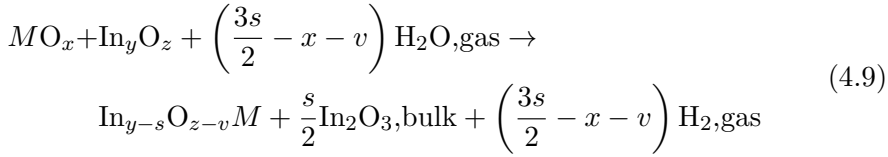
Chapter 4. Metal-promoted metal oxides for green methanol production



**Figure 4.15:** **a)** Side views of bulk and slab models of  $\text{In}_2\text{O}_3$ , with the corresponding top views of the surface and subsurface of (111) termination. The 14 non-equivalent indium are depicted with different shades of green and blue. **b)** Non-equivalent oxygen atoms of the  $\text{In}_2\text{O}_3$  (111) outermost layer represented with different shades of red and orange. The adsorption of metal promoters was explored at top, bridge, and three-fold sites with respect to these oxygen atoms (26 non-equivalent sites). Color code: In (blue and green), O (red and orange), and  $M$  (dark gray).

#### 4.2. Metal promotional effects in $\text{In}_2\text{O}_3$

$E$  was obtained from **Equations 4.9-4.10**. I employed the bulk  $\text{In}_2\text{O}_3$  ( $E_{\text{In}_2\text{O}_3,\text{bulk}}^{\text{DFT}}$ ),  $\text{H}_2$  ( $E_{\text{H}_2,\text{gas}}^{\text{DFT}}$ ),  $\text{H}_2\text{O}$  ( $E_{\text{H}_2\text{O},\text{gas}}^{\text{DFT}}$ ), and the associated oxide of the metal promoters ( $E_{\text{MO}_x}$ ) as energy references. In the case of  $\text{Au-In}_2\text{O}_3$ , I used the metal bulk as the source of Au. The parameter  $s$  indicates the number of In atoms replaced by the metal promoter and  $v$  is the number of oxygen vacancies.  $E_{\text{In}_y\text{O}_z}^{\text{DFT}}$  represents  $E_{\text{In}_{32}\text{O}_{48}}^{\text{DFT}}$  (energy of  $\text{In}_2\text{O}_3$  bulk) when considering the incorporation of metal promoters into bulk sites while it stands for  $E_{\text{In}_{80}\text{O}_{120}}^{\text{DFT}}$  (energy of  $\text{In}_2\text{O}_3$  (111) model) when exploring the incorporation into surface and subsurface sites or the deposition of metal promoters on  $\text{In}_2\text{O}_3$  surface.



$$E = E_{\text{In}_{y-s}\text{O}_{z-v}\text{M}}^{\text{DFT}} + \frac{s}{2} E_{\text{In}_2\text{O}_3,\text{bulk}}^{\text{DFT}} + \left(\frac{3s}{2} - x - v\right) E_{\text{H}_2,\text{gas}}^{\text{DFT}}$$

$$- E_{\text{MO}_x} - E_{\text{In}_y\text{O}_z}^{\text{DFT}} - \left(\frac{3s}{2} - x - v\right) E_{\text{H}_2\text{O},\text{gas}}^{\text{DFT}} \quad (4.10)$$

All the energies in **Equation 4.9-4.10** were obtained with DFT but  $E_{\text{MO}_x}$ . This and  $E_{\text{O}_2,\text{gas}}$  were derived from **Equations 4.11-4.12** employing the tabulated standard formation enthalpies of the metal oxides ( $\Delta E_{\text{f},\text{MO}_x}$ ) and water ( $\Delta E_{\text{f},\text{H}_2\text{O}}$ ),<sup>142</sup> and the computed energies for the bulk metal ( $E_{\text{M},\text{bulk}}^{\text{DFT}}$ ),  $E_{\text{H}_2,\text{gas}}^{\text{DFT}}$  and  $E_{\text{H}_2\text{O},\text{gas}}^{\text{DFT}}$ .

$$E_{\text{MO}_x} = E_{\text{M},\text{bulk}}^{\text{DFT}} + \frac{x}{2} E_{\text{O}_2,\text{gas}} + \Delta E_{\text{f},\text{MO}_x} \quad (4.11)$$

$$E_{\text{O}_2,\text{gas}} = 2 \left( E_{\text{H}_2\text{O},\text{gas}}^{\text{DFT}} - E_{\text{H}_2,\text{gas}}^{\text{DFT}} - \Delta E_{\text{f},\text{H}_2\text{O}} \right) \quad (4.12)$$

Segregation energies ( $E_{\text{seg}}$ ) were calculated with **Equation 4.13** to analyse the tendency of the incorporated metal promoters atoms to move from bulk sites to subsurface and surface positions.

## Chapter 4. Metal-promoted metal oxides for green methanol production

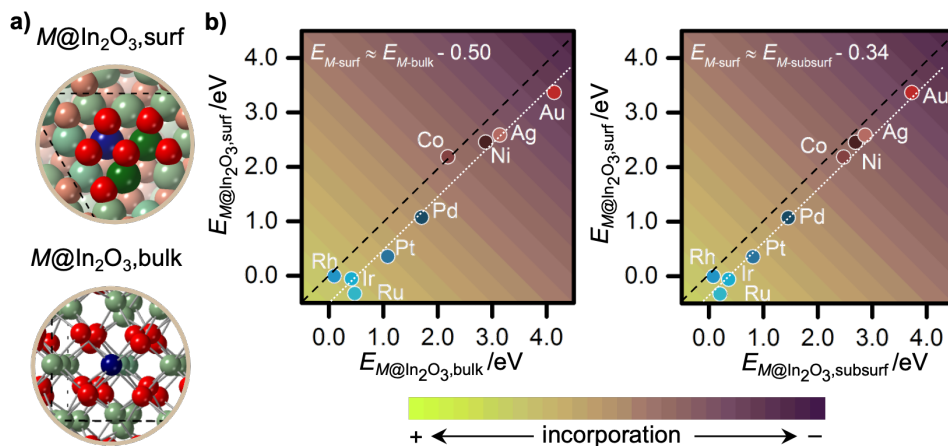
---

$$E_{\text{seg}} = E_{M@{\text{surface/subsurface}}} - E_{M@{\text{bulk}}} \quad (4.13)$$

### 4.2.3 Incorporation and deposition of metals promoters on $\text{In}_2\text{O}_3$

Distinct speciations were observed along the nine metal promoters in the experimental characterization (**Table 4.2**). Therefore, we carried out DFT simulations to evaluate the tendency of each metal promoter to be incorporated into  $\text{In}_2\text{O}_3$  lattice sites or to be deposited on the surface. First, we computed the energy required for each  $M$  to substitute an In atom in each of the non-equivalent bulk, subsurface, and surface sites of  $\text{In}_2\text{O}_3$  **Figure 4.15**. The energies associated with the most favourable incorporation positions are depicted in **Figure 4.16** while other values can be found in **Appendix C, Figure 6.4**. In general, the tendency of metal promoters to be incorporated into indium oxide lattice is low, in particular for Au, Ag, and Ni. This is in line with the formation of Au and Ag nanoparticles showed in the EDX maps, as well as the formation of extended  $\text{InNi}_x$  patches observed in our previous work.<sup>14</sup> Surface sites are favoured over bulk and subsurface positions by approximately 0.50 and 0.34 eV, respectively. Moreover, segregation from bulk to surfaces sites is exothermic for all promoters but Co and Rh (**Appendix C, Figure 6.5**). This is in agreement with the bulk incorporation depicted for Co in XPS and the  $M$ -O and  $M$ -O-In signals observed in the EXAFS spectra of activated Co- and Rh- $\text{In}_2\text{O}_3$  catalysts. Notably, the preferred incorporation bulk/subsurface/surface sites vary among different metal promoters. Thus, we applied Principal Component Analysis (PCA) to the incorporation energies in order to ease the rationalization of the space of structural affinity (**Appendix C, Figure 6.11**). We observed that the most favoured substitution site of each metal promoter is dictated by the coordination environment of each position.

## 4.2. Metal promotional effects in $\text{In}_2\text{O}_3$

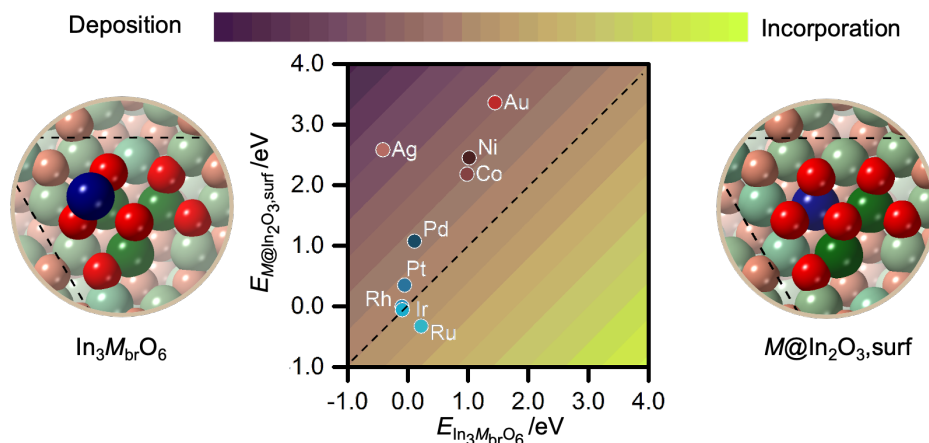


**Figure 4.16:** a) Models with metal promoters incorporated into surface ( $M@In_2O_3,surf$ ) and bulk ( $M@In_2O_3,bulk$ ) sites. Color code: O(red), In(green), and M (blue). a) Potential energies relationship between dopant incorporated into its most favoured surface positions *vs* bulk (left) and subsurface (right) sites. Dashed (black) and dotted (white) lines indicate the relative stability between speciations and the constant offset energy between surface and bulk/subsurface sites, respectively.

Then, we compared the most favourable incorporation energy with the energy required for each metal promoter to be deposited on the surface of  $\text{In}_2\text{O}_3$  in a bridge site between two oxygen atoms ( $\text{In}_3M_{br}O_6$ , **Figure 4.17**). Other deposition positions were explored (**Appendix C**, **Figure 6.4**), but the most stable one is the same for all the metal-dopants. **Figure 4.17** shows that deposition at this site is favoured over incorporation for all metal promoters, except Ru. This is in line with the experimental characterization which indicates that the best metal promoters are highly dispersed on the surface of  $\text{In}_2\text{O}_3$ , in particular Pd and Pt. However, XANES and EXAFS spectra show that all metal promoters exhibit a metallic character in the activated  $M\text{-In}_2\text{O}_3$  catalysts which is incompatible with the  $\text{In}_3M_{br}O_6$  moiety (except Co). Therefore, we assessed the formation of oxygen vacancies

## Chapter 4. Metal-promoted metal oxides for green methanol production

in order to explore alternative speciations and identify the active site for CO<sub>2</sub> hydrogenation to methanol.



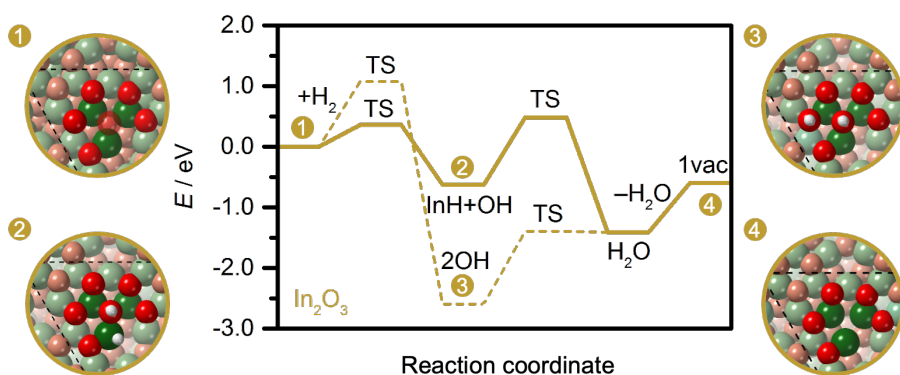
**Figure 4.17:** Potential energies relationship between dopant incorporated into its most favoured surface positions *vs* deposition on bridge sites. Dashed black line indicates the relative stability between speciation. Models with metal promoter incorporated ( $M@In_2O_3,surf$ ) and deposited ( $In_3M_{br}O_6$ ) on  $In_2O_3$  surface. Color code: O(red), In(green), and M (blue).

### 4.2.4 Metal promoters speciation and active site formation

Oxygen vacancies are formed under reaction conditions on  $In_2O_3(111)$  surface, which are key to obtain the  $In_3O_5$  active ensemble towards CO<sub>2</sub> hydrogenation to methanol, as it was shown in a previous work combining experimental testing and characterization with DFT simulations.<sup>204</sup> Therefore, H<sub>2</sub>-TPR experiments were performed on FSP-made  $In_2O_3$  and  $M-In_2O_3$  catalysts. All systems presented similar features revealing the presence of oxygen vacancies in the metal-promoted catalysts. For this reason, we computed the reaction energy profiles associated with the formation of oxygen vacancies on  $In_2O_3$  and  $M-In_2O_3$  systems (**Figures 4.18-4.19**). In

#### 4.2. Metal promotional effects in $\text{In}_2\text{O}_3$

reference to undoped  $\text{In}_2\text{O}_3$ , the mechanism starts with the activation of  $\text{H}_2$  (**Figure 4.18**). We computed the heterolytic and homolytic paths that lead to hydride ( $\text{InH}$ ) and hydroxyl group ( $^*\text{OH}$ ) or two hydroxyl groups ( $2^*\text{OH}$ ), respectively. Then, both paths converge in the formation and desorption of water yielding the  $\text{In}_3\text{O}_5$  active ensemble. The heterolytic mechanism is favoured. However, the high stability of the  $2^*\text{OH}$  is in line with the high degree of surface hydroxylation exhibited by  $\text{In}_2\text{O}_3$  in previous studies<sup>229</sup> and in the XPS O 1s data.

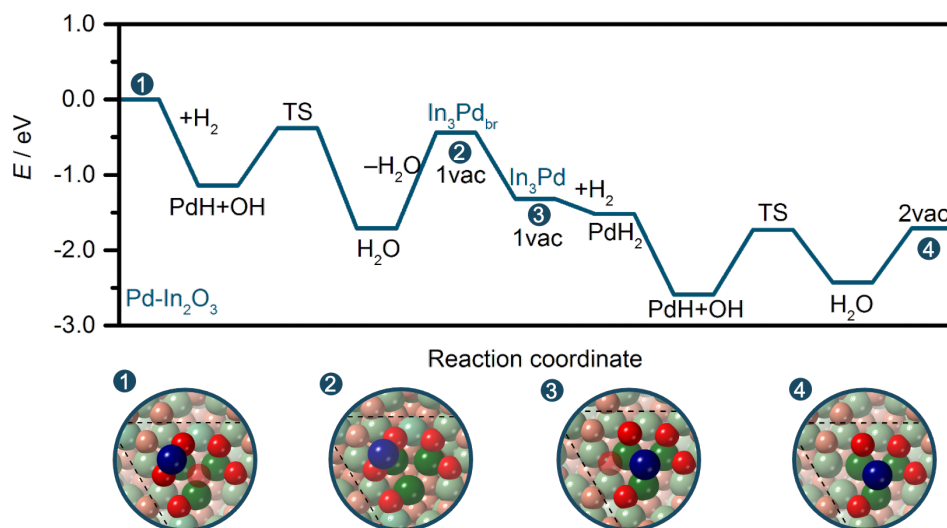


**Figure 4.18:** Reaction energy profile and snapshots of relevant intermediates for oxygen vacancy formation in undoped  $\text{In}_2\text{O}_3$ . Heterolytic and homolytic paths are depicted with solid and dotted yellow lines, respectively. Color code: In (green), O (red), H (white), and oxygen where vacancy is considered (shaded red).

Moving on to the  $M\text{-In}_2\text{O}_3$  systems we considered the  $\text{In}_3M_{\text{br}}\text{O}_x$  moiety as initial point since in general it was identified as the most stable speciation. **Figure 4.19** shows the energy profile for vacancy formation of  $\text{Pd-In}_2\text{O}_3$  while profiles associated with the other systems can be found in **Appendix C, Figures 6.6-6.7**. In analogy to undoped  $\text{In}_2\text{O}_3$  the mechanism starts with the heterolytic dissociation of  $\text{H}_2$  forming the  $M\text{H}+\text{OH}$  pair with concomitant  $\text{H}_2\text{O}$  formation and desorption. At this point, the metal promoter diffuses into the oxygen vacancy site yielding the  $\text{In}_3M\text{O}_x$  moiety,

*Chapter 4. Metal-promoted metal oxides for green methanol production*

which is specially favoured for the best promoters (Pd and Pt). This ensemble is key because the dopant adopts the metallic character observed in the experimental characterization for almost all dopants, specially Pd, Pt, Rh, Rh, and Ru. Since the metal promoter is deposited in the oxygen vacancy site, an additional vacancy is required to activate the  $\text{CO}_2$  to be hydrogenated to methanol. Interestingly, the process starts with a barrierless  $\text{H}_2$  homolytic dissociation for all metal-promoters, but Ag and Au. Then, an analog mechanism to the first vacancy is followed to obtain the  $\text{In}_3\text{MO}_4$  ensemble, which was identified as the active site for  $\text{CO}_2$  hydrogenation on Pd– $\text{In}_2\text{O}_3$  in a previous work.<sup>191</sup>.

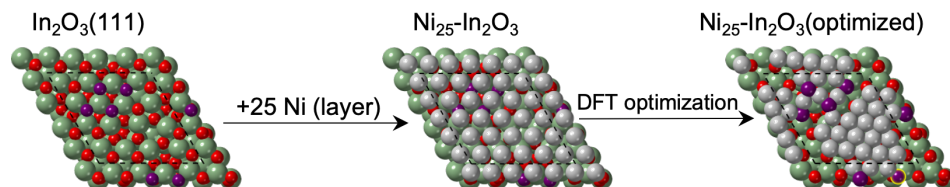


**Figure 4.19:** Reaction energy profile and snapshots of relevant intermediates associated with formation of two oxygen vacancies in Pd- $\text{In}_2\text{O}_3$ . Color code: In (green), O (red), H (white), and oxygen where vacancy is considered (shaded red).

Overall, experimental characterization together with DFT simulations point to the deposition of the dopants on the surface of  $\text{In}_2\text{O}_3$  is general favoured over the incorporation into lattice sites. Indeed, the most prominent

## 4.2. Metal promotional effects in $\text{In}_2\text{O}_3$

speciation for the best promoters (Pd, Pt, Rh, Ir, and Ru) is the formation of the  $\text{In}_3\text{MO}_4$  ensemble. Additionally, this moiety could not be totally disregarded for Co-, Ni-, Ag-, and Au- $\text{In}_2\text{O}_3$  systems. Co is mostly incorporated into bulk sites or forming  $\text{CoO}_x$  nanoparticles. Then, Au and Ag agglomerate into metal nanoparticles. Finally, Ni- $\text{In}_2\text{O}_3$  is a particular system since in our previous work we found that Ni is able to strip surface oxygen atoms of  $\text{In}_2\text{O}_3$  leading to the formation of extended layered  $\text{InNi}_3$  patches (**Figure 4.20**).<sup>14</sup>



**Figure 4.20:** Models representing the reconstruction of  $\text{In}_2\text{O}_3(111)$  surface when a layer of Ni is adsorbed on top of the oxide surface. The high oxidic character of Ni leads to the stripping of surface oxygen atoms of  $\text{In}_2\text{O}_3$ . Adapted from [14].

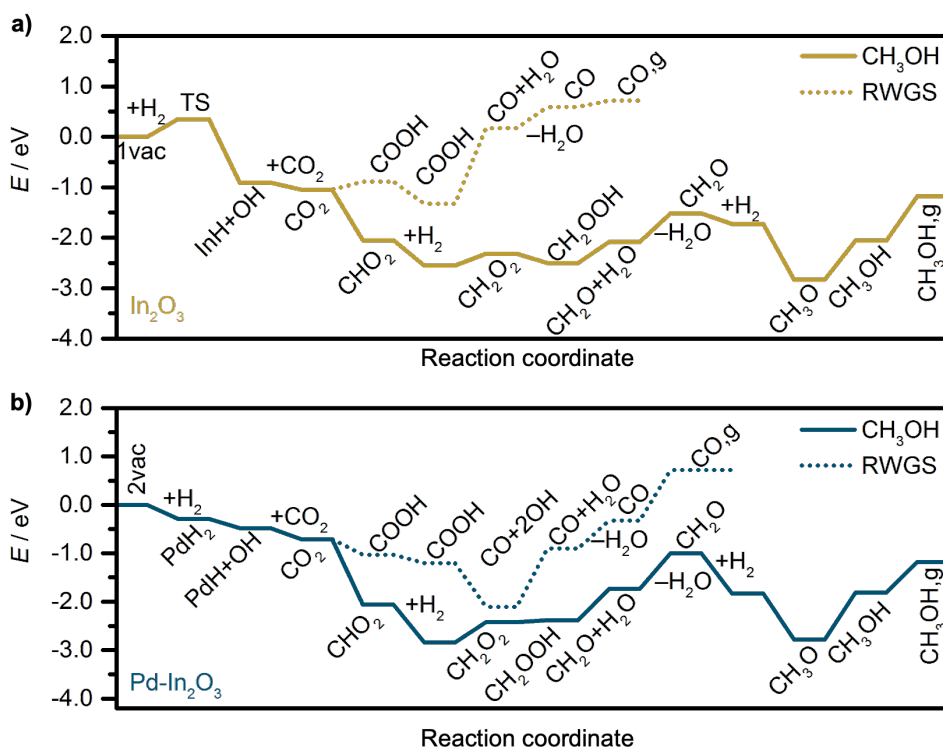
### 4.2.5 Mechanistic insights in $M\text{-In}_2\text{O}_3$ systems

We computed the energy profiles for  $\text{CO}_2$  hydrogenation to methanol and the RWGS side reaction on undoped  $\text{In}_2\text{O}_3$  and all  $M\text{-In}_2\text{O}_3$  systems. For the metal-promoted systems, we employed the models representing a single atom deposited on the oxygen vacancy site ( $\text{In}_3\text{MO}_4$ ). In the case of Ag- and Au- $\text{In}_2\text{O}_3$ , we also computed the energy profiles on  $M(111)$  surfaces as these are the models that best represent the metallic nanoparticles. The formate pathway (**Figure 4.1**), explained in detail for  $\text{ZnZrO}_x$  systems, was followed for  $\text{In}_2\text{O}_3$  and all  $M\text{-In}_2\text{O}_3$  systems (**Figure 4.21**) since it was identified as the most favoured route for methanol formation in previous studies on undoped and metal-doped  $\text{In}_2\text{O}_3$ .<sup>204–206</sup> Moreover, the formation of  $\text{CH}_3\text{OH}$  through the CO path was discarded because the experimental results show that the catalytic activity of all systems decrease in presence of



Chapter 4. Metal-promoted metal oxides for green methanol production

CO. Furthermore, previous studies indicated that at least 3 exposed metal are needed to make this mechanism feasible.<sup>191</sup> Only the reaction energy profile for Pd–In<sub>2</sub>O<sub>3</sub> is shown while the other ones associated with the other *M*-In<sub>2</sub>O<sub>3</sub> systems can be found in **Appendix C, Figures 6.8-6.9**.

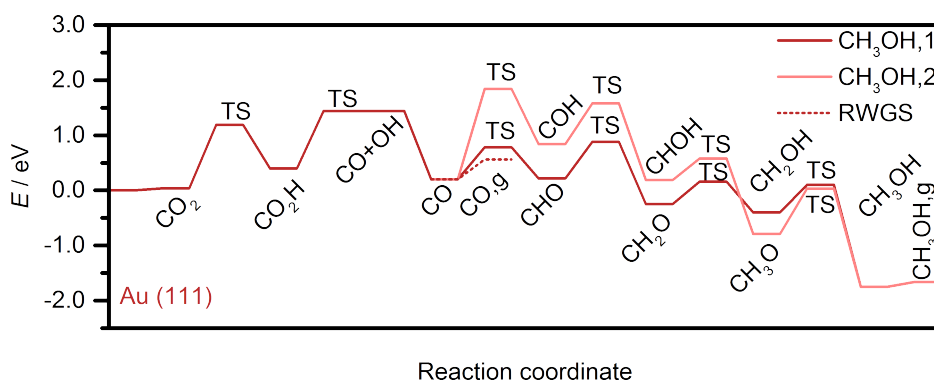


**Figure 4.21:** Reaction energy profiles of CO<sub>2</sub> hydrogenation to methanol and the competitive RWGS on a) undoped and b) Pd-In<sub>2</sub>O<sub>3</sub> systems.

There are not significant differences between the energy profiles obtained for In<sub>2</sub>O<sub>3</sub> and *M*-In<sub>2</sub>O<sub>3</sub> systems. Thus, the promotional effect exhibited by almost all metal dopants cannot be associated to the reaction mechanism. In addition, catalytic tests performed at variable temperature reveals that

#### 4.2. Metal promotional effects in $\text{In}_2\text{O}_3$

there is not any correlation between the determined activation energies (both for methanol and RWGS) and the methanol productivity measured in terms of  $STY$ .<sup>15</sup> This indicates that the reaction rate is controlled by entropic processes such as the availability of activated hydrogen or oxygen vacancies at the active site. Interestingly, we found that the computed activation energy for  $\text{H}_2$  splitting on  $\text{In}_2\text{O}_3$  is 0.35 eV, while the best metal promoters (Pd, Pt, Rh, Ir, and Ru) are able to homolytically split hydrogen with no-barrier on  $\text{In}_3\text{MO}_4$  moiety. This explain the higher methanol productivity exhibited by these systems. Hydrogen splitting is also promoted on  $\text{In}_3\text{Co}(\text{Ni})\text{O}_4$  ensembles, but this is not their most dominant speciation. Finally, the reaction mechanism followed on Au(111) and Ag(111) models was different (**Figure 4.21** and **Appendix C, Figures 6.10**). In this case,  $\text{CO}_2$  is adsorbed, protonated and dehydrogenated yielding CO. Then, CO can be desorbed or lead to methanol after different hydrogen transfers following two different paths. Both Au and Ag surfaces exhibit low ability to activate  $\text{CO}_2$  and CO desorption is favoured over being further hydrogenated to methanol. Thereby, this reveals that the agglomeration into Au and Ag nanoparticles on  $\text{In}_2\text{O}_3$  surface is detrimental for the catalytic activity towards  $\text{CO}_2$  hydrogenation to methanol, which is in line with the catalytic results.

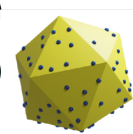
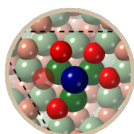


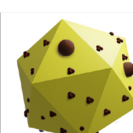
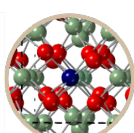



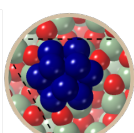




**Figure 4.22:** Reaction energy profile of  $\text{CO}_2$  hydrogenation to methanol and the competitive RWGS on Au(111).

Chapter 4. Metal-promoted metal oxides for green methanol production

4.2.6 Promoters' speciation and catalytic activity

The integration of systematic experimental characterization and DFT simulations on  $\text{In}_2\text{O}_3$  and nine  $M\text{-In}_2\text{O}_3$  allowed us to reveal that the catalytic activity of these systems is strongly ruled by the metal promoters' speciation (**Figure 4.23**). Rh, Ir, Ru, and in particular Pd and Pt are highly dispersed on  $\text{In}_2\text{O}_3$  surface forming  $\text{In}_3\text{MO}_4$  ensemble and promoting the hydrogen activation *via* barrierless homolytic splitting and oxygen vacancy formation. Then, Ni and specially Co exhibited a smaller degree of promotion due to the tendency of alloying with In and the incorporation to  $\text{In}_2\text{O}_3$  bulk sites, respectively, which clearly reduce the availability of  $\text{In}_3\text{MO}_4$  moieties. Finally, the low activity and selectivity of Au- and Ag- $\text{In}_2\text{O}_3$  is attributed to the formation of metal nanoparticles.

Promoter	Speciation	Impact on performance	Features
Pd Pt Rh Ru Ir	 	$\Delta\text{STY}$ $S_{\text{MeOH}}$   50–63%    86–96%	Atomically-dispersed High $S_{\text{MeOH}}$
Ni Co	 	  20–48%    73–76%	Clustered or incorporation $S_{\text{MeOH}}$ less boosted
Ag Au	 	  3–54%    56–67%	Sintering into NPs CO formation favoured

**Figure 4.23:** Summary of metal promoters' speciation and the impact in the catalytic performance of  $\text{In}_2\text{O}_3$  towards  $\text{CO}_2$  hydrogenation to methanol. Adapted from [15].

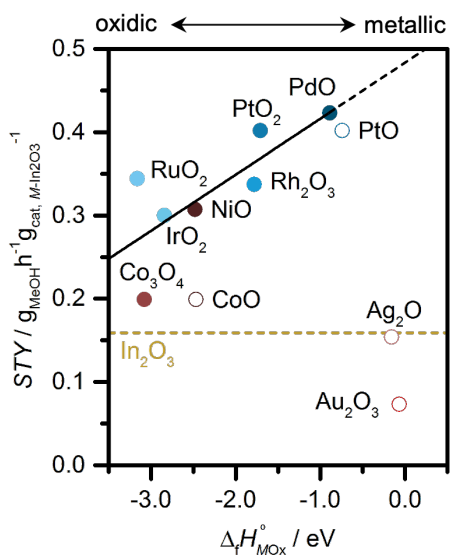
---

## 4.2. Metal promotional effects in $\text{In}_2\text{O}_3$

In order to trace back the dependence between the dopants' speciation and the degree of promotion, we look further into a relation between the catalytic activity of the  $M\text{-In}_2\text{O}_3$  systems and the inherent properties of the dopands. Therefore, we explored the relationship between the methanol *STY* over the standard formation enthalpy ( $\Delta_f H^\circ$ ) of the metal oxide associated with each metal promoter (**Figure 4.24**). We can observe that the best metal promoters (Pd and Pt) are those with higher metallic character (less exothermic  $\Delta_f H^\circ$ ), since they facilitate the activation of hydrogen through homolytic splitting. However, if the promoters are too metallic, such as Ag and Au, they are not able to form oxide-based precursors. Thus, they agglomerate into metal nanoparticles when prepared by flame spray pyrolysis (FSP). Nevertheless, if these metals are highly dispersed on the surface of  $\text{In}_2\text{O}_3$ , they exhibit high catalytic activity.<sup>195,197</sup> Finally, metal promoters with high oxidic character (more exothermic  $\Delta_f H^\circ$ ) tend to be incorporated to  $\text{In}_2\text{O}_3$  lattice (Co) or to strip surface oxygen atoms of the surface (Ni). Thereby, the best metal promoters are those with balanced metallic and oxidic character that are able to be atomically dispersed on the  $\text{In}_2\text{O}_3$  lattice while preserving enough metallicity to promote the hydrogen splitting.

Lastly, it is worth to highlight the particular architecture of the  $\text{In}_3\text{MO}_4$  ensemble. It contains a metallic component ( $M\text{In}_3$  nanoalloy) that promotes the hydrogen activation, which is surrounded by an oxidic part (basic oxygen atoms from the  $\text{In}_2\text{O}_3$  matrix) where  $\text{CO}_2$  is activated and hydrogenated. Therefore, the active species are confined in a small region of the space ensuring a bifunctional mechanism with the desired tight cooperation of the metallic and oxidic components.

Chapter 4. Metal-promoted metal oxides for green methanol production



**Figure 4.24:** Relationship between methanol  $STY$   $M$ - $\text{In}_2\text{O}_3$  catalysts *vs* the experimental standard enthalpy of formation of the most stable metal oxide  $MO_x$  for each metal promoter normalized by the number of metal atoms in metal oxide formula unit ( $\Delta_f H^o_{MO_x}$ ).<sup>142</sup> The black regression line considers all metal oxides marked by filled circles. The  $STY$  associated with undoped  $\text{In}_2\text{O}_3$  is depicted for comparison. Adapted from [15].

4.3. *Metal-metal oxide interactions in Pd-In<sub>2</sub>O<sub>3</sub>/ZrO<sub>2</sub>*

---

## 4.3 Metal-metal oxide interactions in Pd-In<sub>2</sub>O<sub>3</sub>/ZrO<sub>2</sub>

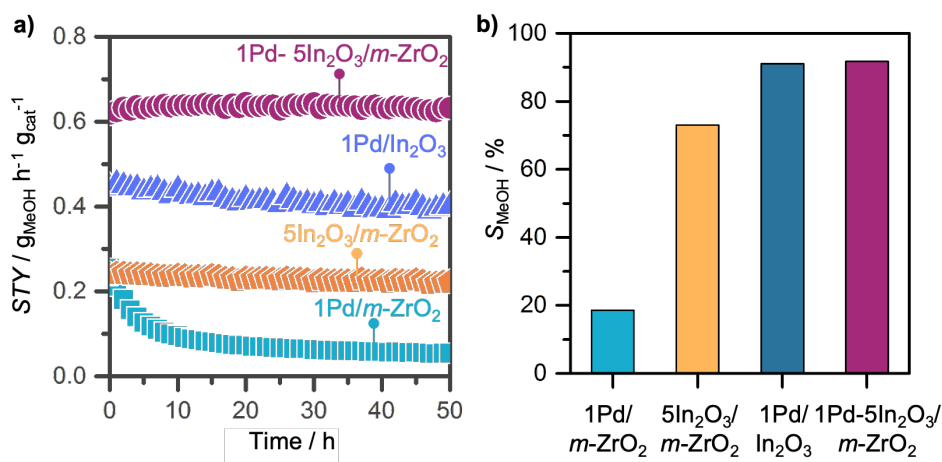
We have rationalized how different metals with a certain architecture are able to improve the methanol productivity of In<sub>2</sub>O<sub>3</sub> by promoting the H<sub>2</sub> splitting and oxygen vacancy formation.<sup>15</sup> Alternatively, Prof. Javier Pérez-Ramírez and coworkers found that oxygen vacancy formation is fostered in In<sub>2</sub>O<sub>3</sub> by its deposition on *m*-ZrO<sub>2</sub> which also renders an enhancement of the catalytic activity.<sup>208</sup> Then, they used FSP to synthesise a ternary Pd-In<sub>2</sub>O<sub>3</sub>/ZrO<sub>2</sub> catalyst to combine these two strategies.<sup>210</sup> This ternary catalyst exhibits even higher methanol productivity than the binary counterparts, which make it a prospect for practical applications. However, the particular architectures and properties of the catalysts achieved by FSP cannot be obtained by impregnation methods, which are commonly used at the industrial scale. Therefore, further development and understanding of the catalysts prepared by more practical and scalable methods are needed.

In this context, our experimental colleagues from Prof. Javier Pérez-Ramírez group synthesised the Pd-In<sub>2</sub>O<sub>3</sub>/ZrO<sub>2</sub> catalyst (1 and 5 wt% for Pd and In<sub>2</sub>O<sub>3</sub>, respectively) by impregnation and its architecture and catalytic activity was compared to the binary counterparts prepared with the same method (Pd/In<sub>2</sub>O<sub>3</sub>, In<sub>2</sub>O<sub>3</sub>/ZrO<sub>2</sub> and Pd/ZrO<sub>2</sub>). Special attention was given to the interaction between the components of the ternary system under reaction conditions because significant reconstructions with high impact in the catalytic activity were previously reported for the binary catalysts.<sup>191,230–232</sup> Thus, in-depth experimental characterization was carried out for fresh, used, and under reaction conditions Pd-In<sub>2</sub>O<sub>3</sub>/ZrO<sub>2</sub> system. I employed DFT simulations to provide insights about the driving forces of potential reconstruction phenomena and the architecture of the active sites at the atomic-scale, which are the central point of this section.

Chapter 4. Metal-promoted metal oxides for green methanol production

4.3.1 Experimental insights in Pd-In<sub>2</sub>O<sub>3</sub>/ZrO<sub>2</sub>

Catalytic tests depict that the ternary Pd-In<sub>2</sub>O<sub>3</sub>/ZrO<sub>2</sub> catalysts is more active, in terms of methanol *STY*, and stable than the binary systems (Figure 4.25a). Moreover, the ternary system and Pd/In<sub>2</sub>O<sub>3</sub> exhibits high methanol selectivity (*ca.* 90 %), while 70 and 20% *S*<sub>MeOH</sub> was obtained for In<sub>2</sub>O<sub>3</sub>/ZrO<sub>2</sub> and Pd/ZrO<sub>2</sub>, respectively (Figure 4.25b).



**Figure 4.25:** a) Methanol *STY* and b) *S*<sub>MeOH</sub> of CO<sub>2</sub> hydrogenation over the ternary catalyst Pd-In<sub>2</sub>O<sub>3</sub>/ZrO<sub>2</sub> and the binary counterparts used as references. Reaction conditions: *T* = 553 K, *P* = 5 MPa, *GHSV* = 24000 cm<sup>3</sup> h<sup>-1</sup> g<sub>cat</sub><sup>-1</sup> and H<sub>2</sub>/CO<sub>2</sub> = 4. Adapted from [16].

The characterization of the fresh and used Pd-containing binary catalysts by STEM-EDX and XRD reveal that Pd sinters into large nanoparticles upon reaction. Additionally, *S*<sub>BET</sub> analysis indicate a significant decrease of the specific surface area of these catalysts under reaction conditions, which explains their low *STY* compared with Pd-In<sub>2</sub>O<sub>3</sub>/ZrO<sub>2</sub>. In contrast, the specific surface area of In<sub>2</sub>O<sub>3</sub>/ZrO<sub>2</sub> remains virtually unchanged with dispersed In<sub>2</sub>O<sub>3</sub> upon reaction. Thus, we attribute its low methanol productivity to the poor ability of this catalyst to activate hydrogen.

---

#### 4.3. Metal-metal oxide interactions in Pd-In<sub>2</sub>O<sub>3</sub>/ZrO<sub>2</sub>

Moving on to the ternary catalyst, in-depth experimental characterization was carried out employing similar techniques that the ones explained in the previous sections for ZnZrO<sub>x</sub> and M-In<sub>2</sub>O<sub>3</sub> catalysts. The main experimental insights and the implications in the models assessed by DFT are summarized in **Table 4.3**. The associated spectra and further detailed information for all the systems under study can be found in [16]. It is worth to highlight that in this case *operando* XANES, EXAFS, and HR-XRD analysis were conducted. Thus, the measurements were performed on the fresh and used catalyst, as well as, increasing the temperature with concomitant exposure of the system to reaction conditions. Moreover, HR-XRD spectra were recorded at different times (time-resolved). In this way, these techniques provided insights of the evolution of the architecture of the catalyst upon reaction. Furthermore, the used catalyst was analysed with high-angle annular dark-field scanning transmission electron microscopy coupled to electron energy-loss spectroscopy (HAADF-STEM-EELS) because domains with low degree of crystallinity were detected on the surface of the ternary system by STEM-EDX.



Chapter 4. Metal-promoted metal oxides for green methanol production

**Table 4.3:** Experimental insights provided by in-depth experimental characterization and their implications in the design of rational DFT models.

Technique	Experimental insights for Pd-In <sub>2</sub> O <sub>3</sub> /m-ZrO <sub>2</sub>	Modelling implications
HAADF-STEM-EDX	Fresh: Pd NPs and In <sub>2</sub> O <sub>3</sub> dispersed on ZrO <sub>2</sub> . Used: In <sub>2</sub> O <sub>3</sub> clustering with Pd forming dispersed particles on ZrO <sub>2</sub> surface. The relative amount of In and Pd in different areas of the particles is heterogeneous. The In <sub>2</sub> O <sub>3</sub> -Pd particles exhibit almost amorphous morphology with more crystalline core.	Two-component models to explore the interaction of In <sub>2</sub> O <sub>3</sub> with Pd and ZrO <sub>2</sub> .
HRTEM	Fresh: Pd and In with oxidic character. Under reaction conditions and used: Pd fully reduced and interacting with indium (InPd <sub>x</sub> ). In <sub>2</sub> O <sub>3</sub> partially reduced to InO <sub>x</sub> and InPd <sub>x</sub> species.	Consider different degrees of reduction in In <sub>2</sub> O <sub>3</sub> models to assess the interaction with Pd and ZrO <sub>2</sub> . Explore the interaction between partially reduced In <sub>2</sub> O <sub>3</sub> patches with different dimensions on top of Pd and InPd <sub>x</sub> models.
<i>Operando</i> XANES	Fresh: Pd-O and In-O contributions. Under reaction conditions and used: Shifted Pd-Pd signals indicating alloy formation. In-O and some In-M contributions.	Assess the adsorption of probe molecules (CO <sub>2</sub> , H <sub>2</sub> , and CO) on different single- and dual-component models to rationalize the catalytic activity. Different models were critically selected following specific guidelines (further explained in the methodology section) due to the high complexity and dynamic character of the Pd-In <sub>2</sub> O <sub>3</sub> /ZrO <sub>2</sub> .
<i>Operando</i> EXAFS	Formation of InPd <sub>2</sub> under reaction conditions and before the analysis of the products is performed (after 30 minutes).	
<i>Operando</i> and time resolved HR-XRD	Indium-palladium particles with a core-shell-like structure. InO <sub>x</sub> patches partially covering InPd <sub>2</sub> /Pd NPs.	
HAADF-STEM-EELS	CO uptake smaller compared to catalysts with Pd NPs. Pd alloying with In.	Compare CO adsorption between Pd and InPd <sub>x</sub> surfaces.
CO chemisorption	Pd alloying with In.	Compare H <sub>2</sub> adsorption between Pd and InPd <sub>x</sub> surfaces.
H <sub>2</sub> -TPR	Absence of PdH signals typical of Pd NPs. Pd alloying with In.	

### 4.3. Metal-metal oxide interactions in Pd-In<sub>2</sub>O<sub>3</sub>/ZrO<sub>2</sub>

---

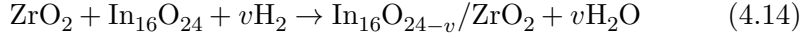
In-depth experimental characterization of Pd-In<sub>2</sub>O<sub>3</sub>/ZrO<sub>2</sub> system revealed that In<sub>2</sub>O<sub>3</sub> and Pd oxidized NPs are dispersed on ZrO<sub>2</sub> in the fresh catalyst and the architecture of the system evolves upon reaction. In particular, In<sub>2</sub>O<sub>3</sub> migrates to some extent from the support to the Pd NPs forming particles with shell-like structure. These particles are composed by InPd<sub>*x*</sub> nanostructures encapsulated by partially reduced In<sub>2</sub>O<sub>3</sub> patches (InO<sub>*x*</sub>). Thereby, we employed DFT simulations to elucidated the driving force of the In<sub>2</sub>O<sub>3</sub> migration upon reaction and to identify the activate sites towards CO<sub>2</sub> hydrogenation to methanol.

#### 4.3.2 Methodology

DFT simulations were carried out with the PBE density functional.<sup>107</sup> Core electrons were represented with PAW pseudopotentials,<sup>137,138</sup> while valence electrons were described with plane-waves with a kinetic cut-off energy of 500 eV. We employed a  $\Gamma$ -centered mesh with a reciprocal grid size narrower than 0.037 Å<sup>-1</sup> to sample the Brillouin zone. Slab models of the relevant terminations of *m*-ZrO<sub>2</sub>, In<sub>2</sub>O<sub>3</sub>, Pd, InPd<sub>2</sub>, and InPd were cleaved from the optimized bulk structures obtained with a kinetic cut-off energy of at least 700 eV (**Table 4.4**). Input and outputs of the simulations can be accessed at <http://dx.doi.org/10.19061/iochem-bd-1-275>.

We compared the interaction of ZrO<sub>2</sub>(-111) and Pd(111) with In<sub>2</sub>O<sub>3</sub>(111) surface with the aim of rationalizing the reconstruction of Pd-In<sub>2</sub>O<sub>3</sub>/ZrO<sub>2</sub> under reaction conditions. We employed *p*(2×2), *p*(5×5) slab models of ZrO<sub>2</sub> and Pd, respectively, and a layer of *p*(1×1) In<sub>2</sub>O<sub>3</sub> model at different degrees of reduction (In<sub>16</sub>O<sub>24-*v*</sub>). These particular expansions of each slab model were selected to ensure the commensurability between the two interacting systems. I used **Equations 4.14-4.15** to obtain the interaction energy between ZrO<sub>2</sub> and In<sub>2</sub>O<sub>3</sub> by indium atom ( $E_{\text{int,In}_2\text{O}_3-\text{ZrO}_2}$ ) and analogs equations were employed for  $E_{\text{int,In}_2\text{O}_3-\text{Pd}}$ . We used an In<sub>2</sub>O<sub>3</sub> layer ( $E_{\text{In}_{16}\text{O}_{24}}^{\text{DFT}}$ ), H<sub>2</sub> ( $E_{\text{H}_2,\text{gas}}^{\text{DFT}}$ ), H<sub>2</sub>O ( $E_{\text{H}_2\text{O,gas}}^{\text{DFT}}$ ), and *m*-ZrO<sub>2</sub>(-111) or Pd(111) surfaces ( $E_{\text{ZrO}_2}^{\text{DFT}}$  and  $E_{\text{Pd}}^{\text{DFT}}$ , respectively) as thermodynamic sinks. 16 is the number of indium atoms and *v* represents the number of oxygen vacancies in the In<sub>16</sub>O<sub>24</sub> layer.

*Chapter 4. Metal-promoted metal oxides for green methanol production*



$$E_{\text{int,In}_2\text{O}_3-\text{ZrO}_2} = \frac{E_{\text{In}_{16}\text{O}_{24-v}/\text{ZrO}_2}^{\text{DFT}} + vE_{\text{H}_2\text{O,gas}}^{\text{DFT}} - E_{\text{ZrO}_2}^{\text{DFT}} - E_{\text{In}_{16}\text{O}_{24}}^{\text{DFT}} - E_{\text{H}_2,\text{gas}}^{\text{DFT}}}{16} \quad (4.15)$$

The formation of  $\text{InPd}_x$  in the ternary catalyst was identified by HR-XRD. Thus, I computed the formation energy of  $\text{InPd}$  and  $\text{InPd}_2$  alloys ( $E_{\text{InPd}_x}$ ) with **Equations 4.16-4.17**.  $E_{\text{In,bulk}}^{\text{DFT}}$  and  $E_{\text{Pd,bulk}}^{\text{DFT}}$  stands for the computed energy of an In and Pd atom in its metallic bulk, respectively.



$$E_{\text{InPd}_x} = E_{\text{InPd}_x}^{\text{DFT}} - E_{\text{In,bulk}}^{\text{DFT}} - xE_{\text{Pd,bulk}}^{\text{DFT}} \quad (4.17)$$

**Table 4.4:** Termination, supercell and number of layers employed for the modelling of different surfaces relevant to rationalize the architecture and catalytic properties of  $\text{Pd-In}_2\text{O}_3/\text{ZrO}_2$  system.

System	Termination	Supercell	Layers (fixed + relaxed)
$m\text{-ZrO}_2$	(-111)	$p(2 \times 2)$	$2+2^a$
$\text{In}_2\text{O}_3$	(111)	$p(1 \times 1)$	$3+2^b$
Pd	(111)	$p(5 \times 5)^c$	$2+2$
$\text{InPd}_2$	(013)	$p(2 \times 1)$	$2+2$
$\text{InPd}$	(101)	$p(3 \times 4)$	$2+2$

<sup>a</sup>Each  $m\text{-ZrO}_2$  layer (O-O-O-Zr-O-Zr-Zr-O-Zr-O-O-O) is formed by 12 atomic layers (**Figure 4.4**). <sup>b</sup>Each  $\text{In}_2\text{O}_3$  layer (O-In-O) is formed by 3 atomic layers (**Figure 4.15**).

<sup>c</sup>A  $p(4 \times 4)$  slab model was employed to assess the adsorption of molecules on Pd surface.

### 4.3. Metal-metal oxide interactions in Pd-In<sub>2</sub>O<sub>3</sub>/ZrO<sub>2</sub>

---

#### Modelling of the catalytic systems

Due to the complex architecture of the binary and ternary catalytic systems under study and the wide number of potential configuration that could arise from the interaction between phases, we defined specific guidelines to build our experimentally-guided models: (i) for single phases we employed the most stable bulk and derived terminations or the ones identified in the experimental characterization; and (ii) different sizes (In<sub>4</sub>O<sub>5</sub>, In<sub>6</sub>O<sub>7</sub> and In<sub>8</sub>O<sub>10</sub>) and configurations of InO<sub>x</sub> clusters were deposited on Pd and InPd<sub>2</sub> to ensure that the adsorption energies obtained for key molecules are independent of the morphology and dimension of the cluster. With this specific guidelines at hand, we built different models representative of the binary and ternary catalysts to assess the adsorption energy ( $E_{\text{ads}}$ ) of CO<sub>2</sub>, CO, and the dissociated products of H<sub>2</sub>.

Thereby, we employed models of the most stable terminations of *m*-ZrO<sub>2</sub> and Pd nanoparticles, (-111) and (111) surfaces, respectively.<sup>222,223</sup> Regarding In<sub>2</sub>O<sub>3</sub>, we used the (111) surface with one oxygen vacancy cleaved from the bixbyite structure, since it was previously identified as the active site for CO<sub>2</sub> hydrogenation (*i.e* the In<sub>3</sub>O<sub>5</sub> ensemble) and is the most abundant termination.<sup>204,227,228</sup> The adsorption of molecules on InPd<sub>x</sub> alloys was carried out on slab models of InPd<sub>2</sub>(013) and InPd(101), as these two alloys were identified on HR-XRD analysis of the ternary catalyst. In reference to the InO<sub>x</sub> patches deposited on the Pd/InPd<sub>x</sub> NPs detected in Pd-In<sub>2</sub>O<sub>3</sub>/ZrO<sub>2</sub> systems by STEM-EELS experiments, they were represented by various partially reduced indium oxide clusters (In<sub>4</sub>O<sub>5</sub>, In<sub>6</sub>O<sub>7</sub> and In<sub>8</sub>O<sub>10</sub>) adsorbed on Pd(111) and InPd<sub>2</sub>(013) slab models. The InO<sub>x</sub> clusters were obtained from the optimized structure of a In<sub>2</sub>O<sub>3</sub> layer at 37.5% degree of reduction on Pd(111), which maximize the In-Pd interactions. In addition, this structure with an additional oxygen vacancy was also used to represent a Pd nanoparticle completely covered by In<sub>2</sub>O<sub>3</sub>, as it preserves a pattern similar to the In<sub>3</sub>O<sub>5</sub> active ensemble.

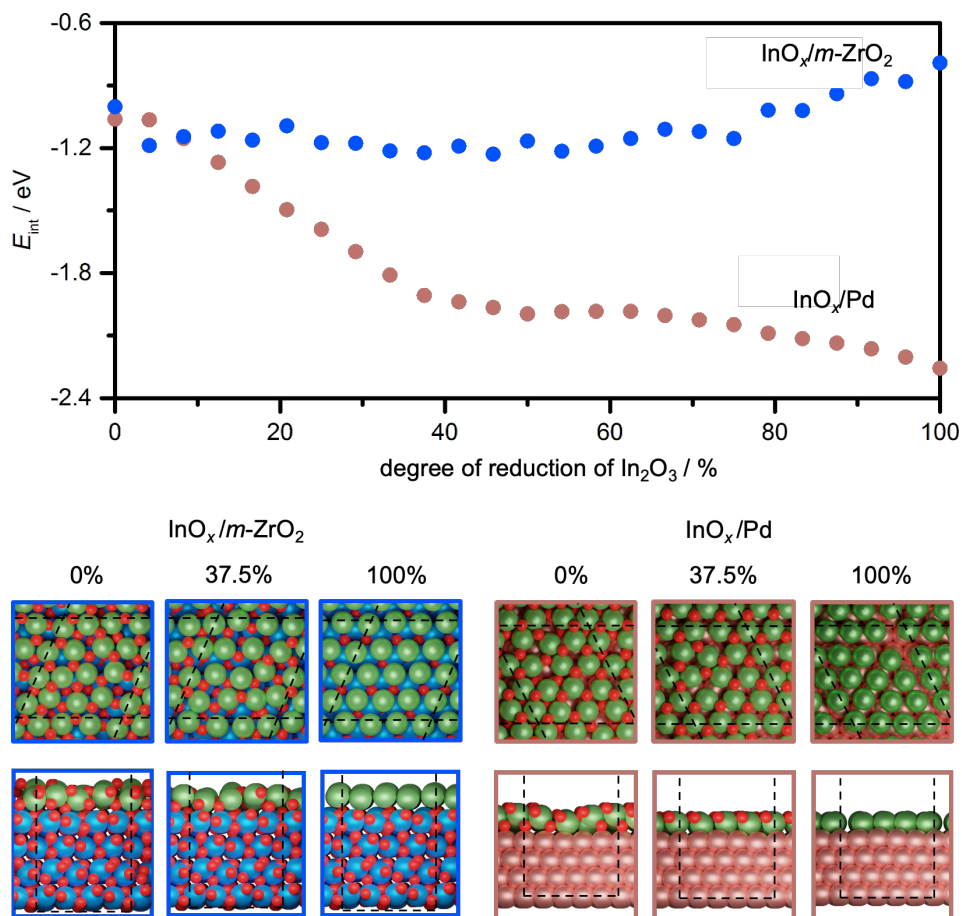
## Chapter 4. Metal-promoted metal oxides for green methanol production

---

### 4.3.3 Reaction-induced reconstruction of Pd-In<sub>2</sub>O<sub>3</sub>/ZrO<sub>2</sub>

In-depth experimental characterization shows that the architecture of the ternary Pd-In<sub>2</sub>O<sub>3</sub>/ZrO<sub>2</sub> is reconstructed upon reaction and this is key to achieve high methanol productivity. Particularly, indium oxide is dispersed on ZrO<sub>2</sub> in the fresh catalyst. In contrast, In<sub>2</sub>O<sub>3</sub> is partially reduced (InO<sub>x</sub> species) and migrates to some extent to Pd particles rendering InPd<sub>x</sub> NPs covered by InO<sub>x</sub> patches under reaction conditions. Thereby, we computed the interaction energy ( $E_{\text{int}}$ ) between a layer of In<sub>2</sub>O<sub>3</sub> at different degrees of reduction with *m*-ZrO<sub>2</sub>(-111) and Pd(111) surfaces (**Equations 4.14-4.15**). **Figure 4.26** depicts that at low degree of reduction of the In<sub>2</sub>O<sub>3</sub> layer (*ca.* 0-17%),  $E_{\text{int}}$  is similar for both surfaces. Thus, as the surface area of ZrO<sub>2</sub> support is clearly higher than the area of Pd NPs, In<sub>2</sub>O<sub>3</sub> is mainly deposited on the support in the fresh catalyst. Then, when the catalyst is heated and exposed to reaction conditions, the formation of oxygen vacancies is fostered in In<sub>2</sub>O<sub>3</sub>.<sup>15,191,204,210,226</sup> This favours the interaction of In<sub>2</sub>O<sub>3</sub> with Pd over ZrO<sub>2</sub>, as indicated by the  $E_{\text{int}}$  values obtained at reduction degrees of In<sub>2</sub>O<sub>3</sub> higher than 17%. At this point, In<sub>2</sub>O<sub>3</sub> experiences a change on their wettability properties because its surface energy and the mobility on ZrO<sub>2</sub> increases.<sup>208</sup> Thus, this is the driving force that leads In<sub>2</sub>O<sub>3</sub> to migrate from ZrO<sub>2</sub> to Pd under reaction conditions. Furthermore, the computed formation energies for InPd and InPd<sub>2</sub> (-0.97 and -1.51 eV) indicate the high tendency of metallic indium to be alloyed with Pd. Therefore, this explains that InPd<sub>x</sub> are formed when In<sub>2</sub>O<sub>3</sub> is reduced. Overall, the Pd-In<sub>2</sub>O<sub>3</sub>/ZrO<sub>2</sub> catalyst exhibits a special case of strong metal-support interactions (SMSI). Instead of the support (ZrO<sub>2</sub>) covering the metallic NPs (Pd), as it was extensively observed previously for other binary systems containing reducible oxides,<sup>233-238</sup> it is an other component of the system (InO<sub>x</sub> species) which is partially encapsulating the metallic NPs. We attribute this phenomena to the higher reducible and mobile character of In<sub>2</sub>O<sub>3</sub> compared with ZrO<sub>2</sub>.

4.3. Metal-metal oxide interactions in Pd-In<sub>2</sub>O<sub>3</sub>/ZrO<sub>2</sub>



**Figure 4.26:** Interaction energy ( $E_{\text{int}}$ ) between  $m$ -ZrO<sub>2</sub> and Pd with an In<sub>2</sub>O<sub>3</sub> monolayer at different degrees of reduction (top), with corresponding top and side views of snapshots of relevant models (bottom). Color code: Zr (blue), In (green), Pd (light pink), and O (red).

## Chapter 4. Metal-promoted metal oxides for green methanol production

---

### 4.3.4 Identification of the active sites

CO<sub>2</sub> hydrogenation to methanol involves the activation of CO<sub>2</sub> and H<sub>2</sub> followed by hydride-protons transfers while avoiding the RWGS, which decrease the  $S_{\text{MeOH}}$  and could trigger CO poisoning. In this context, a bifunctional mechanism between metal oxides (acid-base steps, such as CO<sub>2</sub> activation) and metals (H<sub>2</sub> activation) is key as explained in detail in the introduction of this chapter (**Figure 4.1**). We computed the adsorption energies ( $E_{\text{ads}}$ ) of CO<sub>2</sub>, H<sub>2</sub>, and CO on different single- and multicomponent models in order to identify the active sites of Pd-In<sub>2</sub>O<sub>3</sub>/ZrO<sub>2</sub> and compare its activity with its binary counterparts. Several experimentally-guided models were employed to represent different phases of the catalysts as further explained in the methodology section. The simulation of these  $E_{\text{ads}}$  by DFT is key to rule out the active sites of the complex and dynamic catalysts under study. The use of several models provide local information about the different phases of the systems. In contrast, experimental measurements for the adsorption of the CO<sub>2</sub>, H<sub>2</sub>, and CO (*i.e.* TPD measurements) would not provide significant information about the catalytic process.<sup>239</sup> This is because (i) measurements on the fresh catalysts are not representative of the catalytic activity, as the systems restructure under reaction conditions; and (ii) the final architecture of the catalysts is very convoluted containing different phases and the adsorption properties of each one cannot be distinguished with the experimental measurements.

**Figure 4.27** shows the most favorable  $E_{\text{ads}}$  on the most relevant models while the values associated with other surfaces and configurations can be found in **Appendix D, Figures 6.12-6.13**.  $E_{\text{ads,CO}_2}$  is favoured on the basic oxygen sites of the metal oxides ( $m\text{-ZrO}_2$  and In<sub>2</sub>O<sub>3</sub>) compared to Pd, while this trend is reversed for the dissociation products of H<sub>2</sub>. These findings suggest that in binary catalysts, such as Pd/In<sub>2</sub>O<sub>3</sub> and Pd/ $m\text{-ZrO}_2$ , CO<sub>2</sub> is adsorbed and hydrogenated on metal oxides and H<sub>2</sub> is activated on Pd NPs (**Figure 4.1**). Thus, spillover of the activated hydrogen from Pd to the metal oxides is required, which is a long-range and stochastic process and therefore highly ineffective.<sup>240,241</sup> Furthermore, the high capability of Pd to activate molecular hydrogen as H atoms fosters both RWGS and

### 4.3. Metal-metal oxide interactions in Pd-In<sub>2</sub>O<sub>3</sub>/ZrO<sub>2</sub>

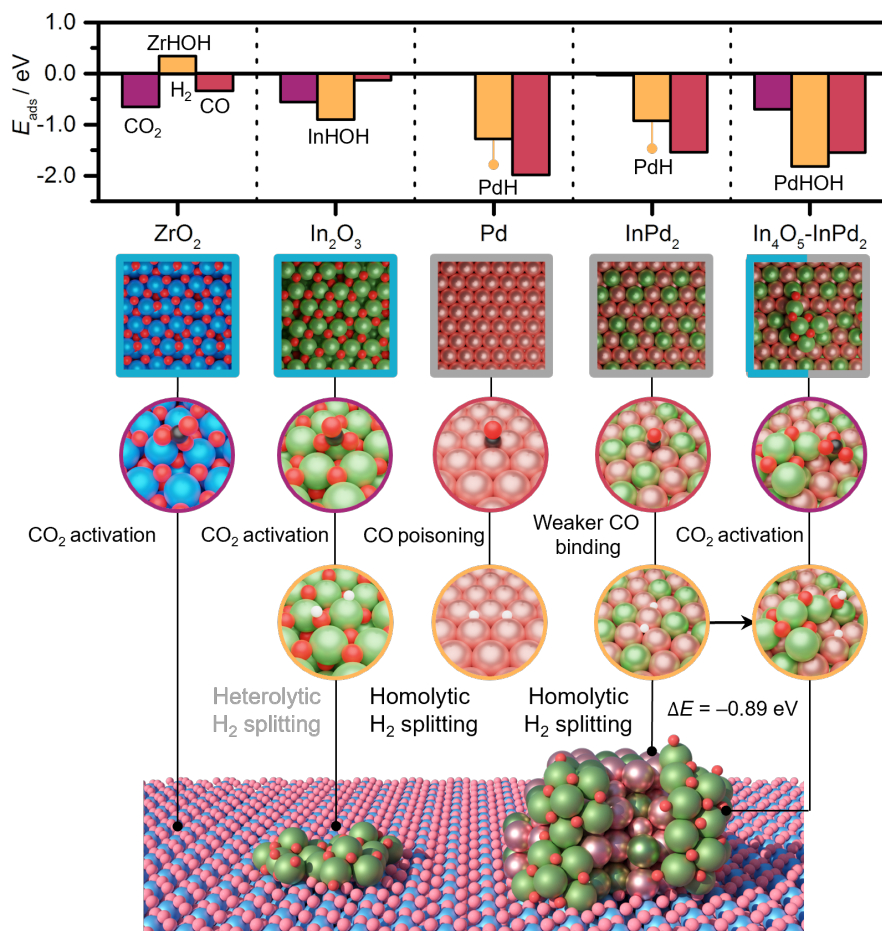
---

methanol formation. On top of this, the very exothermic  $E_{\text{ads,CO}}$  obtained on this phase points to CO poisoning. The experimental characterization indicates that InPd<sub>x</sub> alloys are formed under reaction conditions in the ternary catalyst. Remarkably, the adsorption energies of H<sub>2</sub> and CO are weakened on InPd<sub>x</sub> compared to pure Pd.<sup>242</sup> This allows to control the H coverage and smooth the CO poisoning. Moreover, it should be highlighted that these results are in line with the experimental data of volumetric CO chemisorption of the different catalysts, which clearly show a smaller CO uptake for Pd-In<sub>2</sub>O<sub>3</sub>/ZrO<sub>2</sub> compared to Pd/ZrO<sub>2</sub>.

Going in further detail to the adsorption energies on models related with the ternary system, we can first discard InPd<sub>x</sub> nanoparticles totally covered by InO<sub>x</sub> species, in line with experimental characterization.  $E_{\text{ads,CO}_2}$  on the model of a monolayer of In<sub>2</sub>O<sub>3</sub> on top of Pd is endothermic, which would hinder the activation of CO<sub>2</sub> (**Appendix D, Figure 6.12**). In contrast, CO<sub>2</sub> adsorption on the oxygen of the edges of InO<sub>x</sub> patches deposited both in Pd and InPd<sub>2</sub> is very favoured, highlighting the high basicity of these type of sites. Moreover, H<sub>2</sub> can be homolytically activated on InPd<sub>2</sub> regions with favourable formation of PdH+OH species on the edge of the InO<sub>x</sub> patches ( $\Delta E = -0.89$  eV), which are crucial to obtain high methanol selectivity. Moreover, the areas of the ternary catalysts with In<sub>2</sub>O<sub>3</sub> dispersed on ZrO<sub>2</sub> would also contribute to CO<sub>2</sub> activation and hydrogenation.



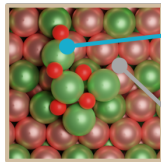
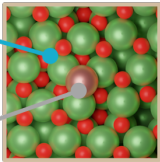
Chapter 4. Metal-promoted metal oxides for green methanol production



**Figure 4.27:** Adsorption energies ( $E_{ads}$ ) of key molecules on models representative of the different components of Pd- $In_2O_3$ / $ZrO_2$  catalyst. Snapshots of adsorbed  $CO_2$  and  $H_2$  indicate the locations at which the activation of these key species are more favoured over the catalyst surface, whereas snapshots of CO adsorption depict surfaces with tendency to be poisoned by this molecule. Models favouring the acid-base steps and/or the  $H_2$  activation are highlighted in blue and gray, respectively. Color code: Zr (blue), In (green), Pd (light pink), O (red), C (dark gray), and H (white). Adapted from [16].

### 4.3. Metal-metal oxide interactions in Pd-In<sub>2</sub>O<sub>3</sub>/ZrO<sub>2</sub>

Overall, the InO<sub>x</sub> patches deposited on InPd<sub>x</sub> NPs in the ternary catalyst allow the efficient activation of CO<sub>2</sub> and H<sub>2</sub>, as well as the selective hydrogenation of the former, in a confined region of the space avoiding the sluggish transport of the active species. In analogy to the FSP *M*-In<sub>2</sub>O<sub>3</sub> systems, the particular architecture of the Pd-In<sub>2</sub>O<sub>3</sub>/ZrO<sub>2</sub> provides the capability to efficiently integrate the properties of the oxidic and metallic components of the catalyst. Furthermore, the same analogy could be established with other previously studied Pd-In<sub>2</sub>O<sub>3</sub> containing catalysts, such as ternary Pd-In<sub>2</sub>O<sub>3</sub>/ZrO<sub>2</sub> system prepared by FSP and Pd-In<sub>2</sub>O<sub>3</sub> catalyst synthesised by coprecipitation and dry impregnation.<sup>191,210</sup> Therefore, distinct catalyst architectures obtained with different synthetic methods lead to similar catalytic properties due to common geometric and electronic features (**Figure 4.28**). In particular, the interaction between the metallic and oxidic phases of these systems lead to architectures where the catalytic properties of the different components are maximized.

Catalyst architectures		Common catalytic properties
 <p>InPd<sub>x</sub> NPs decorated with InO<sub>x</sub> patches</p>	 <p>Atomically-dispersed Pd on InO<sub>x</sub> matrix</p>	<ul style="list-style-type: none"> <li>• High MeOH selectivity</li> <li>• Close proximity of active species</li> <li>• Homolytic H<sub>2</sub> splitting on InPd<sub>x</sub></li> <li>• Acid-base steps on InO<sub>x</sub></li> </ul>

**Figure 4.28:** Active ensembles and associated key geometric and electronic features dictating performance towards CO<sub>2</sub> hydrogenation to methanol of different catalysts discussed along this chapter with distinct architectures and similar catalytic properties. Adapted from [16].

## *Chapter 4. Metal-promoted metal oxides for green methanol production*

---

### 4.4 Conclusions

In this chapter I have systematically assessed the speciation and reactivity towards thermocatalytic CO<sub>2</sub> hydrogenation to methanol of three relevant metal-promoted metal oxide families of catalysts (ZnZrO<sub>x</sub>, M-In<sub>2</sub>O<sub>3</sub>, and Pd-In<sub>2</sub>O<sub>3</sub>/ZrO<sub>2</sub>). In general, it has been demonstrated that the close synergies established between in-depth experimental characterization and DFT simulations play a pivotal role in elucidating the synthesis-structure-performance relationships of intricate catalytic systems. Specifically, a high correlation between the experimental characterizations and the DFT models used to evaluate the catalytic activity of the systems is crucial. It is important to highlight that the properties of these complex materials cannot be fully understood using a single experimental characterization technique or a solitary DFT model. Instead, the integration of distinct representative DFT models with the combination of various characterization techniques applied to fresh, activated, used, and under reaction conditions catalyst, becomes fundamental to gain a comprehensive understanding. The particular conclusions retrieved for each system are outlined below.

**ZnZrO<sub>x</sub>**: Catalysts prepared with the one-step FSP method exhibits boosted methanol productivity and enhanced Zn utilization compared with the CP-made analogs due to:

- Zn is incorporated and highly dispersed on surface sites of ZrO<sub>2</sub> lattice.
- Oxygen vacancy formation drives Zn incorporation.
- Formation of *m*-ZrO<sub>2</sub> phases at the surface of the catalyst under reaction conditions.
- Reaction energy profiles for CO<sub>2</sub> hydrogenation point to *m*-ZrO<sub>2</sub> surface is more active than *t*- and *c*-ZrO<sub>2</sub> counterparts.
- Acidity of Zr cations and the local coordination of Zn dopants were identified as the key electronic and geometric factors dictating the different reactivity between polymorphs.

#### 4.4. Conclusions

---

- The formation of oxygen vacancies in areas without dopant (EPR active,  $V_{\text{O}}^{\bullet}\text{-Zr}^{3+}$  signal) can be used as a proxy of the presence of vacancies next to Zn (EPR silence). Structures associated with  $V_{\text{O}}^{\bullet}\text{-Zr}^{3+}$  signal were only located for the *m*- $\text{ZrO}_2$  polymorph.

***M*- $\text{In}_2\text{O}_3$** : FSP was successfully employed as standardized synthesis platform to assess the metal promotional effect and the speciation of nine dopants on the catalytic activity of  $\text{In}_2\text{O}_3$  towards  $\text{CO}_2$  hydrogenation to methanol:

- Catalysts performance is strongly governed by the promoter's speciation.
- Compromise between metallic and oxidic character of the metal promoters is key for the speciation and thus for the catalytic performance.
- Metal promoters can be classified in three families. The best promoters (Pd, Pt, Rh, Ru, and Ir) are atomically dispersed on the  $\text{In}_2\text{O}_3$  forming the  $\text{In}_3\text{MO}_4$  ensemble that enhances hydrogen activation and oxygen vacancy formation. Then, Co and Ni exhibit less boosted methanol productivity due to the incorporation into bulk sites and the formation of extended-layered alloys, respectively. Finally, Ag and Au sinter into metallic NPs and do not provide any promotional effect.
- The formation of the  $\text{In}_3\text{MO}_4$  ensemble provides an ideal architecture for the selective  $\text{CO}_2$  hydrogenation to methanol.  $\text{H}_2$  activation is promoted on the  $M\text{In}_3$  nanoalloy while  $\text{CO}_2$  is adsorbed and hydrogenated on the nearby basic oxygen atoms of the  $\text{In}_2\text{O}_3$  lattice.

#### Chapter 4. Metal-promoted metal oxides for green methanol production

**Pd-In<sub>2</sub>O<sub>3</sub>/ZrO<sub>2</sub>**: Ternary catalyst prepared with the wet impregnation scalable synthetic method exhibited high activity, selectivity, and stability towards the thermocatalytic CO<sub>2</sub> hydrogenation due to reaction-induced reconstruction:

- InO<sub>x</sub> species migrate from ZrO<sub>2</sub> surface to partially cover the Pd NPs and form InPd<sub>x</sub> under reaction conditions. This leads to InPd<sub>x</sub> particles dispersed on ZrO<sub>2</sub> and decorated with partially reduced In<sub>2</sub>O<sub>3</sub> patches.
- A thermodynamic model indicated that metal-metal oxide interactions at different degrees of In<sub>2</sub>O<sub>3</sub> reduction govern the migration of InO<sub>x</sub> species (*i.e.* strong metal support interactions). In particular, the reconstruction is attributed to the change of the wettability properties of In<sub>2</sub>O<sub>3</sub> triggered by its partially reduction under CO<sub>2</sub> hydrogenation conditions.
- The adsorption energies of key molecules (CO<sub>2</sub>, CO, H<sub>2</sub>) point to the edge of InO<sub>x</sub> patches deposited on InPd<sub>x</sub> particles as the active sites of the Pd-In<sub>2</sub>O<sub>3</sub>/ZrO<sub>2</sub> catalyst. CO<sub>2</sub> is adsorbed and hydrogenated on the basic oxygen atoms of the patches whereas H<sub>2</sub> is activated *via* low energetic process in the nearby regions of the InPd<sub>x</sub> surface.

Interestingly, we found that two catalysts with distinct architectures, Pd-In<sub>2</sub>O<sub>3</sub> and Pd-In<sub>2</sub>O<sub>3</sub>/ZrO<sub>2</sub>, exhibit common catalytic properties due to the similar features of their active sites. Particularly, they contain ensembles that efficiently combine oxidic and metallic character to maximize the catalytic properties of metal oxides and metals on confined regions of the space. Thus, CO<sub>2</sub> and H<sub>2</sub> are effectively activated in nearby regions avoiding the sluggish transport of the active species. Moreover, the oxidic phase assists in the selective hydrogenation of CO<sub>2</sub> to methanol.

Overall, the study carried out in this chapter of ZnZrO<sub>x</sub>, M-In<sub>2</sub>O<sub>3</sub>, and Pd-In<sub>2</sub>O<sub>3</sub>/ZrO<sub>2</sub> catalytic systems provides an atomic-level understanding of the key electronic and geometric features that govern catalytic performance of these metal-promoted metal oxides systems. In particular, how the proper

#### *4.4. Conclusions*

---

combination and interaction of the oxidic and metallic components of these catalytic systems is crucial to obtain high methanol productivity. This paves the way towards the optimal design of catalytic materials for green methanol production and invest efforts to make this process viable on an industrial scale.

Chapter 4. Metal-promoted metal oxides for green methanol production

## Chapter 5

# Conclusions and Outlook

In this thesis, I have modelled catalytic systems for oxygen evolution reaction and CO<sub>2</sub> hydrogenation to methanol. These two chemical conversions are pivotal to face the complex challenge of mitigating the effects of climate change. The rational design of novel catalytic materials is crucial to improve the efficiency of such conversions to overcome our dependence in fossil fuels and advancing into more environmentally conscious socioeconomic models. Therefore, I have employed DFT simulations and established tight synergies with experimental testing and characterization to reveal synthesis-structure-performance relationships of the Earth-abundant based MOF-74 electrocatalysts for OER, and metal-promoted metal oxides (ZnZrO<sub>x</sub>, *M*-In<sub>2</sub>O<sub>3</sub>, and Pd-In<sub>2</sub>O<sub>3</sub>/ZrO<sub>2</sub>) for the thermocatalytic CO<sub>2</sub> hydrogenation to methanol. The particular conclusions retrieved for each catalytic system have been detailed in previous chapters. Therefore, general conclusions and outlook for these materials are outlined bellow:

**Chapter 3:** The experimentally-proved electrocatalytic activity of Fe-MOF-74 towards OER has been associated to defective structures. DFT simulations indicate that these defective structures are key to explain the electrocatalytic activity due to reversible linkers reorganizations and the stabilization of oxo intermediates in bridge positions between two metal centres. Moreover, the computational methodology used was benchmarked



## Chapter 5. Conclusions and Outlook

---

against high-level theory and its reliability and efficient accuracy-cost balance were demonstrated. Therefore, this work provides guidelines for the rational design of MOFs for electrocatalytic applications and remarks the importance of defect engineering. These guidelines and the computational approach used can be further developed to carry out high throughput screening of MOFs in order to accelerate the discovery of new efficient and Earth-abundant materials for catalytic processes related with energy conversion.

**Chapter 4** Key electronic and geometrical features at the atomic level of detail dictating the reactivity towards CO<sub>2</sub> hydrogenation to methanol over ZnZrO<sub>x</sub>, *M*-In<sub>2</sub>O<sub>3</sub>, and Pd-In<sub>2</sub>O<sub>3</sub>/ZrO<sub>2</sub> catalytic systems have been revealed by means of in-depth experimental characterization and DFT simulations. The conclusions for each metal-promoted metal oxide system are provided in the following lines:

- **ZnZrO<sub>x</sub>**: The preparation of ZnZrO<sub>x</sub> materials with flame-spray pyrolysis (FSP) provides catalytic materials with higher methanol productivity compared to the traditional coprecipitation (CP) methods. FSP-made systems enhance the efficient utilization and dispersion of Zn over ZrO<sub>2</sub> surface and the formation of monoclinic ZrO<sub>2</sub> phases at the surface of the catalyst under reaction conditions. DFT simulations show that incorporation of Zn into surface ZrO<sub>2</sub> sites fosters the formation of oxygen vacancies. Moreover, the computation of reaction energy profiles point to Zn-doped monoclinic ZrO<sub>2</sub> surfaces are more active towards CO<sub>2</sub> hydrogenation than analogs tetragonal and cubic ZrO<sub>2</sub> surfaces. The sensitivity of the catalytic activity with respect to the ZrO<sub>2</sub> polymorph was attributed to different acidity of Zr cations and geometrical Zn environment.
- ***M*-In<sub>2</sub>O<sub>3</sub>**: The promotional effect of nine metals dopants introduced in In<sub>2</sub>O<sub>3</sub> by a standardized synthetic method (FSP) dictates the methanol productivity of each *M*-In<sub>2</sub>O<sub>3</sub> system. In turn, the promotional effect is ruled by the speciation of the dopants which is found to be correlated with the inherent properties of the metals. In particular, the best metal promoters (Ru, Ir, Rh, and specially Pd

and Pt) are the ones with a balanced metallic and oxidic character that are highly dispersed on  $\text{In}_2\text{O}_3$  forming a metallic  $\text{In}_3M$  ensemble embedded in the indium oxide matrix. This particular architecture allows the activation of  $\text{H}_2$  and  $\text{CO}_2$  on the metallic ensemble and the oxidic matrix, respectively, as well as the selective hydrogenation to methanol.

- **Pd- $\text{In}_2\text{O}_3$ / $\text{ZrO}_2$ :** The high methanol productivity shown by the ternary Pd- $\text{In}_2\text{O}_3$ / $\text{ZrO}_2$  catalyst prepared with a scalable synthetic method (wet impregnation) is attributed to reaction-induced reconstruction of the material. Partially reduced  $\text{In}_2\text{O}_3$  species ( $\text{InO}_x$ ) migrates from the  $\text{ZrO}_2$  support to Pd nanoparticles leading to the formation of  $\text{InPd}_x$  alloys decorated with  $\text{InO}_x$  species dispersed on  $\text{ZrO}_2$  support. DFT simulations depict that the reconstruction is driven by strong metal-support interactions. In particular, the migration of  $\text{InO}_x$  species is dictated by the change of the wettability properties of  $\text{In}_2\text{O}_3$  when increasing its degree of reduction, which favours the interaction with Pd over  $\text{ZrO}_2$ . The interphase between the  $\text{InO}_x$  patches and  $\text{InPd}_x$  were revealed as the active sites for the selective  $\text{CO}_2$  hydrogenation to methanol. The activation of  $\text{H}_2$  takes places on the surface of the alloy while  $\text{CO}_2$  is adsorbed and selective hydrogenated on the basic oxygen atoms on the edge of  $\text{InO}_x$  patches.

The systematic assessment of these metal-promoted metal oxides systems carried out in this thesis highlights the importance of combining experimental characterization and modelling to rationalize the catalytic activity of these complex materials. In particular, the characterization of fresh, used and under reactions conditions of the catalysts, as well as the combination of different experimentally-guided DFT models will be pivotal to the future search of novel catalytic systems. The intersection between experiments and simulations has allowed the identification of key guidelines for the design of catalysts for the efficient  $\text{CO}_2$  selective hydrogenation to methanol. In this scenario, this thesis revealed that the proper combination of metallic and oxidic phases on confined regions of the space is pivotal to obtain high

## *Chapter 5. Conclusions and Outlook*

---

methanol productivity. This combination maximise the properties of the two phases and allows the efficient activation of  $\text{CO}_2$  and  $\text{H}_2$  in nearby sites (avoiding the sluggish transport of active species) and the selective hydrogenation of the former to methanol. Indeed, it has demonstrated that even catalysts with different architectures but with active sites with the proper metallic and oxidic character present similar catalytic activity. Therefore, future studies will be addressed to achieve a higher control in the final catalyst structure to completely close the loop between experiments and simulations. This will be crucial to make feasible the seek of Earth-abundant based materials for  $\text{CO}_2$  hydrogenation to methanol by means of high throughput screening. Therefore, this work paves the way for the rational design of metal-promoted metal oxides as efficient catalytic systems for green methanol production. Furthermore, the identification of the guidelines needed for optimal development of these kind of materials encourages to invest efforts to scale-up the process at the industrial scale. This will be crucial to make possible the replacement of methanol produced from fossil fuels by green methanol.

## Chapter 6

# Appendix

### 6.1 Appendix A: Electrocatalytic sites of Earth-abundant MOF-74 for OER

**Table 6.1:** Gibbs free energies ( $\Delta G$ , in eV) and theoretical overpotentials ( $\eta_{\text{theor}}$ , in V) associated with models **A** and **B** with interwire ferromagnetic (FM) coupling. Values in bold indicate the PDS.

Models	$\Delta G_1$	$\Delta G_2$	$\Delta G_3$	$\Delta G_4$	$\eta_{\text{theor}}$
<b>A</b>	1.40	<b>1.89</b>	0.94	0.69	0.66
<b>B</b>	0.89	<b>2.34</b>	0.80	0.89	1.11

Chapter 6. Appendix

**Table 6.2:** Spin densities of iron and oxygen atoms associated with the reactive centres of relevant OER intermediates from the pristine (**B**) and defective models (**C** and **D**).

Model	<b>X</b>		<b>X-OH</b>		<b>X<sub>1</sub>-O-X<sub>2</sub></b>			<b>X<sub>1</sub>-OOH-X<sub>2</sub></b>		
	Fe	Fe	O	Fe <sub>1</sub>	O	Fe <sub>2</sub>	Fe <sub>1</sub>	O	Fe <sub>2</sub>	
<b>B</b>	-3.84	-4.42	-0.21	-3.96	-0.20		-4.33	-0.25		
<b>CB-t</b>	3.84	4.42	0.20	4.03	0.18		4.34	0.24		
<b>CB-b</b>	3.84	4.42	0.20	4.34	0.20	3.79	4.40	0.20	3.85	
<b>D-t</b>	3.84	4.41	0.21	4.13	0.25		4.32	0.25		
<b>D-b</b>	3.84	4.41	0.21	4.35	0.27	3.85	4.40	0.12	3.84	
<b>D-b'</b>	3.84	4.41	0.21	4.40	0.21	3.86	4.40	0.10	3.84	

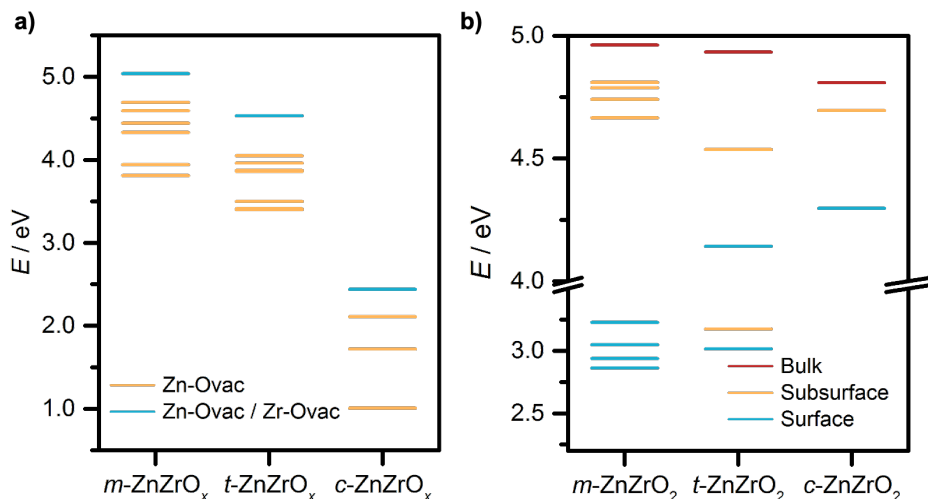
**Table 6.3:** Spin densities of iron and oxygen atoms associated with the reactive centres of OER intermediates of the Fe-MOF-74 cluster model.

DF	$\chi^a$	<b>X</b>		<b>X-OH</b>		<b>X-O</b>		<b>X-OOH</b>	
		Fe	Fe	O	Fe	O	Fe	O	
PBE	0	3.79	4.00	0.32	2.90	0.55	3.93	0.34	
M06-L	0	3.87	4.04	0.33	3.03	0.48	3.97	0.32	
HSE03-13	13	3.87	4.22	0.36	3.28	0.53	4.13	0.36	
B3LYP-15	15	3.82	4.19	0.37	3.23	0.56	4.11	0.36	
B3LYP	20	3.84	4.23	0.35	3.31	0.50	4.16	0.36	
HSE03	25	3.90	4.33	0.36	3.49	0.36	4.25	0.35	
PBE0	25	3.90	4.32	0.34	3.47	0.37	4.24	0.35	

<sup>a</sup> Percentage of nonlocal Hartree-Fock exchange.

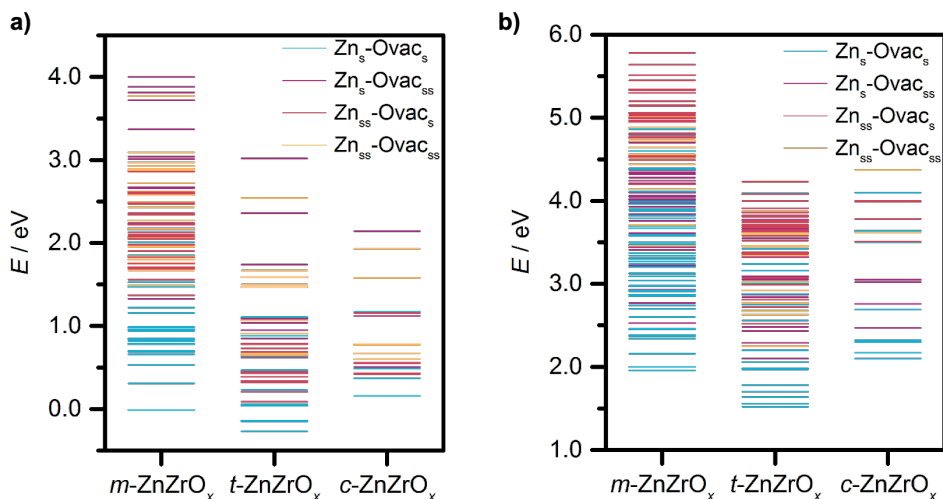
6.2. Appendix B: Zn promotion of zirconia polymorphs

## 6.2 Appendix B: Zn promotion of zirconia polymorphs



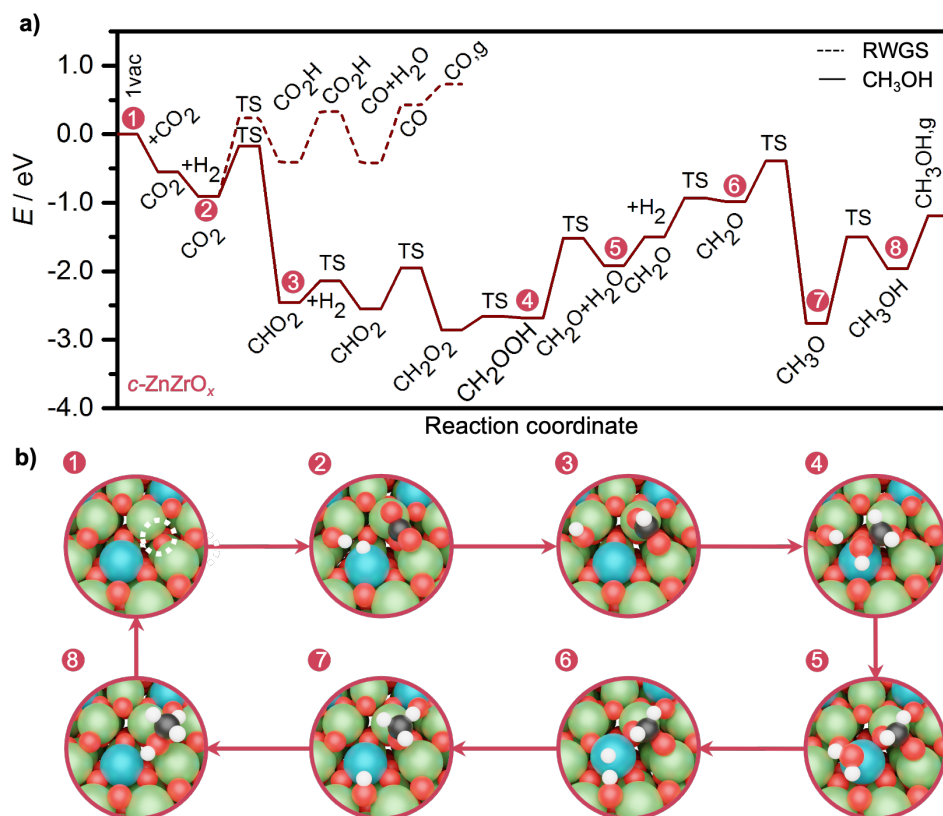
**Figure 6.1:** a) Potential energies ( $E$ ) associated with bulk  $\text{ZnZrO}_x$  models with two oxygen vacancies. I explored oxygen vacancy formation in two O bonded to Zn and Zr (Zn-Ovac) and also in two O with one bonded to Zn and Zr and another one coordinated only with Zr (Zn-Ovac/Zr-Ovac). b) Potential energies ( $E$ ) associated with Zn incorporation into bulks, subsurface, and surface sites of  $m$ -,  $t$ -, and  $c$ - $\text{ZrO}_2$  polymorphs. The incorporation of Zn was assessed in all Zr non-equivalent sites. Adapted from Ref. [13].

Chapter 6. Appendix



**Figure 6.2:** Potential energies ( $E$ ) associated with Zn incorporation into surface ( $Zn_s$ ) and subsurface ( $Zn_{ss}$ ) sites of  $m$ -,  $t$ -, and  $c$ - $ZrO_2$  polymorphs with **a)** one and **b)** two oxygen vacancies. The incorporation of Zn was assessed in all Zr non-equivalent sites. The formation of 1<sup>st</sup> oxygen vacancy was explored in all non-equivalent oxygen sites of the surface ( $Ovac_s$ ) and subsurface ( $Ovac_{ss}$ ) sites. The two most stable  $ZnZrO_x$  structures with one vacancy and Zn at all non-equivalent Zr sites of each polymorph were used as starting point for assessing the 2<sup>nd</sup> vacancy. The labels related with the position of the oxygen vacancy in **b)** indicate the site of the second oxygen vacancy. Adapted from Ref. [13].

6.2. Appendix B: Zn promotion of zirconia polymorphs

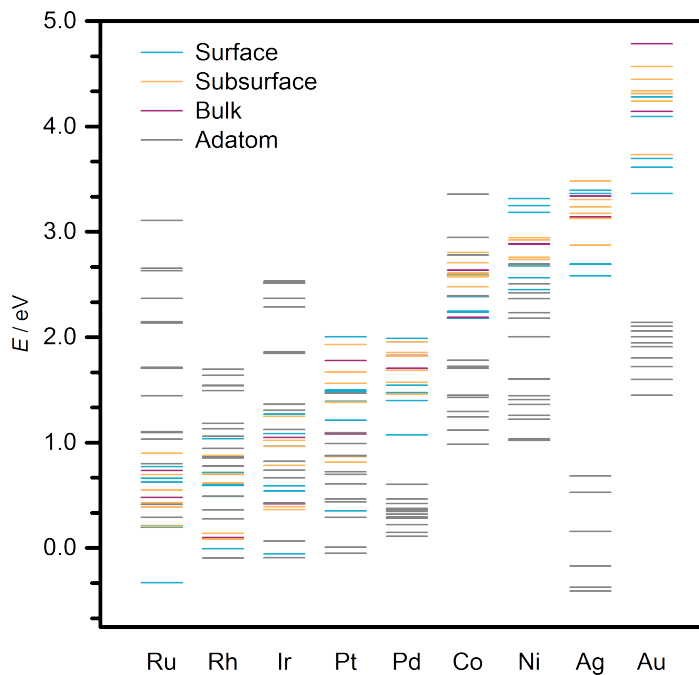


**Figure 6.3:** a) Reaction energy profiles for CO<sub>2</sub> hydrogenation to methanol and RWGS on *c*-ZnZrO<sub>*x*</sub> with one oxygen vacancy. b) snapshots of relevant intermediates associated with the labels in a). Color code: Zr (green), Zn (blue), O (red), C (dark gray), H (white), and oxygen vacancy (dotted white circles). Adapted from [13].



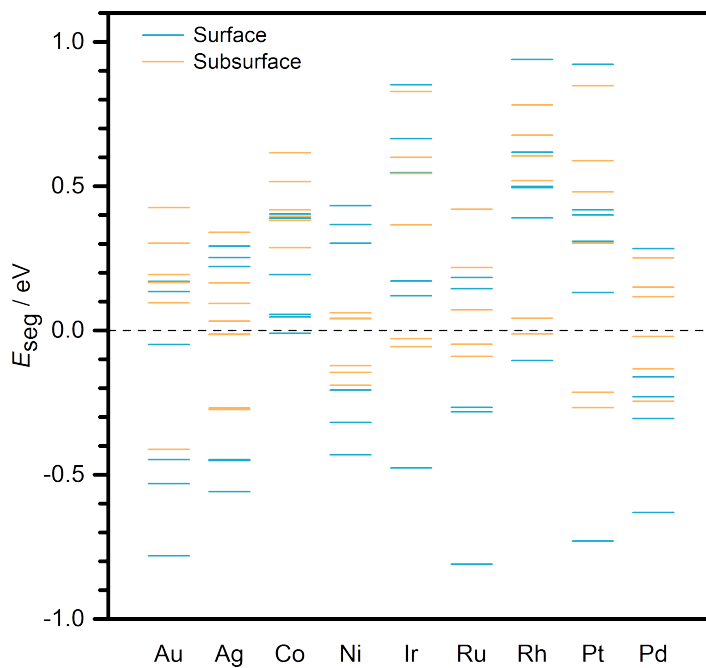
Chapter 6. Appendix

### 6.3 Appendix C: Metal promotional effects in $\text{In}_2\text{O}_3$



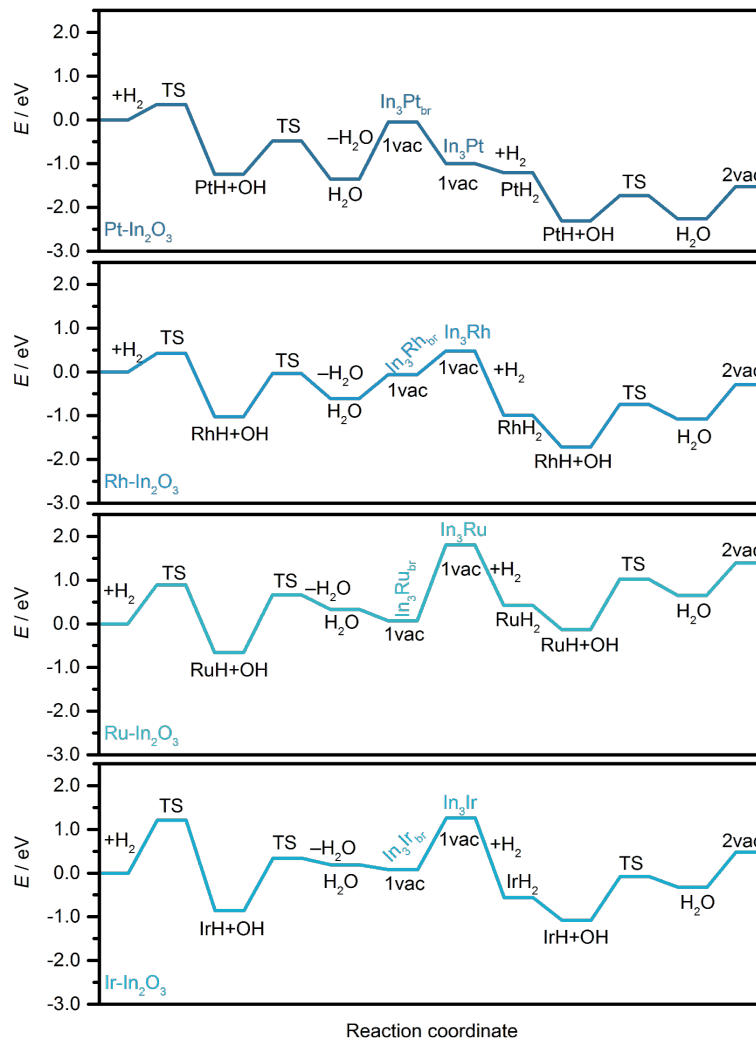
**Figure 6.4:** Potential energies ( $E$ ) associated with the incorporation of the nine metal promoters to surface, subsurface, and bulk sites of  $\text{In}_2\text{O}_3$  or deposited as adatoms. Adapted from [15].

6.3. Appendix C: Metal promotional effects in  $In_2O_3$



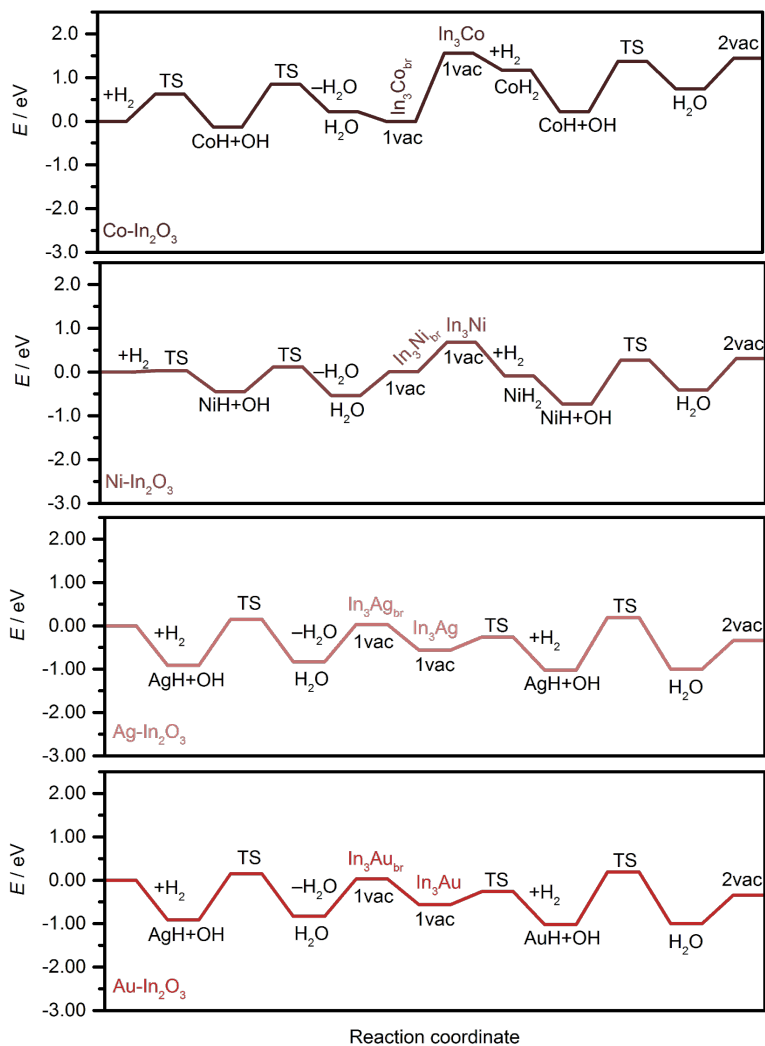
**Figure 6.5:** Segregation energies ( $E_{seg}$ ) required by the metal promoters to move from bulk to surface/subsurface sites of  $In_2O_3$ . Adapted from [15].

Chapter 6. Appendix



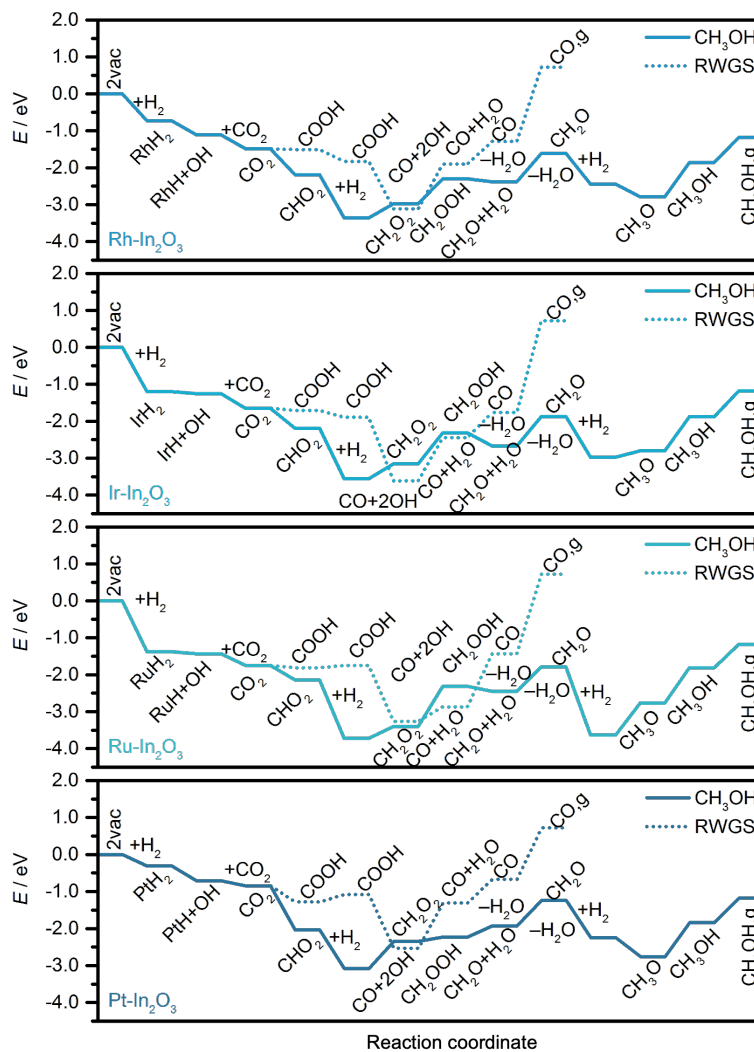
**Figure 6.6:** Reaction energy profiles associated with the formation of 2 oxygen vacancies on Pt-, Rh-, Ru-, Ir-In<sub>2</sub>O<sub>3</sub>.

6.3. Appendix C: Metal promotional effects in  $\text{In}_2\text{O}_3$



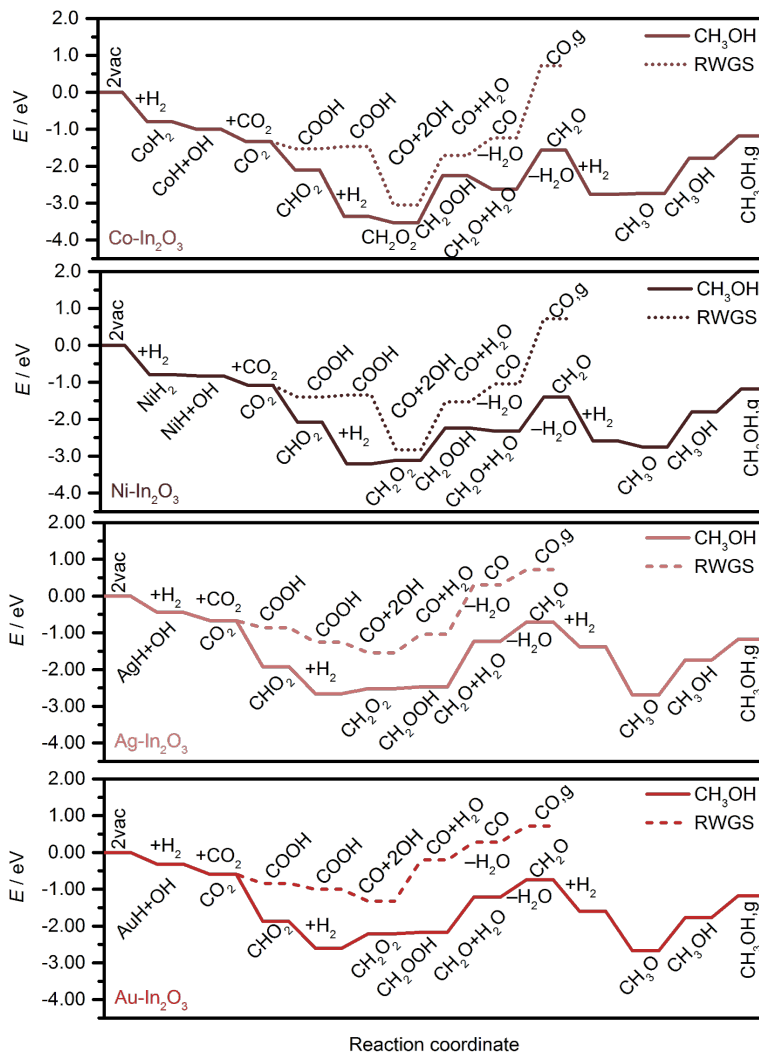
**Figure 6.7:** Reaction energy profiles associated with the formation of 2 oxygen vacancies on Co-, Ni-, Ag-, Au- $\text{In}_2\text{O}_3$ .

Chapter 6. Appendix



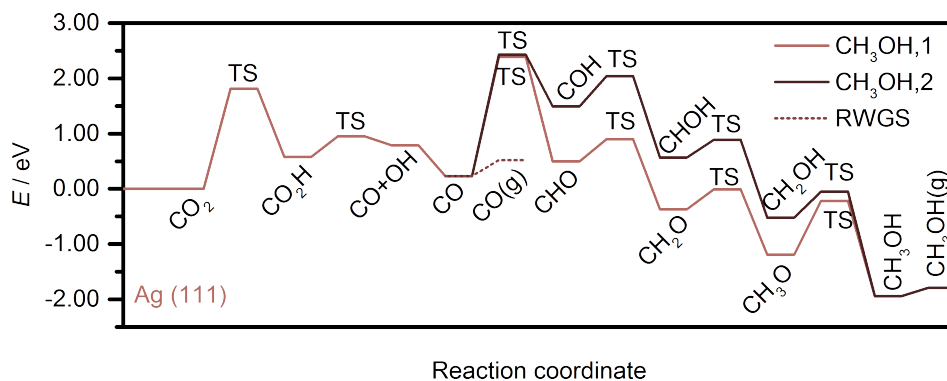
**Figure 6.8:** Reaction energy profile for CO<sub>2</sub> hydrogenation to CH<sub>3</sub>OH and the competing RWGS reaction on Pt-, Rh-, Ru-, Ir-In<sub>2</sub>O<sub>3</sub>.

6.3. Appendix C: Metal promotional effects in  $\text{In}_2\text{O}_3$



**Figure 6.9:** Reaction energy profiles for  $\text{CO}_2$  hydrogenation to  $\text{CH}_3\text{OH}$  and the competing RWGS reaction on Co-, Ni-, Ag-, Au- $\text{In}_2\text{O}_3$ .

Chapter 6. Appendix

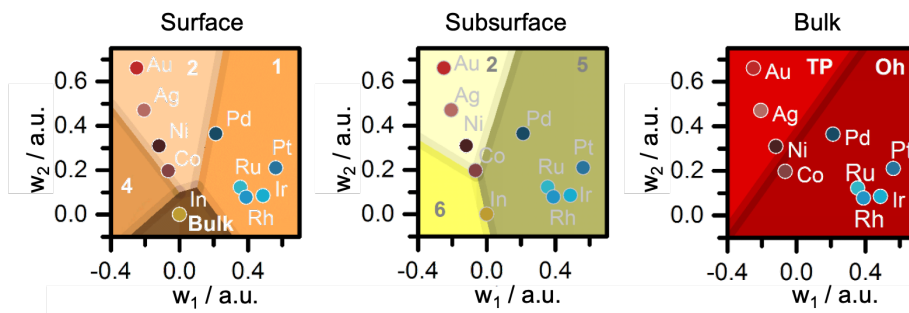


**Figure 6.10:** Reaction energy profile for  $\text{CO}_2$  hydrogenation to  $\text{CH}_3\text{OH}$  and the competing RWGS reaction on  $\text{Ag}(111)$ .

### Metal promoters incorporation into $\text{In}_2\text{O}_3$

I assessed the incorporation of the nine metal promoters into  $\text{In}_2\text{O}_3$  lattice by substituting In in its all non-equivalent sites by each of the nine metal promoters.  $\text{In}_2\text{O}_3$  lattice (**Figure 4.15**). In particular, two bulk, six surface, and six subsurface sites of  $\text{In}_2\text{O}_3$  were explored. This leads to a data matrix with 14 rows and 9 columns representing the different sites and the nine metal promoters, respectively. In general, the incorporation into surface is favoured over bulk and subsurface sites for all metal promoters. Nevertheless, the particular position in which the substitution is most favoured differs among the nine metal promoters. Therefore, Principal Component Analysis was applied following the procedure of a previous work<sup>243</sup> to the data matrix of incorporation energies in order to rationalize the factors dictating the substitution of the metal promoters into different sites of  $\text{In}_2\text{O}_3$ . Two principal components are able to describe 88% of the variability with a mean absolute error (MAE) smaller than 0.08 eV. From these two principal components I retrieved  $w_1$  and  $w_2$  that describes the tendency of the metal promoters to incorporate at a given position of  $\text{In}_2\text{O}_3$  lattice (**Figure 6.11**).

### 6.3. Appendix C: Metal promotional effects in $\text{In}_2\text{O}_3$



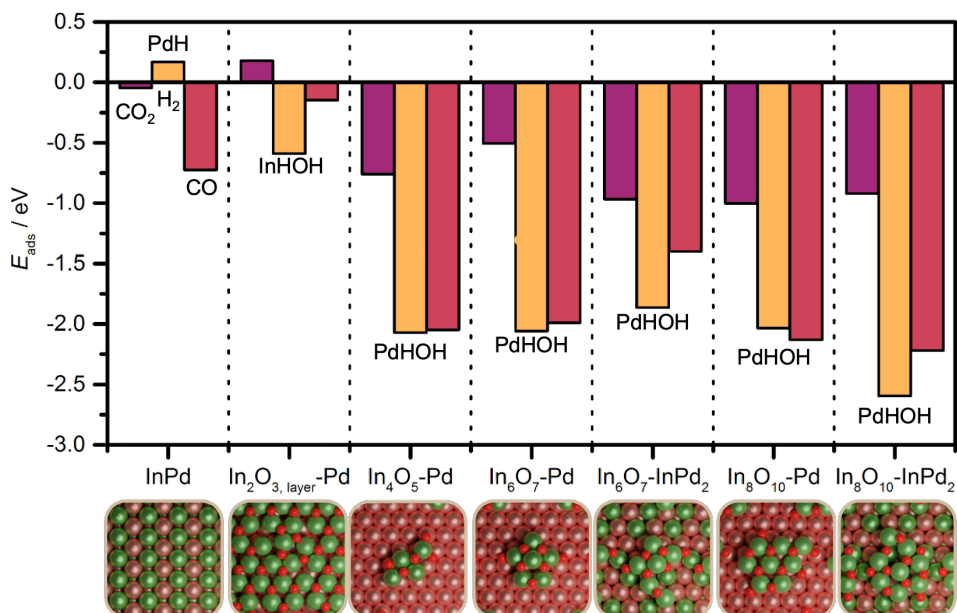
**Figure 6.11:** Diagrams of the most favoured site of incorporation of the metal promotes into surface, subsurface, and bulk sites of  $\text{In}_2\text{O}_3$  lattice. The different areas of the diagrams represent different lattice sites of  $\text{In}_2\text{O}_3$  depicted in **Figure 4.15**.  $w_1$  and  $w_2$  are descriptors retrieved from PCA. Adapted from [15].

The most favoured site of incorporation into  $\text{In}_2\text{O}_3$  surface of Pd, Pt, Rh, Ru, and Ir is the position labelled as 1 in **Figure 4.15**. In contrast, the preferred site for the incorporation of Au and Ag is position 2, while Ni and Co have the same tendency to occupy position 2 and 4. In the case of the bulk sites, Pd, Pt, Rh, Ru, and Ir occupy octahedral (Oh) positions while the substitution of Au and Ag is favoured in a trigonal prismatic (TP) site. In reference to Co and Ni, they present similar tendency to be substituted in Oh and TP positions. Interestingly, metals in site 1 of the surface have an Oh coordination while sites 2 and 4 present a TP environment. Thus, the most favoured incorporation site of the metal promoters in the surface of  $\text{In}_2\text{O}_3$  is tightly related with the preferred coordination environment in bulk positions. Moreover, the same analogy was found for subsurface positions.



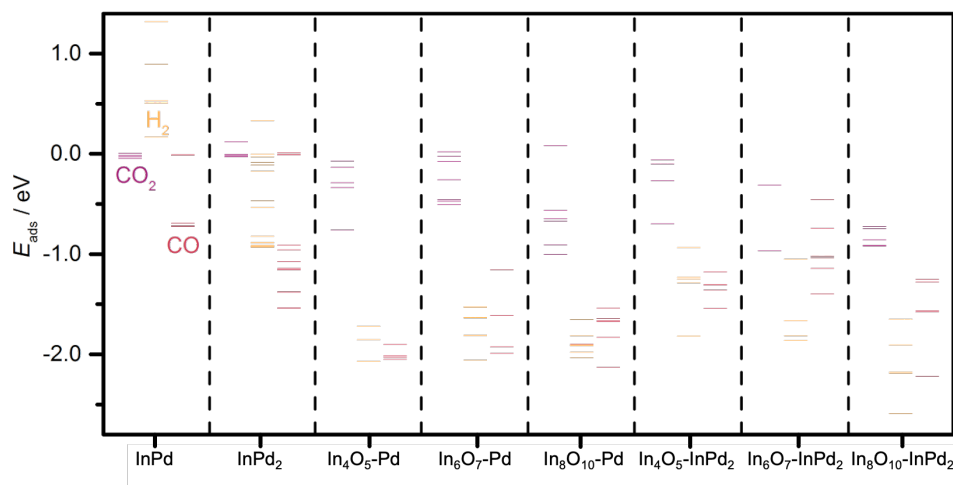
Chapter 6. Appendix

6.4 Appendix D: Metal-metal oxide interaction in Pd-In<sub>2</sub>O<sub>3</sub>/ZrO<sub>2</sub>



**Figure 6.12:** Adsorption energies ( $E_{\text{ads}}$ ) of key species on different models used to rationalize the performance of the ternary Pd-In<sub>2</sub>O<sub>3</sub>/ZrO<sub>2</sub> catalytic system. Top views of the clean surfaces are shown at the bottom panel. Color code: Zr (blue), In (green), Pd (light pink), O (red), and C (dark gray). Adapted from [16].

6.4. Appendix D: Metal-metal oxide interaction in Pd-In<sub>2</sub>O<sub>3</sub>/ZrO<sub>2</sub>



**Figure 6.13:** Adsorption energies ( $E_{\text{ads}}$ ) of key species associated with different configurations on InPd<sub>*x*</sub> alloys and different InO<sub>*x*</sub> clusters deposited on Pd(111) and InPd<sub>2</sub>(013). Adapted from [16].

*Chapter 6. Appendix*

---

# Bibliography

- (1) IEA International Energy Agency, <https://www.iea.org/>, Accessed: 2023-08-09.
- (2) United Nations, <https://population.un.org/wpp/Download/Standard/CSV/>, Accessed: 2023-08-09.
- (3) European Comission, [https://edgar.jrc.ec.europa.eu/report\\_2022](https://edgar.jrc.ec.europa.eu/report_2022), Accessed: 2023-08-09.
- (4) Energy Institute, <https://www.energyinst.org/statistical-review>, Accessed: 2023-08-09.
- (5) Abbass, K.; Qasim, M. Z.; Song, H.; Murshed, M.; Mahmood, H.; Younis, I. A review of the global climate change impacts, adaptation, and sustainable mitigation measures. *Environ. Sci. Pollut. Res.* **2022**, *29*, 42539–42559.
- (6) VijayaVenkataRaman, S.; Iniyan, S.; Goic, R. A review of climate change, mitigation and adaptation. *Renew. Sustain. Energy Rev.* **2012**, *16*, 878–897.
- (7) IEA International Energy Agency, <https://www.iea.org/topics/global-energy-crisis>, Accessed: 2023-08-09.
- (8) Nabera, A.; Istrate, I.-R.; Martin, A. J.; Pérez-Ramírez, J.; Guillén-Gosálbez, G. Energy crisis in Europe enhances the sustainability of green chemicals. *Green Chem.* **2023**, *25*, 6603–6611.

## Bibliography

---

- (9) Guan, Y.; Yan, J.; Shan, Y.; Zhou, Y.; Hang, Y.; Li, R.; Liu, Y.; Liu, B.; Nie, Q.; Bruckner, B., et al. Burden of the global energy price crisis on households. *Nat. Energy* **2023**, *8*, 304–316.
- (10) Morales-Vidal, J.; García-Muelas, R.; Ortuño, M. A. Defects as catalytic sites for the oxygen evolution reaction in Earth-abundant MOF-74 revealed by DFT. *Catal. Sci. Technol.* **2021**, *11*, 1443–1450.
- (11) Seh, Z. W.; Kibsgaard, J.; Dickens, C. F.; Chorkendorff, I.; Nørskov, J. K.; Jaramillo, T. F. Combining theory and experiment in electrocatalysis: Insights into materials design. *Science* **2017**, *355*, eaad4998.
- (12) Suen, N.-T.; Hung, S.-F.; Quan, Q.; Zhang, N.; Xu, Y.-J.; Chen, H. M. Electrocatalysis for the oxygen evolution reaction: recent development and future perspectives. *Chem. Soc. Rev.* **2017**, *46*, 337–365.
- (13) Pinheiro Araújo, T.; Morales-Vidal, J.; Zou, T.; Agrachev, M.; Verstraeten, S.; Willi, P. O.; Grass, R. N.; Jeschke, G.; Mitchell, S.; López, N., et al. Design of Flame-Made ZnZrO<sub>x</sub> Catalysts for Sustainable Methanol Synthesis from CO<sub>2</sub>. *Advanced Energy Materials* **2023**, *13*, 2204122.
- (14) Frei, M. S.; Mondelli, C.; García-Muelas, R.; Morales-Vidal, J.; Philipp, M.; Safonova, O. V.; López, N.; Stewart, J. A.; Ferré, D. C.; Pérez-Ramírez, J. Nanostructure of nickel-promoted indium oxide catalysts drives selectivity in CO<sub>2</sub> hydrogenation. *Nat. Commun.* **2021**, *12*, 1960.
- (15) Pinheiro Araujo, T.; Morales-Vidal, J.; Zou, T.; García-Muelas, R.; Willi, P. O.; Engel, K. M.; Safonova, O. V.; Faust Akl, D.; Krumeich, F.; Grass, R. N., et al. Flame spray pyrolysis as a synthesis platform to assess metal promotion in In<sub>2</sub>O<sub>3</sub>-catalyzed CO<sub>2</sub> hydrogenation. *Adv. Energy Mater.* **2022**, *12*, 2103707.

- (16) Pinheiro Araujo, T.; Morales-Vidal, J.; Giannakakis, G.; Mondelli, C.; Eliasson, H.; Erni, R.; Stewart, J.; Mitchell, S.; Lopez, N.; Pérez-Ramírez, J. Reaction-Induced Metal-Metal Oxide Interactions in Pd-In<sub>2</sub>O<sub>3</sub>/ZrO<sub>2</sub> Catalysts Drive Selective and Stable CO<sub>2</sub> Hydrogenation to Methanol. *Angew. Chem. Int. Ed.*, e202306563.
- (17) González-Garay, A.; Frei, M. S.; Al-Qahtani, A.; Mondelli, C.; Guillén-Gosálbez, G.; Pérez-Ramírez, J. Plant-to-planet analysis of CO<sub>2</sub>-based methanol processes. *Energy Environ. Sci.* **2019**, *12*, 3425–3436.
- (18) Kondratenko, E. V.; Mul, G.; Baltrusaitis, J.; Larrazábal, G. O.; Pérez-Ramírez, J. Status and perspectives of CO<sub>2</sub> conversion into fuels and chemicals by catalytic, photocatalytic and electrocatalytic processes. *Energy Environ. Sci.* **2013**, *6*, 3112–3135.
- (19) Álvarez, A.; Borges, M.; Corral-Pérez, J. J.; Olcina, J. G.; Hu, L.; Cornu, D.; Huang, R.; Stoian, D.; Urakawa, A. CO<sub>2</sub> activation over catalytic surfaces. *ChemPhysChem* **2017**, *18*, 3135–3141.
- (20) Ali, K. A.; Abdullah, A. Z.; Mohamed, A. R. Recent development in catalytic technologies for methanol synthesis from renewable sources: A critical review. *Renew. Sust. Energ. Rev.* **2015**, *44*, 508–518.
- (21) Álvarez, A.; Bansode, A.; Urakawa, A.; Bavykina, A. V.; Wezendonk, T. A.; Makkee, M.; Gascon, J.; Kapteijn, F. Challenges in the greener production of formates/formic acid, methanol, and DME by heterogeneously catalyzed CO<sub>2</sub> hydrogenation processes. *Chem. Rev.* **2017**, *117*, 9804–9838.
- (22) Harris, K.; Grim, R. G.; Huang, Z.; Tao, L. A comparative techno-economic analysis of renewable methanol synthesis from biomass and CO<sub>2</sub>: Opportunities and barriers to commercialization. *Appl. Energy* **2021**, *303*, 117637.
- (23) Vo, C. H.; Mondelli, C.; Hamed, H.; Pérez-Ramírez, J.; Farooq, S.; Karimi, I. A. Sustainability assessment of thermocatalytic conversion of CO<sub>2</sub> to transportation fuels, methanol, and 1-propanol. *ACS Sustainable Chem. Eng.* **2021**, *9*, 10591–10600.

## Bibliography

---

- (24) Dieterich, V.; Buttler, A.; Hanel, A.; Spliethoff, H.; Fendt, S. Power-to-liquid via synthesis of methanol, DME or Fischer–Tropsch-fuels: a review. *Energy Environ. Sci.* **2020**, *13*, 3207–3252.
- (25) Lee, B.; Lee, H.; Lim, D.; Brigljević, B.; Cho, W.; Cho, H.-S.; Kim, C.-H.; Lim, H. Renewable methanol synthesis from renewable H<sub>2</sub> and captured CO<sub>2</sub>: How can power-to-liquid technology be economically feasible? *Appl. Energy* **2020**, *279*, 115827.
- (26) Zhong, J.; Yang, X.; Wu, Z.; Liang, B.; Huang, Y.; Zhang, T. State of the art and perspectives in heterogeneous catalysis of CO<sub>2</sub> hydrogenation to methanol. *Chem. Soc. Rev.* **2020**, *49*, 1385–1413.
- (27) Earth Overshoot Day, <https://www.overshootday.org>, Accessed: 2023-08-09.
- (28) Parmesan, C.; Yohe, G. A globally coherent fingerprint of climate change impacts across natural systems. *Nature* **2003**, *421*, 37–42.
- (29) Fischer, E. M.; Knutti, R. Anthropogenic contribution to global occurrence of heavy-precipitation and high-temperature extremes. *Nat. Clim. Change* **2015**, *5*, 560–564.
- (30) Moon, T.; Ahlstrøm, A.; Goelzer, H.; Lipscomb, W.; Nowicki, S. Rising oceans guaranteed: Arctic land ice loss and sea level rise. *Curr. Clim. Change Rep.* **2018**, *4*, 211–222.
- (31) Nunez, S.; Arets, E.; Alkemade, R.; Verwer, C.; Leemans, R. Assessing the impacts of climate change on biodiversity: is below 2° C enough? *Climatic Change* **2019**, *154*, 351–365.
- (32) Wan, X.; Jiang, G.; Yan, C.; He, F.; Wen, R.; Gu, J.; Li, X.; Ma, J.; Stenseth, N. C.; Zhang, Z. Historical records reveal the distinctive associations of human disturbance and extreme climate change with local extinction of mammals. *Proc. Natl. Acad. Sci. U.S.A.* **2019**, *116*, 19001–19008.
- (33) Lewis, N. S.; Nocera, D. G. Powering the planet: Chemical challenges in solar energy utilization. *Proc. Natl. Acad. Sci. U.S.A.* **2006**, *103*, 15729–15735.

- (34) Jiao, Y.; Zheng, Y.; Jaroniec, M.; Qiao, S. Z. Design of electrocatalysts for oxygen-and hydrogen-involving energy conversion reactions. *Chem. Soc. Rev.* **2015**, *44*, 2060–2086.
- (35) You, B.; Sun, Y. Innovative strategies for electrocatalytic water splitting. *Acc. Chem. Res.* **2018**, *51*, 1571–1580.
- (36) Luo, Y.; Zhang, Z.; Chhowalla, M.; Liu, B. Recent advances in design of electrocatalysts for high-current-density water splitting. *Adv. Mater.* **2022**, *34*, 2108133.
- (37) Turner, J. A. Sustainable hydrogen production. *Science* **2004**, *305*, 972–974.
- (38) Downes, C. A.; Marinescu, S. C. Electrocatalytic metal–organic frameworks for energy applications. *ChemSusChem* **2017**, *10*, 4374–4392.
- (39) Furukawa, H.; Cordova, K. E.; O’Keeffe, M.; Yaghi, O. M. The chemistry and applications of metal-organic frameworks. *Science* **2013**, *341*, 1230444.
- (40) Gagliardi, L.; Yaghi, O. M. The future directiond for metal-organic frameworks. *Chem. Mater* **2023**, *35*, 5711–5712.
- (41) Dissegna, S.; Epp, K.; Heinz, W. R.; Kieslich, G.; Fischer, R. A. Defective metal-organic frameworks. *Adv. Mater.* **2018**, *30*, 1704501.
- (42) Bennett, T. D.; Cheetham, A. K.; Fuchs, A. H.; Coudert, F.-X. Interplay between defects, disorder and flexibility in metal-organic frameworks. *Nat. Chem.* **2017**, *9*, 11–16.
- (43) Cliffe, M. J.; Wan, W.; Zou, X.; Chater, P. A.; Kleppe, A. K.; Tucker, M. G.; Wilhelm, H.; Funnell, N. P.; Coudert, F.-X.; Goodwin, A. L. Correlated defect nanoregions in a metal–organic framework. *Nat. Commun.* **2014**, *5*, 4176.
- (44) Sholl, D. S.; Lively, R. P. Defects in metal–organic frameworks: challenge or opportunity? *J. Phys. Chem. Lett.* **2015**, *6*, 3437–3444.
- (45) Cohen, S. M. The postsynthetic renaissance in porous solids. *J. Am. Chem. Soc.* **2017**, *139*, 2855–2863.



## Bibliography

---

- (46) Islamoglu, T.; Goswami, S.; Li, Z.; Howarth, A. J.; Farha, O. K.; Hupp, J. T. Postsynthetic tuning of metal–organic frameworks for targeted applications. *Acc. Chem. Res.* **2017**, *50*, 805–813.
- (47) Zhou, H.-C.; Long, J. R.; Yaghi, O. M. Introduction to metal–organic frameworks. *Chem. Rev.* **2012**, *112*, 673–674.
- (48) Hendon, C. H.; Rieth, A. J.; Korzynski, M. D.; Dinca, M. Grand challenges and future opportunities for metal–organic frameworks. *ACS Cent. Sci.* **2017**, *3*, 554–563.
- (49) Bavykina, A.; Kolobov, N.; Khan, I. S.; Bau, J. A.; Ramirez, A.; Gascon, J. Metal–organic frameworks in heterogeneous catalysis: recent progress, new trends, and future perspectives. *Chem. Rev.* **2020**, *120*, 8468–8535.
- (50) Wang, K.; Li, Y.; Xie, L.-H.; Li, X.; Li, J.-R. Construction and application of base-stable MOFs: a critical review. *Chem. Soc. Rev.* **2022**, *51*, 6417–6441.
- (51) Freund, R.; Zaremba, O.; Arnauts, G.; Ameloot, R.; Skorupskii, G.; Dincă, M.; Bavykina, A.; Gascon, J.; Ejsmont, A.; Goscianska, J., et al. The current status of MOF and COF applications. *Angew. Chem. Int. Ed.* **2021**, *60*, 23975–24001.
- (52) Jin, S. How to effectively utilize MOFs for electrocatalysis. *ACS Energy Lett.* **2019**, *4*, 1443–1445.
- (53) Radwan, A.; Jin, H.; He, D.; Mu, S. Design engineering, synthesis protocols, and energy applications of MOF-derived electrocatalysts. *Nano-Micro Lett.* **2021**, *13*, 1–32.
- (54) Wang, H.; Zhu, Q.-L.; Zou, R.; Xu, Q. Metal-organic frameworks for energy applications. *Chem* **2017**, *2*, 52–80.
- (55) Jiao, L.; Wang, Y.; Jiang, H.-L.; Xu, Q. Metal–organic frameworks as platforms for catalytic applications. *Adv. Mater.* **2018**, *30*, 1703663.
- (56) Sun, L.; Campbell, M. G.; Dincă, M. Electrically conductive porous metal–organic frameworks. *Angewandte Chemie International Edition* **2016**, *55*, 3566–3579.

- (57) Zhao, S.; Wang, Y.; Dong, J.; He, C.-T.; Yin, H.; An, P.; Zhao, K.; Zhang, X.; Gao, C.; Zhang, L., et al. Ultrathin metal–organic framework nanosheets for electrocatalytic oxygen evolution. *Nat. Ener.* **2016**, *1*, 1–10.
- (58) Duan, J.; Chen, S.; Zhao, C. Ultrathin metal-organic framework array for efficient electrocatalytic water splitting. *Nat. Commun* **2017**, *8*, 15341.
- (59) Wang, L.; Wu, Y.; Cao, R.; Ren, L.; Chen, M.; Feng, X.; Zhou, J.; Wang, B. Fe/Ni metal–organic frameworks and their binder-free thin films for efficient oxygen evolution with low overpotential. *ACS Appl. Mater. Interfaces* **2016**, *8*, 16736–16743.
- (60) Zhou, W.; Huang, D.-D.; Wu, Y.-P.; Zhao, J.; Wu, T.; Zhang, J.; Li, D.-S.; Sun, C.; Feng, P.; Bu, X. Stable hierarchical bimetal–organic nanostructures as highperformance electrocatalysts for the oxygen evolution reaction. *Angew. Chem. Int. Ed.* **2019**, *58*, 4227–4231.
- (61) Boyd, P. G.; Lee, Y.; Smit, B. Computational development of the nanoporous materials genome. *Nat. Rev. Mater.* **2017**, *2*, 1–15.
- (62) Moghadam, P. Z.; Li, A.; Wiggin, S. B.; Tao, A.; Maloney, A. G.; Wood, P. A.; Ward, S. C.; Fairen-Jimenez, D. Development of a Cambridge Structural Database subset: a collection of metal–organic frameworks for past, present, and future. *Chem. Mater.* **2017**, *29*, 2618–2625.
- (63) Chung, Y. G.; Camp, J.; Haranczyk, M.; Sikora, B. J.; Bury, W.; Krungleviciute, V.; Yildirim, T.; Farha, O. K.; Sholl, D. S.; Snurr, R. Q. Computation-ready, experimental metal–organic frameworks: A tool to enable high-throughput screening of nanoporous crystals. *Chem. Mater.* **2014**, *26*, 6185–6192.
- (64) Nazarian, D.; Camp, J. S.; Chung, Y. G.; Snurr, R. Q.; Sholl, D. S. Large-scale refinement of metal-organic framework structures using density functional theory. *Chem. Mater.* **2017**, *29*, 2521–2528.

## Bibliography

---

- (65) Chung, Y. G.; Haldoupis, E.; Bucior, B. J.; Haranczyk, M.; Lee, S.; Zhang, H.; Vogiatzis, K. D.; Milisavljevic, M.; Ling, S.; Camp, J. S., et al. Advances, updates, and analytics for the computation-ready, experimental metal–organic framework database: CoRE MOF 2019. *J. Chem. Eng. Data* **2019**, *64*, 5985–5998.
- (66) Bernales, V.; Ortuño, M. A.; Truhlar, D. G.; Cramer, C. J.; Gagliardi, L. Computational design of functionalized metal–organic framework nodes for catalysis. *ACS Cent. Sci.* **2018**, *4*, 5–19.
- (67) Odoh, S. O.; Cramer, C. J.; Truhlar, D. G.; Gagliardi, L. Quantum-chemical characterization of the properties and reactivities of metal–organic frameworks. *Chem. Rev* **2015**, *115*, 6051–6111.
- (68) Morales-Vidal, J.; Ortuño, M. A. In *Computer Simulation of Porous Materials*, 2021, pp 215–264.
- (69) Zhao, X.; Pattengale, B.; Fan, D.; Zou, Z.; Zhao, Y.; Du, J.; Huang, J.; Xu, C. Mixed-node metal–organic frameworks as efficient electrocatalysts for oxygen evolution reaction. *ACS Energy Lett.* **2018**, *3*, 2520–2526.
- (70) Erans, M.; Sanz-Pérez, E. S.; Hanak, D. P.; Clulow, Z.; Reiner, D. M.; Mutch, G. A. Direct air capture: process technology, techno-economic and socio-political challenges. *Energy Environ. Sci.* **2022**, *15*, 1360–1405.
- (71) United Nations Climate change, <https://unfccc.int/process-and-meetings/the-paris-agreement>, Accessed: 2023-08-14.
- (72) Yarulina, I.; Chowdhury, A. D.; Meirer, F.; Weckhuysen, B. M.; Gascon, J. Recent trends and fundamental insights in the methanol-to-hydrocarbons process. *Nat. Catal.* **2018**, *1*, 398–411.
- (73) IEA The Future of Petrochemicals, <https://www.iea.org/reports/the-future-of-petrochemicals>, Accessed: 2023-08-15.
- (74) Olah, G. A. Beyond oil and gas: the methanol economy. *Angew. Chem. Int. Ed.* **2005**, *44*, 2636–2639.

- (75) IRENA Innovation Outlook: Renewable Methanol, <https://www.irena.org/publications/2021/Jan/Innovation-Outlook-Renewable-Methanol>, Accessed: 2023-08-15.
- (76) Deka, T. J.; Osman, A. I.; Baruah, D. C.; Rooney, D. W. Methanol fuel production, utilization, and techno-economy: A review. *Environ. Chem. Lett.* **2022**, *20*, 3525–3554.
- (77) The Nobel Prize, <https://www.nobelprize.org/prizes/chemistry/2013/summary/>, Accessed: 2023-08-15.
- (78) Fernandez-Garcia, M; Martinez-Arias, A; Hanson, J.; Rodriguez, J. Nanostructured oxides in chemistry: characterization and properties. *Chem. Rev.* **2004**, *104*, 4063–4104.
- (79) Kaiser, S. K.; Chen, Z.; Faust Akl, D.; Mitchell, S.; Pérez-Ramírez, J. Single-atom catalysts across the periodic table. *Chem. Rev.* **2020**, *120*, 11703–11809.
- (80) Qi, P.; Wang, J.; Djitcheu, X.; He, D.; Liu, H.; Zhang, Q. Techniques for the characterization of single atom catalysts. *RSC Adv.* **2022**, *12*, 1216–1227.
- (81) Chang, C. C. Auger electron spectroscopy. *Surf. Sci.* **1971**, *25*, 53–79.
- (82) Jeschke, G. Electron paramagnetic resonance: recent developments and trends. *Curr. Opin. Soli. State Mater. Sci.* **2003**, *7*, 181–188.
- (83) Hurst, N. W.; Gentry, S. J.; Jones, A.; McNicol, B. D. Temperature programmed reduction. *Cat. Rev. Sci. Eng.* **1982**, *24*, 233–309.
- (84) Fierro, J. L.; Banda, J. F. G. D. L. Chemisorption of probe molecules on metal oxides. *Cat. Rev. Sci. Eng.* **1986**, *28*, 265–333.
- (85) Wilkinson, M. D.; Dumontier, M.; Aalbersberg, I. J.; Appleton, G.; Axton, M.; Baak, A.; Blomberg, N.; Boiten, J.-W.; da Silva Santos, L. B.; Bourne, P. E., et al. The FAIR Guiding Principles for scientific data management and stewardship. *Sci. Data* **2016**, *3*, 1–9.

## Bibliography

---

- (86) Álvarez-Moreno, M.; de Graaf, C.; Lopez, N.; Maseras, F.; Poblet, J. M.; Bo, C. Managing the computational chemistry big data problem: the ioChem-BD platform. *J. Chem. Inf. Model.* **2015**, *55*, 95–103.
- (87) Bo, C.; Maseras, F.; López, N. The role of computational results databases in accelerating the discovery of catalysts. *Nat. Catal.* **2018**, *1*, 809–810.
- (88) Carter, E. A. Challenges in modeling materials properties without experimental input. *Science* **2008**, *321*, 800–803.
- (89) Nørskov, J. K.; Rossmeisl, J.; Logadottir, A.; Lindqvist, L.; Kitchin, J. R.; Bligaard, T.; Jónsson, H. Origin of the overpotential for oxygen reduction at a fuel-cell cathode. *J. Phys. Chem. B.* **2004**, *108*, 17886–17892.
- (90) Giustino, F., *Materials modelling using density functional theory: properties and predictions*; Oxford University Press: 2014.
- (91) Schrödinger, E. An undulatory theory of the mechanics of atoms and molecules. *Phys. Rev.* **1926**, *28*, 1049.
- (92) Born, M.; Oppenheimer, R. Zur quantentheorie der molekeln. *Annalen der Physik* **1927**, *389*, 457–484.
- (93) Sholl, D. S.; Steckel, J. A., *Density functional theory: a practical introduction*; John Wiley & Sons: 2009.
- (94) Hohenberg, P.; Kohn, W. Inhomogeneous Electron Gas. *Phys. Rev.* **1964**, *136*, B864–B871.
- (95) Kohn, W.; Sham, L. J. Self-consistent equations including exchange and correlation effects. *Phys. Rev.* **1965**, *140*, A1133.
- (96) Bao, J. L.; Gagliardi, L.; Truhlar, D. G. Self-interaction error in density functional theory: An appraisal. *J. Phys. Chem. Lett.* **2018**, *9*, 2353–2358.
- (97) Cramer, C. J., *Essentials of computational chemistry: theories and models*; John Wiley & Sons: 2013.

- (98) López, N.; Almora-Barrios, N.; Carchini, G.; Błoński, P.; Bellarosa, L.; Garcia-Muelas, R.; Novell-Leruth, G.; Garcia-Mota, M. State-of-the-art and challenges in theoretical simulations of heterogeneous catalysis at the microscopic level. *Catal. Sci. Technol.* **2012**, *2*, 2405–2417.
- (99) Ceperley, D. M.; Alder, B. J. Ground state of the electron gas by a stochastic method. *Phys. Rev. Lett.* **1980**, *45*, 566.
- (100) Gunnarsson, O.; Lundqvist, B.; Wilkins, J. Contribution to the cohesive energy of simple metals: Spin-dependent effect. *Phys. Rev. B* **1974**, *10*, 1319.
- (101) Perdew, J. P.; Chevary, J. A.; Vosko, S. H.; Jackson, K. A.; Pederson, M. R.; Singh, D. J.; Fiolhais, C. Atoms, molecules, solids, and surfaces: Applications of the generalized gradient approximation for exchange and correlation. *Phys. Rev. B* **1992**, *46*, 6671–6687.
- (102) Becke, A. D. Density-functional exchange-energy approximation with correct asymptotic behavior. *Phys. Rev. A* **1988**, *38*, 3098.
- (103) Lee, C.; Yang, W.; Parr, R. G. Development of the Colle-Salvetti correlation-energy formula into a functional of the electron density. *Phys. Rev. B* **1988**, *37*, 785.
- (104) Perdew, J. P.; Wang, Y. Accurate and simple analytic representation of the electron-gas correlation energy. *Phys. Rev. B* **1992**, *45*, 13244–13249.
- (105) Hammer, B.; Hansen, L. B.; Nørskov, J. K. Improved adsorption energetics within density-functional theory using revised Perdew-Burke-Ernzerhof functionals. *Phys. Rev. B* **1999**, *59*, 7413.
- (106) Perdew, J. P.; Ruzsinszky, A.; Csonka, G. I.; Vydrov, O. A.; Scuseria, G. E.; Constantin, L. A.; Zhou, X.; Burke, K. Restoring the density-gradient expansion for exchange in solids and surfaces. *Phys. Rev. Lett.* **2008**, *100*, 136406.
- (107) Perdew, J. P.; Burke, K.; Ernzerhof, M. Generalized gradient approximation made simple. *Phys. Rev. Lett.* **1996**, *77*, 3865.

## Bibliography

---

- (108) Tao, J.; Perdew, J. P.; Staroverov, V. N.; Scuseria, G. E. Climbing the density functional ladder: Nonempirical meta-generalized gradient approximation designed for molecules and solids. *Phys. Rev. Lett.* **2003**, *91*, 146401.
- (109) Sun, J.; Remsing, R. C.; Zhang, Y.; Sun, Z.; Ruzsinszky, A.; Peng, H.; Yang, Z.; Paul, A.; Waghmare, U.; Wu, X., et al. Accurate first-principles structures and energies of diversely bonded systems from an efficient density functional. *Nat. Chem.* **2016**, *8*, 831–836.
- (110) Zhao, Y.; Truhlar, D. G. A new local density functional for main-group thermochemistry, transition metal bonding, thermochemical kinetics, and noncovalent interactions. *J. Chem. Phys.* **2006**, *125*, 194101.
- (111) Peverati, R.; Truhlar, D. G. Performance of the M11 and M11-L density functionals for calculations of electronic excitation energies by adiabatic time-dependent density functional theory. *Phys. Chem. Chem. Phys.* **2012**, *14*, 11363–11370.
- (112) Peverati, R.; Truhlar, D. G. M11-L: A local density functional that provides improved accuracy for electronic structure calculations in chemistry and physics. *J. Phys. Chem. Lett.* **2012**, *3*, 117–124.
- (113) Becke, A. D. Density-functional thermochemistry. III. The role of exact exchange. *J. Chem. Phys.* **1993**, *98*, 5648–6.
- (114) Perdew, J. P.; Ernzerhof, M.; Burke, K. Rationale for mixing exact exchange with density functional approximations. *J. Chem. Phys.* **1996**, *105*, 9982–9985.
- (115) Heyd, J.; Scuseria, G. E.; Ernzerhof, M. Hybrid functionals based on a screened Coulomb potential. *J. Chem. Phys.* **2003**, *118*, 8207–8215.
- (116) Heyd, J.; Scuseria, G. E. Efficient hybrid density functional calculations in solids: Assessment of the Heyd–Scuseria–Ernzerhof screened Coulomb hybrid functional. *J. Chem. Phys.* **2004**, *121*, 1187–1192.

- (117) Krukau, A. V.; Vydrov, O. A.; Izmaylov, A. F.; Scuseria, G. E. Influence of the exchange screening parameter on the performance of screened hybrid functionals. *J. Chem. Phys.* **2006**, *125*, 224106.
- (118) Hubbard, J. Electron correlations in narrow energy bands. II. The degenerate band case. *Proc. R. Soc. A: Math. Phys. Eng. Sci.* **1964**, *277*, 237–259.
- (119) Anisimov, V.; Gunnarsson, O. Density-functional calculation of effective Coulomb interactions in metals. *Phys. Rev. B* **1991**, *43*, 7570.
- (120) Anisimov, V. I.; Aryasetiawan, F.; Lichtenstein, A. First-principles calculations of the electronic structure and spectra of strongly correlated systems: the LDA+ U method. *J. Phys. Condens. Matter Nat. Chem.* **1997**, *9*, 767.
- (121) Dudarev, S. L.; Botton, G. A.; Savrasov, S. Y.; Humphreys, C.; Sutton, A. P. Electron-energy-loss spectra and the structural stability of nickel oxide: An LSDA+ U study. *Phys. Rev. B* **1998**, *57*, 1505.
- (122) Capdevila-Cortada, M.; Łodziana, Z.; López, N. Performance of DFT+ U approaches in the study of catalytic materials, 2016.
- (123) Kulik, H. J. Perspective: Treating electron over-delocalization with the DFT+ U method. *J. Chem. Phys.* **2015**, *142*, 240901.
- (124) Hu, Z.; Metiu, H. Choice of U for DFT+ U calculations for titanium oxides. *J. Phys. Chem. C* **2011**, *115*, 5841–5845.
- (125) Cococcioni, M.; De Gironcoli, S. Linear response approach to the calculation of the effective interaction parameters in the LDA+ U method. *Phys. Rev. B* **2005**, *71*, 035105.
- (126) Cococcioni, M. Accurate and efficient calculations on strongly correlated minerals with the LDA+ U method: review and perspectives. *Rev. Mineral. Geochem.* **2010**, *71*, 147–167.
- (127) Rosa, M.; Corni, S.; Di Felice, R. van der Waals effects at molecule-metal interfaces. *Phys. Rev. B* **2014**, *90*, 125448.



## Bibliography

---

- (128) Grimme, S. Accurate description of van der Waals complexes by density functional theory including empirical corrections. *J. Comput. Chem.* **2004**, *25*, 1463–1473.
- (129) Grimme, S. Semiempirical GGA-type density functional constructed with a long-range dispersion correction. *J. Comput. Chem.* **2006**, *27*, 1787–1799.
- (130) Grimme, S.; Antony, J.; Ehrlich, S.; Krieg, H. A consistent and accurate ab initio parametrization of density functional dispersion correction (DFT-D) for the 94 elements H-Pu. *J. Chem. Phys.* **2010**, *132*, 154104.
- (131) Grimme, S.; Ehrlich, S.; Goerigk, L. Effect of the damping function in dispersion corrected density functional theory. *J. Comput. Chem.* **2011**, *32*, 1456–1465.
- (132) Tkatchenko, A.; Scheffler, M. Accurate molecular van der Waals interactions from ground-state electron density and free-atom reference data. *Phys. Rev. Lett.* **2009**, *102*, 073005.
- (133) Bloch, F. Über die quantenmechanik der elektronen in kristallgittern. *Z. Phys.* **1929**, *52*, 555–600.
- (134) Monkhorst, H. J.; Pack, J. D. Special points for Brillouin-zone integrations. *Phys. Rev. B* **1976**, *13*, 5188.
- (135) Payne, M. C.; Teter, M. P.; Allan, D. C.; Arias, T.; Joannopoulos, a. J. Iterative minimization techniques for ab initio total-energy calculations: molecular dynamics and conjugate gradients. *Rev. Mod. Phys.* **1992**, *64*, 1045.
- (136) Vanderbilt, D. Soft self-consistent pseudopotentials in a generalized eigenvalue formalism. *Phys. Rev. B* **1990**, *41*, 7892.
- (137) Blöchl, P. E. Projector augmented-wave method. *Phys. Rev. B* **1994**, *50*, 17953.
- (138) Kresse, G.; Joubert, D. From ultrasoft pseudopotentials to the projector augmented-wave method. *Phys. Rev. B* **1999**, *59*, 1758.

- (139) Jónsson, H.; Mills, G.; Jacobsen, K. W. In *Classical and quantum dynamics in condensed phase simulations*; World Scientific: 1998, pp 385–404.
- (140) Henkelman, G.; Jónsson, H. Improved tangent estimate in the nudged elastic band method for finding minimum energy paths and saddle points. *J. Chem. Phys.* **2000**, *113*, 9978–9985.
- (141) Henkelman, G.; Uberuaga, B. P.; Jónsson, H. A climbing image nudged elastic band method for finding saddle points and minimum energy paths. *J. Chem. Phys.* **2000**, *113*, 9901–9904.
- (142) David, R. L. et al., *Handbook of chemistry and physics*; CRC Press: 2003.
- (143) Dattila, F.; Seemakurthi, R. R.; Zhou, Y.; López, N. Modeling operando electrochemical CO<sub>2</sub> reduction. *Chem. Rev* **2022**, *122*, 11085–11130.
- (144) Sun, F.; Tang, Q.; Jiang, D.-e. Theoretical Advances in Understanding and Designing the Active Sites for Hydrogen Evolution Reaction. *ACS Catal.* **2022**, *12*, 8404–8433.
- (145) Soriano-Lopez, J.; Schmitt, W.; Garcia-Melchor, M. Computational modelling of water oxidation catalysts. *Curr. Opin. Electrochem.* **2018**, *7*, 22–30.
- (146) Garcia-Ratés, M.; López, N. Multigrid-based methodology for implicit solvation models in periodic DFT. *J. Chem. Theory Comput.* **2016**, *12*, 1331–1341.
- (147) Kresse, G.; Furthmüller, J. Efficiency of ab-initio total energy calculations for metals and semiconductors using a plane-wave basis set. *Comput. Mater. Sci.* **1996**, *6*, 15–50.
- (148) Kresse, G.; Furthmüller, J. Efficient iterative schemes for ab initio total-energy calculations using a plane-wave basis set. *Phys. Rev. B* **1996**, *54*, 11169.
- (149) Makov, G; Payne, M. Periodic boundary conditions in ab initio calculations. *Phys. Rev. B* **1995**, *51*, 4014.

## Bibliography

---

- (150) McCrory, C. C.; Jung, S.; Ferrer, I. M.; Chatman, S. M.; Peters, J. C.; Jaramillo, T. F. Benchmarking hydrogen evolving reaction and oxygen evolving reaction electrocatalysts for solar water splitting devices. *J. Am. Chem. Soc.* **2015**, *137*, 4347–4357.
- (151) Shen, J.-Q.; Liao, P.-Q.; Zhou, D.-D.; He, C.-T.; Wu, J.-X.; Zhang, W.-X.; Zhang, J.-P.; Chen, X.-M. Modular and stepwise synthesis of a hybrid metal–organic framework for efficient electrocatalytic oxygen evolution. *J. Am. Chem. Soc.* **2017**, *139*, 1778–1781.
- (152) Xue, Z.; Li, Y.; Zhang, Y.; Geng, W.; Jia, B.; Tang, J.; Bao, S.; Wang, H.-P.; Fan, Y.; Wei, Z.-w., et al. Modulating electronic structure of metal-organic framework for efficient electrocatalytic oxygen evolution. *Adv. Energy Mater.* **2018**, *8*, 1801564.
- (153) Wang, X.-L.; Dong, L.-Z.; Qiao, M.; Tang, Y.-J.; Liu, J.; Li, Y.; Li, S.-L.; Su, J.-X.; Lan, Y.-Q. Exploring the performance improvement of the oxygen evolution reaction in a stable bimetal–organic framework system. *Angew. Chem. Int. Ed.* **2018**, *57*, 9660–9664.
- (154) Chen, H.; Ouyang, S.; Zhao, M.; Li, Y.; Ye, J. Synergistic activity of Co and Fe in amorphous Co<sub>x</sub>–Fe–B catalyst for efficient oxygen evolution reaction. *ACS Appl. Mater. Interfaces* **2017**, *9*, 40333–40343.
- (155) Gao, J.; Cong, J.; Wu, Y.; Sun, L.; Yao, J.; Chen, B. Bimetallic hofmann-type metal–organic framework nanoparticles for efficient electrocatalysis of oxygen evolution reaction. *ACS Appl. Energy Mater.* **2018**, *1*, 5140–5144.
- (156) Yang, C.; Cai, W.-J.; Yu, B.-B.; Qiu, H.; Li, M.-L.; Zhu, L.-W.; Yan, Z.; Hou, L.; Wang, Y.-Y. Performance enhancement of oxygen evolution reaction through incorporating bimetallic electrocatalysts in two-dimensional metal–organic frameworks. *Catal. Sci. Technol.* **2020**, *10*, 3897–3903.

- (157) Zhang, P.; Yang, X.; Gao, W.; Hou, X.; Mi, J.; Liu, L.; Huang, J.; Dong, M.; Stampfl, C. First-principles design of bifunctional oxygen reduction and evolution catalysts through bimetallic centers in metal-organic frameworks. *Catal. Sci. Technol.* **2018**, *8*, 3666–3674.
- (158) Dietzel, P. D.; Morita, Y.; Blom, R.; Fjellvåg, H. An in situ high-temperature single-crystal investigation of a dehydrated metal-organic framework compound and field-induced magnetization of one-dimensional metal-oxygen chains. *Angew. Chem. Int. Ed.* **2005**, *117*, 6512–6516.
- (159) Rosi, N. L.; Kim, J.; Eddaoudi, M.; Chen, B.; O’Keeffe, M.; Yaghi, O. M. Rod packings and metal-organic frameworks constructed from rod-shaped secondary building units. *J. Am. Chem. Soc.* **2005**, *127*, 1504–1518.
- (160) Mann, G. W.; Lee, K.; Cococcioni, M.; Smit, B.; Neaton, J. B. First-principles Hubbard U approach for small molecule binding in metal-organic frameworks. *J. Chem. Phys.* **2016**, *144*, 174104.
- (161) Tripković, V.; Skúlason, E.; Siahrostami, S.; Nørskov, J. K.; Rossmeisl, J. The oxygen reduction reaction mechanism on Pt (1 1 1) from density functional theory calculations. *Electrochim. Acta* **2010**, *55*, 7975–7981.
- (162) Man, I. C.; Su, H.-Y.; Calle-Vallejo, F.; Hansen, H. A.; Martínez, J. I.; Inoglu, N. G.; Kitchin, J.; Jaramillo, T. F.; Nørskov, J. K.; Rossmeisl, J. Universality in oxygen evolution electrocatalysis on oxide surfaces. *ChemCatChem* **2011**, *3*, 1159–1165.
- (163) Verma, P.; Xu, X.; Truhlar, D. G. Adsorption on Fe-MOF-74 for C1–C3 hydrocarbon separation. *J. Phys. Chem. C* **2013**, *117*, 12648–12660.
- (164) Craig, M. J.; Coulter, G.; Dolan, E.; Soriano-López, J.; Mates-Torres, E.; Schmitt, W.; García-Melchor, M. Universal scaling relations for the rational design of molecular water oxidation catalysts with near-zero overpotential. *Nat. Commun.* **2019**, *10*, 4993.

## Bibliography

---

- (165) Rowan, A. D.; Patterson, C. H.; Gasparov, L. Hybrid density functional theory applied to magnetite: Crystal structure, charge order, and phonons. *Phys. Rev. B* **2009**, *79*, 205103.
- (166) Noh, J.; Osman, O. I.; Aziz, S. G.; Winget, P.; Brédas, J.-L. A density functional theory investigation of the electronic structure and spin moments of magnetite. *Sci. Technol. Adv. Mater* **2014**, *15*, 044202.
- (167) Hegner, F. S.; Herraiz-Cardona, I.; Cardenas-Morcoso, D.; López, N.; Galán-Mascarós, J.-R.; Gimenez, S. Cobalt hexacyanoferrate on BiVO<sub>4</sub> photoanodes for robust water splitting. *ACS Appl. Mater. Interfaces* **2017**, *9*, 37671–37681.
- (168) Frisch, M. J. et al. Gaussian09 Revision E.01, Gaussian Inc. Wallingford CT 2009.
- (169) Hegner, F. S.; Cardenas-Morcoso, D.; Giménez, S.; López, N.; Galan-Mascaros, J. R. Level alignment as descriptor for semiconductor/catalyst systems in water splitting: the case of hematite/cobalt hexacyanoferrate photoanodes. *ChemSusChem* **2017**, *10*, 4552–4560.
- (170) Reiher, M.; Salomon, O.; Artur Hess, B. Reparameterization of hybrid functionals based on energy differences of states of different multiplicity. *Theor. Chem. Acc.* **2001**, *107*, 48–55.
- (171) Hariharan, P. C.; Pople, J. A. The influence of polarization functions on molecular orbital hydrogenation energies. *Theoret. Chim. Acta* **1973**, *28*, 213–222.
- (172) Hehre, W. J.; Lathan, W. A. Self-Consistent Molecular Orbital Methods. XIV. An Extended Gaussian-Type Basis for Molecular Orbital Studies of Organic Molecules. Inclusion of Second Row Elements. *J. Chem. Phys.* **1972**, *56*, 5255–5257.

- (173) Ditchfield, R.; Hehre, W. J.; Pople, J. A. Self-consistent molecular-orbital methods. IX. An extended Gaussian-type basis for molecular-orbital studies of organic molecules. *J. Chem. Phys.* **1971**, *54*, 724–728.
- (174) Dolg, M; Wedig, U; Stoll, H; Preuss, H Energy-adjusted abinitio pseudopotentials for the first row transition elements. *J. Chem. Phys.* **1987**, *86*, 866–872.
- (175) Marenich, A. V.; Cramer, C. J.; Truhlar, D. G. Universal solvation model based on solute electron density and on a continuum model of the solvent defined by the bulk dielectric constant and atomic surface tensions. *J. Phys. Chem. B* **2009**, *113*, 6378–6396.
- (176) Bloch, E. D.; Queen, W. L.; Krishna, R.; Zadrozny, J. M.; Brown, C. M.; Long, J. R. Hydrocarbon separations in a metal-organic framework with open iron (II) coordination sites. *Science* **2012**, *335*, 1606–1610.
- (177) Maurice, R.; Verma, P.; Zadrozny, J. M.; Luo, S.; Borycz, J.; Long, J. R.; Truhlar, D. G.; Gagliardi, L. Single-ion magnetic anisotropy and isotropic magnetic couplings in the metal-organic framework Fe<sub>2</sub> (dobdc). *Inorg. Chem.* **2013**, *52*, 9379–9389.
- (178) Canepa, P.; Chabal, Y. J.; Thonhauser, T. When metal organic frameworks turn into linear magnets. *Phys. Rev. B* **2013**, *87*, 094407.
- (179) De Oliveira, A.; de Lima, G. F.; De Abreu, H. A. Structural and electronic properties of M-MOF-74 (M= Mg, Co or Mn). *Chem. Phys. Lett.* **2018**, *691*, 283–290.
- (180) Xiao, D. J.; Bloch, E. D.; Mason, J. A.; Queen, W. L.; Hudson, M. R.; Planas, N.; Borycz, J.; Dzubak, A. L.; Verma, P.; Lee, K., et al. Oxidation of ethane to ethanol by N<sub>2</sub>O in a metal-organic framework with coordinatively unsaturated iron (II) sites. *Nat. Chem.* **2014**, *6*, 590–595.

## Bibliography

---

- (181) Verma, P.; Vogiatzis, K. D.; Planas, N.; Borycz, J.; Xiao, D. J.; Long, J. R.; Gagliardi, L.; Truhlar, D. G. Mechanism of oxidation of ethane to ethanol at Iron (IV)–oxo sites in magnesium-diluted Fe<sub>2</sub>(dobdc). *J. Am. Chem. Soc.* **2015**, *137*, 5770–5781.
- (182) Koper, M. T. Thermodynamic theory of multi-electron transfer reactions: Implications for electrocatalysis. *J. Electroanal. Chem.* **2011**, *660*, 254–260.
- (183) Busch, M.; Fabrizio, A.; Lubner, S.; Hutter, J.; Corminboeuf, C. Exploring the limitation of molecular water oxidation catalysts. *J. Phys. Chem. C* **2018**, *122*, 12404–12412.
- (184) Tao, L.; Lin, C.-Y.; Dou, S.; Feng, S.; Chen, D.; Liu, D.; Huo, J.; Xia, Z.; Wang, S. Creating coordinatively unsaturated metal sites in metal-organic-frameworks as efficient electrocatalysts for the oxygen evolution reaction: Insights into the active centers. *Nano Energy* **2017**, *41*, 417–425.
- (185) Xue, Z.; Liu, K.; Liu, Q.; Li, Y.; Li, M.; Su, C.-Y.; Ogiwara, N.; Kobayashi, H.; Kitagawa, H.; Liu, M., et al. Missing-linker metal-organic frameworks for oxygen evolution reaction. *Nat. Commun.* **2019**, *10*, 5048.
- (186) Leus, K.; Vandichel, M.; Liu, Y.-Y.; Muylaert, I.; Musschoot, J.; Pyl, S.; Vrielinck, H.; Callens, F.; Marin, G. B.; Detavernier, C., et al. The coordinatively saturated vanadium MIL-47 as a low leaching heterogeneous catalyst in the oxidation of cyclohexene. *J. Catal.* **2012**, *285*, 196–207.
- (187) Vandichel, M.; Biswas, S.; Leus, K.; Paier, J.; Sauer, J.; Verstraelen, T.; Van Der Voort, P.; Waroquier, M.; Van Speybroeck, V. Catalytic Performance of Vanadium MIL-47 and Linker-Substituted Variants in the Oxidation of Cyclohexene: A Combined Theoretical and Experimental Approach. *ChemPlusChem* **2014**, *79*, 1183–1197.
- (188) Svane, K. L.; Bristow, J. K.; Gale, J. D.; Walsh, A. Vacancy defect configurations in the metal–organic framework UiO-66: energetics and electronic structure. *J. Mater. Chem. A* **2018**, *6*, 8507–8513.

- (189) Rosen, A. S.; Notestein, J. M.; Snurr, R. Q. Structure–activity relationships that identify metal–organic framework catalysts for methane activation. *ACS Catal.* **2019**, *9*, 3576–3587.
- (190) He, Y.; Liu, X.; Chen, G.; Pan, J.; Yan, A.; Li, A.; Lu, X.; Tang, D.; Zhang, N.; Qiu, T., et al. Synthesis of Co (II)-Fe (III) hydroxide nanocones with mixed octahedral/tetrahedral coordination toward efficient electrocatalysis. *Chem. Mater.* **2020**, *32*, 4232–4240.
- (191) Frei, M. S.; Mondelli, C.; García-Muelas, R.; Kley, K. S.; Puértolas, B.; López, N.; Safonova, O. V.; Stewart, J. A.; Curulla Ferré, D.; Pérez-Ramírez, J. Atomic-scale engineering of indium oxide promotion by palladium for methanol production via CO<sub>2</sub> hydrogenation. *Nat. Commun.* **2019**, *10*, 3377.
- (192) Sun, K.; Rui, N.; Zhang, Z.; Sun, Z.; Ge, Q.; Liu, C.-J. A highly active Pt/In<sub>2</sub>O<sub>3</sub> catalyst for CO<sub>2</sub> hydrogenation to methanol with enhanced stability. *Green Chem.* **2020**, *22*, 5059–5066.
- (193) Shen, C.; Sun, K.; Zhang, Z.; Rui, N.; Jia, X.; Mei, D.; Liu, C.-j. Highly active Ir/In<sub>2</sub>O<sub>3</sub> catalysts for selective hydrogenation of CO<sub>2</sub> to methanol: experimental and theoretical studies. *ACS Catal.* **2021**, *11*, 4036–4046.
- (194) Wang, J.; Sun, K.; Jia, X.; Liu, C.-j. CO<sub>2</sub> hydrogenation to methanol over Rh/In<sub>2</sub>O<sub>3</sub> catalyst. *Catal. Today* **2021**, *365*, 341–347.
- (195) Sun, K.; Zhang, Z.; Shen, C.; Rui, N.; Liu, C.-j. The feasibility study of the indium oxide supported silver catalyst for selective hydrogenation of CO<sub>2</sub> to methanol. *Green Energy Environ.* **2022**, *7*, 807–817.
- (196) Wu, Q.; Shen, C.; Rui, N.; Sun, K.; Liu, C.-J. Experimental and theoretical studies of CO<sub>2</sub> hydrogenation to methanol on Ru/In<sub>2</sub>O<sub>3</sub>. *J. CO<sub>2</sub> Util.* **2021**, *53*, 101720.



## Bibliography

---

- (197) Rui, N.; Zhang, F.; Sun, K.; Liu, Z.; Xu, W.; Stavitski, E.; Senanayake, S. D.; Rodriguez, J. A.; Liu, C.-J. Hydrogenation of CO<sub>2</sub> to Methanol on a Au<sup>δ+</sup>-In<sub>2</sub>O<sub>3-x</sub> Catalyst. *ACS Catal.* **2020**, *10*, 11307–11317.
- (198) Bavykina, A.; Yarulina, I.; Al Abdulghani, A. J.; Gevers, L.; Hedhili, M. N.; Miao, X.; Galilea, A. R.; Pustovarenko, A.; Dikhtiarenko, A.; Cadiau, A., et al. Turning a methanation Co catalyst into an In–Co methanol producer. *ACS Catal.* **2019**, *9*, 6910–6918.
- (199) Wang, J.; Li, G.; Li, Z.; Tang, C.; Feng, Z.; An, H.; Liu, H.; Liu, T.; Li, C. A highly selective and stable ZnO-ZrO<sub>2</sub> solid solution catalyst for CO<sub>2</sub> hydrogenation to methanol. *Sci. Adv.* **2017**, *3*, e1701290.
- (200) Li, K.; Chen, J. G. CO<sub>2</sub> hydrogenation to methanol over ZrO<sub>2</sub>-containing catalysts: insights into ZrO<sub>2</sub> induced synergy. *ACS Catal.* **2019**, *9*, 7840–7861.
- (201) Han, Z.; Tang, C.; Sha, F.; Tang, S.; Wang, J.; Li, C. CO<sub>2</sub> hydrogenation to methanol on ZnO-ZrO<sub>2</sub> solid solution catalysts with ordered mesoporous structure. *J. Catal.* **2021**, *396*, 242–250.
- (202) Wang, J.; Tang, C.; Li, G.; Han, Z.; Li, Z.; Liu, H.; Cheng, F.; Li, C. High-performance MaZrO<sub>x</sub> (Ma= Cd, Ga) solid-solution catalysts for CO<sub>2</sub> hydrogenation to methanol. *ACS Catal.* **2019**, *9*, 10253–10259.
- (203) Lee, K.; Anjum, U.; Araújo, T. P.; Mondelli, C.; He, Q.; Furukawa, S.; Pérez-Ramírez, J.; Kozlov, S. M.; Yan, N. Atomic Pd-promoted ZnZrOx solid solution catalyst for CO<sub>2</sub> hydrogenation to methanol. *Appl. Catal. B* **2022**, *304*, 120994.
- (204) Frei, M. S.; Capdevila-Cortada, M.; García-Muelas, R.; Mondelli, C.; López, N.; Stewart, J. A.; Ferré, D. C.; Pérez-Ramírez, J. Mechanism and microkinetics of methanol synthesis via CO<sub>2</sub> hydrogenation on indium oxide. *J. Catal.* **2018**, *361*, 313–321.

- (205) Rui, N.; Sun, K.; Shen, C.; Liu, C.-J. Density functional theoretical study of Au<sub>4</sub>/In<sub>2</sub>O<sub>3</sub> catalyst for CO<sub>2</sub> hydrogenation to methanol: The strong metal-support interaction and its effect. *J. CO<sub>2</sub> Util.* **2020**, *42*, 101313.
- (206) Posada-Borbon, A.; Gronbeck, H. A first-principles-based microkinetic study of CO<sub>2</sub> reduction to CH<sub>3</sub>OH over In<sub>2</sub>O<sub>3</sub>(110). *ACS Catal.* **2021**, *11*, 9996–10006.
- (207) Ding, J.; Li, Z.; Xiong, W.; Zhang, Y.; Ye, A.; Huang, W. Structural evolution and catalytic performance in CO<sub>2</sub> hydrogenation reaction of ZnO-ZrO<sub>2</sub> composite oxides. *Appl. Surf. Sci.* **2022**, *587*, 152884.
- (208) Frei, M. S.; Mondelli, C.; Cesarini, A.; Krumeich, F.; Hauert, R.; Stewart, J. A.; Curulla Ferré, D.; Pérez-Ramírez, J. Role of zirconia in indium oxide-catalyzed CO<sub>2</sub> hydrogenation to methanol. *ACS Catalysis* **2019**, *10*, 1133–1145.
- (209) Bachiller-Baeza, B.; Rodriguez-Ramos, I.; Guerrero-Ruiz, A. Interaction of carbon dioxide with the surface of zirconia polymorphs. *Langmuir* **1998**, *14*, 3556–3564.
- (210) Araújo, T. P.; Mondelli, C.; Agrachev, M.; Zou, T.; Willi, P. O.; Engel, K. M.; Grass, R. N.; Stark, W. J.; Safonova, O. V.; Jeschke, G., et al. Flame-made ternary Pd-In<sub>2</sub>O<sub>3</sub>-ZrO<sub>2</sub> catalyst with enhanced oxygen vacancy generation for CO<sub>2</sub> hydrogenation to methanol. *Nat. Commun.* **2022**, *13*, 5610.
- (211) Teoh, W. Y.; Amal, R.; Mädler, L. Flame spray pyrolysis: An enabling technology for nanoparticles design and fabrication. *Nanoscale* **2010**, *2*, 1324–1347.
- (212) Athanassiou, E. K.; Grass, R. N.; Stark, W. J. Chemical aerosol engineering as a novel tool for material science: from oxides to salt and metal nanoparticles. *Aerosol Sci. Technol.* **2010**, *44*, 161–172.
- (213) Koirala, R.; Pratsinis, S. E.; Baiker, A. Synthesis of catalytic materials in flames: opportunities and challenges. *Chem. Soc. Rev.* **2016**, *45*, 3053–3068.

## Bibliography

---

- (214) Mädler, L.; Kammler, H. K.; Mueller, R.; Pratsinis, S. E. Controlled synthesis of nanostructured particles by flame spray pyrolysis. *J. Aerosol Sci.* **2002**, *33*, 369–389.
- (215) Rudin, T.; Wegner, K.; Pratsinis, S. E. Uniform nanoparticles by flame-assisted spray pyrolysis (FASP) of low cost precursors. *J. Nanoparticle Res.* **2011**, *13*, 2715–2725.
- (216) Pokhrel, S.; Mädler, L. Flame-made particles for sensors, catalysis, and energy storage applications. *Energy Fuels* **2020**, *34*, 13209–13224.
- (217) Ding, S.; Chen, H.-A.; Mekasuwandumrong, O.; Hülsey, M. J.; Fu, X.; He, Q.; Panpranot, J.; Yang, C.-M.; Yan, N. High-temperature flame spray pyrolysis induced stabilization of Pt single-atom catalysts. *Appl. Catal. B* **2021**, *281*, 119471.
- (218) Kudoh, Y.; Takeda, H.; Arashi, H. In situ determination of crystal structure for high pressure phase of ZrO<sub>2</sub> using a diamond anvil and single crystal X-ray diffraction method. *Phys. Chem. Miner.* **1986**, *13*, 233–237.
- (219) Xue, Z. Q.; Guo, Y. Q. Carbonization effect on phase structures of zirconium oxides with 2-3 percent yttrium. *Adv. Mater.* **2014**, *936*, 181–186.
- (220) Bondars, B.; Heidemane, G.; Grabis, J.; Laschke, K.; Boysen, H.; Schneider, J.; Frey, F. Powder diffraction investigations of plasma sprayed zirconia. *J. Mater. Sci.* **1995**, *30*, 1621–1625.
- (221) Liang, Z.; Wang, W.; Zhang, M.; Wu, F.; Chen, J.-F.; Xue, C.; Zhao, H. Structural, mechanical and thermodynamic properties of ZrO<sub>2</sub> polymorphs by first-principles calculation. *Phys. B* **2017**, *511*, 10–19.
- (222) Ricca, C.; Ringuedé, A.; Cassir, M.; Adamo, C.; Labat, F. A comprehensive DFT investigation of bulk and low-index surfaces of ZrO<sub>2</sub> polymorphs. *J. Comput. Chem.* **2015**, *36*, 9–21.

- (223) Christensen, A.; Carter, E. A. First-principles study of the surfaces of zirconia. *Phys. Rev. B* **1998**, *58*, 8050.
- (224) Lange, F. Transformation-toughened ZrO<sub>2</sub>: correlations between grain size control and composition in the system ZrO<sub>2</sub>-Y<sub>2</sub>O<sub>3</sub>. *J. Am. Ceram. Soc.* **1986**, *69*, 240–242.
- (225) Kouva, S.; Andersin, J.; Honkala, K.; Lehtonen, J.; Lefferts, L.; Kanervo, J. Water and carbon oxides on monoclinic zirconia: experimental and computational insights. *Phys. Chem. Chem. Phys.* **2014**, *16*, 20650–20664.
- (226) Martin, O.; Martín, A. J.; Mondelli, C.; Mitchell, S.; Segawa, T. F.; Hauert, R.; Drouilly, C.; Curulla-Ferré, D.; Pérez-Ramírez, J. Indium oxide as a superior catalyst for methanol synthesis by CO<sub>2</sub> hydrogenation. *Angew. Chem. Int. Ed.* **2016**, *55*, 6261–6265.
- (227) Albani, D.; Capdevila-Cortada, M.; Vilé, G.; Mitchell, S.; Martin, O.; López, N.; Pérez-Ramírez, J. Semihydrogenation of Acetylene on Indium Oxide: Proposed Single-Ensemble Catalysis. *Angew. Chem. Int. Ed.* **2017**, *56*, 10755–10760.
- (228) Walsh, A.; Catlow, C. R. A. Structure, stability and work functions of the low index surfaces of pure indium oxide and Sn-doped indium oxide (ITO) from density functional theory. *J. Mater. Chem.* **2010**, *20*, 10438–10444.
- (229) Posada-Borbon, A.; Grönbeck, H. Hydrogen adsorption on In<sub>2</sub>O<sub>3</sub>(111) and chIn<sub>2</sub>O<sub>3</sub>(110). *Phys. Chem. Chem. Phys.* **2020**, *22*, 16193–16202.
- (230) Snider, J. L.; Streibel, V.; Hubert, M. A.; Choksi, T. S.; Valle, E.; Upham, D. C.; Schumann, J.; Duyar, M. S.; Gallo, A.; Abild-Pedersen, F., et al. Revealing the synergy between oxide and alloy phases on the performance of bimetallic In–Pd catalysts for CO<sub>2</sub> hydrogenation to methanol. *ACS Catal.* **2019**, *9*, 3399–3412.

## Bibliography

---

- (231) Rui, N.; Wang, Z.; Sun, K.; Ye, J.; Ge, Q.; Liu, C.-j. CO<sub>2</sub> hydrogenation to methanol over Pd/In<sub>2</sub>O<sub>3</sub>: effects of Pd and oxygen vacancy. *App. Catal. B* **2017**, *218*, 488–497.
- (232) Zhang, X.; Kirilin, A. V.; Rozeveld, S.; Kang, J. H.; Pollefeyt, G.; Yancey, D. F.; Chojecki, A.; Vanchura, B.; Blum, M. Support Effect and Surface Reconstruction in In<sub>2</sub>O<sub>3</sub>/m-ZrO<sub>2</sub> Catalyzed CO<sub>2</sub> Hydrogenation. *ACS Catal.* **2022**, *12*, 3868–3880.
- (233) Tauster, S. Strong metal-support interactions. *Acc. Chem. Res.* **1987**, *20*, 389–394.
- (234) Van Deelen, T. W.; Hernández Mejía, C.; de Jong, K. P. Control of metal-support interactions in heterogeneous catalysts to enhance activity and selectivity. *Nat. Catal.* **2019**, *2*, 955–970.
- (235) Niu, Y.; Liu, X.; Wang, Y.; Zhou, S.; Lv, Z.; Zhang, L.; Shi, W.; Li, Y.; Zhang, W.; Su, D. S., et al. Visualizing formation of intermetallic PdZn in a palladium/zinc oxide catalyst: Interfacial fertilization by PdHx. *Angew. Chem. Int. Ed.* **2019**, *58*, 4232–4237.
- (236) Pu, T.; Zhang, W.; Zhu, M. Engineering heterogeneous catalysis with strong metal–support interactions: Characterization, theory and manipulation. *Angew. Chem. Int. Ed.* **2023**, *62*, e202212278.
- (237) Rui, N.; Wang, X.; Deng, K.; Moncada, J.; Rosales, R.; Zhang, F.; Xu, W.; Waluyo, I.; Hunt, A.; Stavitski, E., et al. Atomic Structural Origin of the High Methanol Selectivity over In<sub>2</sub>O<sub>3</sub>–Metal Interfaces: Metal–Support Interactions and the Formation of a InOx Overlayer in Ru/In<sub>2</sub>O<sub>3</sub> Catalysts during CO<sub>2</sub> Hydrogenation. *ACS Catal.* **2023**, *13*, 3187–3200.
- (238) Matsubu, J. C.; Zhang, S.; DeRita, L.; Marinkovic, N. S.; Chen, J. G.; Graham, G. W.; Pan, X.; Christopher, P. Adsorbate-mediated strong metal–support interactions in oxide-supported Rh catalysts. *Nat. Chem.* **2017**, *9*, 120–127.
- (239) Urakawa, A. Mind the gaps in CO<sub>2</sub>-to-methanol. *Nat. Catal.* **2021**, *4*, 447–448.

- (240) Prins, R. Hydrogen spillover. Facts and fiction. *Chem. Rev.* **2012**, *112*, 2714–2738.
- (241) Kamada, T.; Ueda, T.; Fukuura, S.; Yumura, T.; Hosokawa, S.; Tanaka, T.; Kan, D.; Shimakawa, Y. Ultralong Distance Hydrogen Spillover Enabled by Valence Changes in a Metal Oxide Surface. *J. Am. Chem. Soc.* **2023**, *145*, 1631–1637.
- (242) Kauppinen, M.; Grönbeck, H. Hydrogen Adsorption on Pd–In Intermetallic Surfaces. *Top. Catal.* **2022**, 1–8.
- (243) García-Muelas, R.; López, N. Statistical learning goes beyond the d-band model providing the thermochemistry of adsorbates on transition metals. *Nat. Commun.* **2019**, *10*, 4687.

## *Bibliography*

---

# Publications



This document is the Accepted Manuscript version of a Published Work that appeared in final form in *Catal. Sci. Technol.*, copyright © The Royal Society of Chemistry 2017 after peer review and technical editing by the publisher. To access the final edited and published work see: <https://doi.org/10.1039/D0CY02163F>

## Defects as catalytic sites for the oxygen evolution reaction in Earth-abundant MOF-74 revealed by DFT†

Jordi Morales-Vidal,<sup>id</sup> Rodrigo García-Muelas<sup>id</sup> and Manuel A. Ortuño<sup>id</sup>\*

The oxygen evolution reaction (OER) is the bottleneck of hydrogen production *via* water splitting and using efficient electrocatalysts becomes paramount to render this process viable. Metal-organic framework (MOF) catalysts, which are porous solid materials at the frontier between homogeneous and heterogeneous catalysis, have emerged as promising candidates. Earth-abundant MOF-74 materials have recently shown great performance towards the OER, but the true nature of their active sites remains unclear. Here, we employ density functional theory (DFT + *U*) to elucidate the reaction mechanism and rationalize the electrocatalytic activity of Fe-MOF-74. Our results demonstrate that the open metal sites of the pristine catalyst do not promote the OER; instead, metal sites associated with defective structures do. This study provides new insights into guiding the rational synthesis and post-synthetic engineering of MOFs for electrocatalysis.

### 1. Introduction

With the current depletion of fossil fuels and rising carbon dioxide emissions, we face the challenges of devising new sustainable and efficient ways to fulfil the increasing global energy needs.<sup>1</sup> Renewable energies, such as solar or wind, provide a flexible energy supply for production of synthetic fuels; however, these sources are intermittent and energy cannot be efficiently stored yet. In this scenario, electrocatalysis appears as a promising alternative to convert readily accessible molecules (water, oxygen, and carbon dioxide) into high-value products (hydrogen, hydrogen peroxide, formate, *etc.*)<sup>2</sup>

Aiming for a sustainable hydrogen economy, much research is focused on developing efficient catalysts for the oxygen evolution reaction (OER), which is the bottleneck process of efficient water splitting. The OER involves four electrons and four protons and needs to surmount a high thermodynamic hill (4.92 eV).<sup>3</sup> Homogeneous catalysts exhibit well-defined active sites and are easily tunable, but their poor recyclability and their need for solvents present severe limitations for their integration into devices. Heterogeneous systems, on the other hand, are more robust and cost-effective, yet the diversity of active centres makes them difficult to tame. Aiming to bridge the gap between these two catalysts, we turn to metal-organic frameworks (MOFs), a family of porous materials formed by metal nodes connected by organic linkers.<sup>4</sup> These materials are attractive for catalytic

applications due to: (i) their high surface area, which maximizes the amount of active sites per volume, (ii) their tunable structure *via* node and linker modifications, (iii) their porosity, which permits facile reactant and product diffusion, and (iv) the control over ultrathin film deposition. Indeed, the contributions of MOFs in electrocatalysis have dramatically increased in recent years,<sup>5–8</sup> especially for water oxidation catalysis.<sup>9–12</sup>

The best performing materials for the OER are based on noble metal oxides (RuO<sub>2</sub> and IrO<sub>2</sub>), which dramatically limits their commercialisation. Early contributions by Galán-Mascarós and co-workers already pointed out the great performance of Co and Fe metals in Prussian blue analogues.<sup>13</sup> Following extensive work on Earth-abundant transition metals,<sup>14,15</sup> MOFs have recently emerged as efficient electrocatalysts.<sup>16–19</sup> In this line, a number of them have shown OER activity, such as Fe<sub>3</sub>-Co<sub>2</sub>,<sup>20</sup> A/B-MOF-Co/Fe,<sup>21</sup> NNU-22,<sup>22</sup> Co-Fe-B,<sup>23</sup> CoFe-PYZ,<sup>24</sup> and CoFe-MOF.<sup>25</sup> A computational study also predicted high catalytic activity for 2D MOFs based on Co and Fe centres.<sup>26</sup>

Recent contributions have demonstrated the electrocatalytic potential of the well-known MOF-74 family<sup>27,28</sup> towards OER (Fig. 1). Xu and co-workers reported homo- and heterometallic

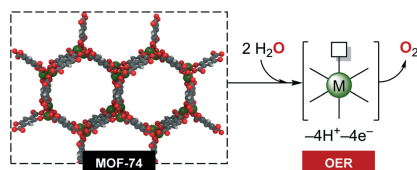


Fig. 1 Oxygen evolution reaction (OER) catalysed by MOF-74.

Institute of Chemical Research of Catalonia (ICIQ), Barcelona Institute of Science and Technology (BIST), Av. Paisos Catalans 16, 43007 Tarragona, Spain.  
E-mail: mortuno@icq.es

MOF-74 catalysts based on Co(n) and Fe(n) nodes showing low overpotentials (*ca.* 0.3–0.4 V in alkaline solutions) and high Faradaic efficiency (*ca.* 90%).<sup>29</sup> Similar results were observed for Ni(n)- and Fe(n)-based MOF-74.<sup>30,31</sup>

Earth-abundant MOF-74 derivatives are thus promising electrocatalysts, yet little information is known about the true nature of their active sites. It has been proven that the presence of defects on the MOF surfaces or within the frameworks can have a strong impact on their properties,<sup>32,33</sup> and particularly in catalytic performance.<sup>34,35</sup> In this scenario, quantum mechanics simulations<sup>36</sup> become crucial in grasping the full electrochemical picture at the atomic level of detail.<sup>37,38</sup> Here, we employ density functional theory (DFT) to understand the OER activity of MOF electrocatalysts and reveal key aspects for future material design.

## 2. Computational methods

All periodic calculations were performed at the density functional theory (DFT) level using the Vienna *ab initio* simulation package (VASP).<sup>39</sup> Core electrons were described by projector augmented wave (PAW) pseudopotentials<sup>40</sup> and valence electrons were represented by plane waves with a kinetic energy cut-off of 450 eV. We employed the PBE density functional<sup>41</sup> supplemented with the D3 dispersion approach<sup>42</sup> and corrected with a  $U$  parameter (DFT +  $U$ )<sup>43</sup> for the  $d$  orbitals of the transition metals: 5.3 eV for Co and 6.5 eV for Fe as suggested by linear response.<sup>44</sup> These  $U$  values are larger than those employed in previous studies<sup>45</sup> but similar to those obtained for related Prussian blue analogs.<sup>46</sup> It is worth noting that previous studies on hematite showed some discrepancies between DFT +  $U$ <sup>47</sup> and hybrid<sup>48</sup> density functionals. However, the large size of our MOF unit cells prevents a full exploration with hybrids, thus we only discuss the PBE +  $U$  results. Indeed, the challenges of describing the electronic structure of first-row transition metal compounds are well reported in the literature.<sup>49</sup>

The initial cell was built from the dehydrated Co(n)-MOF-74 X-ray crystal structure.<sup>28</sup> The computed lattice parameters (optimised with a kinetic energy cut-off of 600 eV) were in agreement with the experimental values with a relative error of <1% (Table S1†). Due to the isostructural character of Co(n)- and Fe(n)-based MOF-74, the optimized unit cell of the former was employed for the latter. The Brillouin zone was sampled with the Monkhorst-Pack method<sup>50</sup> using a  $1 \times 1 \times 2$   $k$ -point mesh and  $\Gamma$ -point for the pristine material ( $a = b = 26.129$  Å and  $c = 6.821$  Å) and the defective model ( $a = b = 26.129$  Å and  $c = 13.642$  Å), respectively (Fig. S1 and S2†). Vibrational partition functions were computed using numerical frequencies at 298.15 K, where only selected atoms were allowed to move and were preserved along each reaction pathway. Low-frequency modes lower than  $200\text{ cm}^{-1}$  were increased to  $200\text{ cm}^{-1}$  to correct for errors associated with the harmonic oscillator model. The thermodynamics of OER were computed following the computational hydrogen electrode

(CHE) method (see ESI†).<sup>51</sup> The solvation energy of H<sub>2</sub>O was computed with the implicit solvation model VASP-MGCM.<sup>52</sup>

All the inputs and outputs can be found online<sup>53</sup> in the open-access ioChem-BD repository.<sup>54,55</sup> The visualization of structures was done with the VESTA<sup>56</sup> and QuteMol<sup>57</sup> software packages.

## 3. Results and discussion

In this section, we present and discuss the computational results for both pristine and defective materials. Gibbs energy profiles are computed following the CHE approach to identify the potential determining step (PDS). Catalytic activity is discussed in terms of theoretical overpotentials, which are calculated from the Gibbs energy of the PDS by subtracting  $1.23/n$  ( $n = 1\text{ |e}^-$ ). Further details can be found in the computational methods and the ESI†

### Pristine M-MOF-74

We considered two homometallic materials, Co(n)-based and Fe(n)-based MOF-74, namely M-MOF-74 (M = Co or Fe). They are built with coordinately unsaturated divalent M(n) cations connected by 2,5-dihydroxybenzene-1,4-dicarboxylate (DOBDC) organic ligands. Such combination of nodes and linkers leads to a three-dimensional honeycomb structure composed of hexagonal channels and one-dimensional metallic wires (Fig. 2). The computed lattice parameters of the unit cell are  $a = b = 26.129$  Å and  $c = 6.821$  Å (Fig. S1†). The unit cell contains 18 transition metals in the high spin state along 6 wires. Regarding magnetic properties, there are two kinds of interactions: couplings within a wire (intrawire) and couplings between wires (interwire). Intrawire interactions always have ferromagnetic (FM) nature; interwire couplings are preferentially antiferromagnetic (AFM), although ferromagnetic behaviour can be observed when applying temperature or an external magnetic field.<sup>28</sup> We computed both interwire configurations for Co- and Fe-MOF-74, resulting in isoenergetic structures with a relative energy difference of only 0.02 eV, in line with previous data.<sup>58</sup>

With the pristine MOF structures at hand, we next evaluated the thermodynamics of the OER process. There are

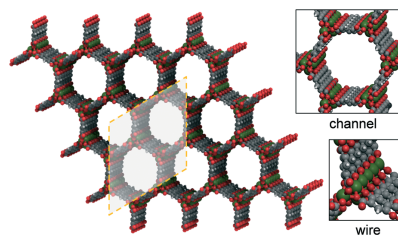


Fig. 2 Computed unit cell (orange) and periodic structure of M-MOF-74. Atom legend: Fe (green); O (red); C (grey); H (white).

two main reaction mechanisms as depicted in Scheme 1a.<sup>38</sup> In the water nucleophilic attack (WNA), the O-O bond is formed between a metal-oxo moiety and a water molecule through a hydroperoxo intermediate. In the oxo coupling (I2M), the O-O bond route is directly formed between two metal-oxo species. Due to the spatial constraints of the framework, the vacant sites of consecutive metal centres point towards different channels, and thus two oxo moieties cannot come close and only the WNA pathway is considered in this study. The initial vacancy, hydroxo, oxo, and hydroperoxo stages are denoted as X, X-OH, X-O, and X-OOH, respectively, where the prefix denotes the type of catalyst or catalytic site (X = A-D, see further text). The four reaction steps involved in the Gibbs energy profile of the WNA process are indicated in Scheme 1b.

First, we optimised the intermediates of the WNA pathway for the models with high spin metals and interwire AFM coupling of Co-MOF-74 (A) and Fe-MOF-74 (B). We computed the Gibbs energies for the four steps of the OER ( $\Delta G_{1-4}$ ) and built the corresponding reaction profiles for A and B as shown in Fig. 3. The structural parameters and spin densities of B-OH and B-O (Table S5†) are in agreement with earlier calculations.<sup>59,60</sup> Comparing the two catalysts,  $\Delta G_3$  and  $\Delta G_4$  are essentially the same, while  $\Delta G_1$  and  $\Delta G_2$  differ in ca. 0.5 eV. The energy values for the structures with interwire FM interactions lead to analogous results (Table S2†). In previous literature, a constant Gibbs energy difference of ca. 3.2 eV between X-OOH and X-OH intermediates was found for metals and metal oxides.<sup>61</sup> Garcia-Melchor and co-workers showed that this correlation also applies to molecular species in general,<sup>62</sup>

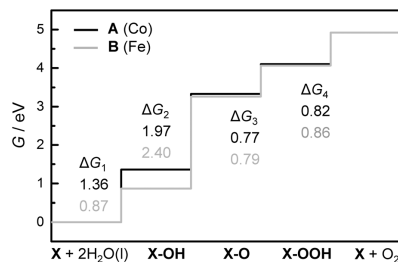


Fig. 3 Gibbs energy profiles of the OER at zero potential ( $u = 0$  V),  $\text{pH} = 0$ , and  $T = 298.15$  K for pristine models A and B.

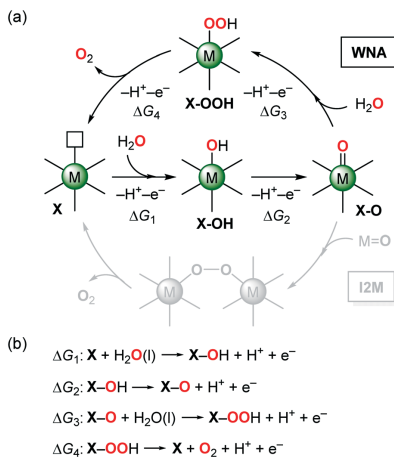
although Corminboeuf and co-workers warned about density functional sensitivity.<sup>63</sup> Concerning the MOF catalysts, previous contributions reported values of 2.8–3.2 eV for a series of bimetallic MOFs<sup>22</sup> and 2.5–3.0 eV for Co- and Fe-based Hofmann-type MOFs.<sup>24</sup> Similar to these reports, we find Gibbs energy differences of 2.74 eV for A and 3.19 eV for B.

The most energetically demanding process, *i.e.* the PDS, is the same for both systems and corresponds to  $\Delta G_2$ , the oxidation of X-OH to X-O. For A, the  $\Delta G_2$  value of 1.97 eV yields a theoretical overpotential of 0.74 V, while for B, the  $\Delta G_2$  value of 2.40 eV results in a theoretical overpotential of 1.17 V. These values are, however, higher than those reported experimentally (ca. 0.4 V).<sup>29</sup> In view of such discrepancy, we next performed additional calculations to validate our computational approach.

To evaluate the local effect of the solvent, we included one explicit water molecule forming an H-bond in X-OH and X-O. The resulting  $\Delta G_2$  values did not change significantly, going from 1.97 and 2.40 eV without water to 1.93 and 2.30 eV with water for A and B, respectively (Table S3†). Thus, we observe little effect of explicit water on the relative energies.

To assess the impact of the methodology, we tested several density functionals using a finite-size 88-atom cluster model for Fe-MOF-74 (Fig. S3†),<sup>64</sup> as hybrid density functionals are prohibitively expensive for plane wave calculations of large unit cells. The spin densities at the periodic PBE + *U* level are similar to those using hybrids (Table S6†), which had been successfully employed for molecules,<sup>62</sup> solids,<sup>65,66</sup> and related materials.<sup>67</sup> The Gibbs energies at the periodic PBE + *U* level also have the same trends as those computed with hybrids (Table S7†). Density functionals with ca. 15% Hartree-Fock exact exchange provide lower overpotentials, but they are still higher than the experimental ones. Therefore, these benchmark calculations support the reliability and use of PBE + *U* as the most cost-efficient approach.

Overall, according to our computed energies and overpotentials, it seems clear that the open metal sites in the pristine MOFs are unlikely to contribute to OER activity. We then hypothesize that the presence of defects, such as missing linkers,<sup>68,69</sup> might account for such activity. In the



Scheme 1 Proposed reaction mechanisms for the OER: (a) water nucleophilic attack (WNA) and oxo coupling (I2M); (b) reaction steps involved in the WNA process.

next section we focus on Fe-MOF-74 to systematically explore new potential catalytic sites.

#### Defective M-MOF-74

As the pristine MOFs rendered high OER overpotentials, we then evaluated whether the presence of defects could impact the activity of the materials. To study in detail such aspects, we only focused on the Fe-based material. In particular, we considered the removal of one DOBDC linker. This situation may represent an internal defect within the framework as well as the external surface of a MOF nanoparticle or film. To properly address this hypothesis from a computational perspective, we made the following adjustments to the pristine model: (i) the  $c$  parameter of the unit cell was doubled ( $c = 13.642 \text{ \AA}$ ) to avoid spurious concentration of defects that may compromise the stability of the framework (Fig. S2†), (ii) the tetra-anionic six-coordinated ligand was replaced by four hydroxides and two water molecules to balance the charges and coordination sites,<sup>70</sup> and (iii) diverse potential active sites were systematically explored.

In **B**, each DOBDC linker has 6 oxygen atoms anchored to 2 wires that we denoted as  $O^C$ , if they belong to a carboxylate group, and  $O^P$ , if they belong to a phenolate moiety. As the first approach, we removed one linker, thus creating defects in two different wires. Mono-coordinated  $O^C$  sites were replaced by two water molecules and bi-coordinated  $O^C$  and  $O^P$  sites were saturated with four hydroxides. This arrangement yields defect **C** (Fig. 4), where both defective wires are identical. In **C**, all Fe atoms, namely  $Fe^{A-D}$ , are five-coordinate octahedra the same as those in pristine **B**, but their ligand environment is different, and their mobility may be increased as the constraints imposed by the linker are gone. To further explore the configurational space, we considered different structures in one wire while maintaining the other wire as exhibited in **C**. By changing the

coordination pattern of one hydroxide, we obtained defect **D** (Fig. 4). Here,  $Fe^A$  and  $Fe^C$  are five-coordinate,  $Fe^B$  is four-coordinate, and  $Fe^D$  is six-coordinate. Structure **D** is only 0.16 eV less stable than **C**, and thus it is thermally accessible and may be relevant to catalysis. Additional optimisation attempts evolved towards **C** and **D**, or rotamers of those.

We next estimated the band gaps of the pristine and defective models. The computed values for **B-D** are 1.86, 1.75, and 1.64 eV, respectively, indicating that the defects behave similarly to the pristine material. Previous reports on UiO-66 came up with the same result, showing that missing linkers do not significantly alter the electronic properties of the MOF.<sup>71</sup>

Once the defects were structurally characterised, we continued with the OER thermodynamics. We started with **C**, where the creation of the defect affects the coordination environment of the four metal atoms. The initial OH binding ( $\Delta G_1$ ) to **C** can occur at four different metal centres,  $Fe^{A-D}$ , resulting in four species  $C^{A-D}-OH$ . For the sake of relevance, only the reactivity of  $C^B-OH$  is discussed here, while the data for  $C^A-OH$ ,  $C^C-OH$ , and  $C^D-OH$  can be found in the ESI† (Table S4). The next step ( $\Delta G_2$ ) involves the removal of one  $H^+/e^-$  to form an oxo group. This process can take place at three different OH positions, one terminal **t** and two bridges **b** and **b'** (Fig. 5a), thus leading to three separate pathways.<sup>72</sup> The reactions continue with OOH formation ( $\Delta G_3$ ) and  $O_2$  release ( $\Delta G_4$ ). The corresponding Gibbs energy reaction profiles for  $C^B$  are shown in Fig. 5a. The  $\Delta G_1$  value of the OH binding is similar to that for both defective  $C^B-OH$  and pristine **B-OH**. The  $\Delta G_2$  value in the oxo formation is the same as that for  $C^B-O-t$  (terminal position) and pristine **B-O**. Interestingly,  $\Delta G_2$  becomes lower for  $C^B-O-b$  (bridge position) due to the stabilisation of the oxo group through multiple metal centres. The oxo species  $C^B-O-b'$  is not stable since removing one  $H^+/e^-$  in **b'** triggers a spontaneous proton transfer from the nearby water ligand; this route is therefore discarded. Minor differences are observed for  $\Delta G_3$  and  $\Delta G_4$ , but they do not impact the process as the overall PDS is still  $\Delta G_2$  for all systems.  $C^B-O-t$  yields a theoretical overpotential of 1.27 V, in line with 1.17 V obtained for **B-O**, while  $C^B-O-b$  provides a value of 0.79 V. Despite the lower overpotentials observed for this type of defect, the absolute values are still somehow far from the experimental measurements.

Next, we move on with structure **D**. There are four different metal centres for OH binding ( $\Delta G_1$ ),  $Fe^{A-D}$ , but we only considered the four-coordinate  $Fe^B$  site via  $D^B-OH$  as the representative case. For simplicity, we drop the **B** superscript and refer to it as **D-OH**. As before, in the oxo formation ( $\Delta G_2$ ), we identify one terminal **t** and two bridge **b** and **b'** positions, resulting in three different reaction profiles (Fig. 5b).<sup>72</sup> The Gibbs energies for the path involving  $D-O-t$  are quite similar to those involving pristine **B-O**, where  $\Delta G_2$  is the PDS with a theoretical overpotential of 1.07 V. However, greater changes appear for  $D-O-b$  and  $D-O-b'$ . The most relevant is that  $\Delta G_2$  and  $\Delta G_3$  become almost isoenergetic with differences of *ca.* 0.1 eV. In  $D-O-b$ , the hydroperoxo formation ( $\Delta G_3$ ) turns out to be the PDS with a theoretical

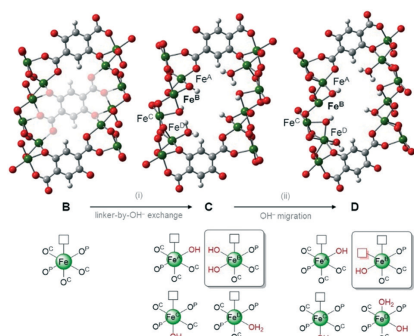


Fig. 4 Structural defects **C** and **D** and local coordination environment of the Fe centres. The boxes indicate the structures discussed in the text. Atom legend: Fe (green); O (red); C (grey); H (white).

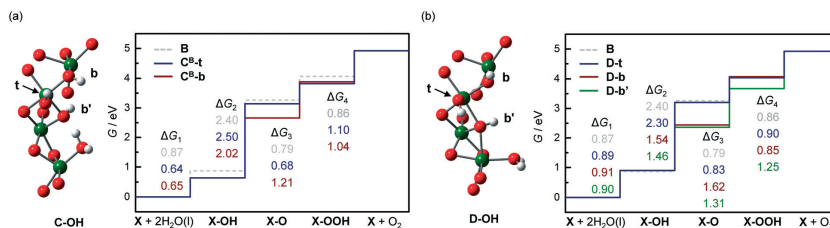


Fig. 5 Gibbs energy profiles of the OER at zero potential ( $u = 0$  V),  $\text{pH} = 0$ , and  $T = 298.15$  K for models (a) C and (b) D. Most atoms from the linkers are omitted in the figure for clarity.

overpotential of 0.39 V; in **D-O-b'**, the oxo formation ( $\Delta G_2$ ) is still the PDS with a theoretical overpotential of 0.23 V. Both cases present significantly lower values than those obtained for pristine **B** and defective **C**, and become closer to the experimental values.

Defects **C** and **D** can both stabilize bridge oxo intermediates, but the latter gives the lowest overpotentials. Such different behaviour is attributed to a dynamic linker reorganisation<sup>70</sup> that occurs in the **D-O** species (Fig. 6). Upon removal of  $\text{H}^+/\text{e}^-$  in **b**, an Fe-OH bond is broken in **D-O-b**, rendering an oxo group bonded to a four-coordinate tetrahedral Fe centre (orange).<sup>73,74</sup> There is an additional reorganisation in a neighbouring Fe atom, where one Fe-O(linker) bond is broken and another one is formed (blue). In a similar way, upon removal of  $\text{H}^+/\text{e}^-$  in **b'**, a Fe-O(linker) bond is broken in **D-O-b'** yielding again an oxo group bonded to a four-coordinate tetrahedral Fe centre (orange). In both cases, the original coordination environment as exhibited in **D-OH** is recovered when forming the hydroperoxo intermediate **D-OOH**. These computational results imply a dynamic rearrangement within the point defects of porous materials. Indeed, transient bond-forming and bond-breaking processes in MOFs

have been invoked to enhance reactivity and break linear scaling relationships.<sup>75</sup>

We note that, while these defects are electrochemically active, other sites might also contribute to the OER activity. In this sense, the stability of Fe-MOF-74 under electrochemical conditions is an important issue to consider. Although data for homometallic materials are scarce, it was observed that heterometallic Co-Fe-MOF-74 can form ultrathin sheets and oxides.<sup>29</sup> This is in line with a recent contribution, where homometallic Ni-MOF-74 was stable during the OER but heterometallic counterparts exhibit the formation of metal (oxy)hydroxides.<sup>76</sup> Indeed, recent computational studies have shown that homometallic Fe<sup>77</sup> and heterometallic M-Fe (oxy)hydroxides are active for OER,<sup>77,78</sup> as well as Ni (oxy)hydroxides with Fe impurities.<sup>79</sup>

We thus suggest investing efforts towards defect characterization and engineering as design strategies in MOF-based electrochemical devices,<sup>80</sup> *e.g.*, using coordinatively deficient linkers<sup>81</sup> during the framework assembly (pre-synthesis) or applying a controlled thermal treatment<sup>82</sup> to create vacant sites in the material (post-synthesis). We also highlight that detailed studies of stability under *in operando* conditions are key to fully understand the nature of active sites as well as the catalytic performance of these materials.

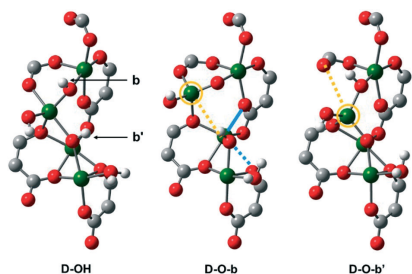


Fig. 6 DFT-optimised structures of **D-OH**, **D-O-b**, and **D-O-b'**. Formed bonds are shown in bold lines and broken ones in dashed lines. Four-coordinate Fe atoms are depicted with orange circles. Most atoms from the linkers are omitted in the figure for clarity. Atom legend: Fe (green); O (red); C (grey); H (white).

## 4. Conclusions

In this work, we computationally studied the OER process catalysed by pristine and defective Fe-based MOF-74. DFT +  $U$  simulations demonstrate that:

- (i) the oxidation of terminal hydroxo to terminal oxo ( $\Delta G_2$ ) is energy demanding and not sensitive to the coordination environment, where similar energetics and overpotentials were found for pristine **B** and defective **C** and **D**;
- (ii) the oxidation of bridge hydroxo to bridge oxo ( $\Delta G_2$ ) is only feasible at defect sites and results in more stable intermediates for **C** and **D**, leading to lower overpotentials;
- (iii) among the defects evaluated in this study, the most favourable paths with lowest overpotentials proceed *via* species **D**, which introduce flexibility within the framework and allow transient coordination rearrangements.

Overall, the pristine material is inactive while defective structures yield theoretical overpotentials comparable to experimental data. These results can guide future steps to address whether the enhanced activity of heterometallic MOFs is linked to the nature and/or the number of defective sites and provide new hints for defect engineering of MOF-based electrochemical devices.

## Conflicts of interest

There are no conflicts to declare.

## Acknowledgements

J. M.-V. and R. G.-M. acknowledge the Spanish Ministry of Science and Innovation (RTI2018-101394-B-I00) for financial support. M. A. O. acknowledges the support of the Beatriu de Pinós postdoctoral programme of the Government of Catalonia's Secretariat of Universities and Research (2017-BP-00039). The authors thankfully acknowledge the computer resources at MareNostrum and the technical support provided by the Barcelona Supercomputing Center (RES-QCM-2019-2-0018 and RES-QS-2020-1-0024).

## References

- 1 *Global Energy & CO<sub>2</sub> Status Report 2019*, International Energy Agency, <https://www.iea.org/reports/global-energy-co2-status-report-2019> [accessed 16/10/2020].
- 2 Z. W. Seh, J. Kibsgaard, C. F. Dickens, I. Chorkendorff, J. K. Nørskov and T. F. Jaramillo, *Science*, 2017, **355**, eaad4998.
- 3 N.-T. Suen, S.-F. Hung, Q. Quan, N. Zhang, Y.-J. Xu and H. M. Chen, *Chem. Soc. Rev.*, 2017, **46**, 337.
- 4 H. Furukawa, K. E. Cordova, M. O'Keeffe and O. M. Yaghi, *Science*, 2013, **341**, 1230444.
- 5 C. A. Downes and S. C. Marinescu, *ChemSusChem*, 2017, **10**, 4374.
- 6 S. Jin, *ACS Energy Lett.*, 2019, **4**, 1443.
- 7 S. Dou, X. Li and X. Wang, *ACS Mater. Lett.*, 2020, **2**, 1251.
- 8 H.-F. Wang, L. Chen, H. Pang, S. Kaskel and Q. Xu, *Chem. Soc. Rev.*, 2020, **49**, 1414.
- 9 Y. Yan, T. He, B. Zhao, K. Qi, H. Liu and B. Y. Xia, *J. Mater. Chem. A*, 2018, **6**, 15905.
- 10 Q. Shao, J. Yang and X. Huang, *Chem. - Eur. J.*, 2018, **24**, 15143.
- 11 J. Qi, W. Zhang and R. Cao, *ChemCatChem*, 2018, **10**, 1206.
- 12 S. Mukhopadhyay, O. Basu, R. Nasani and S. K. Das, *Chem. Commun.*, 2020, **56**, 11735.
- 13 (a) S. Pintado, S. Goberna-Ferrón, E. C. Escudero-Adán and J. R. Galán-Mascarós, *J. Am. Chem. Soc.*, 2013, **135**, 13270; (b) L. Han, P. Tang, A. Reyes-Carmona, B. Rodríguez-García, M. Torrén, J. R. Morante, J. Arbiol and J. R. Galán-Mascarós, *J. Am. Chem. Soc.*, 2016, **138**, 16037.
- 14 B. M. Hunter, H. B. Gray and A. M. Müller, *Chem. Rev.*, 2016, **116**, 14120.
- 15 B. Zhang, X. Zheng, O. Voznyy, R. Comin, M. Bajdich, M. García-Melchor, L. Han, J. Xu, M. Liu, L. Zheng, F. P. García de Arquer, C. T. Dinh, F. Fan, M. Yuan, E. Yassitepe, N. Chen, T. Regier, P. Liu, Y. Li, P. De Luna, A. Janmohamed, H. L. Xin, H. Yang, A. Vojvodic and E. H. Sargent, *Science*, 2016, **352**, 333.
- 16 S. Zhao, Y. Wang, J. Dong, C.-T. He, H. Yin, P. An, K. Zhao, X. Zhang, C. Gao, L. Zhang, J. Lv, J. Wang, J. Zhang, A. M. Khattak, N. A. Khan, Z. Wei, J. Zhang, S. Liu, H. Zhao and Z. Tang, *Nat. Energy*, 2016, **1**, 16184.
- 17 L. Wang, Y. Wu, R. Cao, L. Ren, M. Chen, X. Feng, J. Zhou and B. Wang, *ACS Appl. Mater. Interfaces*, 2016, **8**, 16736.
- 18 J. Duan, S. Chen and C. Zhao, *Nat. Commun.*, 2017, **8**, 15341.
- 19 W. Zhou, D.-D. Huang, Y.-P. Wu, J. Zhao, T. Wu, J. Zhang, D.-S. Li, C. Sun, P. Feng and X. Bu, *Angew. Chem., Int. Ed.*, 2019, **58**, 4227.
- 20 J.-Q. Shen, P.-Q. Liao, D.-D. Zhou, C.-T. He, J.-X. Wu, W.-X. Zhang, J.-P. Zhang and X.-M. Chen, *J. Am. Chem. Soc.*, 2017, **139**, 1778.
- 21 Z. Xue, Y. Li, Y. Zhang, W. Geng, B. Jia, J. Tang, S. Bao, H.-P. Wang, Y. Fan, Z.-W. Wei, Z. Zhang, Z. Ke, G. Li and C.-Y. Su, *Adv. Energy Mater.*, 2018, **8**, 1801564.
- 22 X.-L. Wang, L.-Z. Dong, M. Qiao, Y.-J. Tang, J. Liu, Y. Li, S.-L. Li, J.-X. Su and Y.-Q. Lan, *Angew. Chem., Int. Ed.*, 2018, **57**, 9660.
- 23 H. Chen, S. Ouyang, M. Zhao, Y. Li and J. Ye, *ACS Appl. Mater. Interfaces*, 2017, **9**, 40333.
- 24 J. Gao, J. Cong, Y. Wu, L. Sun, J. Yao and B. Chen, *ACS Appl. Energy Mater.*, 2018, **1**, 5140.
- 25 C. Yang, W.-J. Cai, B.-B. Yu, H. Qiu, M.-L. Li, L.-W. Zhu, Z. Yan, L. Hou and Y.-Y. Wang, *Catal. Sci. Technol.*, 2020, **10**, 3897.
- 26 P. Zhang, X. Yang, W. Gao, X. Hou, J. Mi, L. Liu, J. Huang, M. Dong and C. Stampfl, *Catal. Sci. Technol.*, 2018, **8**, 3666.
- 27 N. L. Rosi, J. Kim, M. Eddaoudi, B. Chen, M. O'Keeffe and O. M. Yaghi, *J. Am. Chem. Soc.*, 2005, **127**, 1504.
- 28 P. D. C. Dietzel, Y. Morita, R. Blom and H. Fjellvåg, *Angew. Chem., Int. Ed.*, 2005, **44**, 6354.
- 29 X. Zhao, B. Pattengale, D. Fan, Z. Zou, Y. Zhao, J. Du, J. Huang and C. Xu, *ACS Energy Lett.*, 2018, **3**, 2520.
- 30 J. Xing, K. Guo, Z. Zou, M. Cai, J. Du and C. Xu, *Chem. Commun.*, 2018, **54**, 7046.
- 31 Q. Wang, F. Wei, D. Manoj, Z. Zhang, J. Xiao, X. Zhao, F. Xiao, H. Wang and S. Wang, *Chem. Commun.*, 2019, **55**, 11307.
- 32 D. S. Sholl and R. P. Lively, *J. Phys. Chem. Lett.*, 2015, **6**, 3437.
- 33 (a) A. K. Cheetham, T. D. Bennett, F.-X. Coudert and A. L. Goodwin, *Dalton Trans.*, 2016, **45**, 4113; (b) T. D. Bennett, A. K. Cheetham, A. H. Fuchs and F.-X. Coudert, *Nat. Chem.*, 2017, **9**, 11.
- 34 P. Valvèkens, F. Vermoortele and D. De Vos, *Catal. Sci. Technol.*, 2013, **3**, 1435.
- 35 (a) J. Canivet, M. Vandichel and D. Farrusseng, *Dalton Trans.*, 2016, **45**, 4090; (b) S. Dissegna, K. Epp, W. R. Heinz, G. Kieslich and R. A. Fischer, *Adv. Mater.*, 2018, **30**, 1704501.
- 36 (a) S. O. Odoh, C. J. Cramer, D. G. Truhlar and L. Gagliardi, *Chem. Rev.*, 2015, **115**, 6051; (b) J. L. Mancuso, A. M. Mroz, K. N. Le and C. H. Hendon, *Chem. Rev.*, 2020, **120**, 8641.

- 37 E. Fabbri, A. Haberer, K. Waltar, R. Kötz and T. J. Schmidt, *Catal. Sci. Technol.*, 2014, **4**, 3800.
- 38 J. Soriano-López, W. Schmitt and M. García-Melchor, *Curr. Opin. Electrochem.*, 2018, **7**, 22.
- 39 (a) G. Kresse and J. Furthmüller, *Phys. Rev. B: Condens. Matter Mater. Phys.*, 1996, **54**, 11169; (b) G. Kresse and J. Furthmüller, *Comput. Mater. Sci.*, 1996, **6**, 15.
- 40 G. Kresse and D. Joubert, *Phys. Rev. B: Condens. Matter Mater. Phys.*, 1999, **59**, 1758.
- 41 J. P. Perdew, K. Burke and M. Ernzerhof, *Phys. Rev. Lett.*, 1996, **77**, 3865.
- 42 S. Grimme, J. Antony, S. Ehrlich and H. Krieg, *J. Chem. Phys.*, 2010, **132**, 154104.
- 43 S. L. Dudarev, G. A. Botton, S. Y. Savrasov, C. J. Humphreys and A. P. Sutton, *Phys. Rev. B: Condens. Matter Mater. Phys.*, 1998, **57**, 1505.
- 44 G. W. Mann, K. Lee, M. Cococcioni, B. Smit and J. B. Neaton, *J. Chem. Phys.*, 2016, **144**, 174104.
- 45 (a) K. Lee, J. D. Howe, L.-C. Lin, B. Smit and J. B. Neaton, *Chem. Mater.*, 2015, **27**, 668; (b) B. Vlasisavljevic, J. Huck, Z. Hulvey, K. Lee, J. A. Mason, J. B. Neaton, J. R. Long, C. M. Brown, D. Alfé, A. Michaelides and B. Smit, *J. Phys. Chem. A*, 2017, **121**, 4139.
- 46 F. S. Hegner, J. R. Galán-Mascarós and N. López, *Inorg. Chem.*, 2016, **55**, 12851.
- 47 (a) A. Hellman, B. Iandolo, B. Wickman, H. Grönbeck and J. Baltrusaitis, *Surf. Sci.*, 2015, **640**, 45; (b) M.-T. Nguyen, S. Piccinini, N. Seriani and R. Gebauer, *ACS Catal.*, 2015, **5**, 715.
- 48 R. B. Chang and A. Hellman, *J. Phys. Chem. C*, 2019, **123**, 2820.
- 49 (a) Q. Zhao and H. J. Kulik, *J. Chem. Theory Comput.*, 2018, **14**, 670; (b) K. D. Vogiatzis, M. V. Polynski, J. K. Kirkland, J. Townsed, A. Hashemi, C. Liu and E. A. Pidko, *Chem. Rev.*, 2019, **119**, 2453.
- 50 H. J. Monkhorst and J. D. Pack, *Phys. Rev. B: Solid State*, 1976, **13**, 5188.
- 51 J. K. Nørskov, J. Rossmeisl, A. Logadotir, L. Lindqvist, J. R. Kitchin, T. Bligaard and H. Jónsson, *J. Phys. Chem. B*, 2004, **108**, 17886.
- 52 M. Garcia-Ratés and N. López, *J. Chem. Theory Comput.*, 2016, **12**, 1331.
- 53 C. Bo, F. Maseras and N. López, *Nat. Catal.*, 2018, **1**, 809.
- 54 M. Álvarez-Moreno, C. de Graaf, N. López, F. Maseras, J. M. Poblet and C. Bo, *J. Chem. Inf. Model.*, 2015, **55**, 95.
- 55 J. Morales-Vidal, *ioChem-BD database*, DOI: 10.19061/iochem-bd-1-188, link: <https://iochem-bd.icicq.es/browse/handle/100/27445>.
- 56 K. Momma and F. Izumi, *J. Appl. Crystallogr.*, 2011, **44**, 1272.
- 57 M. Tarini, P. Cignoni and C. Montani, *IEEE Trans. Vis. Comput. Graph.*, 2006, **12**, 1237.
- 58 P. Canepa, Y. J. Chaval and T. Thonhauser, *Phys. Rev. B: Condens. Matter Mater. Phys.*, 2013, **87**, 094407.
- 59 D. J. Xiao, J. A. Mason, W. L. Queen, M. R. Hudson, N. Planas, J. Borycz, A. L. Dzubak, P. Verma, K. Lee, F. Bonino, V. Crocellà, J. Yano, S. Bordiga, D. G. Truhlar, L. Gagliardi, C. M. Brown and J. R. Long, *Nat. Chem.*, 2014, **6**, 590.
- 60 P. Verma, K. D. Vogiatzis, N. Planas, J. Borycz, D. J. Xiao, J. R. Long, L. Gagliardi and D. G. Truhlar, *J. Am. Chem. Soc.*, 2015, **137**, 5770.
- 61 (a) M. T. M. Koper, *J. Electroanal. Chem.*, 2011, **660**, 254; (b) I. C. Man, H. Su, F. Calle-Vallejo, H. A. Hansen, J. I. Martínez, N. G. Inoglu, J. Kitchin, T. F. Jaramillo, J. K. Nørskov and J. Rossmeisl, *ChemCatChem*, 2011, **3**, 1159.
- 62 M. J. Craig, G. Coulter, E. Dolan, J. Soriano-López, E. Mates-Torres, W. Schmitt and M. García-Melchor, *Nat. Commun.*, 2019, **10**, 4993.
- 63 M. Busch, A. Fabrizio, S. Lubber, J. Hutter and C. Corminboeuf, *J. Phys. Chem. C*, 2018, **122**, 12404.
- 64 P. Verma, X. Xu and D. G. Truhlar, *J. Phys. Chem. C*, 2013, **117**, 12648.
- 65 (a) A. D. Rowan, C. H. Patterson and L. V. Gasparov, *Phys. Rev. B: Condens. Matter Mater. Phys.*, 2009, **79**, 205103; (b) J. Noh, O. I. Osman, S. G. Aziz, P. Winget and J.-L. Brédas, *Sci. Technol. Adv. Mater.*, 2014, **15**, 044202.
- 66 Z. D. Pozun and G. Henkelman, *J. Chem. Phys.*, 2011, **134**, 224706.
- 67 F. S. Hegner, I. Herraiz-Cardona, D. Cardenas-Morcoso, N. López, J. R. Galán-Mascarós and S. Giménez, *ACS Appl. Mater. Interfaces*, 2017, **9**, 37671.
- 68 L. Tao, C.-Y. Lin, S. Dou, S. Feng, D. Chen, D. Liu, J. Huo, Z. Xia and S. Wang, *Nano Energy*, 2017, **41**, 417.
- 69 Z. Xue, K. Liu, Q. Liu, Y. Li, M. Li, C.-Y. Su, N. Ogiwara, H. Kobayashi, H. Kitagawa, M. Liu and G. Li, *Nat. Commun.*, 2019, **10**, 5048.
- 70 (a) K. Leus, M. Vandichel, Y.-Y. Liu, I. Muylaert, J. Musschoot, S. Pyl, H. Vrielineck, F. Callens, G. B. Marin, C. Detavernier, P. V. Wipier, Y. Z. Khimyak, M. Waroquier, V. Van Speybroeck and P. Van Der Voort, *J. Catal.*, 2012, **285**, 196; (b) M. Vandichel, S. Biswas, K. Leus, J. Paier, J. Sauer, T. Verstraelen, P. Van Der Voort, M. Waroquier and V. Van Speybroeck, *ChemSusChem*, 2014, **7**, 1183.
- 71 K. L. Svane, J. K. Bristow, J. D. Gale and A. Walsh, *J. Mater. Chem. A*, 2018, **6**, 8507.
- 72 The minor Gibbs energy discrepancies in the formation of X-OH for t, b, and b' come from small entropic contributions when computing vibrations numerically (i.e., different sets of atoms are allowed to move in each pathway).
- 73 Y. He, X. Liu, G. Chen, J. Pan, A. Yan, A. Li, X. Lu, D. Tang, N. Zhang, T. Qiu, R. Ma and T. Sasaki, *Chem. Mater.*, 2020, **32**, 4232.
- 74 Attempts to obtain intermediate and low spin state configurations were unsuccessful; they either converged to the high spin state or artificially delocalized the spin density along the whole periodic material.
- 75 A. S. Rosen, J. M. Notestein and R. Q. Snurr, *ACS Catal.*, 2019, **9**, 3576.
- 76 S. Zhao, C. Tan, C.-T. He, P. An, F. Xie, S. Jiang, Y. Zhu, K.-H. Wu, B. Zhang, H. Li, J. Zhang, Y. Chen, S. Liu, J. Dong and Z. Tang, *Nat. Energy*, 2020, **5**, 881.
- 77 M. Vandichel, M. Busch and K. Laasonen, *ChemCatChem*, 2020, **12**, 1436.

- 78 H. Xiao, H. Shin and W. A. Goddard III, *Proc. Natl. Acad. Sci. U. S. A.*, 2018, **115**, 5872.
- 79 Y. Zhou and N. López, *ACS Catal.*, 2020, **10**, 6254.
- 80 (a) Z. Fang, B. Bueken, D. E. De Vos and R. A. Fischer, *Angew. Chem., Int. Ed.*, 2015, **54**, 7234; (b) H. B. Aiyappa, J. Masa, C. Andronesco, M. Muhler, R. A. Fischer and W. Schuhmann, *Small Methods*, 2019, **3**, 1800415.
- 81 (a) D. F. Wu, W. Q. Yan, H. S. Xu, E. P. Zhang and Q. W. Li, *Inorg. Chim. Acta*, 2017, **460**, 93; (b) J. A. Villajos, N. Jagorel, S. Reinsch and F. Emmerling, *Front. Mater.*, 2019, **6**, 230.
- 82 I. Agirrezabal-Telleria, I. Luz, M. A. Ortuño, M. Oregui-Bengoechea, I. Gandarias, N. López, M. A. Lail and M. Soukri, *Nat. Commun.*, 2019, **10**, 2076.





RESEARCH ARTICLE

# Design of Flame-Made ZnZrO<sub>x</sub> Catalysts for Sustainable Methanol Synthesis from CO<sub>2</sub>

Thaylan Pinheiro Araújo, Jordi Morales-Vidal, Tangsheng Zou, Mikhail Agrachev, Simon Verstraeten, Patrik O. Willi, Robert N. Grass, Gunnar Jeschke, Sharon Mitchell, Núria López, and Javier Pérez-Ramírez\*

Mixed zinc-zirconium oxides, ZnZrO<sub>x</sub>, are highly selective and stable catalysts for CO<sub>2</sub> hydrogenation to methanol, a pivotal energy vector. However, their activity remains moderate, and descriptors to design improved systems are lacking. This work applies flame spray pyrolysis (FSP), a one-step and scalable method, to synthesize a series of ZnZrO<sub>x</sub> catalysts, and systematically compares them to coprecipitated (CP) analogs to establish deeper synthesis–structure–performance relationships. FSP systems (up to 5 mol%) generally display a threefold higher methanol productivity compared to their CP counterparts. In-depth characterization and theoretical simulations show that, unlike CP, FSP maximizes the surface area and formation of atomically dispersed Zn<sup>2+</sup> sites incorporated in lattice positions within the ZrO<sub>2</sub> surface, which is key to improving performance. Analysis by in situ electron paramagnetic resonance (EPR) spectroscopy reveals that the specific architecture of the flame-made catalyst markedly fosters the generation of oxygen vacancies. Together with surrounding Zn and Zr-O atoms, the oxygen vacancies create active ensembles that favor methanol formation through the formate path while suppressing undesired CO production, as confirmed by kinetic modeling. This study elucidates the nature of active sites and their working mechanism, pushing forward ZnZrO<sub>x</sub>-catalyzed methanol synthesis by providing a new benchmark for this cost-effective and earth-abundant catalyst family.

casted to exceed production capacities by 2023.<sup>[1,2]</sup> It can be used as a fuel additive or directly applied to power fuel cells and, as is done nowadays, combustion engines used in the maritime shipping industry.<sup>[1–3]</sup> However, methanol production presently relies on fossil feedstocks and therefore needs to urgently align with global efforts tackling climate change by lowering carbon footprint.<sup>[1,2,4,5]</sup> In this context, thermocatalytic conversion of captured carbon dioxide (CO<sub>2</sub>) and renewable hydrogen (H<sub>2</sub>) into methanol (CO<sub>2</sub> + 3H<sub>2</sub> ⇌ CH<sub>3</sub>OH + H<sub>2</sub>O) is a strategic route to enable its sustainable production and, consequently, defossilization of various chemical and energy value chains.<sup>[1,2,5,6]</sup> In the past decade, major efforts have been devoted to identify promising catalytic materials, which can be broadly divided into copper (Cu), palladium (Pd), indium oxide (In<sub>2</sub>O<sub>3</sub>), and zinc-zirconia (ZnZrO<sub>x</sub>) based families.<sup>[2,5,7–9]</sup> Among them, mixed reducible oxides, such as ZnZrO<sub>x</sub>, represent cost effective and earth abundant competitive choices.<sup>[10–13]</sup> In particular, these systems

display a high methanol selectivity by limiting the undesired carbon monoxide (CO) formation through the reverse water-gas shift (RWGS) reaction (CO<sub>2</sub> + H<sub>2</sub> ⇌ CO + H<sub>2</sub>O).<sup>[10–12]</sup> Moreover, ZnZrO<sub>x</sub> catalysts show excellent stability for several

## 1. Introduction

Methanol (CH<sub>3</sub>OH) is a versatile energy carrier, with an annual capacity of over 4 million metric ton and demand fore-

T. Pinheiro Araújo, T. Zou, S. Verstraeten, P. O. Willi, R. N. Grass, S. Mitchell, J. Pérez-Ramírez  
Institute of Chemical and Bioengineering  
Department of Chemistry and Applied Biosciences  
ETH Zurich  
Vladimir-Prelog-Weg 1, Zurich 8093, Switzerland  
E-mail: jpr@chem.ethz.ch

The ORCID identification number(s) for the author(s) of this article can be found under <https://doi.org/10.1002/aenm.202204122>.

© 2023 The Authors. Advanced Energy Materials published by Wiley-VCH GmbH. This is an open access article under the terms of the Creative Commons Attribution-NonCommercial-NoDerivs License, which permits use and distribution in any medium, provided the original work is properly cited, the use is non-commercial and no modifications or adaptations are made.

DOI: 10.1002/aenm.202204122

J. Morales-Vidal, N. López  
Institute of Chemical Research of Catalonia (ICIQ)  
The Barcelona Institute of Science and Technology  
Av. Països Catalans 16, Tarragona 43007, Spain  
J. Morales-Vidal  
Universitat Rovira i Virgili  
Av. Catalunya 35, Tarragona 43002, Spain  
M. Agrachev, G. Jeschke  
Laboratory of Physical Chemistry  
Department of Chemistry and Applied Biosciences  
ETH Zurich  
Vladimir-Prelog-Weg 2, Zurich 8093, Switzerland

hundred hours on stream and high resistance to poisoning by impurities present in CO<sub>2</sub>-containing streams, such as hydrogen sulfide, sulfur dioxide, and CO.<sup>[10,14]</sup>

In general, ZnZrO<sub>x</sub> catalysts are prepared by coprecipitation (CP) instead of impregnation methods as forming a solid solution phase was considered key to obtaining high space-time yields of methanol.<sup>[10,12,13,15]</sup> Specifically, CO<sub>2</sub> and H<sub>2</sub> activation to produce methanol reportedly proceeds via a bifunctional mechanism involving both Zn<sup>2+</sup> and Zr<sup>4+</sup> cations acting as active sites. Hence, introducing single zinc sites into the lattice of ZrO<sub>2</sub> was considered a vital step.<sup>[10,12,13]</sup> However, these catalytic systems still require productivity improvements to reach effective industrial implementation, which is hindered by several factors. Firstly, CP tends to induce zinc incorporation not only into lattice positions within the ZrO<sub>2</sub> surface but especially into its bulk phase, which leads to detrimental effects such as materials with relatively low specific surface area (i.e., 30–40 m<sup>2</sup> g<sub>cat</sub><sup>-1</sup>).<sup>[10,12,15]</sup> Besides, zinc fosters the formation of tetragonal ZrO<sub>2</sub> (*t*-ZrO<sub>2</sub>), which possesses inferior CO<sub>2</sub> adsorption capacity compared to monoclinic ZrO<sub>2</sub> (*m*-ZrO<sub>2</sub>).<sup>[10,11,16,17]</sup> More importantly, while a deep understanding of descriptors governing reactivity and stability is paramount to guide catalyst design, such crucial aspects are still poorly understood for ZnZrO<sub>x</sub>. To our knowledge, no study has addressed the impact of catalyst architecture (i.e., zirconia polymorph and zinc location and speciation) on the performance thoroughly. Furthermore, it is well established that surface oxygen vacancies act as active sites for other relevant reducible oxides (i.e., In<sub>2</sub>O<sub>3</sub><sup>[18–20]</sup>). Still, their role in forming catalytic ensembles, and their structure and working mechanism remain elusive for ZnZrO<sub>x</sub>. Based on these observations, it is clear that the rational design of superior ZnZrO<sub>x</sub> catalysts requires alternative synthesis methods and detailed investigations devised to uncover synthesis–structure–performance relationships.

In this contribution, we applied flame spray pyrolysis (FSP) to prepare and systematically investigate a platform of ZnZrO<sub>x</sub> catalysts with a broad range of compositions (i.e., 0–100 mol% Zn), which exhibit superior performance compared to state-of-the-art CP materials. FSP was selected as a one-step and scalable synthesis method that offers effective control over the nanostructure of the synthesized materials.<sup>[20–23]</sup> Specially, FSP favors the surface deposition of active metal species on carriers without promoting bulk incorporation, a classic drawback of CP methods.<sup>[20,23,24]</sup> Indeed, the flame-made ZnZrO<sub>x</sub> catalysts exhibit enhanced surface area and preferential formation of atomically dispersed Zn<sup>2+</sup> sites incorporated in lattice positions at the ZrO<sub>2</sub> surface, as revealed by extensive in-depth characterization and density functional theory (DFT) simulations. Combined in situ electron paramagnetic resonance (EPR) spectroscopy, DFT, and kinetic modeling investigations offer insights into the relationship between the catalyst architecture and oxygen vacancy formation, the resulting structure of active ensembles, and reactivity patterns in CO<sub>2</sub> hydrogenation to methanol. Our study provides an atomic-level rationalization of active sites, their correlation to experimental fingerprints and their working mechanism, and reveals a new benchmark for ZnZrO<sub>x</sub>-catalyzed methanol synthesis.

## 2. Results and Discussion

### 2.1. Optimal Catalyst Synthesis Route and Zinc Content

Mixed zinc-zirconia catalysts of varying composition were prepared by FSP (Figure 1, 0.75–95 mol% Zn, coded as  $\gamma$ ZnZrO<sub>x</sub>,  $\gamma = 0.75$ –95) and CP (1.5–28 mol% Zn, coded as  $\gamma$ ZnZrO<sub>x</sub>,CP,  $\gamma = 1.5$ –28). X-ray fluorescence spectroscopy (XRF) confirmed that the zinc content matched closely the nominal value for all materials (Table S1, Supporting Information). Evaluation in CO<sub>2</sub> hydrogenation to methanol at typical reaction conditions (593 K and 5 MPa) showed that FSP catalysts considerably outperform their coprecipitated counterparts in terms of methanol space-time yield (STY, Figure 2a and Table S2, Supporting Information). In general, methanol productivity over CP catalysts follows a typical volcano trend, reaching maximum performance at 13 mol% of zinc (STY = 0.27 g<sub>MeOH</sub> h<sup>-1</sup> g<sub>cat</sub><sup>-1</sup>), with higher content (i.e., 28 mol%) leading to ≈35% drop in methanol STY (Figure 2a), which is likely caused by phase segregation, in line with a previous report.<sup>[10]</sup> In contrast, methanol STY over FSP systems starkly increases with zinc content up to 5 mol% (STY = 0.46 g<sub>MeOH</sub> h<sup>-1</sup> g<sub>cat</sub><sup>-1</sup>), slightly decreases for the 13 and 28ZnZrO<sub>x</sub> samples (STY = 0.39–0.42 g<sub>MeOH</sub> h<sup>-1</sup> g<sub>cat</sub><sup>-1</sup>), and then significantly diminishes upon addition of higher contents (STY = 0.29 g<sub>MeOH</sub> h<sup>-1</sup> g<sub>cat</sub><sup>-1</sup>), due to ZnO becoming the main phase, which is less active (Figure 2a). Interestingly, the 5ZnZrO<sub>x</sub> catalyst prepared by FSP displays an approximately twofold higher methanol STY compared to the most active CP system (13ZnZrO<sub>x</sub>,CP) with a ≈60% lower zinc content. This suggests that the inferior performance of CP catalysts is likely due to the synthesis approach, triggering incorporation of a substantial portion of zinc within the bulk of zirconia. Assessing methanol selectivity (*S*<sub>MeOH</sub>) at similar CO<sub>2</sub> conversion (*X*<sub>CO<sub>2</sub></sub>) levels indicates that the trend in methanol STY with respect to zinc content observed for FSP and CP catalysts is directly linked to that of *S*<sub>MeOH</sub> (Figure 2b). In fact, *S*<sub>MeOH</sub> remains virtually unchanged over FSP systems containing 5–28 mol% of zinc (≈80%), whereas it clearly reaches its maximum for 13ZnZrO<sub>x</sub>,CP (≈80%) and drops to 50% for 28ZnZrO<sub>x</sub>,CP. This hints that FSP offers a better control than CP at maximizing active sites that limit CO formation through the RWGS. Additionally, when compared at the same *X*<sub>CO<sub>2</sub></sub> (7%), CP and FSP samples featuring 13 mol% of zinc show similar *S*<sub>MeOH</sub> (≈80%, Figure 2b), suggesting that their active sites for methanol formation likely possess similar structure. Hence, their performance difference originates from FSP systems being more active in comparison to CP catalysts (Table S2, Supporting Information).

### 2.2. Characterization of Zinc Speciation and Zirconia Structure

In-depth characterization was carried out to rationalize the behavior of FSP and CP systems. Determination of the crystal structure and phase composition of the catalysts by X-ray diffraction (XRD, Figure 3a, Figures S1 and S2 and Tables S3 and S4, Supporting Information) showed that fresh FSP catalysts (up to 28 mol% Zn) contain a mixture of monoclinic (20–40%)

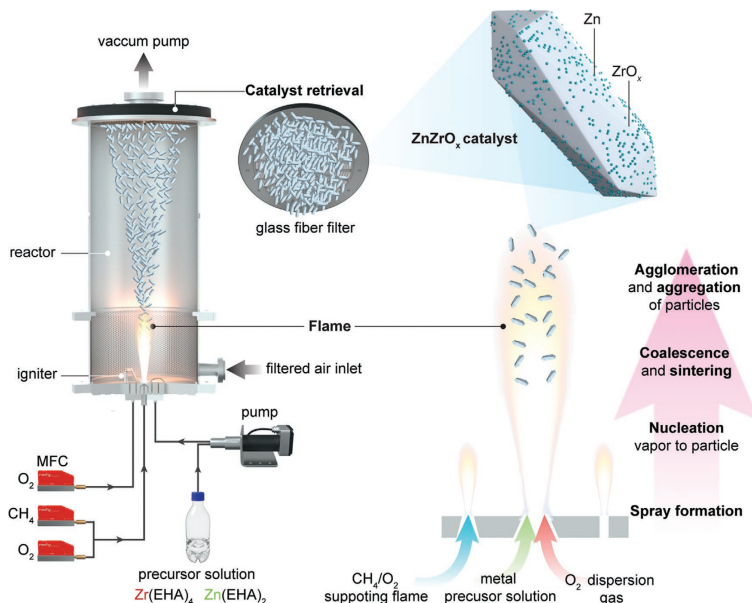
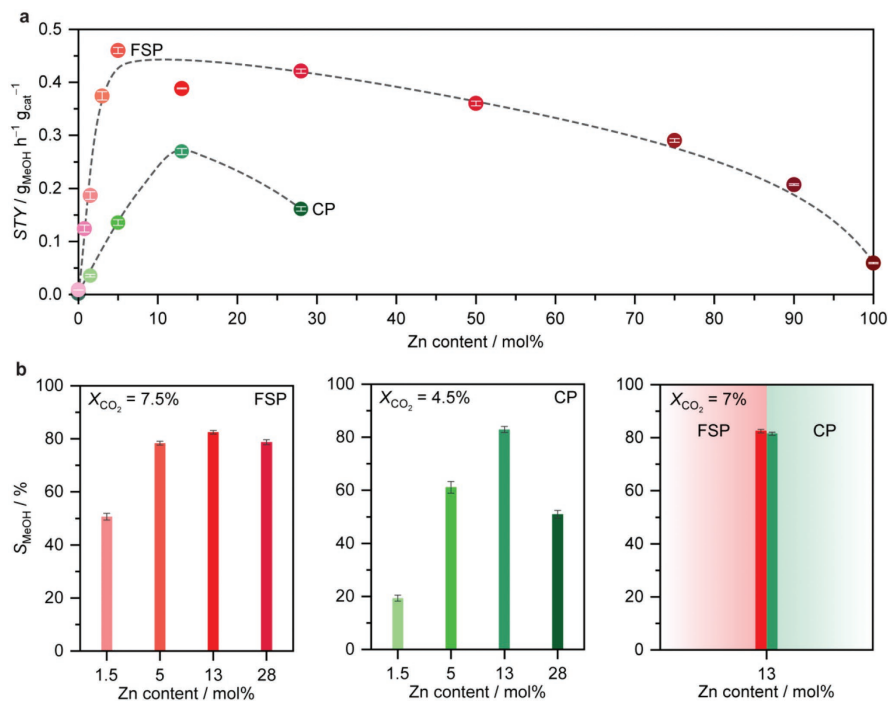


Figure 1. Scheme of the flame spray pyrolysis (FSP) setup and method used for the preparation of  $\text{ZnZrO}_x$  catalysts.

and tetragonal or cubic (60–80%) zirconia (*m*-, *t*-, and *c*- $\text{ZrO}_2$ , respectively), as *t* and *c* phases cannot be distinguished by XRD (Figure 3a and Figure S1 and Table S3, Supporting Information). The *m*- and *t*- or *c*- $\text{ZrO}_2$  relative compositions show no correlation with the zinc content whereas zinc oxide (ZnO) is detected and becomes the predominant phase upon addition of 13 and 75 mol% of zinc, respectively (Figure 3a and Figure S1 and Table S3, Supporting Information). At lower contents, zinc is most likely embedded into the  $\text{ZrO}_2$  lattice, forming a solid solution, or supported as ZnO clusters or nanoparticles smaller than  $\approx 4$  nm, the detection limit of the XRD instrument. In contrast, CP catalysts in fresh form generally crystallize into a pure *t*- $\text{ZrO}_2$  phase, with *m*- $\text{ZrO}_2$  (17%) and ZnO (20%) phases being detected only for the 1.5 and 28 $\text{ZnZrO}_x$ CP samples, respectively (Figure S2 and Table S4, Supporting Information), which is in line with previous reports.<sup>[10,12]</sup> The presence of *m*- $\text{ZrO}_2$  is likely due to the low zinc content in the 1.5 $\text{ZnZrO}_x$ CP sample, which is insufficient to stabilize the *t*- $\text{ZrO}_2$  polymorph, whereas ZnO is formed because the amount of zinc could still be higher than the saturation point of the  $\text{ZnZrO}_x$  solid solution; triggering phase segregation.<sup>[10]</sup> Upon reaction, the amount of *m*- $\text{ZrO}_2$  and ZnO slightly increased while that of *t*- $\text{ZrO}_2$  decreased for all FSP systems containing up to 28 mol% of zinc (Figure 3a and Figure S1 and Table S3, Supporting Information), hinting at some degree of catalyst restructuring. In the case of CP materials in used form (catalysts recovered after 12 h on stream), no detectable

change in the  $\text{ZrO}_2$  phase composition was observed, except for the 1.5 $\text{ZnZrO}_x$ CP sample in which the content of *m*- $\text{ZrO}_2$  increased to 25%, likely due to *t*-*m* transformation triggered by water formed under reaction (Figure S3 and Table S4, Supporting Information).<sup>[25]</sup> The crystallite size of *m*- and *t*- $\text{ZrO}_2$  was also estimated for fresh and used catalysts using the Scherrer equation (Tables S2 and S4, Supporting Information), but no correlation with the synthesis method, Zn content, or catalytic performance is observed. Consistent with the expected incorporation of zinc into lattice positions of the  $\text{ZrO}_2$  bulk phase, the main reflection characteristic of *t*- $\text{ZrO}_2$  ( $=30^\circ 2\theta$ ) shifts to higher angles with increasing Zn content (Figure S3a, Supporting Information), indicating that zinc is incorporated at lattice positions within the  $\text{ZrO}_2$  bulk phase, confirming the formation of a solid solution.<sup>[10]</sup> Remarkably, this phenomenon is not observed for FSP catalysts (Figure S3b, Supporting Information), suggesting that this method does not lead to bulk incorporation of zinc atoms, but rather disperse them at surface lattice positions of the  $\text{ZrO}_2$  carrier, with the metal surplus likely agglomerating into ZnO clusters and/or nanoparticles. X-ray photoelectron spectroscopy (XPS, Table S5, Supporting Information) revealed closely matched zinc surface and bulk compositions for 5 $\text{ZnZrO}_x$ , which remain unaltered upon reaction, indicating that zinc is indeed highly dispersed and located at the surface rather than the bulk sites of  $\text{ZrO}_2$ . Similarly, the presence of ZnO detected by XRD for 13 and 28 $\text{ZnZrO}_x$ , is accompanied by a



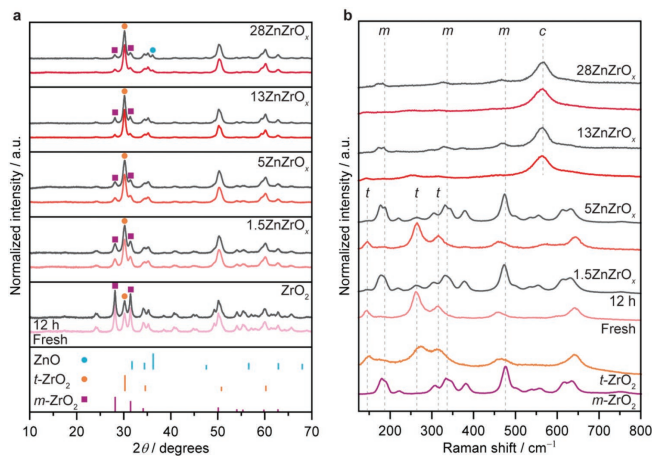
**Figure 2.** a) Methanol space-time yield (STY) and b) selectivity ( $S_{\text{MeOH}}$ ) during  $\text{CO}_2$  hydrogenation over  $\text{ZnCrO}_x$  catalysts prepared by flame spray pyrolysis (FSP) and coprecipitation (CP). Averaged values measured over 12 h on stream are presented with their corresponding error bars. Reaction conditions:  $T = 593 \text{ K}$ ,  $P = 5 \text{ MPa}$ ,  $\text{H}_2/\text{CO}_2 = 4$ , and  $\text{GHSV} = 24\,000 \text{ cm}^3 \text{ h}^{-1} \text{ g}_{\text{cat}}^{-1}$ .

decrease in the Zn surface concentration (Table S5, Supporting Information), which is expected as sintering diminishes the amount of Zn atoms exposed at the catalyst surface. Finally, the amount of Zn at the surface of all fresh and used CP materials is significantly lower compared to its total content (Table S5, Supporting Information), which further confirms that a substantial portion of zinc is incorporated into  $\text{ZrO}_2$  bulk phase during CP (Figure S3a, Supporting Information). A detailed discussion on zinc surface composition of FSP and CP catalysts can be found in Section S1.1 (Supporting Information).

To gain additional insights into the surface structure of the catalysts, fresh and used samples were analyzed by UV Raman spectroscopy using a 325 nm laser (Figure 3b). In principle, by varying the laser source, one can identify which oxide phase is present at different particle depths, from bulk to skin layers ( $\approx 10 \text{ nm}$ ).<sup>[26,27]</sup> Interestingly, two distinct trends emerge for FSP catalysts. The surface of fresh samples with low Zn content (i.e., 1.5 and 5 mol%) mainly comprise of  $t\text{-ZrO}_2$  (bands located at 145, 265, 315, 460, and 642  $\text{cm}^{-1}$ ),<sup>[28–30]</sup> which almost

fully transformed into a monoclinic phase (bands located at 180, 305, 378, 473, and 625  $\text{cm}^{-1}$ )<sup>[28]</sup> upon  $\text{CO}_2$  hydrogenation. In contrast, higher zinc contents (i.e., 13 and 28 mol%) lead to catalysts with enriched cubic surface structure (bands located at 564  $\text{cm}^{-1}$ )<sup>[10]</sup> in fresh form, which remains virtually unaltered upon reaction, except for some  $m\text{-ZrO}_2$  being also formed. Unfortunately, CP catalysts revealed themselves fluorescent when exposed to the 325 nm laser, which prevented the acquisition of Raman spectra. Such behavior has been reported for  $\text{ZrO}_2$ ,<sup>[28,31,32]</sup> and more generally for other metal oxides, and attributed to the defect generation in the lattice.<sup>[27]</sup> This observation corroborates XRD and XPS findings showing that CP catalysts experience incorporation of zinc to the bulk of  $\text{ZrO}_2$ , which likely creates additional structural defects.

Investigations by microscopy coupled to energy-dispersive X-ray (EDX) spectroscopy revealed that FSP promotes atomic dispersion of zinc on  $\text{ZrO}_2$  for contents up to 5 mol%, while the formation of  $\text{ZnO}$  nanoparticles occurs with higher amounts of zinc (Figure 4a). This “switch” in zinc speciation



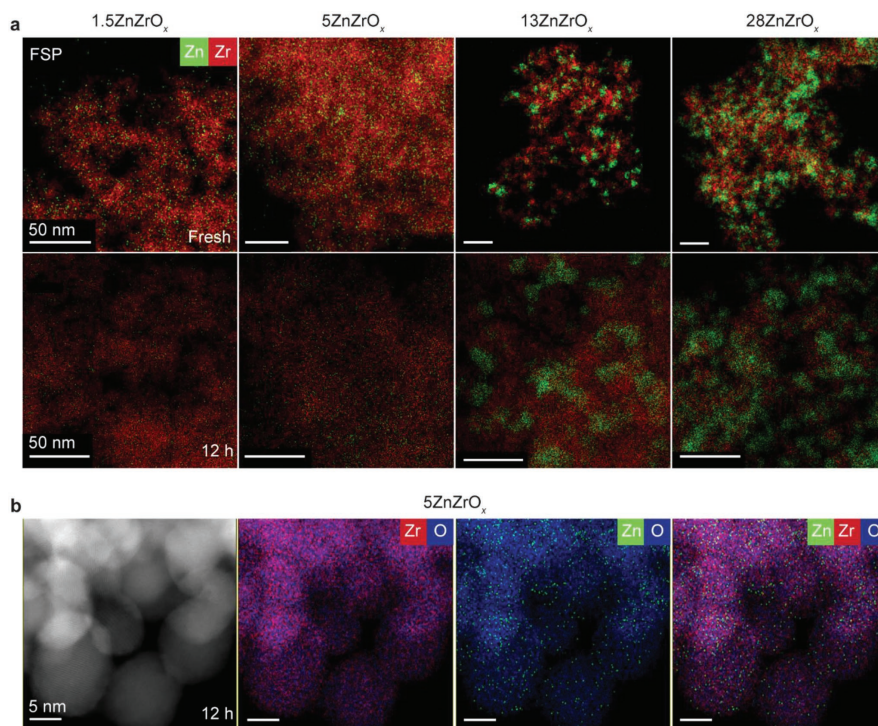
**Figure 3.** a) X-ray diffraction (XRD) patterns and b) Raman spectra of flame spray pyrolysis (FSP) made ZnZrO<sub>x</sub> catalysts in fresh form and after CO<sub>2</sub> hydrogenation for 12 h with *t*- and *m*-ZrO<sub>2</sub> carriers serving as reference. Reference patterns of pure phases are shown with vertical lines in the bottom panel. Reaction conditions: T = 593 K, P = 5 MPa, H<sub>2</sub>/CO<sub>2</sub> = 4, and GHSV = 24 000 cm<sup>3</sup> h<sup>-1</sup> g<sub>cat</sub><sup>-1</sup>.

for FSP systems coincides with the plateau in methanol STY experienced by 13 and 28ZnZrO<sub>x</sub> (Figure 2a) and suggests that atomically dispersed species likely saturate the surface sites at 5 mol% and excess zinc present in ZnO nanoparticles formed at higher contents likely spectate in the reaction. The zinc speciation remains unaltered over FSP catalysts upon reaction, particularly for the 5ZnZrO<sub>x</sub> sample (Figure 4a,b). In contrast, while zinc is also atomically dispersed in freshly coprecipitated materials even at high contents (i.e., 13 mol%, Figure S4, Supporting Information), most used samples (1.5 and 5ZnZrO<sub>x</sub>CP) show some degree of sintering. Still, the 13ZnZrO<sub>x</sub>CP is markedly stable with no sign of zinc agglomeration whereas severe phase segregation is present in both fresh and used 28ZnZrO<sub>x</sub>CP (Figure S4, Supporting Information). This observation most likely explains the volcano-shaped trend of CP catalysts (Figure 2), as ZnO is much less active in CO<sub>2</sub> hydrogenation to methanol<sup>[10]</sup> and can potentially cover and block some active sites of ZnZrO<sub>x</sub>. Finally, characterization of 5ZnZrO<sub>x</sub> 13ZnZrO<sub>x</sub>CP catalysts by high resolution transmission microscopy (HRTEM, Figure S5, Supporting Information) confirmed the high crystalline order in both samples. Consistent with the high dispersion of Zn, the observed lattice fringes correspond to ZrO<sub>2</sub>. In agreement with XRD findings, the fresh and used 5ZnZrO<sub>x</sub> samples exhibit *d*-spacings characteristic of the tetragonal and monoclinic phases, while only the former are present in 13ZnZrO<sub>x</sub>CP.

Quasi in situ X-ray absorption near-edge structure spectra at the Zn K-edge (XANES, Figure 5a) of used FSP 5 and 13ZnZrO<sub>x</sub>, directly isolated from the reactor without exposure to air, indicate the presence of Zn<sup>2+</sup> in both catalysts, especially when compared to those of hexagonal ZnO (*h*-ZnO) and Zn metal foil references (Figure 5a). Still, some features present

in the XANES spectrum of *h*-ZnO are substantially dampened in the lower-content catalyst, hinting at higher disorder in the Zn local structure, which could be explained by its atomic dispersion and thus stronger interaction with the ZrO<sub>2</sub> lattice, in line with previous reports.<sup>[33,34]</sup> For 13ZnZrO<sub>x</sub>, its XANES spectrum closely resemble that of *h*-ZnO, which agrees with microscopy findings evidencing the formation of ZnO nanoparticles (Figure 4a). Analysis of the extended X-ray absorption fine structure (EXAFS), Figure 5b and Table S6, Supporting Information) shows that both Zn–O and Zn–Zn scattering paths are present in the 13ZnZrO<sub>x</sub> catalyst whereas only the Zn–O feature with the total number of first oxygen neighbors of ≈2 was observed for 5ZnZrO<sub>x</sub>.<sup>[33,34]</sup> This confirms that the latter comprises of highly dispersed and isolated zinc atoms located within the surface lattice of ZrO<sub>2</sub>, while ZnO particles additionally exist in higher-content samples. XPS (Figure S6a,b, Supporting Information) further supported that surface zinc species are oxidized in all fresh and used FSP samples, as suggested by the absence of signals characteristic of metallic zinc in the Zn LMM Auger spectra.

Considering that FSP generally produces materials with improved textural properties,<sup>[35]</sup> the specific surface area (*S*<sub>BET</sub>) of both CP and FSP samples was determined by N<sub>2</sub> sorption (Figure 6a and Tables S3 and S4, Supporting Information). Remarkably, FSP materials display a twofold higher *S*<sub>BET</sub> in comparison to their CP counterparts, which is consistent with their superior catalytic performance. More specifically, the *S*<sub>BET</sub> of freshly coprecipitated systems drastically diminishes (from ≈70 to 20 m<sup>2</sup> g<sup>-1</sup>) with increasing zinc content (from 0 to 28 mol%), hinting at zinc behaving as a detrimental structure modifier, likely due to its incorporation into the bulk phase of ZrO<sub>2</sub>. In contrast, the *S*<sub>BET</sub> of FSP catalysts in fresh form

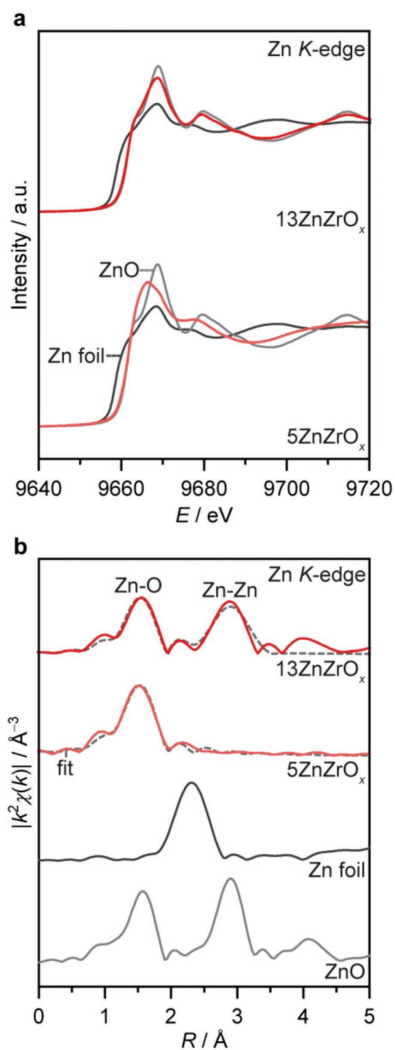


**Figure 4.** a) Energy-dispersive X-ray (EDX) maps of flame spray pyrolysis (FSP) made  $ZnZrO_x$  catalysts in fresh form and after  $CO_2$  hydrogenation for 12 h. b) High magnification scanning transmission electron microscopy high-angle annular dark-field (STEM-HAADF) image and corresponding EDX maps of the FSP-made  $5ZnZrO_x$  catalyst after  $CO_2$  hydrogenation for 12 h. Reaction conditions:  $T = 593$  K,  $P = 5$  MPa,  $H_2/CO_2 = 4$ , and  $GHSV = 24000$   $cm^3$   $h^{-1}$   $g_{cat}^{-1}$ .

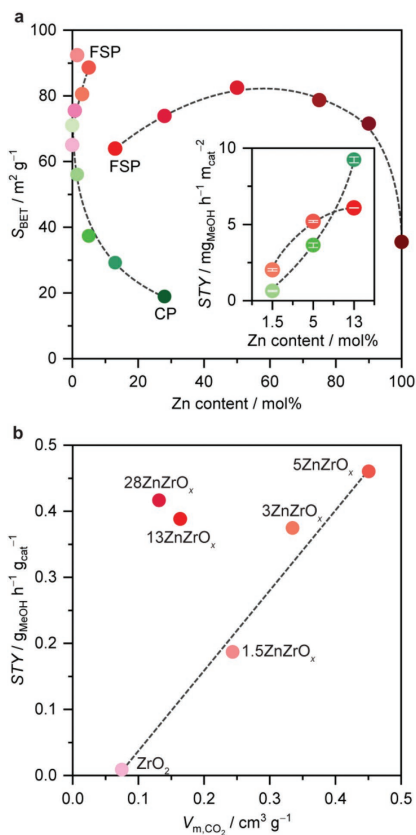
increases (from 65 to 90  $m^2$   $g^{-1}$ ) with the amount of zinc (up to 5 mol%), but decreases ( $\approx 65$ – $30$   $m^2$   $g^{-1}$ ) for higher-content samples (i.e., 13–100 mol% Zn) owing to the formation of ZnO nanoparticles. No significant variation in the  $S_{BET}$  was detected for used CP and FSP catalysts (Tables S3 and S4, Supporting Information), which is line with their stable methanol productivity. Besides, methanol STY values normalized by  $S_{BET}$  (see inset Figure 6a) further highlight that the enhanced surface area of FSP in comparison with CP samples noticeably contributes to their improved performance at low zinc content (up to 5 mol%), where the zinc speciation is homogenous. Interestingly, volumetric  $CO_2$  chemisorption measured at reaction temperature (593 K, Figure 6b) revealed that methanol STY linearly correlates with the  $CO_2$  uptake of FSP catalysts containing up to 5 mol% of Zn. This provides additional evidence that highly dispersed and isolated zinc sites present at the catalyst surface, particularly for  $5ZnZrO_x$ , are paramount to form the catalytic

ensemble and suggest that maximizing such speciation is crucial to ensure maximal methanol productivity.

With sound experimental analyses indicating that the most active FSP and CP systems possess analogous catalytic ensembles, their structure was further examined by DFT. Since all three  $ZrO_2$  polymorphs (*m*- $ZrO_2$ , *t*- $ZrO_2$ , and *c*- $ZrO_2$ ) were detected for  $ZnZrO_x$  catalysts, their relative stability in undoped and Zn-doped forms was investigated. The computed formation energy ( $E_f$ , Equations S1 and S2, Supporting Information) shows that monoclinic is the most stable polymorph of zinc-free  $ZrO_2$ , followed by *t*- and *c*- which are 0.11 and 0.21 eV per formula unit less stable, respectively. Considering that zinc incorporation was shown to occur at distinct sites of  $ZrO_2$  depending on the preparation method, and that the stability of the resulting  $ZrO_2$  polymorph is governed by the interplay between the zinc structure and location, as well as the creation of oxygen vacancies, the potential effects were assessed for both bulk and surfaces of

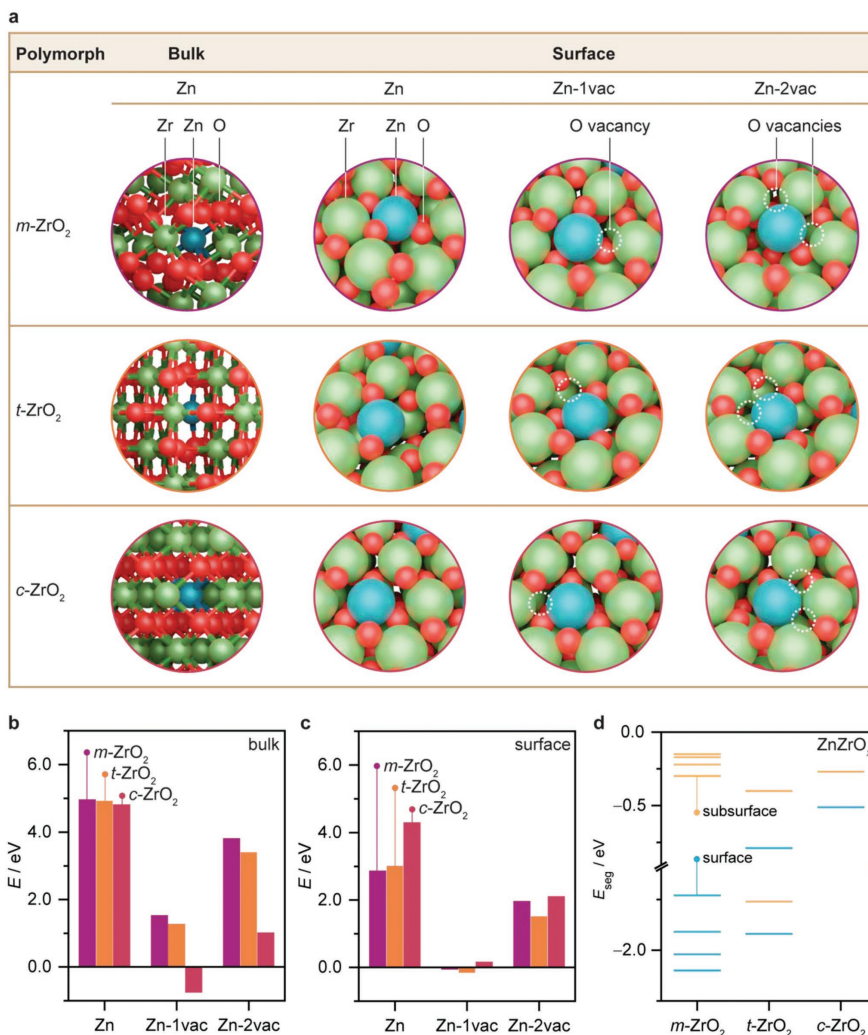


**Figure 5.** a) *k*-weighted Zn K-edge X-ray absorption near-edge structure (XANES), and b) extended X-ray absorption fine structure (EXAFS) spectra of flame spray pyrolysis (FSP) made ZnZrO<sub>x</sub> systems, with fit model and spectra of ZnO and metallic Zn serving as references, for catalysts after CO<sub>2</sub> hydrogenation for 20 h. Reaction conditions: *T* = 593 K, *P* = 5 MPa, H<sub>2</sub>/CO<sub>2</sub> = 4, and GHSV = 24 000 cm<sup>3</sup> h<sup>-1</sup> g<sub>cat</sub><sup>-1</sup>.



**Figure 6.** Correlation between a) Brunauer-Emmett-Teller (BET) surface area (S<sub>BET</sub>) and zinc content, and b) methanol space-time yield (STY) and volumetric CO<sub>2</sub> uptake (V<sub>m,CO<sub>2</sub></sub>) of flame spray pyrolysis (FSP) made ZnZrO<sub>x</sub> systems. Inset depicts methanol STY of selected coprecipitated (CP) and FSP catalysts normalized by their corresponding S<sub>BET</sub>. Averaged values measured over 12 h on stream are presented with their corresponding error bars. Reaction conditions: *T* = 593 K, *P* = 5 MPa, H<sub>2</sub>/CO<sub>2</sub> = 4, and gas hourly space velocity (GHSV) = 24 000 cm<sup>3</sup> h<sup>-1</sup> g<sub>cat</sub><sup>-1</sup>.

ZrO<sub>2</sub> polymorphs (Equations (S3) and (S4), Supporting Information). For this reason, supercells were used to simulate bulk phases (Figure S7, Supporting Information) whereas slab models of the most thermodynamically stable termination of each polymorph to assess surface and subsurface sites (Figures S7 and S8, Supporting Information).<sup>[36,37]</sup> A detailed discussion of all zinc incorporation sites and oxygen vacancies explored can be found in Section S1.2, Figures S10–S14, Supporting Information.



**Figure 7.** a) Density functional theory (DFT) models and potential energies ( $E$ ) associated with the most stable structures with one incorporated zinc atom (Zn) and one (Zn-1vac) and two (Zn-2vac) oxygen vacancies at b) bulk and c) surface sites of monoclinic (*m*), tetragonal (*t*), and cubic (*c*) ZrO<sub>2</sub> polymorphs. d) Segregation energies ( $E_{\text{seg}}$ ) for a zinc atom to move from bulk to surface and subsurface sites in distinct ZrO<sub>2</sub> polymorphs.

The incorporation of Zn to bulk sites is generally more favored for *t*-ZrO<sub>2</sub> and *c*-ZrO<sub>2</sub> compared to *m*-ZnZrO<sub>2</sub>, and in all cases is accompanied by the formation of oxygen vacancies.

This explains the presence of *t*-ZrO<sub>2</sub> on CP systems even though it is less stable than *m*-ZrO<sub>2</sub> (Figure 7a,b, and Table S8, Supporting Information). Similarly, replacing Zr by Zn on the

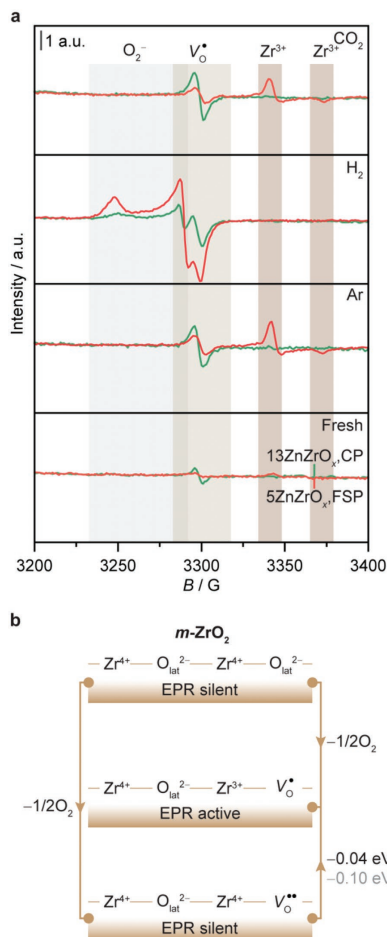


most stable surfaces is fostered by the formation of vacancies and follows the same trend observed for bulk phases (Figure 7a,c, and Table S9, Supporting Information). These observations are further supported by the Raman spectra of fresh FSP catalysts, which contains  $t$ - and  $c$ -ZrO<sub>2</sub> phases on the surface (Figure 3b). Finally, Zn segregation energies ( $E_{\text{seg}}$ , Equation (S5), Supporting Information) show that surface sites are more thermodynamically stable compared to bulk positions for the three polymorphs, in particular for  $m$ -ZnZrO<sub>2</sub> (Figure 7d and Table S10, Supporting Information). This is in line with experimental findings showing that FSP induces preferential location of Zn atoms at the catalyst surface whereas bulk incorporation is favored by CP. In principle, the high temperatures experienced by materials during the FSP synthesis likely drive zinc toward occupying surface positions while the fast cooling rates, which is also characteristic of this synthesis method, assists on stabilizing such catalyst architecture, as previously reported for other systems.<sup>138,391</sup> Additionally,  $c$ -ZnZrO<sub>x</sub> exhibits the less favored segregation energies, which could also explain the formation of these phase on the catalyst surface only at high Zn contents (i.e., 13 mol%, Figure 3b).

### 2.3. Insights into the Vacancy Formation Mechanism

Oxygen vacancies ( $V_{\text{O}}$ ) are common defects in reducible oxides and generally dictate their properties (Section S1.3, Figures S16–S18, Supporting Information). Nonetheless, despite their importance for promoting CO<sub>2</sub> conversion on ZnZrO<sub>x</sub> systems, there is still a lack of fundamental understanding of the formation and dynamics of such sites for this particular catalyst family.<sup>401</sup> For this reason, in situ electron paramagnetic spectroscopy (EPR) was applied to investigate the defect chemistry on the FSP 5ZnZrO<sub>x</sub> and CP 13ZnZrO<sub>x</sub> catalysts under practically relevant gaseous atmospheres (Figure 8a). As expected, the signal typically assigned to  $V_{\text{O}}$  is relatively weak for the fresh samples. When heated to 593 K in an inert atmosphere, a narrow and stronger isotropic signal (centered at  $g = 2.003$ ) appears for both catalysts, whereas only 5ZnZrO<sub>x</sub> shows an anisotropic feature at higher field with an axial  $g$  ( $g_{\text{xx}} = g_{\text{yy}} = 1.977$ ,  $g_{\text{zz}} = 1.959$ ). These signals are attributed to magnetically isolated unpaired electrons in oxygen vacancy ( $V_{\text{O}}^{\bullet}$ , electrons are represented by  $\bullet$ ) and to reduced Zr atoms with one unpaired  $d$  electron ( $\text{Zr}^{3+}$ ), respectively,<sup>41–43</sup> indicating that thermally induced vacancy generation predominates over FSP and CP catalysts.  $V_{\text{O}}^{\bullet}$  and  $\text{Zr}^{3+}$  are formed by trapping the electrons which are released after the formation of an oxygen vacancy ( $\text{O}_{\text{lat}}^{2-} \rightleftharpoons \text{O}_2 + 2e^-$ ).

By investigating oxygen vacancies in pure and Zn-containing ZrO<sub>2</sub> surfaces using DFT simulations (Figures S13 and S15, Supporting Information), we uncovered that  $V_{\text{O}}^{\bullet}$ -Zr<sup>3+</sup> moieties (EPR active) are indeed more stable than  $V_{\text{O}}^{\bullet}$ -Zr<sup>4+</sup> (EPR silent) by 0.04 eV (or 0.10 eV when calculated using a hybrid functional HSE03<sup>44,45</sup>) with 13%<sup>46</sup> of nonlocal Hartree-Fock exchange, Figure 8b). Moreover, the simulations predict the preferential formation of  $V_{\text{O}}^{\bullet}$ -Zr<sup>3+</sup> moieties over monoclinic zinc-free zirconia regions (Figure 8b). This behavior is in line with the stronger EPR signal observed for 5ZnZrO<sub>x</sub> (Figure 8a), which



**Figure 8.** a) In situ electron paramagnetic spectroscopy (EPR) spectra of the flame spray pyrolysis (FSP) made 5ZnZrO<sub>x</sub> and coprecipitated (CP) 13ZnZrO<sub>x</sub> catalysts measured first under flowing Ar (100 min), followed by H<sub>2</sub> (100 min), and finally CO<sub>2</sub> (100 min). Activation conditions:  $T = 593$  K,  $P = 0.1$  MPa,  $m_{\text{cat}} = 10$  mg, and  $\text{flow}(\text{Ar}) = \text{flow}(\text{H}_2) = \text{flow}(\text{CO}_2) = 20$  cm<sup>3</sup> min<sup>-1</sup>. b) Oxygen vacancy formation mechanism for  $m$ -ZrO<sub>2</sub> showing EPR active and silent structures obtained by density functional theory (DFT) simulations ( $-0.04$  and  $-0.10$  eV (in gray) were obtained with the Perdew–Burke–Ernzerhof (PBE) and HSE03 functional, respectively).

contains  $m\text{-ZrO}_2$ , and suggests that  $V_O$  located at the catalytic ensemble of  $\text{ZnZrO}_x$  are likely not directly detected by EPR. Analysis of the vacancy formation energies ( $E_{\text{vac}}$ , Figure S9, Supporting Information), which indicate that generating  $V_O$  close to Zn atoms is significantly more favored than in zinc-free zirconia regions (Figure S15, Supporting Information), further supports this hypothesis. Indeed, the former structure is very exothermic in  $\text{ZnZrO}_x$  for the three zirconia polymorphs ( $E_{\text{vac}} = -3.06, -4.42, \text{ and } -3.93$  for  $m-, t-, \text{ and } c\text{-ZnZrO}_x$ , respectively), and thereby more relevant for catalytic purposes (Figure S19, Supporting Information). However, defect sites close to Zn result in EPR silent species ( $V_O^{**}$ ) and, thus, cannot be directly probed by EPR measurements.

In situ EPR measurements under  $\text{H}_2$  feeds revealed the formation of superoxide species ( $\text{O}_2^-$ ) on both samples, generating a characteristic anisotropic signal with an orthorhombic  $g$  ( $g_{xx} = 2.007, g_{yy} = 2.014, g_{zz} = 2.041$ , Figure 8a).<sup>[47]</sup> DFT simulations suggest that the  $\text{O}_2^-$  species are formed and stabilized owing to hydrogen incorporation into the oxygen vacancy (EPR silent, Figure S20a,b, Supporting Information). Specifically, zinc incorporation into the  $m\text{-ZrO}_2$  lattice creates these vacancies and peroxide species, with the latter evolving into superoxo  $\text{O}_2^-$  species (EPR active) upon  $\text{H}_2$  exposure (Figure S20b, Supporting Information). In principle, the  $\text{O}_2^-$  signals provide indirect information about the density of  $\text{H}_2$ -induced EPR silent  $V_O$  located at the catalyst ensemble of  $\text{ZnZrO}_x$  systems. In fact,  $13\text{ZnZrO}_x\text{-CP}$  shows significantly weaker  $\text{O}_2^-$  signals than  $5\text{ZnZrO}_x$  (Figure 8a), indicating that the latter promotes  $V_O$  formation substantially, which is in line with its superior methanol productivity. Additionally,  $\text{Zr}^{3+}$  signals disappear upon exposure to  $\text{H}_2$ , indicating that the excess electron associated with  $\text{Zr}^{3+}$  is either trapped in empty vacancies<sup>[41]</sup> or not localized at a single zirconium cation (Figure S20a, Supporting Information). Finally, under a  $\text{CO}_2$ -containing atmosphere,  $V_O^{\bullet}-\text{Zr}^{3+}$  signals recover due to the formation of  $\text{H}_2\text{O}$  from  $\text{O}_2^-$  species (Figure S20a, Supporting Information). Overall,  $V_O^{\bullet}, \text{Zr}^{3+}$ , and  $\text{O}_2^-$  EPR signals can be considered proxies to probe the total amount of oxygen vacancies generated over  $\text{ZnZrO}_x$  systems.

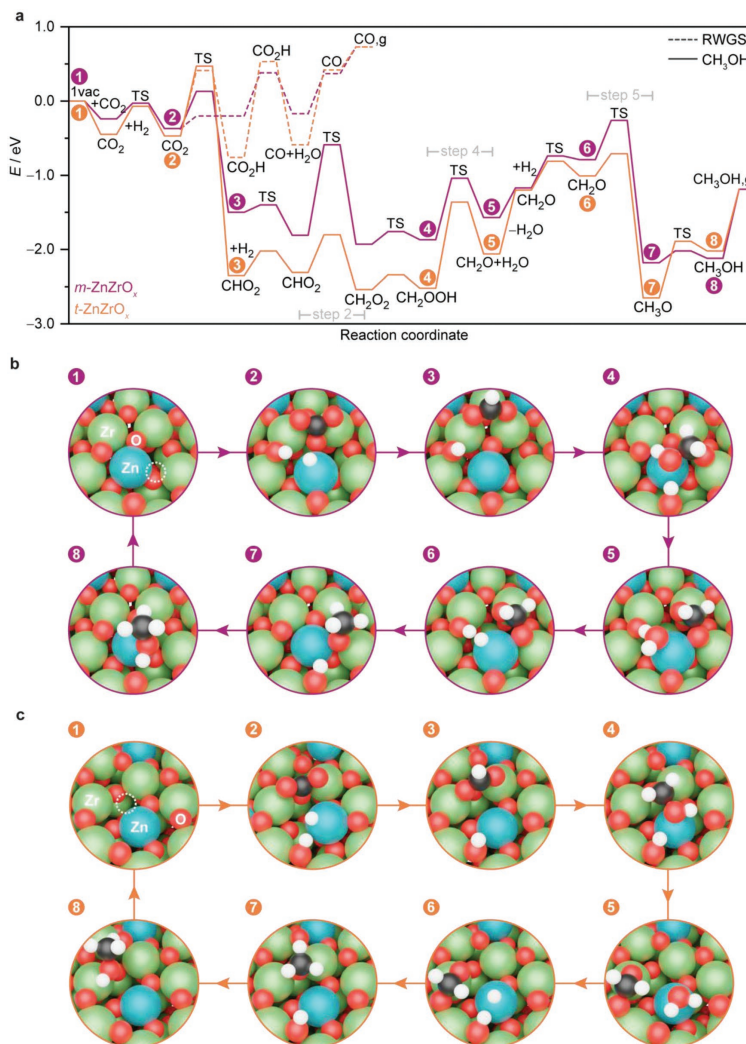
#### 2.4. Mechanism and Kinetic Modeling

To explain the reactivity of FSP and CP catalysts, energy profiles for methanol ( $\text{CH}_3\text{OH}$ ) and CO formation were calculated for the three Zn-containing  $\text{ZrO}_2$  polymorphs containing one oxygen vacancy (Figure 9 and Figures S21–S24, Supporting Information). Since previous studies on  $\text{ZnZrO}_x$ <sup>[10]</sup> and other oxides (i.e.,  $\text{In}_2\text{O}_3$ <sup>[19]</sup> and metal-doped  $\text{In}_2\text{O}_3$ <sup>[18,24]</sup>) have shown that  $\text{CO}_2$  hydrogenation to  $\text{CH}_3\text{OH}$  is more favored through the formate pathway, this route was selected to study all three  $\text{ZrO}_2$  polymorphs. The process starts with  $\text{CO}_2$  activation through chemisorption as carbonate with the two oxygens interacting with open Zr metal sites.<sup>[48]</sup> This step is followed by the heterolytic activation of molecular  $\text{H}_2$  leading to a  $\text{ZnH-OH}$  pair. Then, the hydride is transferred to  $\text{CO}_2$  to obtain formate ( $\text{CHO}_2$ ), which is either subsequently protonated to form formic acid ( $\text{CHOOH}$ ) or hydrogenated to  $\text{CH}_2\text{O}_2$  following the heterolytic dissociation of a second  $\text{H}_2$  molecule. The

second path is favored for the three polymorphs, in particular for  $t\text{-ZnZrO}_x$  (Figures S25–S27, Supporting Information). The formation of  $\text{CH}_2\text{O}_2$  is followed by its protonation to  $\text{CH}_2\text{OOH}$  and concomitant dehydration leading to  $\text{CH}_3\text{O}$  and  $\text{H}_2\text{O}$ . The transfer of a hydride and a proton, produced by dissociative activation of a third  $\text{H}_2$  molecule, yields methanol. In contrast, the RWGS reaction to form CO starts with the protonation of  $\text{CO}_2$  leading to a carboxylate ( $\text{COOH}$ ), which is further protonated and dehydrated forming CO and  $\text{H}_2\text{O}$ .  $\text{CH}_3\text{OH}$  formation is favored over CO for the three polymorphs. Following this prediction and the stable methanol STY experienced by  $5\text{ZnZrO}_x$  (FSP) and  $13\text{ZnZrO}_x$  (CP) when evaluated in the hydrogenation of hybrid  $\text{CO}_2\text{-CO}$  feeds (60 h) containing equimolar ratios of both carbon feedstocks (Figure S28, Supporting Information), we can conclude that methanol formation through the CO route is very unlikely. Additionally, analysis of high-angle annular dark-field scanning transmission electron microscopy EDX (HAADF-STEM-EDX) images (Figure S29, Supporting Information) shows only slight zinc aggregation in  $5\text{ZnZrO}_x$  (FSP) and  $13\text{ZnZrO}_x$  (CP) samples retrieved after the long-term evaluation, consistent with their remarkable stable performance. This confirms that regardless of the synthesis method used,  $\text{ZnZrO}_x$  catalysts possess remarkable robustness against feed composition fluctuations and overreduction by stronger reducing species such as CO, a common byproduct in  $\text{CO}_2$  hydrogenation.

When comparing the three  $\text{ZrO}_2$  polymorphs, their energy profiles show that key intermediates, such as  $\text{CHO}_2, \text{CH}_2\text{O}_2, \text{CH}_2\text{OOH}$ , and  $\text{CH}_3\text{O}$ , are overstabilized on  $t-$  and  $c\text{-ZnZrO}_x$  (Figure 9 and Figure S21, Supporting Information). We attribute these differences to the local coordination of Zn in the active site of these polymorphs (Figure S30, Supporting Information). While Zn adopts a square planar geometry on  $m\text{-ZnZrO}_x$ , the coordination on  $t-$  and  $c\text{-ZnZrO}_x$  is a distorted tetrahedra similar to the tetrahedral coordination of Zn in its bulk ZnO oxide. Additionally, oxygen atoms of the overstabilized intermediates interact with open Zr sites and some of them also with Zn. Therefore, we put forward the distinct acidity of surface metal cations as a key reason for differences in reactivity between  $m\text{-ZnZrO}_x$  and the other two Zn-containing zirconia polymorphs (Section S1.4, Figure S31, Supporting Information).

A practical kinetic model was developed for the most active catalyst to link the DFT-derived insights on energetics and kinetic barriers over the active  $m\text{-ZnZrO}_x$  polymorph at the atomic scale with reaction rates at the reactor level (Section S1.5, Supporting Information). To build the model we employed 93 experimental data points obtained from the results of  $\text{CO}_2$  hydrogenation over the FSP-made  $5\text{ZnZrO}_x$  at different  $T, P$ , gas hourly space velocity (GHSV), and  $\text{H}_2/\text{CO}_2$  ratios. A Langmuir–Hinshelwood–Hougen–Watson (LHHW) mechanism was employed for modeling the adsorption, elementary surface reaction, and desorption steps corresponding to the DFT reaction mechanism (Figure 9). Three models were evaluated and compared assuming different rate-determining steps (rds A = step 2, B = step 4, and C = steps 4 + 5, Figure 9a) and a one-site mechanism (two species adsorbed on the same site, \*, Table S12, Supporting Information). The latter offers the best fit to the data and hints that the lumped fourth and fifth



**Figure 9.** a) Reaction energy profiles for CO<sub>2</sub> hydrogenation to CH<sub>3</sub>OH (solid line) and the competing RWGS reaction (dashed line) on *m*-ZnZrO<sub>x</sub> (purple) and *t*-ZnZrO<sub>x</sub> (orange) systems containing one oxygen vacancy. Intermediates labels (1–8) are the same for both systems. Snapshots of representative intermediates for b) *m*-ZnZrO<sub>x</sub> and c) *t*-ZnZrO<sub>x</sub> models. Color code: Zr (green), Zn (blue), O (red), C (dark gray), H (white), and oxygen vacancy (dotted white circles).

hydrogenation steps, combining those with the largest kinetic barrier (i.e., protonation of  $\text{CH}_2\text{OOH}^*$  followed by dissociation to  $\text{CH}_2\text{O}^*$  and  $\text{H}_2\text{O}^*$ , and further hydrogenation of  $\text{CH}_2\text{O}^*$  leading to  $\text{CH}_3\text{O}^*$ , Figure 9) is the rds.

Moreover, DFT suggests a different adsorption site depending on the intermediate pointing to a two-site mechanism (two species adsorbed on different sites, \* and #). However, including this atomistic detail brings no statistical improvement in the model (Figure 10a,b and Tables S12 and S13, Supporting Information). This is because the two-site mechanism assumes that both sites behave as totally independent variables, but the number of vacancies (required for  $\text{CO}_2$  trapping) and available oxygens (useful in  $\text{H}_2$  activation) are interdependent (i.e., if a vacancy is present  $\text{H}_2$  cannot be activated and vice versa). Thus, spatially resolved adsorption sites does not directly mean that their site counting is directly uncoupled. Then, the one-site model C was used to obtain the expressions and fitted parameters for the MeOH formation and RWGS reactions (Table S13, Supporting Information). From the overall rate constants, the apparent activation energies of the MeOH formation and the RWGS reaction pathways are 109.7 and 124.5  $\text{kJ mol}^{-1}$ , respectively, in line with experimental observations as well as DFT simulations that CO formation has a higher activation barrier while methanol formation is comparatively favorable. As for other catalysts methanol and water desorption steps have significant barriers but not limiting.

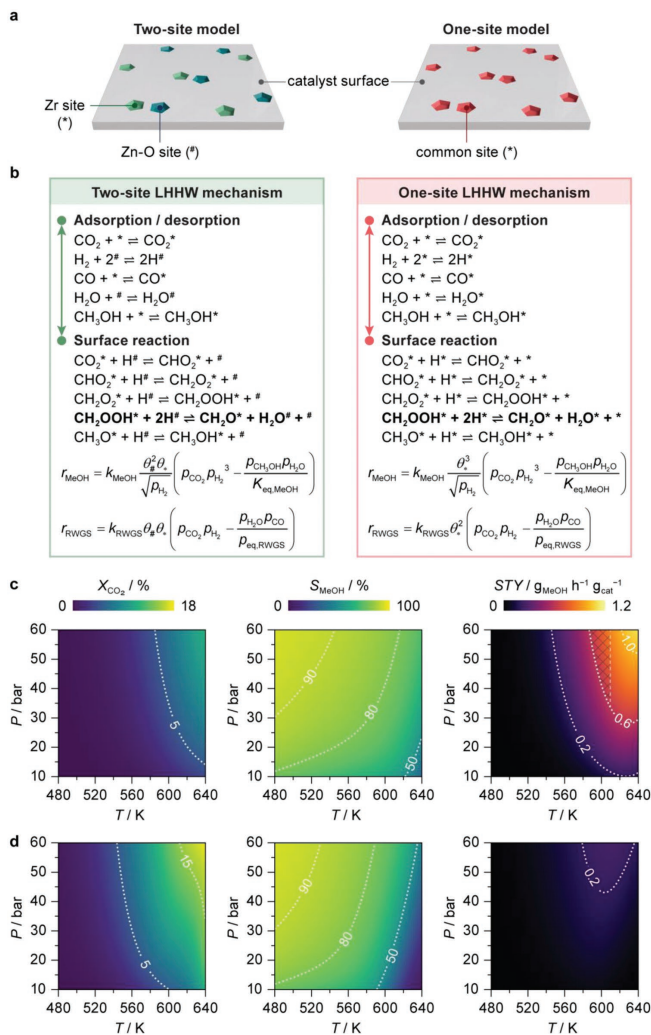
Model predictions of single-pass  $X_{\text{CO}_2}$ ,  $S_{\text{MeOH}}$ , and methanol STY are plotted in Figure 10c,d for a reactor operating in a process-relevant temperature and pressure range under continuous flow at high and low space velocities. At  $\text{GHSV} = 8000 \text{ cm}^3 \text{ h}^{-1} \text{ g}_{\text{cat}}^{-1}$ , overall  $\text{CO}_2$  conversion approaches the limit dictated by thermodynamic equilibrium, at the expense of low  $S_{\text{MeOH}}$ . On the other hand, at  $\text{GHSV} = 48\,000 \text{ cm}^3 \text{ h}^{-1} \text{ g}_{\text{cat}}^{-1}$ , the reaction is kinetically controlled as  $X_{\text{CO}_2}$  remains below 5% at temperatures lower than 600 K with higher  $S_{\text{MeOH}}$ , as well as superior methanol STY theoretically exceeding  $1 \text{ g}_{\text{MeOH}} \text{ h}^{-1} \text{ g}_{\text{cat}}^{-1}$  at sufficient pressures. Based solely on thermodynamic arguments, one could imagine using FSP catalysts at lower temperatures but higher pressures. However, since hydrogen activation, and related oxygen vacancy formation, are limited at lower temperatures, methanol productivity also decreases with this parameter. Since  $S_{\text{MeOH}}$  is still relatively high at 593 K and 50 bar ( $\approx 80\%$ , Table S2, Supporting Information), it would not significantly improve by decreasing the operating temperatures. Indeed, the ideal operating window for maximizing single-pass MeOH yield, considering also catalyst deactivation which becomes significant when operating at extremely high temperatures, lies around 580–610 K. This is a higher temperature range than that for  $\text{In}_2\text{O}_3$ -based catalysts, and in turn higher than that for Cu-based catalysts. The positive variation of all performance indicators with increasing  $P$ , as well as the trade-off between  $X_{\text{CO}_2}$  with  $S_{\text{MeOH}}$  with changing  $T$  and  $\text{GHSV}$ , are evident trends common to  $\text{CO}_2$ -to-methanol over different MeOH synthesis catalysts.

Overall, the catalyst surface area noticeably impacts the performance difference between FSP and CP systems, but it is not the only factor. FSP also improves zinc utilization and maximizes its location and atomic dispersion at surface lattice

positions of the  $\text{ZrO}_2$  phase, which is also critical for obtaining improved methanol productivity. Additionally, FSP is a scalable and one-step preparation method, which requires no postsynthetic treatments such as washing and calcination steps. Still, FSP and CP catalysts containing atomically dispersed zinc species possess identical active ensembles, which comprise an oxygen vacancy and neighboring zinc, zirconium, and an oxygen associated with zirconium atoms. Due to their intricate and dynamic nature, estimating the number of active ensembles requires determination of both the density of oxygen vacancies and surface Zn dispersion under operando conditions. However, methodologies for quantifying these parameters are lacking, which hinders the calculation of turnover frequencies of both FSP and CP catalysts and, therefore, should be tackled in future studies.

### 3. Conclusions

In summary, we presented  $\text{ZnZrO}_x$  catalysts attained by a one-step FSP method and featuring improved zinc utilization that significantly outperform the state-of-the-art coprecipitated systems in  $\text{CO}_2$  hydrogenation to methanol, especially with Zn contents up to 5 mol%. The holistic approach integrating catalytic evaluation, in-depth characterization, DFT simulations, and kinetic modeling permitted a thorough comparison of FSP and CP catalysts and hence derive detailed synthesis–structure–performance relationships. In general, methanol productivity is boosted over systems containing a high concentration of atomically dispersed  $\text{Zn}^{2+}$  sites doped at lattice positions within the  $\text{ZrO}_2$  surface, which is present on both FSP and CP catalysts and was identified as their common catalytic ensemble. However, unlike CP, FSP grants materials with enhanced surface area (60–90 versus 20–50  $\text{m}^2 \text{ g}^{-1}$ ), owing to its ability to maximize isolated surface  $\text{Zn}^{2+}$  species without inducing zinc incorporation into the bulk phase of the  $\text{ZrO}_2$  carrier, a common feature of CP that negatively impacts textural properties of  $\text{ZnZrO}_x$  materials. In addition, the unique architecture of the flame-made catalyst facilitates the creation of oxygen vacancies upon reaction, as evidenced by in situ EPR spectroscopy. DFT simulations further elucidated that  $\text{V}_\text{O}^\bullet$ ,  $\text{Zr}^{3+}$ , and  $\text{O}_2^-$  EPR fingerprints used to probing the vacancy dynamics, act as proxy to also detecting defects close to the  $\text{Zn}^{2+}$  sites, which are more easily formed than those next to  $\text{Zr}^{4+}$  ions but are generally EPR silent. More importantly, active ensembles comprising an oxygen vacancy and neighboring zinc, zirconium, and an oxygen associated with zirconium atoms markedly foster methanol formation through the formate path, particularly for zinc-doped monoclinic  $\text{ZrO}_2$ , while hindering CO production. Finally, kinetic analyses enabled the development of models with significant predictive power of the catalytic performance at process-relevant conditions. Overall, this study advances the atomic-level understanding of  $\text{ZnZrO}_x$  catalytic systems, and offers a promising design and practical guidelines for their implementation in methanol production from  $\text{CO}_2$ . The FSP approach reported can also potentially revitalize research efforts toward more sustainable and efficient heterogeneous catalytic materials for diverse energy-related applications.



**Figure 10.** a) Schematic representation of the two- and one-site kinetic models, depicted on the left and right, respectively. b) Elementary steps and rate expressions for the two model variants with the rate-determining step (rds, which results from the lumped fourth and fifth hydrogenation steps depicted in Figure 9a. That is, the protonation of  $\text{CH}_2\text{OOH}^*$  followed by dissociation to  $\text{CH}_2\text{O}^*$  and  $\text{H}_2\text{O}^*$ , and the hydrogenation of  $\text{CH}_2\text{O}^*$  leading to  $\text{CH}_3\text{O}^*$ ) marked in bold. The one-site model predictions of overall  $\text{CO}_2$  conversion, methanol selectivity, and methanol space-time yield (STY) for  $\text{CO}_2$  hydrogenation over the  $5\text{ZnZrO}_x$  catalyst prepared by flame spray pyrolysis (FSP) as a function of reaction temperature and total pressure, at c) high and d) low space velocities. Reaction conditions:  $\text{H}_2/\text{CO}_2=4$ , and c) gas hourly space velocity (GHSV) =  $48\,000\text{ cm}^3\text{ h}^{-1}\text{ g}_{\text{cat}}^{-1}$ , d) GHSV =  $8000\text{ cm}^3\text{ h}^{-1}\text{ g}_{\text{cat}}^{-1}$ . Dotted contour lines show values referenced in the discussion as a guide for readers.

#### 4. Experimental Section

**Catalyst Synthesis-Flame Spray Pyrolysis:** ZnZrO<sub>x</sub> catalysts with a Zn content ranging from 0 to 100 mol% were synthesized by FSP (denoted as ZnZrO<sub>x</sub>/CP). Zinc(II) and zirconium(IV) 2-ethylhexanoate in the desired molar ratio were dissolved in 2-ethylhexanoate and tetrahydrofuran (EHA/THF mass ratio of 2:1) to yield a 5.9 wt% solution of Zn:Zr equivalents. The precursor solution was then injected into a 0.4 mm nozzle at a flow rate of 5 L min<sup>-1</sup>, where it was dispersed by a 5 L min<sup>-1</sup> stream of oxygen at 1.5 bar. Pilot flames sustained by a 2:1 oxygen/methane feed at 3.6 L min<sup>-1</sup> ensured ignition of the spray. Such conditions have been reported to generate average flame temperature of 2500–3000 K.<sup>[23,49,50]</sup> The resulting nanoparticles were collected on a glass fiber filter (GF/A-6) and used in CO<sub>2</sub> hydrogenation without further treatment.

Catalysts with a molar zinc content ranging from 1.5 to 28 mol% (denoted as ZnZrO<sub>x</sub>/CP) were prepared by coprecipitation, based on a reported procedure.<sup>[10]</sup> The method is described for a zinc content of 13 mol%. Briefly, zinc nitrate hexahydrate (1.3 g, Zn(NO<sub>3</sub>)<sub>2</sub>·6H<sub>2</sub>O, Sigma-Aldrich, >99%) and zirconyl chloride octahydrate (9.7 g, ZrOCl<sub>2</sub>·8H<sub>2</sub>O, Sigma-Aldrich, 98%) were dissolved in deionized water (200 cm<sup>3</sup>). Separately, ammonium carbonate (6.4 g, (NH<sub>4</sub>)<sub>2</sub>CO<sub>3</sub>, Sigma-Aldrich, >30% NH<sub>3</sub> basis) was dissolved in deionized water (200 cm<sup>3</sup>). The precipitant solution was added dropwise to the precursor solution at 343 K under magnetic stirring (~500 rpm) until reaching pH 8. After 2 h of aging in the same conditions, the resulting suspension was cooled down to room temperature. The precipitant was then recovered by centrifugation (6000 rpm, 5 min), washed four times with deionized water (240 cm<sup>3</sup> each time), dried in a vacuum oven (2 kPa, 333 K, 12 h), and calcined for 3 h in static air at 773 K (2 K min<sup>-1</sup>).

**Catalyst Characterization:** X-ray fluorescence spectroscopy (XRF) was performed using an Orbis Micro-EDXRF spectrometer equipped with a Rh source operated at 35 kV and 500 μA and a silicon drift detector. Nitrogen sorption at 77 K was carried out using a Micromeritics TriStar II analyzer. Prior to the measurements, samples were degassed at 473 K under vacuum for 12 h. The total surface area (S<sub>BET</sub>) was determined using the Brunauer-Emmett-Teller (BET) method. XRD was conducted using a Rigaku SmartLab diffractometer with a D/teX Ultra 250 detector using Cu Kα radiation (λ = 0.1541 nm) and operating in the Bragg-Brentano geometry. Data was acquired in the 20–70° 2θ range with an angular step size of 0.025° and a counting time of 1.5 s per step. HAADF-STEM and HRTEM images and EDX spectroscopy maps were collected using a Talos F200X instrument operated at an acceleration potential of 200 kV. Samples were dusted on lacey-carbon coated copper grids. Raman spectroscopy was performed using a Horiba: LabRAM HR Evolution UV-VIS-NIR confocal Raman system comprising a 325 nm HeCd laser with 2.5 mW power, a 40x objective lens with a numerical aperture of 0.95 (Nikon PlanApo), and a fiber coupled grating spectrometer (1800 lines per mm). Spectra were collected in a single run with 60 s acquisition time. For data evaluation, the intensities were normalized by the highest measured intensity after subtraction of a linear background. XPS was performed using a Physical Electronics (PHI) Quantum 2000 X-ray photoelectron spectrometer featuring monochromatic Al Kα radiation, generated from an electron beam operated at 15 kV and 32.3 W, and a hemispherical capacitor electron-energy analyzer, equipped with a channel plate and a position-sensitive detector. Samples were firmly pressed onto aluminum foil, which was then mounted onto a sample platen and introduced into the spectrometer. Analyses were conducted under ultra-high vacuum (residual pressure = 6 × 10<sup>-9</sup> Pa) with an electron take-off angle of 45°, operating the analyzer in the constant pass energy mode. X-ray absorption spectroscopy (XAS) was measured at the Swiss-Norwegian beamlines (SNBL, BM31) at the European Synchrotron Radiation Facility (ESRF).<sup>[51]</sup> The energy was selected by a double-crystal Si(111) monochromator,<sup>[51]</sup> and calibrated using a Zn foil (9.6586 keV), which was measured simultaneously with the specimen of interest. The incident X-ray beam was focused on a 0.25 × 1 mm<sup>2</sup> spot. Activated samples (T = 593 K, P = 5 MPa, H<sub>2</sub>/CO<sub>2</sub> = 4, GHSV = 24 000 cm<sup>3</sup> h<sup>-1</sup> B<sub>cat</sub><sup>-1</sup>,

and TOS = 20 h) were transferred from the reactor to a quartz capillary and sealed under inert atmosphere. Reference ZnO was measured in transmission mode as a pellet diluted with cellulose. Three 15-cm long ionization chambers filled with 50 vol% N<sub>2</sub> in Ar at 2 bar were used to monitor the incident beam intensity, transmission through the sample, and the reference foil. The XAS spectra of 5 and 13ZnZrO<sub>x</sub> samples were measured using a fluorescence detection mode using a 5-element SDD detector (SGX) and step-by-step data acquisition mode. The spectra were calibrated and averaged with the in-house developed ProEXAFS software and further analyzed using the Demeter software package.<sup>[52]</sup> k<sup>2</sup>-weighted EXAFS spectra were fitted in the optimal k- and R-windows (Table S6, Supporting Information). An amplitude reduction factor (S<sub>0</sub><sup>2</sup>) of 1.2 was determined by fitting of the EXAFS spectrum of a Zn foil. The scattering paths for the fitting were produced using known crystallographic structures of metallic Zn and hexagonal ZnO. In situ electron paramagnetic resonance EPR spectroscopy experiments were performed using a custom-built setup (microwave frequency = 9.2 GHz, center field = 300 mT, sweep width = 50 mT, modulation amplitude = 3 G, modulation frequency = 100 kHz, microwave power = 1.986 mW, power attenuation = 20 dB, conversion time = 86.55 ms, time constant = 20.48 ms.). A quartz capillary (d<sub>i</sub> = 0.8 mm) was loaded with the catalyst, and placed inside an EPR quartz tube (Wilmad; d<sub>i</sub> = 2.8 mm). The EPR tube was placed at the center of a homemade water-cooled high-temperature resonator,<sup>[53]</sup> which was installed into a continuous wave EPR spectrometer (Bruker EMX) operating at X-band frequencies. The gas flow was directed from the top of the capillary through the catalyst bed and then through the space between the capillary outer walls and the EPR tube inner walls. The reactor was heated in an Ar flow to the desired temperature (T = 593 K) and allowed to stabilize for 20 min. The two reactant gases were sequentially admitted to the reactor, i.e., a H<sub>2</sub> (20 cm<sup>3</sup> min<sup>-1</sup>) was kept flowing for 2 h, followed by CO<sub>2</sub> (20 cm<sup>3</sup> min<sup>-1</sup>) for 2 h. The gases were dosed by a set of digital mass flow controllers and the outcome was monitored online via a Pfeiffer Vacuum Thermo-Star GSD 320 TI mass spectrometer. The EPR spectra were continuously acquired upon flowing the gases and separately stored, using a 2D acquisition mode, thus enabling a time-resolved monitoring of the process.

**Catalyst Evaluation:** The gas-phase hydrogenation of CO<sub>2</sub> to methanol was performed in a PID Eng&Tech high-pressure continuous-flow setup comprising four parallel fixed-bed reactors, as described elsewhere.<sup>[54]</sup> Undiluted catalysts (mass, m<sub>cat</sub> = 0.1 g; particle size = 0.2–0.4 mm) were loaded into each reactor tube (internal diameter 4 mm), held in place by a quartz-wool bed set on a quartz frit, and purged in flowing He (40 cm<sup>3</sup> min<sup>-1</sup>, PanGas, 4.6) for 30 min at ambient pressure. Under the same flow, the pressure was increased to 5.5 MPa for a leak test. The reaction was carried out by feeding a mixture of H<sub>2</sub> (PanGas, 5.0), CO<sub>2</sub> (40 vol% in H<sub>2</sub>, Messer, 4.5), and, in the case of hybrid feeds, also CO (Messer, 5.0), with a molar H<sub>2</sub>/CO<sub>2</sub> (CO<sub>2</sub> = CO<sub>2</sub> + CO) ratio of 4 at 593 K, 5 MPa, and GHSV of 24 000 cm<sup>3</sup> h<sup>-1</sup> B<sub>cat</sub><sup>-1</sup>, unless stated otherwise. The selectivity of the catalysts was compared at a constant degree of CO<sub>2</sub> conversion (X<sub>CO<sub>2</sub></sub>) as described in Figure 2 by adjusting the GHSV for each system. Further catalyst evaluation data points used in the fitting and validation of the kinetic model were obtained in a secondary self-built continuous flow setup equipped with a single fixed-bed reactor of 2.2 mm internal diameter, as described elsewhere.<sup>[19]</sup> The full list of conditions (T, P, H<sub>2</sub>/CO<sub>2</sub>, GHSV, and m<sub>cat</sub>) can be viewed the supplementary Excel file found in the Zenodo repository (<https://doi.org/10.5281/zenodo.7359881>). The testing procedure and quantification calculations are identical to those for the parallel reactor setup and give the same results within 5% error.

The effluent streams were analyzed by gas chromatography every 1 h and 15 min for the parallel and single setups, respectively. Response factors (F<sub>i</sub>) for each compound i, respective to the internal standard (20 vol% C<sub>2</sub>H<sub>6</sub> in He, Messer, purity 3.5), in the GC analysis were determined by Equation (1):

$$F_i = \frac{A_{C_2H_6} / m_{C_2H_6}^i}{A_i / m_i^i} \quad (1)$$

where  $A_i$  is the integrated area determined for the peak of compound  $i$  and  $n_{in}$  is the corresponding known molar flow at the reactor inlet. An average of five points around the expected analyte concentration was used. The unknown effluent molar flow of compound  $i$  was determined using Equation (2):

$$n_i^{out} = \frac{A_i \times F_i}{A_{C_2H_4}} \times n_{C_2H_4}^{out} \quad (2)$$

Conversion ( $X_i$ ), selectivity ( $S_i$ ), and production rate ( $r_i$ ) were calculated using Equations (3)–(5):

$$X_i = \frac{n_i^{in} - n_i^{out}}{n_i^{in}} \quad (3)$$

$$S_i = \frac{n_i^{in} - n_i^{out}}{n_{CO_2}^{in} - n_{CO_2}^{out}} \quad (4)$$

$$r_i = \frac{n_i^{in} - n_i^{out}}{m_{cat}} \quad (5)$$

The methanol space-time yield (STY) is the product of  $r_{MeOH}$  and the molar weight of methanol (32.04 g mol<sup>-1</sup>). The carbon balance was determined for each experiment according to Equation (6):

$$\varepsilon_c = \left( 1 - \frac{n_{CO_2}^{out} + n_{MeOH}^{out} + n_{CO}^{out}}{n_{CO_2}^{in}} \right) \quad (6)$$

and was always within a 5% margin.

**Theoretical Simulations:** DFT simulations were carried out with Vienna ab initio simulation package (VASP),<sup>[55,56]</sup> employing the Perdew–Burke–Ernzerhof (PBE) density functional.<sup>[57]</sup> Valence electrons were expanded with plane-waves with a kinetic cut-off energy of 500 eV while core electrons were described by projector augmented wave (PAW) pseudopotentials.<sup>[58]</sup> The Brillouin zone was sampled by a  $\Gamma$ -centered mesh with a reciprocal grid size narrower than 0.037 Å<sup>-1</sup>, generated with the Monkhorst–Pack method.<sup>[59]</sup>

Bulk lattice parameters of three ZrO<sub>2</sub> polymorphs were optimized with a kinetic energy cut-off of 700 eV. The three polymorphs are monoclinic ( $m$ ), tetragonal ( $t$ ), and cubic ( $c$ ), which belongs to  $P2_1/c$ ,  $P4_2/nmc$ , and  $Fm\bar{3}m$  space groups, respectively. The calculated lattice parameters are in good agreement with experiments and previous theoretical studies (Table S7, Supporting Information).<sup>[36,60–63]</sup> The presence of Zn on the three polymorphs was assessed by replacing one Zr atom in  $2 \times 2 \times 2$  (monoclinic and cubic) and  $2 \times 2 \times 3$  (tetragonal) supercells (Figure S7a (Supporting Information) and Section S1.2.2, Supporting Information). These supercells were also used to explore oxygen vacancy formation, both in the undoped and Zn-doped ZrO<sub>2</sub> systems. See Section S1.2.2 (Supporting Information) for a detailed explanation of the oxygen selected to form the vacancies.

Periodic boundary conditions were employed to model oxygen terminated slabs representing the most stable surface of each polymorph, which are ( $\bar{1}11$ ), (101), and (111) for  $m$ -,  $t$ -, and  $c$ -ZrO<sub>2</sub>, respectively.<sup>[36,37]</sup> In all cases, the slabs contained four layers being the two bottom ones fixed to bulk positions and the two outermost were allowed to relax. A vacuum region of 15 Å between slabs and a dipole correction along the  $z$  axes was applied in the three models.<sup>[64]</sup> The morphology of each polymorph is different, and their models were accordingly built (Figure S7b, Supporting Information).  $m$ -ZrO<sub>2</sub> ( $\bar{1}11$ ) was modeled as a  $p(1 \times 1)$  slab where each of the four layers is composed by four ZrO<sub>2</sub> formula units grouped in 12 atomic layers (O–O–Zr–O–Zr–O–Zr–O–Zr–O–O).  $t$ -ZrO<sub>2</sub> (101) was represented with a  $p(1 \times 2)$  slab with each layer formed by five atomic layers (O–O–Zr–O–O) and 4 ZrO<sub>2</sub> formula units. Finally,  $c$ -ZrO<sub>2</sub>(111) was built as  $p(2 \times 2)$  slab where each layer contains three atomic layers (O–Zr–O)

with four ZrO<sub>2</sub> formula units. Overall, the slabs for the three ZrO<sub>2</sub> polymorphs contain the same number of layers, ZrO<sub>2</sub> formula units, and ratio of relaxed/fixed atoms, although the Zr–O motifs are different (Figure S7b and Section S1.2.3, Supporting Information). The presence of Zn on the three surfaces was evaluated by replacing each of the non-equivalent Zr atoms of the two outermost layers (surface and subsurface), as depicted in Figure S8 (Supporting Information). The formation of oxygen vacancies was also assessed on the undoped and Zn-doped ZrO<sub>2</sub> slab models (Figure S9, Supporting Information). See Section S1.2.3 (Supporting Information) for a detailed explanation of the oxygen selected to form the vacancies. In addition, single points of relevant structures for the discussion of the oxygen vacancy formation and its link to EPR results were carried out with a hybrid functional HSE03<sup>[44,45]</sup> with 13%<sup>[46]</sup> of nonlocal Hartree–Fock exchange. Energy profiles for CO<sub>2</sub> hydrogenation to CH<sub>3</sub>OH and the competitive RWGS were computed on the ZnZrO<sub>2</sub> models of the three polymorphs with one Zn replacing a Zr atom on surface sites and one oxygen vacancy. The Zn doped surfaces with one vacancy, CO<sub>2</sub>, H<sub>2</sub>, and H<sub>2</sub>O were employed as thermodynamic sinks. Transition states were located using the climbing image nudged elastic band (CI-NEB) method.<sup>[65]</sup> The nature of transitions states was confirmed by computing numerical frequencies with a step size of  $\pm 0.015$  Å.

## Supporting Information

Supporting Information is available from the Wiley Online Library or from the author.

## Acknowledgements

This publication was created as part of NCCR Catalysis (Grant number 180544), a National Centre of Competence in Research funded by the Swiss National Science Foundation. The Scientific Center for Optical and Electron Microscopy (ScopeM) at the ETH Zurich is thanked for access to their facilities. Dr. Frank Krumeich, Mr. Dario Faust Ak, and Mr. Henrik Eliasson are thanked for acquiring the HAADF-STEM-EDX and HR-TEM data. The authors are grateful to Prof. Christophe Copéret, Mr. Enzo Brack, and Mr. Domenico Giffre for assistance with sample preparation for XAS measurements. T.Z. thanks the Agency for Science, Technology and Research (A\*STAR) Singapore for support through a graduate fellowship. The Spanish Ministry of Science and Innovation is acknowledged for financial support (RTI2018-101394-B-I00, PID2021-122516OB-I00, and Severo Ochoa Grant MCIN/AEI/10.13039/501100011033 CEX2019-000925-S) and the Barcelona Supercomputing Center-MareNostrum (BSC-RES) for providing generous computer resources. The Swiss Norwegian beamlines (SNBL, ESRF) are acknowledged for provision of beamtime and its staff for invaluable support.

Open access funding provided by Eidgenössische Technische Hochschule Zurich.

## Conflict of Interest

The authors declare no conflict of interest.

## Data Availability Statement

The data that support the findings of this study are openly available in Zenodo at <https://doi.org/10.5281/zenodo.7359881>, reference number 7359881.<sup>[66]</sup> Inputs and outputs for all DFT simulations can be found online in the ioChem-BD repository<sup>[67,68]</sup> at <http://doi.org/10.19061/iochem-bd-1-259>.

## Keywords

CO<sub>2</sub> hydrogenation, flame spray pyrolysis, oxygen vacancies, sustainable methanol, ZnZrO<sub>x</sub> catalysts

Received: December 2, 2022

Revised: January 18, 2023

Published online:

- [1] K. Narine, J. Mahabir, N. Koylass, N. Samaroo, S. Singh-Gryzbon, A. Baboolal, M. Guo, K. Ward, *J. CO<sub>2</sub> Util.* **2021**, *44*, 101399.
- [2] J. Sehested, *J. Catal.* **2019**, *371*, 368.
- [3] L. Van Hoecke, L. Laffineur, R. Campe, P. Perreault, S. W. Verbruggen, S. Lenaerts, *Energy Environ. Sci.* **2021**, *14*, 815.
- [4] M. Erans, E. S. Sanz-Pérez, D. P. Hanak, Z. Clulow, D. M. Reiner, C. A. Mutch, *Energy Environ. Sci.* **2022**, *15*, 1360.
- [5] A. González-Garay, M. S. Frei, A. Al-Qahtani, C. Mondelli, C. Guillén-Gosalbez, J. Pérez-Ramírez, *Energy Environ. Sci.* **2019**, *12*, 3425.
- [6] G. A. Olah, A. Goeppert, G. K. S. Prakash, *Beyond Oil Gas*, Wiley, Weinheim, Germany **2018**, p. 205, <https://doi.org/10.1002/9783527805662.ch10>.
- [7] X. Jiang, X. Nie, X. Guo, C. Song, J. G. Chen, *Chem. Rev.* **2020**, *120*, 7984.
- [8] J. Zhong, X. Yang, Z. Wu, B. Liang, Y. Huang, T. Zhang, *Chem. Soc. Rev.* **2020**, *49*, 1385.
- [9] M. Suvarna, T. P. Araújo, J. Pérez-Ramírez, *Appl. Catal., B* **2022**, *315*, 121530.
- [10] J. Wang, G. Li, Z. Li, C. Tang, Z. Feng, H. An, H. Liu, T. Liu, C. Li, *Sci. Adv.* **2017**, *3*, e1701290.
- [11] K. Li, J. G. Chen, *ACS Catal.* **2019**, *9*, 7840.
- [12] Z. Han, C. Tang, F. Sha, S. Tang, J. Wang, C. Li, *J. Catal.* **2021**, *396*, 242.
- [13] J. Wang, C. Tang, G. Li, Z. Han, Z. Li, H. Liu, F. Cheng, C. Li, *ACS Catal.* **2019**, *9*, 10253.
- [14] T. P. Araújo, A. H. Hergesell, D. Faust-Akl, S. Büchele, J. A. Stewart, C. Mondelli, J. Pérez-Ramírez, *ChemSusChem* **2021**, *14*, 2914.
- [15] J. Ding, Z. Li, W. Xiong, Y. Zhang, A. Ye, W. Huang, *Appl. Surf. Sci.* **2022**, *587*, 152884.
- [16] M. S. Frei, C. Mondelli, A. Cesarini, F. Krumeich, R. Hauert, J. A. Stewart, D. Curulla Ferré, J. Pérez-Ramírez, *ACS Catal.* **2020**, *10*, 1133.
- [17] B. Bachiller-Baeza, I. Rodríguez-Ramos, A. Guerrero-Ruiz, *Langmuir* **1998**, *14*, 3556.
- [18] M. S. Frei, C. Mondelli, R. García-Muelas, K. S. Kley, B. Puértolas, N. López, O. V. Safonova, J. A. Stewart, D. Curulla Ferré, J. Pérez-Ramírez, *Nat. Commun.* **2019**, *10*, 3377.
- [19] M. S. Frei, M. Capdevila-Cortada, R. García-Muelas, C. Mondelli, N. López, J. A. Stewart, D. Curulla Ferré, J. Pérez-Ramírez, *J. Catal.* **2018**, *361*, 313.
- [20] T. Pinheiro Araújo, C. Mondelli, M. Agrachev, T. Zou, P. O. Willli, K. M. Engel, R. N. Grass, W. J. Stark, O. V. Safonova, G. Jeschke, S. Mitchell, J. Pérez-Ramírez, *Nat. Commun.* **2022**, *13*, 5610.
- [21] W. Y. Teoh, R. Amal, L. Mädler, *Nanoscale* **2010**, *2*, 1324.
- [22] E. K. Athanassiou, R. N. Grass, W. J. Stark, *Aerosol Sci. Technol.* **2010**, *44*, 161.
- [23] R. Koirala, S. E. Pratsinis, A. Baiker, *Chem. Soc. Rev.* **2016**, *45*, 3053.
- [24] T. Pinheiro Araújo, J. Morales-Vidal, T. Zou, R. García-Muelas, P. O. Willli, K. M. Engel, O. V. Safonova, D. Faust Akl, F. Krumeich, R. N. Grass, C. Mondelli, N. López, J. Pérez-Ramírez, *Adv. Energy Mater.* **2022**, *12*, 2103707.
- [25] J. Chevalier, L. Gremillard, A. V. Virkar, D. R. Clarke, *J. Am. Ceram. Soc.* **2009**, *92*, 1901.
- [26] C. Yang, C. Pei, R. Luo, S. Liu, Y. Wang, Z. Wang, Z. J. Zhao, J. Gong, *J. Am. Chem. Soc.* **2020**, *142*, 19523.
- [27] H. Kim, K. M. Kosuda, R. P. Van Duyne, P. C. Stair, *Chem. Soc. Rev.* **2010**, *39*, 4820.
- [28] M. Li, Z. Feng, G. Xiong, P. Ying, Q. Xin, C. Li, *J. Phys. Chem. B* **2001**, *105*, 8107.
- [29] M. Li, Z. Feng, P. Ying, Q. Xin, C. Li, *Phys. Chem. Chem. Phys.* **2003**, *5*, 5326.
- [30] T. L. Weiss, H. J. Chun, S. Okada, S. Vitha, A. Holzenburg, J. Laane, T. P. Devarenne, *J. Biol. Chem.* **2010**, *285*, 32458.
- [31] S. Tada, K. Larmier, R. Büchel, C. Copéret, *Catal. Sci. Technol.* **2018**, *8*, 2056.
- [32] C. Li, M. Li, *J. Raman Spectrosc.* **2002**, *33*, 301.
- [33] D. Salusso, E. Borfecchia, S. Bordiga, *J. Phys. Chem. C* **2021**, *125*, 22249.
- [34] P. Šot, G. Noh, I. C. Weber, S. E. Pratsinis, C. Copéret, *Helv. Chim. Acta* **2022**, *105*, 202200007.
- [35] L. Mädler, H. K. Kammler, R. Mueller, S. E. Pratsinis, *J. Aerosol Sci.* **2002**, *33*, 369.
- [36] C. Ricca, A. Ringuédé, M. Cassir, C. Adamo, F. Labat, *J. Comput. Chem.* **2015**, *36*, 9.
- [37] A. Christensen, E. A. Carter, *Phys. Rev. B* **1998**, *58*, 8050.
- [38] S. Loher, W. J. Stark, M. Maciejewski, A. Baiker, S. E. Pratsinis, D. Reichardt, F. Maspero, F. Krumeich, D. Günther, *Chem. Mater.* **2005**, *17*, 36.
- [39] J. A. Kemmler, S. Pokhrel, J. Birkenstock, M. Schowalter, A. Rosenauer, N. Bärson, U. Weimar, L. Mädler, *Sens. Actuators, B* **2012**, *161*, 740.
- [40] K. Lee, U. Anjum, T. P. Araújo, C. Mondelli, Q. He, S. Furukawa, J. Pérez-Ramírez, S. M. Kozlov, N. Yan, *Appl. Catal., B* **2022**, *304*, 120994.
- [41] C. Gionco, M. C. Paganini, E. Giamello, R. Burgess, C. Di Valentin, G. Pacchioni, *Chem. Mater.* **2013**, *25*, 2243.
- [42] E. V. Frolova, M. I. Ivanovskaya, *Mater. Sci. Eng., C* **2006**, *26*, 1106.
- [43] H. Liu, L. Feng, X. Zhang, Q. Xue, *J. Phys. Chem.* **1995**, *99*, 332.
- [44] J. Heyd, G. E. Scuseria, M. Ernzerhof, *J. Chem. Phys.* **2003**, *118*, 8207.
- [45] J. Heyd, G. E. Scuseria, M. Ernzerhof, *J. Chem. Phys.* **2006**, *124*, 219906.
- [46] F. S. Hegner, D. Cardenas-Morcoso, S. Giménez, N. López, J. R. Galan-Mascaros, *ChemSusChem* **2017**, *10*, 4552.
- [47] E. Giamello, M. Volante, B. Fubini, F. Geobaldo, C. Morterra, *Mater. Chem. Phys.* **1991**, *29*, 379.
- [48] S. Kouva, J. Andersin, K. Honkala, J. Lehtonen, L. Lefferts, J. Kanervo, *Phys. Chem. Chem. Phys.* **2014**, *16*, 20650.
- [49] A. J. Gröhn, S. E. Pratsinis, A. Sánchez-Ferrer, R. Mezzenga, K. Wegner, *Ind. Eng. Chem. Res.* **2014**, *53*, 10734.
- [50] R. N. Grass, S. Tsantilis, S. E. Pratsinis, *AIChE J.* **2006**, *52*, 1318.
- [51] W. van Beek, O. V. Safonova, G. Wiker, H. Emerich, *Phase Transitions* **2011**, *84*, 726.
- [52] B. Ravel, M. Newville, *J. Synchrotron Radiat.* **2005**, *12*, 537.
- [53] G. Zichittella, Y. Polyhach, R. Tschaggelar, G. Jeschke, J. Pérez-Ramírez, *Angew. Chem., Int. Ed.* **2021**, *60*, 3596.
- [54] T. P. Araújo, A. Shah, C. Mondelli, J. A. Stewart, D. Curulla Ferré, J. Pérez-Ramírez, *Appl. Catal., B* **2021**, *285*, 119878.
- [55] G. Kresse, J. Furthmüller, *Comput. Mater. Sci.* **1996**, *6*, 15.
- [56] G. Kresse, J. Furthmüller, *Phys. Rev. B* **1996**, *54*, 11169.
- [57] J. P. Perdew, K. Burke, M. Ernzerhof, *Phys. Rev. Lett.* **1996**, *77*, 3865.
- [58] P. E. Blochl, *Phys. Rev. B* **1994**, *50*, 17953.
- [59] H. J. Monkhorst, J. D. Pack, *Phys. Rev. B* **1976**, *13*, 5188.
- [60] Y. Kudoh, H. Takeda, H. Arashi, *Phys. Chem. Miner.* **1986**, *13*, 233.
- [61] Z. Q. Xue, Y. Q. Guo, *Adv. Mater.* **2014**, *936*, 181.



- [62] B. Bondars, G. Heidemane, J. Grabis, K. Laschke, H. Boysen, J. Schneider, F. Frey, *J. Mater. Sci.* **1995**, *30*, 1621.
- [63] Z. Liang, W. Wang, M. Zhang, F. Wu, J.-F. Chen, C. Xue, H. Zhao, *Phys. B* **2017**, *511*, 10.
- [64] G. Makov, M. C. Payne, *Phys. Rev. B* **1995**, *51*, 4014.
- [65] G. Henkelman, B. P. Uberuaga, H. Jónsson, *J. Chem. Phys.* **2000**, *113*, 9901.
- [66] T. Pinheiro Araújo, J. Morales-Vidal, T. Zou, M. Agrachev, S. Verstraeten, P. O. Willi, R. N. Grass, G. Jeschke, S. Mitchell, N. López, J. Pérez-Ramírez, *Zenodo*. **2022**, <https://doi.org/10.5281/zenodo.7359881>.
- [67] M. Álvarez-Moreno, C. de Graaf, N. López, F. Maseras, J. M. Poblet, C. Bo, *J. Chem. Inf. Model.* **2015**, *55*, 95.
- [68] C. Bo, F. Maseras, N. López, *Nat. Catal.* **2018**, *1*, 809.



RESEARCH ARTICLE

# Flame Spray Pyrolysis as a Synthesis Platform to Assess Metal Promotion in $\text{In}_2\text{O}_3$ -Catalyzed $\text{CO}_2$ Hydrogenation

Thaylan Pinheiro Araújo, Jordi Morales-Vidal, Tangsheng Zou, Rodrigo García-Muelas, Patrik O. Willi, Konstantin M. Engel, Olga V. Safonova, Dario Faust Akl, Frank Krumeich, Robert N. Grass, Cecilia Mondelli, Núria López,\* and Javier Pérez-Ramírez\*

A plethora of metal promoters have been applied to enhance the performance of  $\text{In}_2\text{O}_3$  in  $\text{CO}_2$  hydrogenation to methanol, a prospective energy carrier. However, the lack of systematic catalyst preparation and evaluation precludes a direct comparison of their speciation and promotional effects, and consequently, the design of an optimal system. Herein, flame spray pyrolysis (FSP) is employed as a standardized synthesis method to introduce nine metal promoters (0.5 wt.%) into  $\text{In}_2\text{O}_3$ . Methanol productivity generally increased on  $M\text{-In}_2\text{O}_3$  with selectivity following  $\text{Pd} \approx \text{Pt} > \text{Rh} \approx \text{Ru} \approx \text{Ir} > \text{Ni} \approx \text{Co} > \text{Ag} \approx \text{In}_2\text{O}_3 > \text{Au}$ . In-depth characterization, kinetic analyses, and theoretical calculations reveal a range of metal-dependent speciation which dictate catalyst architecture and degree of promotion. Atomically-dispersed promoters (Pd, Pt, Rh, Ru, and Ir) grant the highest improvement in performance, particularly Pd and Pt, which markedly promote hydrogen activation while hindering undesired CO formation. In contrast, metals in clustered (Ni and Co) and nanoparticle (Ag and Au) forms display moderate and no promotion, respectively. This study provides an atomic-level understanding of  $\text{In}_2\text{O}_3$  promotion based on a unified protocol, and highlights the potential of FSP to engineer complex catalytic systems toward more efficient energy transformations.

## 1. Introduction

With a global annual demand of 80 million tonnes projected to further grow by 4% annually, methanol ( $\text{CH}_3\text{OH}$ ) is a key platform chemical and prospective energy carrier envisaged to play a crucial role in global efforts tackling climate change by lowering the carbon footprint.<sup>[1–4]</sup> To this end, captured carbon dioxide ( $\text{CO}_2$ ) and renewable hydrogen ( $\text{H}_2$ ) attained from water electrolysis should be used as the feedstock to generate the so-called e-methanol. The thermocatalytic hydrogenation of  $\text{CO}_2$  using heterogeneous nanostructured catalysts offers an efficient approach to realize this route.<sup>[4–6]</sup> Among many catalytic materials studied, indium oxide ( $\text{In}_2\text{O}_3$ ) has emerged as an attractive active catalyst due to its high methanol selectivity and stability.<sup>[7]</sup> Owing to its anisotropic surface, oxygen vacancies are selectively generated under reaction conditions forming an  $\text{In}_3\text{O}_5$  ensemble, which is capable of activating and hydrogenating  $\text{CO}_2$  to methanol very selectively, while the competitive reverse water-gas shift reaction (RWGS) forming carbon monoxide is energetically hindered.<sup>[8]</sup> Since hydrogen activation is the most demanding step in the mechanism, a plethora of metal promoters was investigated to alleviate this drawback and boost the catalyst activity.

Palladium nanoparticles incorporated by dry impregnation (0.9 wt.%)<sup>[9]</sup> were shown to cause substantial selectivity loss due to their RWGS activity, as well as stability issues owing to excessive  $\text{In}_2\text{O}_3$  reduction by the spilled hydrogen.<sup>[10]</sup> Coprecipitation forming low-nuclearity palladium clusters anchored to the oxide surface (0.75 wt.%) curtailed these detrimental impacts, attaining the highest sustained methanol productivity of  $0.96 \text{ g}_{\text{MeOH}} \text{ g}_{\text{cat}}^{-1} \text{ h}^{-1}$  among  $\text{In}_2\text{O}_3$ -based catalysts.<sup>[10]</sup> The same synthetic protocol was used to introduce platinum (0.58 wt.%) forming atomically dispersed  $\text{Pt}^{+}$  species granting a remarkable selectivity increase.<sup>[11]</sup> Platinum, rhodium, ruthenium, and silver introduced by deposition-precipitation (1.07, 1.07, 1.00, and 0.33 wt.%, respectively) as highly dispersed species also allowed to reach a very high selectivity but at very low reaction temperatures, where the RWGS reaction is thermodynamically unfavored.<sup>[12–15]</sup> A methanol space-time

T. Pinheiro Araújo, T. Zou, P. O. Willi, K. M. Engel, D. Faust Akl, F. Krumeich, R. N. Grass, C. Mondelli, J. Pérez-Ramírez  
Institute of Chemical and Bioengineering  
Department of Chemistry and Applied Biosciences  
ETH Zurich  
Vladimir-Prelog-Weg 1, Zurich 8093, Switzerland  
E-mail: jpr@chem.ethz.ch

J. Morales-Vidal, R. García-Muelas, N. López  
Institute of Chemical Research of Catalonia (ICIQ)  
The Barcelona Institute of Science and Technology  
Av. Països Catalans 16, Tarragona 43007, Spain  
E-mail: nlopez@icq.es

O. V. Safonova  
Paul-Scherrer Institute  
Forschungsstrasse 111, Villigen 5232, Switzerland

The ORCID identification number(s) for the author(s) of this article can be found under <https://doi.org/10.1002/aenm.202103707>.

© 2022 The Authors. Advanced Energy Materials published by Wiley-VCH GmbH. This is an open access article under the terms of the Creative Commons Attribution-NonCommercial License, which permits use, distribution and reproduction in any medium, provided the original work is properly cited and is not used for commercial purposes.

DOI: 10.1002/aenm.202103707

yield (STY) of  $0.76 \text{ g}_{\text{MeOH}} \text{ h}^{-1} \text{ g}_{\text{cat}}^{-1}$  was achieved over iridium-promoted indium oxide produced by wetness impregnation, but applying 10 wt.% Ir.<sup>[16]</sup> Despite the high metal content, the promoter formed nanoparticles of only  $\approx 1 \text{ nm}$ , which favored methanol formation through the RWGS route.<sup>[16]</sup> Similarly sized nanoparticles of gold (1 wt.%) on indium oxide generated by deposition-precipitation enabled a promotional effect owing to the creation of  $\text{Au}^{\delta-}\text{-In}_2\text{O}_3\text{-x}$  interfacial sites.<sup>[17]</sup> Oxygen vacancy formation is also enhanced at similar  $\text{Ag-In}_2\text{O}_3$  and  $\text{Rh-In}_2\text{O}_3$  interfaces, resulting in increased  $\text{CO}_2$  activation on catalysts containing low loadings of silver (0.33 wt.%) and rhodium (0.64 wt.%), respectively.<sup>[15,18]</sup> Cobalt nanoparticles decorated by  $\text{In}_2\text{O}_3$  were attained by coprecipitation,<sup>[19]</sup> with charge transfer between oxide and metal curtailing the methanation properties typical of cobalt and fostering methanol production. A similar result was reported following a MOF-based route,<sup>[20]</sup> generating a composite containing indium and cobalt oxides as well as mixed carbides of the two elements. The addition and interaction of nickel with  $\text{In}_2\text{O}_3$  has been more widely studied with a larger variety of synthesis methods and metal loadings. An optimal promotional effect was attained at 1 wt.% loading applying dry impregnation, with the formation of two-dimensional  $\text{InNi}_3$  nanostructures supplying activated hydrogen, but not converting  $\text{CO}_2$  into methane.<sup>[21]</sup> The latter only took place for nickel contents exceeding 15 wt.%, with the formation of some metallic nickel particles exhibiting their intrinsic behavior. Strong interaction of Ni with  $\text{In}_2\text{O}_3$  without alloying has concurrently been theorized at higher loadings, for flame-synthesized  $\text{Ni-In}_2\text{O}_3$  up to 6 wt.%<sup>[22]</sup> as well as a 10 wt.% system prepared by wet chemical reduction.<sup>[23,24]</sup> Overall, metal promoters supported on  $\text{In}_2\text{O}_3$  as low-nuclearity species appear to improve methanol productivity to a greater extent. Nonetheless, metal promoters were introduced using dissimilar synthesis methods and loadings on differently prepared  $\text{In}_2\text{O}_3$  leading to different architectures, and the resulting catalysts were tested under diverse temperature and pressure conditions,

making comparison of catalytic data impractical. These scattered approaches preclude a direct and reliable comparison of speciation and promotional effects among metal-promoted  $\text{In}_2\text{O}_3$  catalysts, which is critical for the design of an optimal system.

Here, we employ flame spray pyrolysis (FSP) as a unified synthetic protocol to assess  $\text{In}_2\text{O}_3$  promotion by palladium, platinum, rhodium, ruthenium, iridium, nickel, cobalt, gold, and silver, on the basis of a metal loading of 0.5 wt.%. Equivalent catalytic evaluation, extensive density functional theory (DFT) simulations, in-depth characterization, and kinetic analyses unveil the metal speciations and their effects on oxygen vacancy formation, hydrogen splitting, as well as activity patterns in  $\text{CO}_2$  hydrogenation to methanol and in the competing RWGS. Our study provides an atomic-level rationalization of  $\text{In}_2\text{O}_3$  promotion and uncovers common trends and descriptors for different metal dopants based on a standardized synthesis approach, with potential for extrapolation to other catalysts for energy applications.

## 2. Results and Discussion

### 2.1. Impact of Promoters on Catalytic Performance

FSP (Figure 1) was selected as the method to synthesize the series of metal-promoted  $\text{In}_2\text{O}_3$  catalysts due to its superior control over crystal size, morphology, and specific surface area of the synthesized materials.<sup>[25–27]</sup> Additionally, FSP permits a more efficient utilization of expensive metal promoters since it often leads to spatially controlled deposition of metal entities on the surface of carriers without promoting bulk incorporation, a classic drawback of coprecipitation methods.<sup>[28]</sup> Finally, FSP is an up-scalable technology capable of producing multi-component materials with well-specified composition, high purity, and thermal stability in a single-step approach, without the need of solvent-intensive washing and post-thermal treatments commonly required for other synthesis methods.<sup>[26,29–31]</sup>

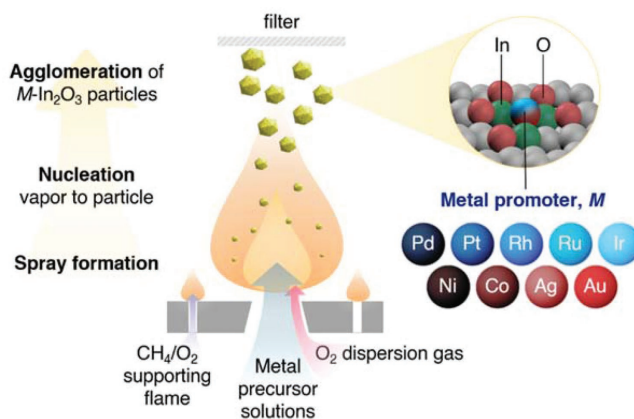
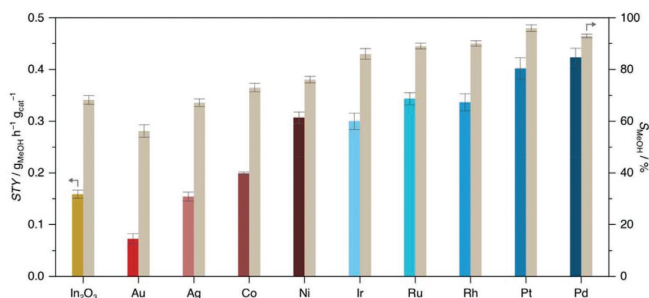


Figure 1. Scheme of the FSP method for the preparation of  $M\text{-In}_2\text{O}_3$  catalysts.



**Figure 2.** Methanol space-time yield (STY, colored bars) and selectivity ( $S_{\text{MeOH}}$ , beige bars) during  $\text{CO}_2$  hydrogenation over undoped  $\text{In}_2\text{O}_3$  and  $M\text{-In}_2\text{O}_3$  catalysts (0.5 wt.% of metal) prepared by FSP. The methanol STY is assessed at  $WHSV = 24000 \text{ cm}^3 \text{ h}^{-1} \text{ g}_{\text{cat}}^{-1}$ , while  $S_{\text{MeOH}}$  at constant  $\text{CO}_2$  conversion ( $\approx 3\%$ ) and variable  $WHSV$ . Averaged values measured over 24 h on stream are presented with their corresponding error bars. Reaction conditions:  $T = 553 \text{ K}$ ,  $P = 5 \text{ MPa}$ , and  $\text{H}_2/\text{CO}_2 = 4$ .

After screening the effect of varying loadings up to 2 wt.% with Pd and Pt (vide infra), the nominal loading of 0.5 wt.% was chosen to favor the formation of atomically-resolved promoter structures on  $\text{In}_2\text{O}_3$  necessary for the purpose of the study. The actual metal loadings of the promoted catalysts as determined by inductively coupled plasma optical emission spectroscopy (ICP-OES, Table S1, Supporting Information) closely matched the nominal loadings. X-ray diffraction (XRD) profiles (Figure S1, Supporting Information) show that  $\text{In}_2\text{O}_3$  is present in all fresh catalysts as a crystalline phase, while reflections corresponding to the pure metals are absent indicating the lack of nanoparticles larger than 4 nm. The chosen flame and flow parameters result in consistent  $\text{In}_2\text{O}_3$  average crystallite sizes ( $d_{\text{In}_2\text{O}_3}$ ) of 25–29 nm for all freshly promoted catalysts (Table S2, Supporting Information), except for Ni- $\text{In}_2\text{O}_3$  with moderately larger particles (34 nm). Surface areas of the promoted catalysts were also lower than that of  $\text{In}_2\text{O}_3$  prepared by the same method, in line with previous evidence for catalysts attained by different routes.<sup>[10,21]</sup>

$\text{CO}_2$  hydrogenation to methanol was conducted at 553 K and 5 MPa over pristine and metal-promoted  $\text{In}_2\text{O}_3$ . The catalytic data (Figure 2 and Figure S2, Supporting Information) indicate that, except for Au- and Ag-doped systems, all other catalysts exceeded the overall  $\text{CO}_2$  conversion ( $X_{\text{CO}_2}$ ) and methanol STY of pure  $\text{In}_2\text{O}_3$ , reaching a maximum of 7.8% and  $0.42 \text{ g}_{\text{MeOH}} \text{ h}^{-1} \text{ g}_{\text{cat}}^{-1}$  for Pt- $\text{In}_2\text{O}_3$ . Increasing the metal promoter loading of the two most active catalysts, Pt- $\text{In}_2\text{O}_3$  and Pd- $\text{In}_2\text{O}_3$ , beyond 0.5 wt.% did not further enhance the conversion significantly. By comparing the methanol selectivity at a constant  $\text{CO}_2$  conversion ( $\approx 3\%$ ), the promoters can be classified into three families. The first includes Au and Ag, which favor the formation of CO, resulting in inferior or similar methanol selectivity (56% and 67%), respectively, compared to undoped  $\text{In}_2\text{O}_3$ . The second covers Co and Ni, which slightly improve the methanol selectivity (72% and 75%, respectively). The third encompasses Ir, Ru, Rh, Pd, and Pt, which favor methanol production unlocking highly superior methanol selectivities (85–95%). These results were generally in line with those of equivalent metal-promoted  $\text{In}_2\text{O}_3$  catalysts with low loadings in the literature, synthesized by coprecipitation,<sup>[10,32,33]</sup>

impregnation,<sup>[10,16,21]</sup> deposition-precipitation methods,<sup>[15,34]</sup> as well as FSP,<sup>[22]</sup> which also corroborates the superior performance of Pd and Pt. However, the performance of Au- $\text{In}_2\text{O}_3$  was markedly lower than that of a previous study,<sup>[17]</sup> hinting a limitation and fundamental difference of FSP compared with the deposition-precipitation method.

Since Ni- and Pd- $\text{In}_2\text{O}_3$  catalysts prepared by dry impregnation and coprecipitation, respectively, were reported to experience distinct deactivation levels during hydrogenation of hybrid  $\text{CO}_2\text{-CO}$  feeds,<sup>[32]</sup> the sensitivity of all systems to co-fed CO was also investigated using a feed with  $\text{CO}_2/\text{CO}$  ratio = 4 at otherwise the same  $T$ ,  $P$ ,  $\text{H}_2/\text{CO}_{\text{ox}}$ , and  $WHSV$  conditions (Figure S3, Supporting Information). Ir-, Ru-, Rh-, Pt-, and Pd- $\text{In}_2\text{O}_3$  catalysts still show superior performance. However, except for Co- $\text{In}_2\text{O}_3$ , methanol productivity is generally inferior for all catalysts in the hybrid  $\text{CO}_2\text{-CO}$  feed in comparison to  $\text{CO}_2$  hydrogenation, most likely due to inhibition of active sites by CO. Specifically for Ni- $\text{In}_2\text{O}_3$ , the formation of volatile Ni-carbonyl compounds promoting the sintering into metal nanoparticles is known to contribute to its irreversible deactivation.<sup>[32]</sup> Similar to undoped  $\text{In}_2\text{O}_3$ , the presence of CO does not induce a detrimental effect on methanol production over the Co- $\text{In}_2\text{O}_3$  catalyst, whose catalytic activity could be attributed to undoped  $\text{In}_2\text{O}_3$  active sites.

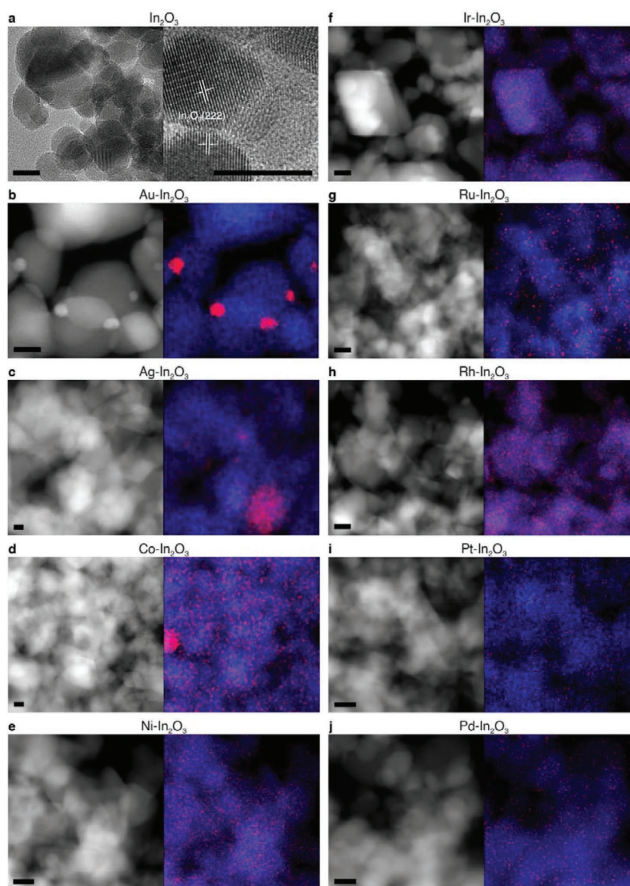
For unpromoted  $\text{In}_2\text{O}_3$  and Au-, Ag-, Co-, and Ni-promoted  $\text{In}_2\text{O}_3$ , sintering occurs upon exposure to the reaction mixture and slightly increases during 24 h on stream, as evidenced by the corresponding increase in  $d_{\text{In}_2\text{O}_3}$  as determined by XRD (Table S2, Supporting Information). This trend is also reflected in the marked decrease of Brunauer-Emmett-Teller (BET) surface area ( $S_{\text{BET}}$ ) upon use for all catalysts, with the exceptions of Ir- and, notably, Ru-doped solids, which stand out as the most robust. In general, both  $S_{\text{BET}}$  and  $d_{\text{In}_2\text{O}_3}$  further decrease and increase, respectively, upon exposure of catalysts to the hybrid  $\text{CO}_2\text{-CO}$  feeds (Table S2), which likely explains their diminished performance in such conditions. Overall, the methanol STY remained unaltered from 2 to at least 24 h on stream for all catalysts except for Au- $\text{In}_2\text{O}_3$ , and therefore reflects stable performance. 2 h was thus considered as the time needed for catalyst activation under in situ conditions. Overall, the similar

$\text{In}_2\text{O}_3$  crystallite sizes and the lack of large differences in the BET surface area of activated catalysts show that bulk porous properties would not be a significant confounding factor.

## 2.2. Promoter Speciation

The speciation of the metal promoters was elucidated by a battery of experimental and theoretical characterization

techniques. The promoters were expected to be adsorbed on the  $\text{In}_2\text{O}_3$  surface, to be incorporated into the  $\text{In}_2\text{O}_3$  lattice, or to segregate into nanoparticles. Characterization was performed on the activated (2 h under reaction conditions) and used (24 h) catalysts. High-resolution electron transmission microscopy (HRTEM, Figure 3a and Figures S4 and S5, Supporting Information) confirmed that highly crystalline  $\text{In}_2\text{O}_3$  particles are present in both undoped and promoted catalysts, as indicated by XRD (Figure S1, Supporting Information).



**Figure 3.** a) HRTEM micrographs of  $\text{In}_2\text{O}_3$  and b–j) HAADF-STEM micrographs with EDX maps of  $M\text{-In}_2\text{O}_3$  after activation in  $\text{CO}_2$  hydrogenation for 2 h. Scale bars are equivalent to 10 nm unless otherwise indicated. Indium and metal promoter  $M$  are colored in blue and red in EDX maps, respectively. Activation conditions:  $T = 553\ \text{K}$ ,  $P = 5\ \text{MPa}$ ,  $\text{H}_2/\text{CO}_2 = 4$ , and  $\text{WHSV} = 24000\ \text{cm}^3\ \text{h}^{-1}\ \text{g}_{\text{cat}}^{-1}$ .

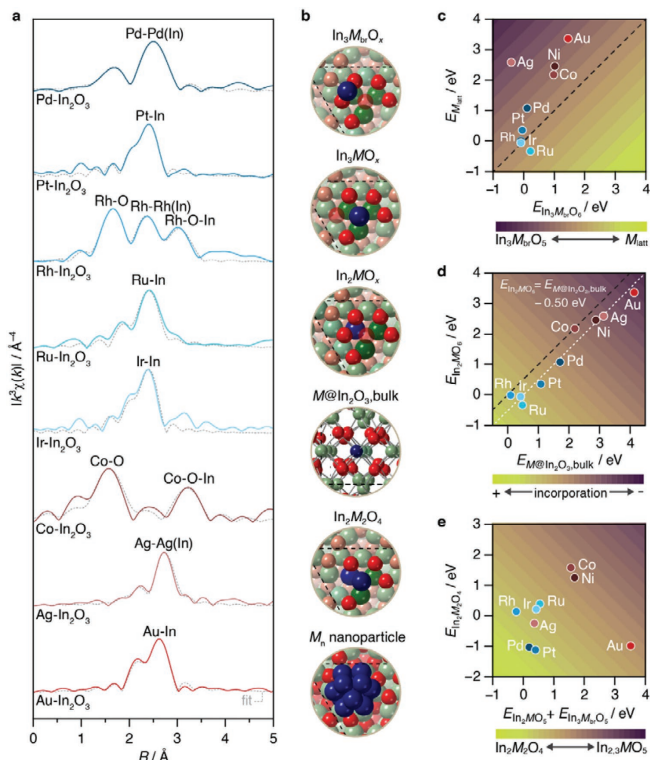
For Au- and Ag-In<sub>2</sub>O<sub>3</sub>, some metal nanoparticles with variable sizes were clearly visible in the HRTEM images (Figures S4 and S5, Supporting Information). In addition, Au, Ag, and Co nanoparticles and smaller clusters are also evidenced by high-angle annular dark-field scanning transmission electron microscopy coupled to energy-dispersive X-ray spectroscopy (HAADF-STEM-EDX, Figure 3b–d). Interestingly, no metal nanoparticles were detected for any of the other promoters (Figure 3e–i), which are highly dispersed on In<sub>2</sub>O<sub>3</sub> as low-nuclearity species, with Ir, Ru, Rh, Pt, and Pd likely less clustered than Co and Ni. These findings are well in line with previous studies in which nanoparticles were only observed at metal loadings well above the 0.5 wt.% chosen to attain an atomic dispersion.<sup>[12,16,21]</sup> Additionally, temperature-programmed reduction with hydrogen (H<sub>2</sub>-TPR, Figure S6, Supporting Information) revealed no distinguishable signals indicative of the reduction of promoters to pure metallic nanoparticles, not even for Au- and Ag-In<sub>2</sub>O<sub>3</sub>, suggesting that all catalysts feature strong metal–support interactions.

Most of the promoters are fully reduced to metallic species under reaction conditions, except for Co- and Rh-In<sub>2</sub>O<sub>3</sub>, as indicated by X-ray absorption near-edge structure spectra (XANES, Figure S7, Supporting Information). While the spectra of these two catalysts resemble that of cationic Co<sup>2+</sup> and Rh<sup>3+</sup> in CoO and Rh<sub>2</sub>O<sub>3</sub>, respectively, the white-line intensity and position are not identical to those of the corresponding reference oxides. This suggests that these promoters are indeed in an oxidic state, but strongly interacting with In<sub>2</sub>O<sub>3</sub>. Changes in the electronic structure of metallic Au, Ni, Ir, Ru, and Pt, with respect to the corresponding metal foils, upon interaction with In<sub>2</sub>O<sub>3</sub>, are also observed, hinting the presence of M–In bonds. Analysis of the extended X-ray absorption fine structure (EXAFS, Figure 4a and Table S5, Supporting Information) in fact revealed mainly M–In bonds in the first coordination shell of Ir, Ru, and Pt with coordination numbers of ≈3–5. This confirms high dispersion of these metals and (considering a strong correlation between the Debye-Waller factors with the number of neighbors) is in line with the theoretical models of atomic dispersed dopants, In<sub>3</sub>MO<sub>x</sub> in Figure 4b. The coordination number of the Au–In shell is higher, indicating clustering of Au, in agreement with microscopy findings (Figure 3a). The presence of M–M along with M–In bonds cannot be completely excluded, due to similar scattering factors of indium and metals such as palladium, rhodium, and silver. Nonetheless, based on the low metal loading, high dispersion of Pd and Rh, and, more importantly, the harsh catalyst synthesis and CO<sub>2</sub> hydrogenation conditions, these elements are likely to also form small intermetallic clusters with indium, as suggested in previous studies.<sup>[10]</sup> Since no oxygen shell is present for Au- and Ag-In<sub>2</sub>O<sub>3</sub>, these metals are very unlikely to be incorporated into the oxide bulk structure, and therefore, they form a mixture of nanoparticles and low nuclearity species, as supported by XANES and microscopy findings. In contrast, M–O and M–O–In bonds are clearly present in Co- and Rh-promoted systems, indicating that In<sub>2</sub>O<sub>3</sub> contains a significant population of cobalt and rhodium species incorporated into its lattice structure, at least near the surface. Furthermore, cobalt forms surface CoO<sub>x</sub> clusters and nanoparticles in line with microscopy and XANES. On the other hand, similarly to other promoters (i.e., palladium, iridium, platinum, and ruthenium), rhodium

also forms surface MIn<sub>3</sub> ensembles. Besides, nickel may alloy with indium into extended structures, as previously reported.<sup>[21]</sup> It is worth noting that a weak signal at the oxygen shell is evidenced for Pd-In<sub>2</sub>O<sub>3</sub> catalysts, suggesting the formation of M–O bonds, while such signals are absent for Ir-, Ru-, and Pt-In<sub>2</sub>O<sub>3</sub>. Still, only a few palladium atoms are expected to be bound to oxygen upon reaction conditions, mostly incorporated to surface lattice sites as In<sub>2</sub>MO<sub>x</sub> (Figure 4b). X-ray photoelectron spectroscopy (XPS) confirmed that all metal promoters are present at the surface (In<sub>3</sub>MO<sub>x</sub> in Figure 4b), although cobalt is most likely incorporated into bulk In<sub>2</sub>O<sub>3</sub> (Co@In<sub>2</sub>O<sub>3</sub>, bulk in Figure 4b), as suggested by the particularly low intensity of the Co 2p signal for Co-In<sub>2</sub>O<sub>3</sub> (Figure S8, Supporting Information) and computed Bader charges and XPS signals (Figure S19, Supporting Information). In contrast to XANES, most promoters appear partially or fully oxidized according to XPS. Such contrasting results are likely owing to samples being shortly exposed to air before XPS measurements. For Au-In<sub>2</sub>O<sub>3</sub>, metallic Au is detected but its binding energy is shifted to lower values, indicating a strong metal–oxide interaction between Au nanoparticles and In<sub>2</sub>O<sub>3</sub> at interfacial sites, as previously reported for Au-In<sub>2</sub>O<sub>3,x</sub> systems. This observation is further corroborated by XANES findings (Figure S7, Supporting Information), in which a more intense white line peak is evidenced for Au-In<sub>2</sub>O<sub>3</sub> compared to the metallic gold foil reference. In addition, microscopy images and EDX maps (Figure 3 and Figure S5, Supporting Information) clearly show the presence of Au nanoparticles supported on In<sub>2</sub>O<sub>3</sub>.

Experimental characterization shows that FSP in general maximizes the dispersion of the metal promoter atoms on the In<sub>2</sub>O<sub>3</sub> surface, making their presence as single sites or as low-nuclearity clusters more feasible as compared to incorporation of the atoms into the lattice. Therefore, DFT was employed to explore the presence of promoters as adatoms at the 26 non-equivalent adsorption sites on the In<sub>2</sub>O<sub>3</sub>(111) surface. They correspond to top, bridge, and three-fold positions, as shown in Figure S13, Supporting Information. This surface is corrugated and features a pocket and a protrusion, being the latest active site for CO<sub>2</sub> hydrogenation upon vacancy formation.<sup>[8,10]</sup> Interestingly, the most favored adsorption site for all metal promoters is the bridge position (In<sub>3</sub>M<sub>br</sub>O<sub>6</sub> in Figure 4b) between two oxygen atoms in the protrusion (Table S7, Supporting Information). In turn, adsorption at this position is more favorable than incorporation into lattice sites for all metals, except Ru (Figure 4c and Figure S15, Supporting Information). Au does not easily incorporate nor deposit, which fosters the formation of nanoparticles (M<sub>n</sub> in Figure 4b). The large Au nanoparticles were modeled as an Au(111) surface whereas the smallest possible Au<sub>n</sub> cluster capable of blocking an In<sub>2</sub>O<sub>3</sub> active site was modeled as an InAu<sub>3</sub> ensemble, whose formation is strongly exothermic (–0.98 eV, Figure S20, Supporting Information).

Under the CO<sub>2</sub> hydrogenation conditions, H<sub>2</sub> dissociates heterolytically on a surface M–O pair forming hydride (MH) and hydroxy (<sup>2</sup>OH) groups on the In<sub>3</sub>M<sub>br</sub>O<sub>6</sub> ensemble, followed by concomitant water formation and desorption leading to the In<sub>3</sub>M<sub>br</sub>O<sub>5</sub> moiety (Figures S22 and S23, Supporting Information). Then, the diffusion of the metal from the bridge to the oxygen vacancy position is feasible, forming the In<sub>3</sub>MO<sub>5</sub> ensemble. This structure is in line with the metallic character



**Figure 4.** a) EXAFS with model fit for  $\text{M-In}_2\text{O}_3$  catalysts after activation in  $\text{CO}_2$  hydrogenation for 2 h (K-edge for Ag, Co, Ni, Ru, Rh, and Pd whereas  $\text{L}_{2,3}$ -edge for Au, Ir, and Pt). b) Models employed in DFT simulations to rationalize different metal promoters speciation and promotional effects. Oxygen, indium, and metal promoter atoms are shown in red, green, and blue, respectively. Shaded red atoms represent oxygen atoms where the vacancy formation is considered. Potential energies relationship between c) dopant incorporated into its most favored  $\text{In}_2\text{O}_3$  lattice site versus dopant deposited as adatom at a bridge site ( $E_{M_{\text{surf}}}$  and  $E_{\text{In}_2\text{M}_n\text{O}_x}$ , respectively); and d) surface versus bulk incorporated species ( $E_{\text{In}_2\text{MO}_x}$  and  $E_{\text{M}@In_2O_3, \text{bulk}}$ , respectively). Dashed and dotted black lines indicate the relative stability of most stable speciation and the constant offset energy required to incorporate at surface and bulk sites, respectively. e) Energy required to form  $\text{In}_2\text{M}_2\text{O}_4$  ( $E_{\text{In}_2\text{M}_2\text{O}_4}$ ) metal promoter dimers versus the sum of their precursors potential energies ( $E_{\text{In}_2\text{MO}_x} + E_{\text{In}_2\text{M}_n\text{O}_x}$ ). Activation conditions:  $T = 553 \text{ K}$ ,  $P = 5 \text{ MPa}$ ,  $\text{H}_2/\text{CO}_2 = 4$ , and  $\text{WHSV} = 24000 \text{ cm}^3 \text{ h}^{-1} \text{ g}_{\text{cat}}^{-1}$ .

adopted by the metal promoters in the XANES spectra (Figure S7, Supporting Information) and  $\text{M-In}$  signals showed in the EXAFS spectra (Figure 4a) for the activated catalysts, and in particular for Pd, Pt, Ru, and Ir. Additionally, we explored the possibility that the metal promoters could be incorporated into the  $\text{In}_2\text{O}_3$  lattice, either at bulk or surface positions ( $\text{M}@In_2O_3, \text{bulk}$  and  $\text{In}_2\text{MO}_x$  in Figure 4b), as shown in Section S2.1, Figures S14–S18, and Table S8, Supporting Information. However, this speciation would only be likely for Co and Rh (Figure 4d and Figure S16, Supporting Information) and such sites would not be relevant for catalysis. Finally, Pd and Rh can form  $\text{In}_2\text{M}_2\text{O}_4$  clusters, with a catalytic activity akin

to that of  $\text{In}_2\text{MO}_x$  (Figure 4e, Section S2.2, and Table S9, Supporting Information).<sup>[10]</sup>

To summarize, the metal speciation derived from experimental characterization and DFT modeling show that under  $\text{CO}_2$  hydrogenation conditions, the most active promoters (Pd, Pt, Rh, Ru, and Ir) are deposited on the  $\text{In}_2\text{O}_3$  surface predominantly as  $\text{In}_2\text{MO}_x$ . This ensemble cannot be discarded for Co, Ni, Ag, and Au. Co is mostly present in an oxidic state, either as single atoms incorporated into the bulk  $\text{In}_2\text{O}_3$  sites ( $\text{Co}@In_2O_3, \text{bulk}$ ) or as  $\text{CoO}_x$  clusters and nanoparticles. Additionally, Ni can alloy with the support,<sup>[21]</sup> and Ag and Au can form metallic nanoparticles. As metals are generally favored

to be deposited on the  $\text{In}_2\text{O}_3$  surface rather than incorporated into the  $\text{In}_2\text{O}_3$  lattice by substituting an In atom, the  $\text{In}_3\text{MO}_5$  and  $M@(\text{In}_2\text{O}_3)_x$  bulk models are not considered. As such, the models that are relevant in further mechanistic evaluations are the single site  $\text{In}_3\text{MO}_x$  (all metals) and the  $M(111)$  surface (Ag and Au nanoparticles).

### 2.3. Effect of Promoters on Vacancy Formation

To investigate the impact of the promoters on the formation of oxygen vacancies,  $\text{H}_2$ -TPR experiments were conducted for all fresh samples (Figure S6, Supporting Information). Generally, all catalysts show three features in the low-temperature range (273–700 K), which are associated with hydrogen consumption to form surface oxygen vacancies. There is no significant increase in the peak intensities except for  $\text{Ni-In}_2\text{O}_3$ , which is capable of stripping many surface oxygen atoms based on a previous study.<sup>[21]</sup> XPS was also measured to gather additional information about oxygen vacancies on the activated catalysts by fitting the XPS O 1s spectra (Figure S9a, Supporting Information) with the signals signifying oxygen atoms next to a defect ( $\text{O}_{\text{defect}}$ ) indirectly (vide infra) assigned to oxygen vacancies (Table S3, Supporting Information).<sup>[7,32,34]</sup> The  $\text{O}_{\text{defect}}$  proportion remains virtually unchanged upon activation for all metal-promoted systems compared to  $\text{In}_2\text{O}_3$  (14–19% and 17%, respectively), with the notable exception of  $\text{Pd-In}_2\text{O}_3$  (34%). This is in line with previous results on this system prepared by coprecipitation.<sup>[10]</sup> DFT models also show that additional oxygen vacancy formation is favored for  $\text{Pd-In}_2\text{O}_3$  systems (Table S11, Supporting Information), both for models with the Pd atom deposited at surface bridge and a position previously occupied by an oxygen atom ( $\text{In}_3\text{M}_b\text{O}_6$  and  $\text{In}_3\text{MO}_3$ ) as well as incorporated into the surface  $\text{In}_2\text{O}_3$  lattice ( $\text{In}_2\text{MO}_6$ ). However, it must be noted that quantification of oxygen vacancies using such XPS analyses is not foolproof as surface adventitious hydroxyl signals are measured in lieu of actual vacancies that heal upon exposure to air, and contributions from OH groups to the O 1s signal in the  $\text{O}_{\text{defect}}$  region have been computationally suggested to be difficult to separate.<sup>[35,36]</sup> Hence, further complementary in situ or operando studies (e.g., EPR) would be required to attain a more accurate quantitative assessment of the density of oxygen vacancies. No detrimental over-reduction of  $\text{In}_2\text{O}_3$  up to metallic indium occurs under reaction conditions, as evidenced by the InMNN Auger spectra showing that indium species are always in the 3+ state (Figure S9b, Supporting Information), supporting the XRD results. Alloy formation between reduced  $\text{In}_2\text{O}_3$  and metal promoters is therefore not likely. However, at different synthetic or reaction conditions where the metal promoters and  $\text{In}_2\text{O}_3$  could be reduced, alloy formation cannot be completely discarded as predicted by DFT (Table S12, Supporting Information).

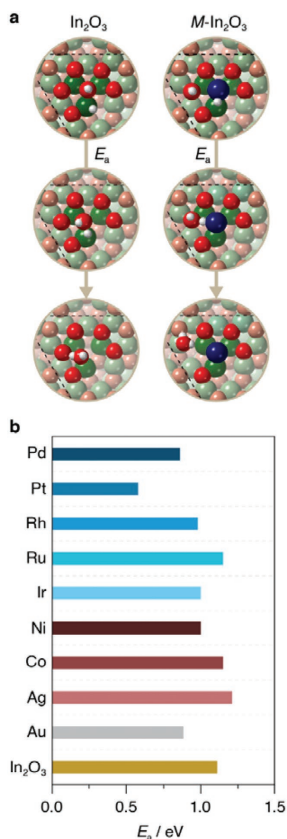
To compare the ease of forming surface oxygen vacancies on undoped  $\text{In}_2\text{O}_3$  and  $M\text{-In}_2\text{O}_3$ , such mechanisms were computed for the thermodynamically favored clean  $\text{In}_2\text{O}_3(111)$  surface (Figure S21, Supporting Information) and for  $\text{In}_3\text{MO}_3$  surface models (Figures S22 and S23, Supporting Information). For undoped  $\text{In}_2\text{O}_3$ , vacancy formation eventually leads to the active  $\text{In}_3\text{O}_3$  ensemble for  $\text{CO}_2$  hydrogenation as

described earlier. The mechanism begins with either homolytic or heterolytic dissociation of  $\text{H}_2$ , to form two surface  $^*\text{OH}$  species ( $\Delta E_{2^*\text{OH}} = -2.60$  eV,  $E_a = 1.08$  eV) or an  $\text{InH}+^*\text{OH}$  pair ( $\Delta E_{\text{InH}+^*\text{OH}} = 0.64$  eV,  $E_a = 0.36$  eV). The high stability of the hydroxyl groups suggests that the surface can be highly hydroxylated under reaction conditions, in line with a previous report<sup>[36]</sup> and our XPS data (Table S3, Supporting Information). The vacancy formation proceeds then with water formation and desorption, being the heterolytic path going through  $\text{InH}+^*\text{OH}$  the most favored (Figure S21 and Table S13, Supporting Information). For the doped systems, the formation of a second oxygen vacancy on the already reduced  $\text{In}_3\text{MO}_3$  configuration leads to the  $\text{In}_3\text{MO}_4$  active ensemble. This process starts with the homolytic dissociation of  $\text{H}_2$  on the metal dopant, followed by the formation of MH and adjacent  $^*\text{OH}$  groups, then combining into a water molecule that finally desorbs (Figures S22 and S23, Supporting Information). Exceptionally, an additional third vacancy can be formed, and such a process is most exothermic for  $\text{Pd-In}_2\text{O}_3$  (Table S11, Supporting Information) in agreement with its XPS-determined  $\text{O}_{\text{defect}}$  proportion (Table S3, Supporting Information). The mechanism of  $\text{CO}_2$  hydrogenation would not be affected by the presence of the third vacancy, as only two are needed to accommodate the metal and the adsorbed  $\text{CO}_2$ . In contrast to the undoped  $\text{In}_2\text{O}_3$  system, the homolytic  $\text{H}_2$  dissociation is barrierless for all  $M\text{-In}_2\text{O}_3$  catalysts except for Ag and Au promoters ( $E_a = 2.15$  and 1.75 eV, respectively). These two metals lead to an alternative mechanism, where  $\text{H}_2$  is heterolytically dissociated on an  $M\text{-O}$  pair leading to  $^*\text{OH}$  and MH groups ( $E_a = 0.39$  and 0.30 eV for Au and Ag, respectively). Hydrogen splitting is then followed by water formation and desorption (Figure S22, Supporting Information). In addition, the most demanding elementary step to generate the active ensemble, both for clean and doped systems ( $\text{In}_3\text{O}_3$  and  $\text{M}_3\text{O}_4$ , respectively), is water formation from  $\text{MH} + ^*\text{OH}$  ( $E_a$  between 0.88 and 1.21 eV, except for Pt,  $E_a = 0.58$  eV, Figure 5 and Table S13, Supporting Information). The water desorption step was found to be in a narrow range between 0.66 and 0.81 eV, easily surmountable under  $\text{CO}_2$  hydrogenation conditions.

### 2.4. Kinetic and Mechanistic Insights

Kinetic analyses were conducted to experimentally assess the mechanistic origin of promotional effects. Previous theoretical studies on  $M\text{-In}_2\text{O}_3$  showed that CO can act as an intermediate in the  $\text{CO}_2$  hydrogenation to methanol, a process that is preferred when small clusters typically containing 4 metal atoms are formed around the active site.<sup>[14–16,24]</sup> However, this mechanism requires at least 3 exposed metal atoms, as observed in a previous  $\text{Pd-In}_2\text{O}_3$  study.<sup>[10]</sup> Such a mechanism should not apply to  $M\text{-In}_2\text{O}_3$  catalysts synthesized by FSP, as a general decrease in methanol productivity was observed for  $\text{CO-CO}_2$  feeds (Figure S3, Supporting Information). Moreover, experimental and DFT characterization carried out in this work point to single-metal sites ( $\text{In}_3\text{MO}_x$ ) as the dominant speciation of the most active  $M\text{-In}_2\text{O}_3$  systems (Pd, Pt, Rh, Ru, Ir). It may also be present for the remaining metals, but less likely Au and Co. Therefore, only the alternative path having formate ( $\text{HCO}_2^*$ ) as





**Figure 5.** a) Schematic of water formation through heterolytic  $\text{H}_2$  splitting and subsequent formation of the  $\text{In}_2\text{O}_3$  and  $\text{In}_3\text{MO}_4$  active ensembles, for clean and doped  $\text{In}_2\text{O}_3(111)$ , respectively. Oxygen, indium, metal promoter, and hydrogen atoms are shown in red, green, blue, and white, respectively, in the initial (top), transition (middle), and final (bottom) states. b) Activation energy ( $E_a$ ) of forming a water molecule, the most demanding elementary step in the formation of the  $\text{In}_2\text{O}_3$  or  $\text{In}_3\text{MO}_4$  active ensemble for all systems except Pt- $\text{In}_2\text{O}_3$ . The bar for Au is shown in gray as there is no evidence that the  $\text{In}_3\text{AuO}_4$  ensemble exists in detectable quantities.

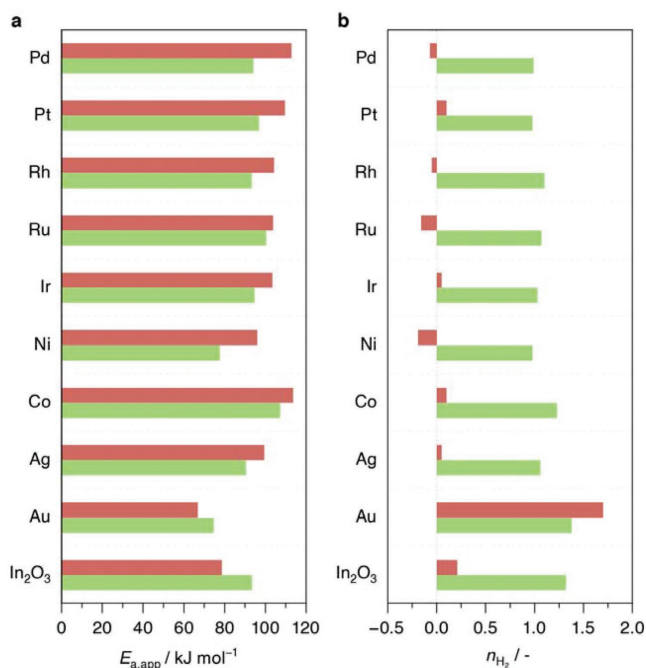
the key intermediate<sup>[8,10,38,39]</sup> is responsible for  $\text{CO}_2$  hydrogenation to methanol. This mechanism requires that the active sites already contain an oxygen vacancy ( $\text{In}_2\text{O}_3$  and  $\text{In}_3\text{MO}_4$  for clean and doped systems, respectively) to accommodate the  $\text{CO}_2$  molecule. It begins with the adsorption of  $\text{CO}_2$  and  $\text{H}_2$  on these ensembles, and then diverges into the methanol and CO paths.

In the methanol path, two hydrides are transferred to the C of  $\text{CO}_2$  leading to  $\text{CHO}_2^*$  and then  $\text{CH}_2\text{O}_2^*$ , which is protonated to  $\text{CH}_2\text{O}^*\text{OH}$ . The C–OH bond then breaks and the OH is desorbed as water upon a proton transfer to obtain formaldehyde ( $\text{CH}_2\text{O}^*$ ). Finally, a proton and a hydride are transferred to  $\text{CH}_2\text{O}^*$  to form  $\text{CH}_3\text{OH}^*$ , which desorbs. In contrast, the RWGS competing path starts when  $\text{CO}_2$  is protonated to form a carboxylate ( $^*\text{COOH}$ ) which is protonated and dehydrated to produce CO.

The apparent activation energies for methanol synthesis and the RWGS reaction (Figure 6a), derived from catalytic tests conducted at variable temperature (Figure S10, Supporting Information), show some general trends with selectivity patterns. For instance, activation barriers for methanol synthesis are generally lower than for the RWGS reaction for all promoted systems in comparison to undoped  $\text{In}_2\text{O}_3$ , with Au- $\text{In}_2\text{O}_3$  being an exception. For the latter, the smaller activation energy for the RWGS reaction rationalizes its lower selectivity to methanol compared to undoped  $\text{In}_2\text{O}_3$  and the other M- $\text{In}_2\text{O}_3$  systems. It is noteworthy that some systems, including  $\text{In}_2\text{O}_3$ , show slightly lower activation barriers for RWGS than for methanol formation, even though these systems are more selective to methanol. Besides, there is no correlation between the apparent activation energies and the observed reaction rates (Figure S12, Supporting Information), suggesting that there is an important contribution of other phenomena which do not depend exponentially on  $1/T$  (i.e., gas diffusion, on-surface diffusion, adsorption, etc.) to drive selectivity. In principle, the higher degree of hydroxylations/defects on these systems (Table S3, Supporting Information) could also play a role as more surface oxygen atoms bound to protons could reduce the entropic penalty to form CO, or in the final step to form methanol.<sup>[37]</sup> The excess of hydroxyl groups can also interconvert to hydrides<sup>[38]</sup> favoring C–H hydrogenations.

Since promotion of  $\text{In}_2\text{O}_3$  is often related to the ability of metal dopants to facilitate hydrogen activation, apparent reaction orders with respect to this reactant were determined from experiments at variable partial pressures of  $\text{H}_2$  in the feed (Figure 6b and Figure S11, Supporting Information). For methanol synthesis, the reaction order decreased for all metal-promoted systems compared to  $\text{In}_2\text{O}_3$  except for Au- $\text{In}_2\text{O}_3$ . Pd- and Pt- $\text{In}_2\text{O}_3$  reach the lowest values ( $\approx 0.9$  instead of 1.3 for undoped  $\text{In}_2\text{O}_3$ ), suggesting a higher availability of hydrides (MH) and therefore a promotion of all C–H hydrogenation reactions for these systems. For the RWGS reaction, the reaction orders significantly increased for Au- $\text{In}_2\text{O}_3$ , while remaining at their lowest for all other systems, indicating that split  $\text{H}_2$  is predominantly involved in the CO pathway on Au as opposed to the other promoted systems. Given the limited insights, these trends from kinetic analysis were supplemented by DFT-derived mechanistic elucidations in order to better account for the structure-selectivity patterns of each individual promoter.

Energy profiles for methanol and CO formation for undoped  $\text{In}_2\text{O}_3$  and the nine metal-promoted  $\text{In}_2\text{O}_3$  systems are presented in Figures S24–S26, Supporting Information. The  $\text{In}_3\text{MO}_4$  ensemble was selected as the most representative for the promotion considering all experimental characterization and previous theoretical simulations, to explore the reactivity toward  $\text{CO}_2$  hydrogenation. Significant differences between the profiles for clean  $\text{In}_2\text{O}_3$  and M- $\text{In}_2\text{O}_3$  were not found. Thus, the  $\text{CO}_2$  to methanol reaction mechanism does not have a significant contribution

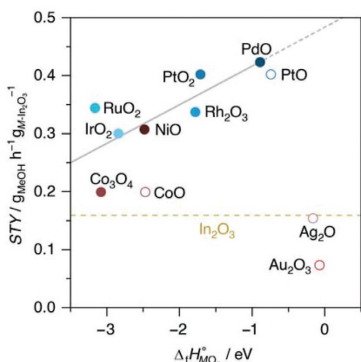


**Figure 6.** a) Apparent activation energies ( $E_{a,app}$ ) and b) reaction order with respect to H<sub>2</sub> ( $n_{H_2}$ ) for CO<sub>2</sub> hydrogenation to methanol (green) and the RWGS reaction (red), over undoped In<sub>2</sub>O<sub>3</sub> and M-In<sub>2</sub>O<sub>3</sub> catalysts. Arrhenius plots with data regressions used to determine the activation energy and reaction order values are depicted in Figures S10 and S11, Supporting Information.

in the promotional effect exhibited by M-In<sub>2</sub>O<sub>3</sub> systems. Besides, the lack of correlation between the apparent activation energies and the STY reveals that an entropic process is controlling the net rate (Figure S12, Supporting Information), which could be the availability of either vacancies or MH species at the active site. In addition, in order to explore the activity of Ag and Au nanoparticles, energy profiles were computed on Ag(111) and Au(111) surfaces (Figure S27, Supporting Information). The CO<sub>2</sub> conversion to methanol follows a different mechanism on bulk metals, where CO<sub>2</sub> adsorbs and is then protonated and dehydrated to form CO. Then, CO either desorbs or follows two parallel paths that after concomitant hydrogen transfers lead to methanol. Au and Ag metal surfaces strongly hinder the CO<sub>2</sub> adsorption and favored desorption rather than hydrogenation of CO, which explains the lack of activity and selectivity of Au- and Ag-In<sub>2</sub>O<sub>3</sub> towards methanol formation, as they contain mostly metal nanoparticles. In addition, inactive Au<sub>n</sub> ensembles containing as few as 3 Au atoms (Figure S20, Supporting Information) can form on the In<sub>3</sub>AuO<sub>x</sub> ensemble and block additional In<sub>3</sub>O<sub>3</sub> active sites, thus lowering the activity and selectivity to methanol.

To provide a comprehensive rationalization of the promoters' speciation in M-In<sub>2</sub>O<sub>3</sub> catalysts under CO<sub>2</sub> hydrogenation conditions and its impact on methanol selectivity and productivity, we correlated the methanol STY over M-In<sub>2</sub>O<sub>3</sub> for each promoter with the standard formation enthalpy ( $\Delta_f H^\circ$ ) of its oxide MO<sub>x</sub> (Figure 7 and Figure S28, Supporting Information). As a general rule, the most active promoters are those more metallic with a less exothermic  $\Delta_f H^\circ$ , as they promote homolytic hydrogen splitting. Yet, if the promoter has a poor affinity to oxygen, it will not form oxidic precursors and therefore will rather nucleate into metallic nanoclusters and nanoparticles under FSP synthesis conditions (i.e., Ag and Au). In contrast, if these metals were stabilized as adatoms on In<sub>2</sub>O<sub>3</sub> surface (In<sub>3</sub>MO<sub>x</sub>), they will be highly active.<sup>[17,39]</sup> In cases where the promoter has a high affinity to oxygen, such as Co, it will tend to incorporate to the bulk or to form bulk metal oxides.

The key findings attained by performance assessment, characterization, and DFT simulations are graphically summarized in Figure 8. Overall, the promotional effect in M-In<sub>2</sub>O<sub>3</sub>



**Figure 7.** Relationship between methanol STY during CO<sub>2</sub> hydrogenation over *M*-In<sub>2</sub>O<sub>3</sub> catalysts versus the experimental standard enthalpy of formation of the most stable metal oxide MO<sub>x</sub> for each metal promoter (Δ<sub>f</sub>H<sup>0</sup><sub>MO<sub>x</sub></sub>) normalized by the number of metal atoms in the stoichiometric unit.<sup>[56–58]</sup> The equivalent plot normalized by the number of oxygen atoms is shown in Figure S28, Supporting Information. The gray regression line considers all metals marked by filled circles. Ag<sub>2</sub>O and Au<sub>2</sub>O<sub>3</sub> are less stable when compared with their pure metals and thus sinter, and lie beyond the activity cliff.<sup>[59]</sup> Data for CoO and PtO are also plotted to show that this measure is rather independent of the oxide chosen. The STY obtained over undoped In<sub>2</sub>O<sub>3</sub> is marked for comparison.

is crucially related to the speciation of the metal promoters. It can be traced back to the ability of In<sub>3</sub>M and In<sub>2</sub>M<sub>2</sub> sites to lower the homolytic H<sub>2</sub> splitting barrier increase the availability

of H. These sites are more widespread on Ir-, Ru-, Rh-, Pt-, and Pd-In<sub>2</sub>O<sub>3</sub>, especially the latter two comprising highly dispersed promoters, than on Co- and Ni-In<sub>2</sub>O<sub>3</sub> where the density of single metal atom sites is inferior to other promoter architectures, and on Ag- and Au-In<sub>2</sub>O<sub>3</sub> where these sites are too sparse to significantly activate any reactants. In addition, the formation of small Au<sub>n</sub> nanoclusters containing as few as three atoms would block the active site. Lastly, undoped In<sub>2</sub>O<sub>3</sub> sites could also be assumed to significantly contribute to the catalytic activity of the Co-In<sub>2</sub>O<sub>3</sub> system, since its performance is only marginally improved in comparison to the undoped oxide phase. Still, the interplay between promoter and active phase is more complex for this catalyst, owing to cobalt exhibiting varied speciation (i.e., nanoparticles, clusters, single atoms). Hence, unlike other promoters, its role as a dopant is still indeed not fully understood and deserves to be tackled in future studies. In a broader context, the best promoter balances the affinity to oxygen and hydrogen. Metals that are too oxophilic (such as Co) overly incorporate into the In<sub>2</sub>O<sub>3</sub> lattice whereas metals that are too noble (such as Au) do not disperse efficiently. If they are well dispersed, those with higher affinity to hydrogen will become better catalysts, which emphasizes that metals such as Au and Ni would benefit from further studies tackling the optimization of the FSP protocol to improve their dispersion into low-nuclearity species.

### 3. Conclusions

Through a comparative study using FSP as a standardized synthesis platform, we have successfully obtained a detailed analysis on the speciation and promotional effects of nine

promoter	speciation	impact on performance		structural and mechanistic insights
		$\Delta$ STY  50–63%	$S_{MeOH}$  86–96%	<ul style="list-style-type: none"> <li>Atomically-dispersed promoter species</li> <li>High density of In<sub>3</sub>M or In<sub>2</sub>M<sub>2</sub> ensembles</li> <li>Higher availability of MH</li> <li>MeOH formation favored</li> </ul>
		 20–48%	 73–76%	<ul style="list-style-type: none"> <li>Clustering and bulk incorporation of promoters</li> <li>Low density of In<sub>3</sub>M or In<sub>2</sub>M<sub>2</sub> ensembles</li> <li>Lower availability of MH</li> <li>MeOH selectivity less boosted</li> </ul>
		 3–54%	 67–56%	<ul style="list-style-type: none"> <li>Sintering into nanoparticles</li> <li>Homolytic H<sub>2</sub> splitting hindered</li> <li>Au<sub>n</sub> ensembles inhibit methanol formation</li> <li>CO formation favored</li> </ul>

**Figure 8.** Summary of promoter speciation and their associated structural-mechanistic features dictating performance of *M*-In<sub>2</sub>O<sub>3</sub> catalysts.

metal-promoted indium oxide ( $M\text{-In}_2\text{O}_3$ ,  $M = \text{Au, Ag, Co, Ni, Ir, Ru, Rh, Pt, and Pd}$ ) catalysts in  $\text{CO}_2$  hydrogenation to methanol. These systematically synthesized materials were fully assessed by an integrated catalytic evaluation, in-depth characterization, kinetic analyses, and DFT. This holistic approach enabled the identification of three main catalyst families, for which performance is strongly governed by the promoters' speciation. The first encompasses systems containing atomically-dispersed and well-stabilized, mostly through  $M\text{-In}$  bonds, Pd, Pt, Rh, Ru, and Ir species on the  $\text{In}_2\text{O}_3$  surface, which reached a methanol selectivity of up to 95%. The second covers Co- and Ni- $\text{In}_2\text{O}_3$ , with a less boosted methanol selectivity ( $\approx 75\%$ ) owing to promoters forming large oxidic and indium alloy-containing clusters, respectively, and in the case of Co, to its partial incorporation into the bulk of  $\text{In}_2\text{O}_3$ . The third family includes Au and Ag, which sinter into nanoparticles, resulting in inferior or similar methanol selectivity (56 and 67%) to undoped  $\text{In}_2\text{O}_3$ , respectively. DFT simulations further elucidated that methanol formation is greatly enhanced over systems containing a high concentration of isolated promoter atoms, particularly Pd and Pt, owing to the creation of  $\text{In}_3\text{M}$  and  $\text{In}_2\text{M}_2$  ensembles, which strongly facilitate homolytic  $\text{H}_2$  splitting and increase the availability of hydrides, which in turn participate in C-H hydrogenations. As expected, the surface population of the active sites diminishes upon clustering or bulk incorporation of metal promoters such as Ni, Ag, and Co, thereby translating into inferior methanol productivity. Specifically, the formation of larger Au nanoparticles block the active ensembles for  $\text{CO}_2$  hydrogenation and explains the low activity of this Au- $\text{In}_2\text{O}_3$ . Overall, this study marks a new step toward the atomic-level understanding of  $\text{In}_2\text{O}_3$  promotion by relevant metal promoters, revealing that the degree of promotion is metal speciation-dependent and likely dictated by the density and stability of space resolved  $\text{In}_3\text{M}$  and  $\text{In}_2\text{M}_2$  ensembles. This offers key guidelines for the design of an optimal system to propel green methanol production. Going beyond  $\text{CO}_2$  hydrogenation, our strategy to engineer promotion using a universal and scalable preparation method such as FSP holds great potential for tailoring new or existing catalytic systems applicable in diverse energy conversions.

#### 4. Experimental Section

**Catalyst Preparation:**  $M\text{-In}_2\text{O}_3$  ( $M = \text{Ag, Au, Co, Ir, Ni, Pd, Pt, Rh, Ru}$ ) catalysts with a nominal metal promoter content of 0.5 wt.% were prepared by FSP. Briefly, a precursor solution of dissolved indium and promoter complexes (see Table S1, Supporting Information, for a full list) in the desired ratio was pumped through a 0.4 mm nozzle at a flow rate of  $5 \text{ L min}^{-1}$  and dispersed into a fine spray by flowing oxygen at 1.5 bar at a flow rate of  $5 \text{ L min}^{-1}$ . The spray was ignited by a supporting flame generated using  $2.4 \text{ L min}^{-1}$  of oxygen and  $1.2 \text{ L min}^{-1}$  of methane. Such particle-generating flames have been well characterized and reported to reach average flame temperatures of 2500–3000 K, with very fast cooling rates ( $\approx 10^5 \text{ K s}^{-1}$ )<sup>[29,40–42]</sup>. The resulting nanoparticles were collected on a glass fiber filter (GF/A-6) and used in  $\text{CO}_2$  hydrogenation without further treatment.

**Catalyst Characterization:** Inductively coupled plasma optical emission spectroscopy (ICP-OES) was performed using a Horiba Ultra 2 instrument equipped with a photomultiplier tube detector. Samples were dissolved in hot aqua regia (353 K) for 12 h prior to analysis. Nitrogen

sorption at 77 K was carried out using a Micromeritics TriStar II analyzer. Prior to the measurements, samples were degassed under vacuum (10 Pa) at 473 K for 12 h. The total surface area ( $S_{\text{BET}}$ ) was determined using the Brunauer–Emmett–Teller method, and the single point pore volume ( $V_{\text{pore}}$ ) was determined at  $p/p_0 \geq 0.98$ . X-ray diffraction (XRD) was conducted using a Rigaku SmartLab diffractometer with a D/tex Ultra 250 detector using  $\text{Cu K}\alpha$  radiation ( $\lambda = 0.1541 \text{ nm}$ ) and operating in the Bragg-Brentano geometry. Data were acquired in the  $20\text{--}70^\circ 2\theta$  range with an angular step size of  $0.025^\circ$  and a counting time of 1.5 s per step. Temperature-programmed reduction with hydrogen ( $\text{H}_2\text{-TPR}$ ) was conducted at ambient pressure using a Micromeritics AutoChem HP II coupled to a Pfeiffer OMNIStar mass spectrometer. Samples were loaded into a quartz tube, dried at 423 K in Ar (PanGas, purity 5.0) for 1 h ( $10 \text{ K min}^{-1}$ ) and cooled down to 223 K ( $20 \text{ K min}^{-1}$ ) using liquid nitrogen. The temperature-programmed reduction was then carried out using 5 vol.%  $\text{H}_2$  in Ar (Messer) and increasing the temperature to 1023 K ( $5 \text{ K min}^{-1}$ ), which was held for 30 min. High-resolution transmission electron microscopy (HRTEM) and high-angle annular dark-field scanning transmission electron microscopy (HAADF-STEM) images were collected using a Talos F200X instrument operated at an acceleration potential of 200 kV and an aberration-corrected JEM-ARM300F microscope (GrandARM, JEOL) operated at 300 kV in Z contrast mode. Energy-dispersive X-ray (EDX) spectroscopy and elemental maps were measured using the Talos instrument equipped with four silicon drift detectors (SDD). XPS was conducted using a Physical Electronics (PHI) Quantum 2000 XPS featuring monochromatic Al  $\text{K}\alpha$  radiation, generated from an electron beam operated at 15 kV and 32.3 W, and a hemispherical capacitor electron-energy analyzer, equipped with a channel plate and a position-sensitive detector. Analyses were conducted at  $2 \times 10^{-7}$  Pa, with an electron take-off angle of  $45^\circ$ , operating the analyzer in the constant pass energy mode. X-ray absorption spectroscopy (XAS) was measured at the SuperXAS beamline at the Swiss Light Source.<sup>[43]</sup> The incident beam was provided by the 2.9-T super bent source. The X-ray beam was collimated by a Si- (for XAS < 10 keV), Rh- (10–20 keV), or Pt-coated (>20 keV), mirror at 2.5–2.9 mrad and focused by a toroidal Rh (below 20 keV) or Pt-coated (above 20 keV) mirror. The energy was selected by a Si(111) (for Co K, Ni K, Ir L<sub>3</sub>, Pt L<sub>3</sub>, Au L<sub>3</sub>, Rh K, Pd K) and a Si(311) (Ru K and Ag K edges) channel-cut monochromator,<sup>[44]</sup> and calibrated using the corresponding metallic foil of each promoter, which was measured simultaneously with the specimen of interest at suitable absorption edges (Table S4, Supporting Information). The incident X-ray beam was focused on a  $0.25 \times 1 \text{ mm}^2$  spot. Activated samples were transferred from the reactor to a quartz capillary and sealed under inert atmosphere. Reference oxides for each promoter were measured in transmission mode as a pellet diluted with cellulose. Three 15-cm long ionization chambers filled with nitrogen (below 15 keV) at 2 bar or 50%  $\text{N}_2$  in Ar at 2 bar (above 15 keV) were used to monitor the incident beam intensity,<sup>[44]</sup> transmission through the sample, and the reference metallic foils. For Rh K, Ru K, Pd K, and Ag K edges XAS, quick fluorescence detection mode with a PIPS diode detector (1 Hz monochromator oscillation, 5–10 min data acquisition) was used. For Co K, Ni K, Ir L<sub>3</sub>, Pt L<sub>3</sub>, Au L<sub>3</sub> XAS of catalysts, an SDD detector and a step-by-step acquisition mode (30–90 min data acquisition) were applied. The spectra were calibrated and averaged with the in-house developed ProXAS software and further analyzed using the Demeter software package.<sup>[45]</sup>  $k^2$ -weighted EXAFS spectra were fitted in the optimal  $k$ - and  $R$ -windows for each metal. Amplitude reduction factors ( $S_0^2$ ) were determined by fitting of the EXAFS spectrum of pure metal foils (Table S4, Supporting Information). The scattering paths for the fitting were produced using known crystallographic structures and models attained by DFT of metallic, oxidic, and alloy phases of each promoter and indium, as indicated in Table S5, Supporting Information.

**Catalyst Evaluation:** The gas-phase hydrogenation of  $\text{CO}_2$  and hybrid  $\text{CO}_2\text{:CO}$  feeds to methanol was performed in a PID Eng&Tech high-pressure continuous-flow setup comprising four parallel fixed-bed reactors, as described elsewhere.<sup>[32]</sup> Undiluted catalysts (mass,  $m_{\text{cat}} = 0.1 \text{ g}$ ; particle size = 0.2–0.4 mm) were loaded into each reactor tube (internal diameter 4 mm), held in place by a quartz-wool bed set on a quartz frit,

and purged in flowing He (40 cm<sup>3</sup> STP min<sup>-1</sup>, PanGas, 4.6) for 30 min at ambient pressure. Under the same flow, the pressure was increased to 5.5 MPa for a leak test. The reaction was carried out by feeding a mixture of H<sub>2</sub> (PanGas, 5.0), CO<sub>2</sub> (40 vol.% in H<sub>2</sub>, Messer, 4.5), and, in the case of hybrid feeds, also CO (Messer, 5.0), with a molar H<sub>2</sub>/CO<sub>2</sub> (CO<sub>2</sub> = CO<sub>2</sub> + CO) ratio of 4 at 553 K, 5 MPa, and a weight hourly space velocity (WHSV) of 24 000 cm<sup>3</sup> STP h<sup>-1</sup> g<sub>cat</sub><sup>-1</sup>, unless stated otherwise. The selectivity of the catalysts was compared at a constant degree of CO<sub>2</sub> conversion (X<sub>CO<sub>2</sub></sub>) of 3% by adjusting the WHSV for each system. Kinetic investigations were carried out at doubled WHSV (except for Au-In<sub>2</sub>O<sub>3</sub>) attained by using a catalyst mass of 0.05 g. To determine activation energies of methanol and CO formation, the reaction was initiated at 473 K and stepwise increased to 573 K in 10-K increments at 5 MPa (m<sub>cat</sub> = 0.05 g, and H<sub>2</sub>/CO<sub>2</sub> = 4 at specified WHSV). Reaction orders with respect to H<sub>2</sub> were acquired by applying a constant flow of CO<sub>2</sub> (8 cm<sup>3</sup> STP min<sup>-1</sup>) and increasing the flow of H<sub>2</sub>, while using He to balance the total flow to 44 cm<sup>3</sup> STP min<sup>-1</sup> (m<sub>cat</sub> = 0.055 g) at 553 K and 5 MPa.

The effluent streams were analyzed by gas chromatography every 1 h. Response factors (F<sub>i</sub>) for each compound *i*, respective to the internal standard (20 vol.% C<sub>2</sub>H<sub>6</sub> in He, Messer, purity 3.5), in the GC analysis were determined by Equation (1):

$$F_i = \frac{A_{C_2H_6} / n_{C_2H_6}^{in}}{A_i / n_i^{in}} \quad (1)$$

where A<sub>i</sub> is the integrated area determined for the peak of compound *i* and n<sub>in</sub> is the corresponding known molar flow at the reactor inlet. An average of 5 points around the expected analyte concentration was used. The unknown effluent molar flow of compound *i* was determined using Equation (2):

$$\dot{n}_i^{out} = \frac{A_i \times F_i}{A_{C_2H_6}} \times \dot{n}_{C_2H_6}^{out} \quad (2)$$

Conversion (X<sub>i</sub>), selectivity (S<sub>i</sub>), and production rate (r<sub>i</sub>) were calculated using Equations (3–5):

$$X_i = \frac{\dot{n}_i^{in} - \dot{n}_i^{out}}{\dot{n}_i^{in}} \quad (3)$$

$$S_i = \frac{\dot{n}_i^{in} - \dot{n}_i^{out}}{\dot{n}_{CO_2}^{in} - \dot{n}_{CO_2}^{out}} \quad (4)$$

$$r_i = \frac{\dot{n}_i^{in} - \dot{n}_i^{out}}{m_{cat}} \quad (5)$$

The methanol STY is the product of r<sub>MeOH</sub> and the molar weight of methanol (32.04 g mol<sup>-1</sup>). The carbon balance was determined for each experiment according to Equation 6:

$$\varepsilon_C = \left( 1 - \frac{\dot{n}_{CO_2}^{out}}{\dot{n}_{CO_2}^{in}} + \dot{n}_{MeOH}^{out} + \dot{n}_{CO}^{out} \right) \quad (6)$$

and was always within a 5% margin.

**Theoretical Simulations:** DFT studies were carried out employing the Vienna ab initio simulation package (VASP)<sup>[46,47]</sup> using the Perdew-Burke-Ernzerhof (PBE) exchange-correlation functional.<sup>[48]</sup> Core electrons were described by projector augmented-wave (PAW) pseudopotentials<sup>[49]</sup> and valence electrons were expanded with plane-waves with a kinetic cut-off energy of 500 eV. The Brillouin zone was sampled by a Γ-centered mesh generated through the Monkhorst-Pack method<sup>[50]</sup> with a reciprocal grid size narrower than 0.021 Å<sup>-1</sup>. Transition states were obtained with the climbing image nudged elastic band (CI-NEB) method.<sup>[51]</sup> Spin polarization was included when necessary.

In<sub>2</sub>O<sub>3</sub> was represented by the cubic bixbyite structure as determined in previous studies<sup>[52]</sup> from which the In<sub>2</sub>O<sub>3</sub>(111) termination, the

experimentally most stable and abundant (Figure S14, Supporting Information), was built.<sup>[8,52,53]</sup> The slab was modeled as a p(1 × 1) containing five O–In–O trilayers. The two outermost layers were allowed to relax, whereas the three bottommost were fixed to their bulk positions. A vacuum region larger than 12 Å was added between the slabs and the dipole correction was applied along the z axis to account for the asymmetry in the relaxation. Metal promoters were modeled in 26 non-equivalent positions as adatoms and 14 sites where they replaced an In atom in the In<sub>2</sub>O<sub>3</sub> lattice (Figures S13 and S14, Supporting Information). Then, their relative stabilities were assessed from their energies as described in the Supporting Information (Data Processing), taking bulk In<sub>2</sub>O<sub>3</sub>, the promoter as a bulk oxide, H<sub>2</sub>, H<sub>2</sub>O, and CO<sub>2</sub> in gas phase as energy references (Equations S1–S5 and Table S6, Supporting Information). The mechanism for vacancy formation and CO<sub>2</sub> reduction to methanol and CO were computed following previous studies.<sup>[8,10,21,36]</sup>

## Supporting Information

Supporting Information is available from the Wiley Online Library or from the author.

## Acknowledgements

T.P.A., J.M.-V., and T.Z. equally contributed to this work. This publication was created as part of NCCR Catalysis, a National Centre of Competence in Research funded by the Swiss National Science Foundation. The Scientific Center for Optical and Electron Microscopy (ScopeM) at the ETH Zurich and the SuperXAS beamline at PSI, are thanked for access to their facilities. The authors are grateful to Prof. Christophe Copéret, Dr. Gina Noh, and Mr. Jan Alfke for assistance with sample preparation for XAS measurements. T.Z. thanks the Agency for Science, Technology, and Research (A\*STAR) Singapore for support through a graduate fellowship. The Spanish Ministry of Science and Innovation is acknowledged for financial support (RTI2018-101394-B-I00 and Severo Ochoa Grant MCIN/AEI/10.13039/501100011033 CEX2019-000925-S) and the Barcelona Supercomputing Center-MareNostrum (BSC-RES) for providing generous computer resources.

Open access funding provided by Eidgenössische Technische Hochschule Zurich.

## Conflict of Interest

The authors declare no conflict of interest.

## Data Availability Statement

The data that support the findings of this study are available from the corresponding author upon reasonable request. All DFT data can be found online<sup>[54]</sup> in the ioChem-BD repository<sup>[55]</sup> at <https://doi.org/10.19061/iochem-bd-1-219>.

## Keywords

CO<sub>2</sub> hydrogenation, green methanol, indium oxide, metal speciation, promotion

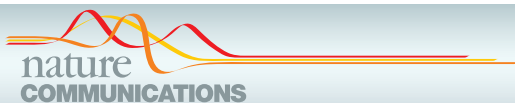
Received: November 26, 2021

Revised: February 5, 2022

Published online:

[1] A. González-Garay, M. S. Frei, A. Al-Qahtani, C. Mondelli, G. Guillén-Gosálbez, J. Pérez-Ramírez, *Energy Environ. Sci.* **2019**, *12*, 3425.

- [2] A. Goepfert, M. Czaun, J.-P. Jones, G. K. S. Prakash, G. A. Olah, *Chem. Soc. Rev.* **2014**, *43*, 7995.
- [3] K. Harris, R. G. Grim, Z. Huang, L. Tao, *Appl. Energy* **2021**, *303*, 117637.
- [4] C. H. Vo, C. Mondelli, H. Hamed, J. Pérez-Ramírez, S. Farooq, I. A. Karimi, *ACS Sustainable Chem. Eng.* **2021**, *9*, 10591.
- [5] V. Dieterich, A. Buttler, A. Hanel, H. Spliethoff, S. Fendt, *Energy Environ. Sci.* **2020**, *13*, 3207.
- [6] B. Lee, H. Lee, D. Lim, B. Brigljević, W. Cho, H. S. Cho, C. H. Kim, H. Lim, *Appl. Energy* **2020**, *279*, 115827.
- [7] O. Martin, A. J. Martín, C. Mondelli, S. Mitchell, T. F. Segawa, R. Hauert, C. Drouilly, D. Curulla Ferré, J. Pérez-Ramírez, *Angew. Chem., Int. Ed.* **2016**, *55*, 6261.
- [8] M. S. Frei, M. Capdevila-Cortada, R. García-Muelas, C. Mondelli, N. López, J. A. Stewart, D. Curulla Ferré, J. Pérez-Ramírez, *J. Catal.* **2018**, *361*, 313.
- [9] N. Rui, Z. Wang, K. Sun, J. Ye, Q. Ge, C. J. Liu, *Appl. Catal. B* **2017**, *218*, 488.
- [10] M. S. Frei, C. Mondelli, R. García-Muelas, K. S. Kley, B. Puértolas, N. López, O. V. Safonova, J. A. Stewart, D. Curulla Ferré, J. Pérez-Ramírez, *Nat. Commun.* **2019**, *10*, 3377.
- [11] Z. Han, C. Tang, J. Wang, L. Li, C. Li, *J. Catal.* **2021**, *394*, 236.
- [12] K. Sun, N. Rui, Z. Zhang, Z. Sun, Q. Ge, C. J. Liu, *Green Chem.* **2020**, *22*, 5059.
- [13] J. Wang, K. Sun, X. Jia, C. J. Liu, *Catal. Today* **2021**, *365*, 341.
- [14] Q. Wu, C. Shen, N. Rui, K. Sun, C. J. Liu, *J. CO<sub>2</sub> Util.* **2021**, *53*, 101720.
- [15] K. Sun, Z. Zhang, C. Shen, N. Rui, C. J. Liu, *Green Energy Environ.* **2021**, <https://doi.org/10.1016/j.gjee.2021.05.004>.
- [16] C. Shen, K. Sun, Z. Zhang, N. Rui, X. Jia, D. Mei, C. J. Liu, *ACS Catal.* **2021**, *11*, 4036.
- [17] N. Rui, F. Zhang, K. Sun, Z. Liu, W. Xu, E. Stavitski, S. D. Senanayake, J. A. Rodriguez, C. J. Liu, *ACS Catal.* **2020**, *10*, 11307.
- [18] N. H. M. Dostagir, C. Thompson, H. Kobayashi, A. M. Karim, A. Fukuoka, A. Shrotri, *Catal. Sci. Technol.* **2020**, *10*, 8196.
- [19] A. Bavykina, I. Yarulina, A. J. Al Abdulghani, L. Gevers, M. N. Hedhili, X. Miao, A. R. Galilea, A. Pustovarenko, A. Dikhtiarenko, A. Cadiou, A. Aguilar-Tapia, J.-L. Hazemann, S. M. Kozlov, S. Oud-Chikh, L. Cavallo, J. Gascon, *ACS Catal.* **2019**, *9*, 6910.
- [20] Z. Shi, Q. Tan, D. Wu, *AIChE J.* **2019**, *65*, 1047.
- [21] M. S. Frei, C. Mondelli, R. García-Muelas, J. Morales-Vidal, M. Philipp, O. V. Safonova, N. López, J. A. Stewart, D. Curulla Ferré, J. Pérez-Ramírez, *Nat. Commun.* **2021**, *12*, 1960.
- [22] J. Zhu, F. Cannizzaro, L. Liu, H. Zhang, N. Kosinov, I. A. W. Filot, J. Rabeah, A. Brückner, E. J. M. Hensen, *ACS Catal.* **2021**, *11*, 11371.
- [23] X. Jia, K. Sun, J. Wang, C. Shen, C. J. Liu, *J. Energy Chem.* **2020**, *50*, 409.
- [24] C. Shen, Q. Bao, W. Xue, K. Sun, Z. Zhang, X. Jia, D. Mei, C. J. Liu, *J. Energy Chem.* **2022**, *65*, 623.
- [25] E. K. Athanassiou, R. N. Grass, W. J. Stark, *Aerosol Sci. Technol.* **2010**, *44*, 161.
- [26] L. Mädler, H. K. Kammler, R. Mueller, S. E. Pratsinis, *J. Aerosol Sci.* **2002**, *33*, 369.
- [27] T. Rudin, K. Wegner, S. E. Pratsinis, *J. Nanopart. Res.* **2011**, *13*, 2715.
- [28] W. Y. Teoh, R. Amal, L. Mädler, *Nanoscale* **2010**, *2*, 1324.
- [29] R. Koirala, S. E. Pratsinis, A. Baiker, *Chem. Soc. Rev.* **2016**, *45*, 3053.
- [30] S. Pokhrel, L. Mädler, *Energy Fuels* **2020**, *34*, 13209.
- [31] S. Ding, H. A. Chen, O. Mekasuwandumrong, M. J. Hülsey, X. Fu, Q. He, J. Panpranot, C. M. Yang, N. Yan, *Appl. Catal. B* **2021**, *281*, 119471.
- [32] T. P. Araújo, A. Shah, C. Mondelli, J. A. Stewart, D. Curulla Ferré, J. Pérez-Ramírez, *Appl. Catal. B* **2021**, *285*, 119878.
- [33] D. Schanke, S. Vada, E. A. Blekkan, A. M. Hilmen, A. Hoff, A. Holmen, *J. Catal.* **1995**, *156*, 85.
- [34] C. Janowitz, V. Scherer, M. Mohamed, A. Krapf, H. Dwell, R. Manzke, Z. Galazka, R. Uecker, K. Irmscher, R. Fornari, M. Michling, D. Schmeißer, J. R. Weber, J. B. Varley, C. G. Van De Walle, *New J. Phys.* **2011**, *13*, 085014.
- [35] H. Idriss, *Surf. Sci.* **2021**, *712*, 121894.
- [36] A. Posada-Borbón, H. Grönbeck, *Phys. Chem. Chem. Phys.* **2020**, *22*, 16193.
- [37] M. Wagner, B. Meyer, M. Setvin, M. Schmid, U. Diebold, *Nature* **2021**, *592*, 722.
- [38] A. Posada-Borbón, H. Grönbeck, *ACS Catal.* **2021**, *11*, 9996.
- [39] N. Rui, K. Sun, C. Shen, C. J. Liu, *J. CO<sub>2</sub> Util.* **2020**, *42*, 101313.
- [40] P. W. Morrison, R. Raghavan, A. J. Timponi, C. P. Artelt, S. E. Pratsinis, *Chem. Mater.* **1997**, *9*, 2702.
- [41] A. J. Gröhn, S. E. Pratsinis, A. Sánchez-Ferrer, R. Mezzenga, K. Wegner, *Ind. Eng. Chem. Res.* **2014**, *53*, 10734.
- [42] R. N. Grass, S. Tsantilis, S. E. Pratsinis, *AIChE J.* **2006**, *52*, 1318.
- [43] P. M. Abdala, O. V. Safonova, G. Wiker, W. Van Beek, H. Emerich, J. A. V. Bokhoven, J. Sá, J. Sziachetko, M. Nachttegaal, *Chimia* **2012**, *66*, 699.
- [44] O. Müller, M. Nachttegaal, J. Just, D. Lützenkirchen-Hecht, R. Frahm, *J. Synchrotron Radiat.* **2016**, *23*, 260.
- [45] B. Ravel, M. Newville, *J. Synchrotron Radiat.* **2005**, *12*, 537.
- [46] G. Kresse, J. Furthmüller, *Phys. Rev. B* **1996**, *54*, 11169.
- [47] G. Kresse, J. Furthmüller, *Comput. Mater. Sci.* **1996**, *6*, 15.
- [48] J. P. Perdew, K. Burke, M. Ernzerhof, *Phys. Rev. Lett.* **1996**, *77*, 3865.
- [49] P. E. Blöchl, *Phys. Rev. B* **1994**, *50*, 17953.
- [50] H. J. Monkhorst, J. D. Pack, *Phys. Rev. B* **1976**, *13*, 5188.
- [51] G. Henkelman, B. P. Uberuaga, H. Jónsson, *J. Chem. Phys.* **2000**, *113*, 9901.
- [52] D. Albani, M. Capdevila-Cortada, G. Vilé, S. Mitchell, O. Martin, N. López, J. Pérez-Ramírez, *Angew. Chem., Int. Ed.* **2017**, *56*, 10755.
- [53] A. Walsh, C. R. A. Catlow, *J. Mater. Chem.* **2010**, *20*, 10438.
- [54] C. Bo, F. Maseras, N. López, *Nat. Catal.* **2018**, *1*, 809.
- [55] M. Álvarez-Moreno, C. de Graaf, N. López, F. Maseras, J. M. Poblet, C. Bo, *J. Chem. Inf. Model.* **2014**, *55*, 95.
- [56] V. Stevanović, S. Lany, X. Zhang, A. Zunger, *Phys. Rev. B* **2012**, *85*, 115104.
- [57] D. R. Lide, *CRC Handbook of Chemistry and Physics*, CRC Press, London **1994**.
- [58] S. J. Ashcroft, E. Schwarzmann, *J. Chem. Soc., Faraday Trans. 1* **1972**, *68*, 1360.
- [59] J. Pérez-Ramírez, N. López, *Nat. Catal.* **2019**, *2*, 971.



ARTICLE



<https://doi.org/10.1038/s41467-021-22224-x>

OPEN

# Nanostructure of nickel-promoted indium oxide catalysts drives selectivity in CO<sub>2</sub> hydrogenation

Matthias S. Frei<sup>1</sup>, Cecilia Mondelli <sup>1</sup>, Rodrigo García-Muelas <sup>2</sup>, Jordi Morales-Vidal <sup>2</sup>, Michelle Philipp<sup>1</sup>, Olga V. Safonova <sup>3</sup>, Núria López <sup>2</sup>, Joseph A. Stewart <sup>4</sup>, Daniel Curulla Ferré<sup>4</sup> & Javier Pérez-Ramírez <sup>1✉</sup>

Metal promotion in heterogeneous catalysis requires nanoscale-precision architectures to attain maximized and durable benefits. Herein, we unravel the complex interplay between nanostructure and product selectivity of nickel-promoted In<sub>2</sub>O<sub>3</sub> in CO<sub>2</sub> hydrogenation to methanol through in-depth characterization, theoretical simulations, and kinetic analyses. Up to 10 wt.% nickel, InNi<sub>3</sub> patches are formed on the oxide surface, which cannot activate CO<sub>2</sub> but boost methanol production supplying neutral hydrogen species. Since protons and hydrides generated on In<sub>2</sub>O<sub>3</sub> drive methanol synthesis rather than the reverse water-gas shift but radicals foster both reactions, nickel-lean catalysts featuring nanometric alloy layers provide a favorable balance between charged and neutral hydrogen species. For nickel contents >10 wt.%, extended InNi<sub>3</sub> structures favor CO production and metallic nickel additionally present produces some methane. This study marks a step ahead towards green methanol synthesis and uncovers chemistry aspects of nickel that shall spark inspiration for other catalytic applications.

<sup>1</sup>Institute for Chemical and Bioengineering, Department of Chemistry and Applied Biosciences, ETH Zürich, Zürich, Switzerland. <sup>2</sup>Institute of Chemical Research of Catalonia (ICIQ), The Barcelona Institute of Science and Technology, Tarragona, Spain. <sup>3</sup>Paul Scherrer Institute, Villigen, Switzerland. <sup>4</sup>Total Research & Technology Feluy, Zone Industrielle Feluy C, Seneffe, Belgium. ✉email: [jpr@chem.ethz.ch](mailto:jpr@chem.ethz.ch)

In heterogeneous catalysis, numerous systems rely on metal promotion to maximize process throughput<sup>1,2</sup>. Since these additives might carry stand-alone activity for undesired reactions jeopardizing selectivity and/or contribute to catalyst deactivation in conventional forms such as supported nanoparticles, specific nanostructures need to be designed to stabilize metal speciations displaying tailored electronic and geometric properties that minimize drawbacks while preserving benefits<sup>3-7</sup>. This often is a challenging task since the uniform production and in-depth characterization of precise atom-resolved structures lie at the frontier of current technologies.

In the frame of mitigating global environmental changes and lessening our reliance on fossil feedstocks<sup>8-11</sup>, indium oxide was introduced as a breakthrough catalyst for CO<sub>2</sub> hydrogenation to methanol<sup>12</sup>, exhibiting extraordinary high selectivity and superior activity and stability when supported on monoclinic ZrO<sub>2</sub><sup>13-15</sup>. Mechanistic investigations indicated that vacancies formed at a specific surface lattice position mediate CO<sub>2</sub> activation and H<sub>2</sub> heterolytic splitting<sup>16-19</sup>, the latter unlocking the preferential formation of methanol instead of CO via the reverse water-gas shift (RWGS) reaction<sup>18</sup>. Still, since heterolytic H<sub>2</sub> activation is energetically demanding and limits the methanol synthesis rate, promotion with various hydrogenation elements was explored<sup>20-30</sup>.

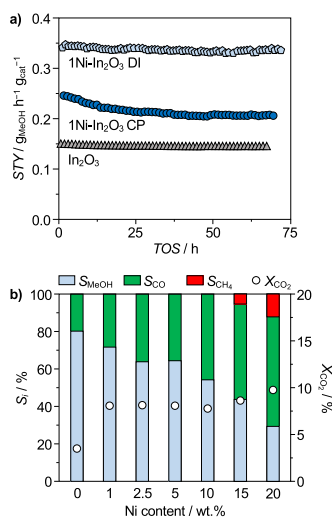
Platinum and palladium nanoparticles were shown to boost catalyst performance by aiding H<sub>2</sub> splitting, thus fostering CO<sub>2</sub> hydrogenation and generating additional vacancies on In<sub>2</sub>O<sub>3</sub>, but led to inferior methanol selectivity due to intrinsic RWGS activity and substantial reduction-induced In<sub>2</sub>O<sub>3</sub> sintering. These pitfalls were mitigated by anchoring low-nuclearity (ca. 3 atoms) clusters to the In<sub>2</sub>O<sub>3</sub> lattice in the case of gold and palladium<sup>29,31</sup>. Ruthenium and cobalt, typical metals leading to methane, were successfully employed when the first was alloyed with indium and the second encapsulated with In<sub>x</sub>O<sub>y</sub><sup>23,28</sup>. In view of these findings, the low-cost alternative nickel, also a prototypic methanation metal<sup>32</sup>, could find effective application in CO<sub>2</sub> hydrogenation if a favorable structure is identified. A recent study showed that metallic nickel on In<sub>2</sub>O<sub>3</sub> did not produce methane in CO<sub>2</sub>-based methanol synthesis, but clear support to its segregation from the oxide was not provided<sup>26</sup>. Another work indicated that CO<sub>2</sub> hydrogenation on Ni catalysts can be driven to CO and methanol by doping with indium<sup>33</sup>. In methane dry reforming on In<sub>x</sub>Ni<sub>y</sub> catalysts<sup>34,35</sup>, CO adsorption on nickel was fully suppressed upon doping with indium, suggesting their alloying. In CO<sub>2</sub> dry reforming on InNi/SiO<sub>2</sub>, the surface of Ni–In alloy particles was progressively covered with In<sub>x</sub>O<sub>y</sub> upon use<sup>36</sup>, as for cobalt-promoted In<sub>2</sub>O<sub>3</sub>. These radical deviations of the behavior of pure nickel from its characteristic chemistry call for a rationalization of the nanostructures underpinning them, in comparison to the other metal promoters.

Herein, the synergistic interaction of nickel with indium oxide in CO<sub>2</sub>-based methanol synthesis was explored through a comprehensive experimental and theoretical program. The nickel speciation was studied contrasting the behavior of coprecipitated and impregnated catalysts upon testing under industrially relevant conditions, with electronic effects being further evaluated on nickel deposited onto In–Al mixed oxides with distinct indium content. The nickel content was varied on the better performing impregnated catalysts identifying a clear impact on the product selectivity. In situ spectroscopy and diffraction methods along with thermal, volumetric, and microscopy analyses uncovered the nanometric construction of the selective nickel-poor and the unselective nickel-rich samples. Density functional theory (DFT) sheds light on the unique structural rearrangements of nickel deposited on In<sub>2</sub>O<sub>3</sub> and the reactivity of complementary promoted surfaces, which was linked to experimental kinetic

parameters. Alloying of nickel with In<sub>2</sub>O<sub>3</sub> emerged as key to provide uncharged hydrogen atoms to active sites on In<sub>2</sub>O<sub>3</sub> while curtailing the nickel-mediated detrimental methanation pathway. Overall, this work gathers a fundamental understanding of a relevant system for sustainable methanol production and unravels structural and electronic features at the basis of the tunable selectivity of nickel in CO<sub>2</sub> hydrogenation routes.

## Results

**Impact of nickel content and synthesis method on activity and selectivity.** Nickel was incorporated into In<sub>2</sub>O<sub>3</sub> by dry impregnation (DI, 1–20 wt.%, coded as xNi–In<sub>2</sub>O<sub>3</sub>,  $x = 1-20$ ) and coprecipitation (CP, 1–2.5 wt.%) aiming at a deposition on the oxide surface and formation of solid solutions to appreciate the role of metals intermixing and of the nickel oxidation state and chemical environment. N<sub>2</sub> sorption and X-ray fluorescence spectroscopy (XRF) indicated that all catalysts featured sufficiently high surface areas and nominal metal contents were closely matched (Supplementary Table 1). Assessing the samples containing 1 wt.% of nickel in CO<sub>2</sub> hydrogenation evidenced a higher methanol space-time yield (STY) compared to pure In<sub>2</sub>O<sub>3</sub> (STY = 0.16 g<sub>MeOH</sub> h<sup>-1</sup> g<sub>cat</sub><sup>-1</sup>, Fig. 1a), which, after 65-h equilibration, remained at a ca. twofold higher value (0.34 g<sub>MeOH</sub> h<sup>-1</sup> g<sub>cat</sub><sup>-1</sup>) for the DI catalyst and levelled to a 25% higher value (0.20 g<sub>MeOH</sub> h<sup>-1</sup> g<sub>cat</sub><sup>-1</sup>) for the CP catalyst. The stable behavior of the former contrasts palladium-promoted In<sub>2</sub>O<sub>3</sub> prepared through DI, which experienced fast deactivation (Supplementary Fig. 1)<sup>31</sup>. The inferior performance of the CP catalyst is likely due to the synthesis approach burying a substantial portion of the promoter within the bulk of In<sub>2</sub>O<sub>3</sub>, but the presence of more nickel added by this method did not yield materials



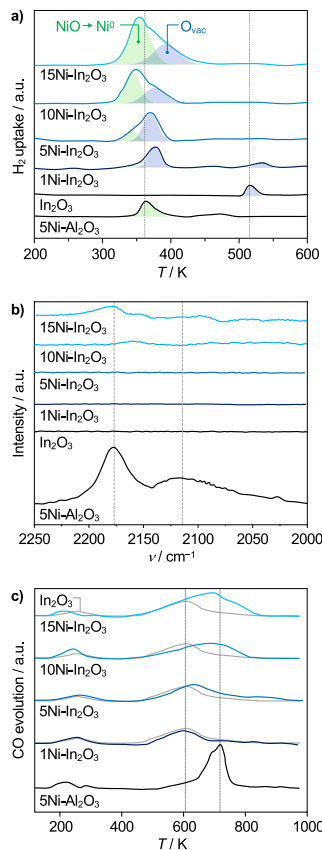
**Fig. 1** Catalytic performance of nickel-promoted In<sub>2</sub>O<sub>3</sub> catalysts. **a** Space-time yield (STY) of methanol as a function of time-on-stream (TOS) over Ni–In<sub>2</sub>O<sub>3</sub> containing 1 wt.% of nickel incorporated by dry impregnation (DI) and coprecipitation (CP) and unpromoted In<sub>2</sub>O<sub>3</sub> as a reference. **b** CO<sub>2</sub> conversion and product selectivity of catalysts produced by DI as a function of the nominal nickel content on In<sub>2</sub>O<sub>3</sub>. Reaction conditions:  $T = 553$  K,  $P = 5$  MPa, molar H<sub>2</sub>:CO<sub>2</sub> = 4, and WHSV = 24,000 cm<sub>3</sub>TP<sup>-3</sup> h<sup>-1</sup> g<sub>cat</sub><sup>-1</sup>.



superior to those produced by DI (Supplementary Fig. 2). Considering the more favorable DI synthesis (Fig. 1b), methanol formation was progressively lowered in favor of the RWGS reaction up to a nickel content of 20 wt.%, while the CO<sub>2</sub> conversion was practically unchanged at ca. 8%, suggesting that sites activating CO<sub>2</sub> are unlikely located on the nickel phase. Methane formation was observed only at higher promoter contents ( $S_{\text{CH}_4}$  = 6 and 13% at 15 and 20 wt.% nickel, respectively). This hints that In<sub>2</sub>O<sub>3</sub> exerts a strong influence on the nickel properties and, only for high contents, a fraction of promoter remains unperturbed and can express its intrinsic behavior. To further address the selectivity switch, the amount of indium required to trigger it was explored by supporting 5 wt.% nickel on mixed indium-aluminum oxides with variable indium content (0–100 mol% In, Supplementary Fig. 3). While nickel on pure alumina was highly selective to methane ( $S_{\text{CH}_4}$  > 98%), 25 mol% of indium in the support sufficed to suppress methanation almost entirely ( $S_{\text{CH}_4}$  = 3%). At the same time, the CO<sub>2</sub> conversion significantly dropped (from  $X_{\text{CO}_2}$  = 18 to 4%), corroborating that indium-modulated nickel species are significantly less active compared to pure nickel.

**Characterization of nickel speciation.** In-depth investigations were conducted to rationalize the behavior of the DI systems. Concerning catalyst reducibility, temperature-programmed reduction with hydrogen (H<sub>2</sub>-TPR, Fig. 2a, Supplementary Table 2) evidenced that NiO conversion into metallic nickel occurs at ca. 340 K in all samples, preceding surface In<sub>2</sub>O<sub>3</sub> reduction (370 K), which is substantially facilitated compared to the pure oxide (521 K). Based on the signal intensity in the profile of the 5Ni-Al<sub>2</sub>O<sub>3</sub> reference, nickel was fully reduced in all cases. In 1Ni-In<sub>2</sub>O<sub>3</sub>, some In<sub>2</sub>O<sub>3</sub> still reduced at its standard temperature, likely because the nickel amount was insufficient to facilitate reduction of the entire In<sub>2</sub>O<sub>3</sub> surface. Diffuse reflectance infrared Fourier transform spectroscopy of adsorbed carbon monoxide (CO-DRIFTS) evidenced a weak signal specific to linearly bound CO (2176 cm<sup>-1</sup>) only for 10Ni-In<sub>2</sub>O<sub>3</sub> and 15Ni-In<sub>2</sub>O<sub>3</sub> (Fig. 2b), while pronounced bands of linear, bridged, (2119 cm<sup>-1</sup>), and three-fold (2066 cm<sup>-1</sup>) adsorbed CO was detected for the 5Ni-Al<sub>2</sub>O<sub>3</sub> reference. Temperature-programmed desorption of carbon monoxide (CO-TPD, Fig. 2c) corroborated that the contribution of nickel to the adsorption of this molecule is significantly inferior when this metal is in contact with In<sub>2</sub>O<sub>3</sub>. These findings suggest remarkable electronic effects, i.e., metal-support interactions and/or alloying of nickel and indium<sup>37</sup>, implying high dispersion, for the majority of nickel present, and small particle size for nickel unaffected by indium oxide adsorbing CO.

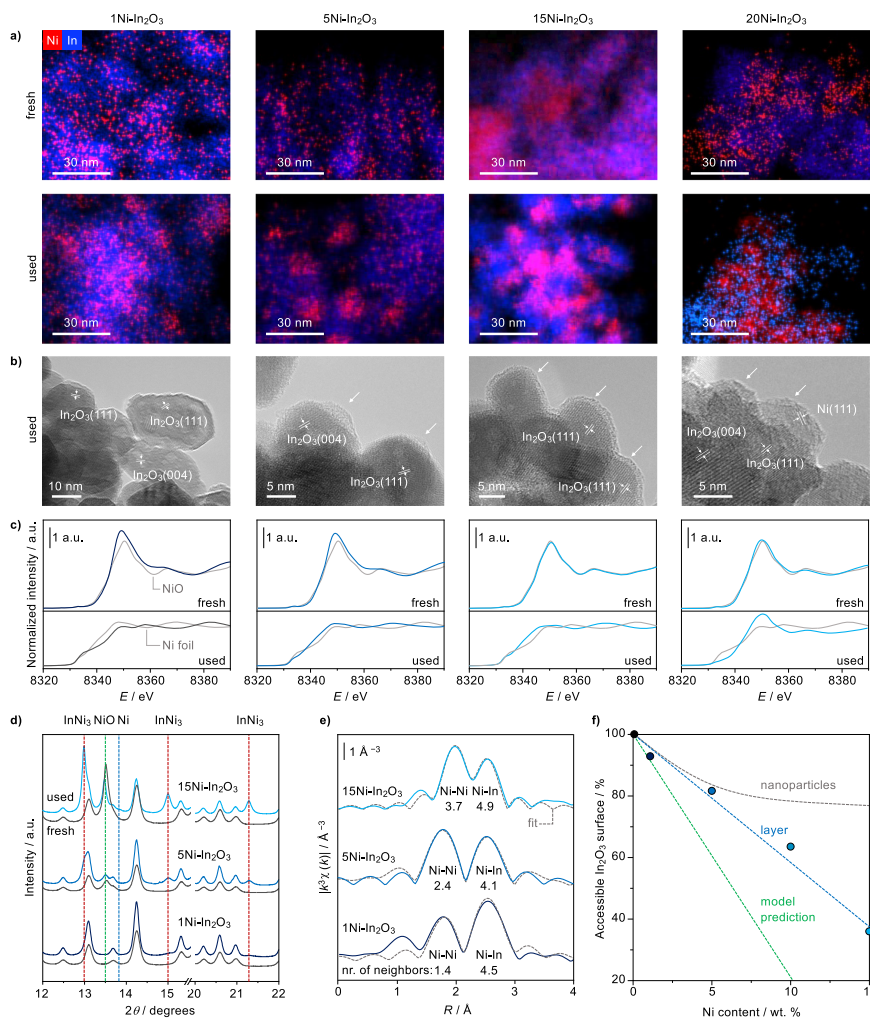
To shed further light on the promoter's features, catalysts were analyzed by additional methods. Scanning transmission electron microscopy coupled to energy-dispersive X-ray spectroscopy (STEM-EDX, Fig. 3a) revealed highly and almost homogeneously dispersed nickel in fresh lower-content specimens (1 and 5 wt.% Ni) and more agglomerated structures in fresh higher-content samples (15 and 20 wt.% Ni). Only in 20Ni-In<sub>2</sub>O<sub>3</sub>, some of the promoters appeared fully segregated from indium oxide. Slight nickel agglomeration is evident for all samples upon use in the reaction. Investigations by high-resolution transmission electron microscopy (HRTEM) of used materials did not visualize any nickel-based phases in 1Ni-In<sub>2</sub>O<sub>3</sub> (Fig. 3b), although the magnification was chosen such that, based on the STEM-EDX results, some nickel must have been present within the imaged areas. In the 5 wt.% Ni sample, some amorphous islands can be found on In<sub>2</sub>O<sub>3</sub>, which might tentatively correspond to nickel-rich structures, due to their lower contrast compared to In<sub>2</sub>O<sub>3</sub>. In 15Ni-In<sub>2</sub>O<sub>3</sub>, a similar phase forms a ca. 1-nm thick layer covering many of the imaged In<sub>2</sub>O<sub>3</sub> particles, which are additionally



**Fig. 2** Sensitivity of nickel-promoted In<sub>2</sub>O<sub>3</sub> catalysts to H<sub>2</sub> and CO. **a** H<sub>2</sub>-TPR at 5 MPa of pressure, **b** CO-DRIFTS, and **c** CO-TPD of Ni-In<sub>2</sub>O<sub>3</sub> catalysts prepared by DI containing 1–15 wt.% nickel, with unpromoted In<sub>2</sub>O<sub>3</sub> and 5Ni-Al<sub>2</sub>O<sub>3</sub> serving as references. Deconvoluted signals specific to nickel reduction and oxygen vacancy formation on In<sub>2</sub>O<sub>3</sub> are colored in green and blue in **(a)**. a.u. = arbitrary units.

accompanied by poorly crystalline nickel-based particles in the 20 wt.% catalyst.

X-ray absorption near-edge structure spectra (XANES, Fig. 3c) of fresh 15 and 20Ni-In<sub>2</sub>O<sub>3</sub> closely resemble that of Ni<sup>2+</sup> in NiO, while some discrepancies are observed for the lower-content solids, which can be explained by higher dispersion and stronger interaction with In<sub>2</sub>O<sub>3</sub>. In all but the highest nickel content catalyst, cationic nickel completely transformed into metallic species different from those in pure nickel metal upon use in the reaction, strongly suggesting alloying with indium. In 20Ni-In<sub>2</sub>O<sub>3</sub>, nickel is present in both metallic and oxidic states, likely because some NiO particles do not fully reduce due to their large size<sup>32</sup>.



**Fig. 3** Structural and electronic elucidation of nickel-promoted  $\text{In}_2\text{O}_3$  catalysts. **a** STEM-EDX maps of  $\text{Ni-In}_2\text{O}_3$  catalysts containing 1–20 wt.% Ni in fresh and used forms. **b** HRTEM images, with phases identified by fringe analysis and features of interest indicated, and **c**  $k$ -weighted Ni K-edge XANES, with spectra of NiO and metallic nickel serving as references, for the same used catalysts. **d** XRD patterns collected in monochromatic light and **e** EXAFS with model fit and an indication of neighbors' number along a specific scattering path for selected fresh and used samples. **f** Percentage of  $\text{In}_2\text{O}_3$  surface not covered by nickel as a function of the nominal nickel content, determined by volumetric  $\text{CO}_2$  chemisorption. The qualitative trend respective to nanoparticle formation and the coverage predicted by DFT is indicated. a.u. = arbitrary units.

High-resolution X-ray diffraction (XRD, Fig. 3d, Supplementary Fig. 4) measured in monochromatic light ( $\lambda = 0.49292 \text{ \AA}$ ) indicated that NiO, present in the fresh materials, reduced indeed forming  $\text{InNi}_3$  alloys. Their average crystal size is  $<1$ ,  $2.7 \pm 0.7$ , and  $7.3 \pm 0.9 \text{ nm}$  for the catalysts containing 1, 5, and 15 wt.%

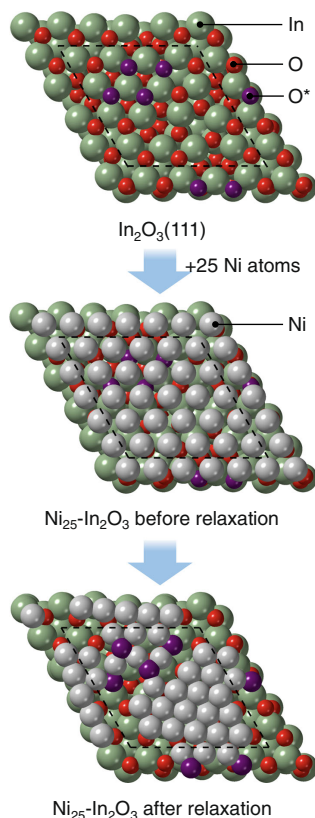
nickel, respectively, in good agreement with the microscopy analyses. Alloy formation with indium shall be key to anchor the intermetallic phase strongly to the catalyst surface, preventing significant sintering. Only for 15Ni- $\text{In}_2\text{O}_3$ , weak reflections specific to metallic nickel nanoparticles (ca. 1.2 nm) were also

detected, confirming the origin of methane production over this catalyst. Since this analysis necessitated catalyst operation directly within the capillary used for diffraction analysis and the consequent application of significantly lower flow rates than in the reactor, some NiO is still detected in the used solids. However, other characterization techniques mirroring the reaction environment more closely exclude that this phase exists upon reaction for these catalysts.

Analysis of the extended X-ray absorption fine structure (EXAFS, Fig. 3e, Supplementary Table 3) shows Ni–Ni and Ni–In bonds in the first coordination shell of nickel. The total number of first neighbors around nickel is 5.9, 6.5, and 8.6 for 1, 5, and 15Ni–In<sub>2</sub>O<sub>3</sub>, respectively. Since 12 neighbors are expected for nickel atoms in the bulk metal and the InNi<sub>3</sub> alloy, the alloy on all catalysts shall be well dispersed. Moreover, the number of Ni–Ni bonds progressively increases with higher nickel contents, i.e., 1.4, 2.4, and 3.7 for 1, 5, and 15Ni–In<sub>2</sub>O<sub>3</sub>, respectively. This is indicative of stronger nickel interaction with indium and suggests a two-dimensional layer-like morphology for the for the catalysts with lower nickel contents, whereas particles additionally exist in higher-content samples.

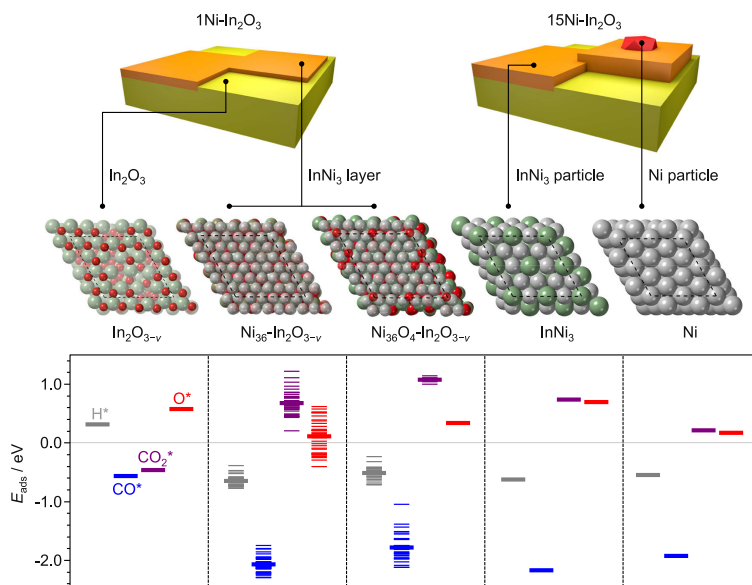
Volumetric CO<sub>2</sub> chemisorption enabled to determine a linear decrease of the exposed In<sub>2</sub>O<sub>3</sub> surface at increasing nickel content, consistent with a Stranski–Krastanov film growth (layer followed by nanoparticle formation)<sup>38</sup>. Indeed, an asymptotic decrease would be expected if nickel species formed agglomerates following a Volmer–Weber film growth<sup>39</sup> (Fig. 3f), as previously observed for the Pd–In<sub>2</sub>O<sub>3</sub> system<sup>31</sup>. Although In<sub>2</sub>O<sub>3</sub> should be fully covered at a nickel content of 12.5 wt.% (Supplementary Table 4), it is likely that inhomogeneous precursor distribution upon impregnation and the large anisotropy of the In<sub>2</sub>O<sub>3</sub> surface prevented the formation of a perfectly uniform layer. Hence, ca. 40% of the In<sub>2</sub>O<sub>3</sub> surface remained still exposed at a nickel content of 15 wt.%.

With a sound understanding of the DI systems, their structure was further investigated by first principles density functional theory. To represent the two-dimensional nickel phase, Ni(111) layers were placed on top of In<sub>2</sub>O<sub>3</sub>(111), identified previously and herein as the most abundant indium oxide termination (Supplementary Table 5)<sup>18</sup>. Based on the stability of nickel atoms with six neighbors each and to commensurate the oxide lattice (Supplementary Table 6), a slightly compressed nickel layer with 36 atoms per unit cell of In<sub>2</sub>O<sub>3</sub> was considered more relevant than uncompressed layers with fewer nickel atoms (25–27). Interestingly, upon relaxation, nickel atoms in this discrete layer became more densely packed and extracted oxygen atoms from the underlying In<sub>2</sub>O<sub>3</sub> (Fig. 4, Supplementary Movie 1). The driving force for this reconstruction can be traced back to the relative bond strengths, since Ni–In affinities are higher with respect to those of In–In and Ni–Ni (Supplementary Table 7), and is in line with other hydrogenation systems for which distinct but pronounced metal–support interactions were described, such as Cu–ZnO, Pt–TiO<sub>2</sub>, Pt–CeO<sub>2</sub>, and Pd–In<sub>2</sub>O<sub>3</sub> (Supplementary Figs. 5 and 6, Supplementary Tables 8 and 9). The oxygen atoms extracted emerge to the outermost catalyst surface and are readily stripped as water by the hydrogen present in the reaction environment, which rationalizes the alloying of nickel with indium. Considering these dynamics, the oxygen atoms on the In<sub>2</sub>O<sub>3</sub> termination were removed prior to placing the nickel layer. The most stable structure was found to be Ni<sub>36</sub>–In<sub>2</sub>O<sub>3–*v*</sub>, which presents the maximal number of oxygen vacancies (*v*) on the oxide and nickel atoms (12 and 36, respectively, Supplementary Fig. 7). Still, since it cannot be excluded that a small fraction of the oxygen atoms that emerged at the outermost surface is dynamically stored on the InNi<sub>3</sub> patches upon CO<sub>2</sub> hydrogenation, the effect of residual four oxygen atoms at the most



**Fig. 4 Reconstruction of an In<sub>2</sub>O<sub>3</sub>(111) unit cell bearing a metallic nickel layer.** The sketches show the restructuring of the interface between a nickel layer and the underlying In<sub>2</sub>O<sub>3</sub>. The pristine oxide surface is covered with a commensurate nickel layer, in this case containing 25 atoms. This structure is relaxed following a standard energy minimization algorithm. Given the corrugation of the In<sub>2</sub>O<sub>3</sub> surface and the Ni–O and Ni–Ni relative binding energies, some oxygen atoms are stripped from the oxide (colored purple) and isolated hexagonally arranged Ni-patches are formed upon the relaxation. The dashed lines in the models indicate the border of the unit cell of In<sub>2</sub>O<sub>3</sub> along with the (111) termination. The relaxation process is shown in Supplementary Movie 1.

stabilized positions was also explored (Ni<sub>36</sub>O<sub>4</sub>–In<sub>2</sub>O<sub>3–*v*</sub>). Finally, since the presence of isolated nickel species can also not be discarded, nickel atoms were alternatively deposited onto In<sub>2</sub>O<sub>3</sub>(111), i.e., Ni<sub>*x*</sub>–In<sub>2</sub>O<sub>3</sub>, *x* = 1–4. These Ni<sub>*x*</sub>–In<sub>2</sub>O<sub>3</sub> structures are less stable than the nickel layer but more stable than NiO under a reducing atmosphere such as upon CO<sub>2</sub> hydrogenation. For instance, Ni<sub>2</sub>–In<sub>2</sub>O<sub>3</sub> is less stable than Ni<sub>36</sub>–In<sub>2</sub>O<sub>3–*v*</sub> by +0.36 eV per nickel atom. Overall, the catalysts with up to 10 wt.% nickel are better represented by a combination of Ni<sub>36</sub>–In<sub>2</sub>O<sub>3–*v*</sub>,



**Fig. 5 Adsorption energies of reaction species on nickel-promoted  $\text{In}_2\text{O}_3$  catalysts.** Visualization of the structures of Ni- $\text{In}_2\text{O}_3$  catalysts with 1 and 15 wt.% nickel content loading (top), surfaces representative of the different catalyst constituents generated by DFT (middle), and adsorption energies ( $E_{\text{ads}}$ ) of species relevant to the reaction associated with them (bottom). The multiple energy levels for individual species for models containing nickel layer relate to the presence of a distinct number of oxygen atoms. The subscript  $v$  stands for vacancy.  $\text{CO}_2$  adsorption at the boundary between unpromoted  $\text{In}_2\text{O}_3$ (111) and a strip of Ni(111) (layer equivalent to  $\text{Ni}_{36}\text{-In}_2\text{O}_{3-v}$ ) is shown in Supplementary Fig. 11.

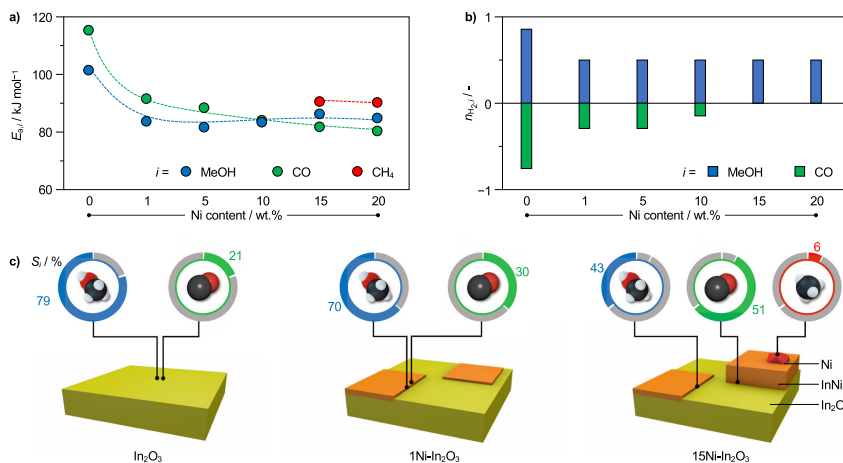
$\text{InNi}_3$ (111), and  $\text{In}_2\text{O}_3$ (111), while for higher-content materials  $\text{InNi}_3$ (111) and Ni(111) terminations, along with potentially  $\text{Ni}_2\text{-In}_2\text{O}_3$  (vide infra), are additionally significant<sup>40</sup>.

**Reaction mechanism and kinetics.** To explain the reactivity of the DI catalysts, the adsorption energies ( $E_{\text{a}}$ ) of reactants on the distinct models were calculated (>200 adsorption calculations, Fig. 5). Ni(111) is associated with a mildly endothermic  $\text{CO}_2$  adsorption, which can still be overcome (0.22 eV, Fig. 5), and barrierless hydrogen splitting and will readily transform carbon-based adsorbates into methane. In contrast,  $\text{CO}_2$  adsorption is significantly weakened on clean  $\text{InNi}_3$ (111) (0.74 eV, Fig. 5), while hydrogen splits more exothermically and without an energy barrier. The chemical behavior of all layered nickel structures simulated is very similar to  $\text{InNi}_3$ (111) (Supplementary Fig. 8). Hence, any alloy type shall be virtually inert in converting  $\text{CO}_2$  into any product on its own, but can provide hydrogen to the active site of  $\text{In}_2\text{O}_3$ (111) for coverages lower than one monolayer<sup>18,31</sup>. Nevertheless, the bulk alloy is expected to provide hydrogen radicals at a faster rate than the layer, due to its overall more metallic character. Even considering the presence of residual oxygen atoms upon catalyst operation,  $\text{CO}_2$  adsorption remains far weaker on the nickel layers than on  $\text{In}_2\text{O}_3$ (111) or Ni(111). The structure retaining some oxygen atoms ( $\text{Ni}_{36}\text{O}_4\text{-In}_2\text{O}_{3-v}$ ) features inhibited CO adsorption compared to  $\text{Ni}_{36}\text{-In}_2\text{O}_{3-v}$ . Considering the suppressed CO adsorption ability of the catalysts in CO-DRIFTS and CO-TPD analyses, it is conceivable that some

oxygen or hydroxide species populate the alloy film during reaction.

When considering low-content samples, the  $\text{CO}_2$  hydrogenation performance can be seen as the convolution of that of a (multi)layer of  $\text{InNi}_3$ , pure  $\text{In}_2\text{O}_3$ , and nickel dimers on  $\text{In}_2\text{O}_3$ . The unpromoted  $\text{In}_2\text{O}_3$  ensembles adsorb  $\text{CO}_2$  and activate  $\text{H}_2$  heterolytically<sup>18</sup>. Then, hydrides and protons are transferred to  $\text{CO}_2$  forming methanol. On  $\text{InNi}_3$ (111) and  $\text{Ni}_{36}\text{-In}_2\text{O}_{3-v}$ ,  $\text{CO}_2$  and CO adsorption are either endothermic or weaker than on  $\text{In}_2\text{O}_3$ , whereas homolytic  $\text{H}_2$  adsorption is exothermic and  $\text{CO}_2$  activated at the  $\text{In}_2\text{O}_3$  ensemble on clean  $\text{In}_2\text{O}_3$ (111) shall be hydrogenated both with hydrogen split on the same active site and with hydrogen spilled from nickel layers<sup>16</sup>, whereby sites at the periphery of the patches will be most relevant in the latter process (Supplementary Fig. 9). The fact that methanol selectivity is higher in nickel-poor catalysts than in nickel-rich ones suggests that hydrides and protons generated on  $\text{In}_2\text{O}_3$  are still quite strongly utilized, since hydrogen radicals produced on the alloy favor both methanol and CO formation. In contrast to alloyed phases, low-nuclearity nickel clusters at the  $\text{In}_2\text{O}_3$  ensemble, in particular  $\text{Ni}_2\text{-In}_2\text{O}_3$ , are expected to be highly active in the competing RWGS (Supplementary Figs. 10 and 11), in striking contrast to low-nuclearity palladium clusters anchored to the same ensemble.

To corroborate the DFT findings, kinetic analyses were carried out over all catalysts to experimentally assess the mechanistic origin of the promotional effect (Fig. 6a). The apparent activation energies for both methanol synthesis and the RWGS reaction,



**Fig. 6** Nanostructure-driven kinetics and selectivity of nickel-promoted  $\text{In}_2\text{O}_3$  catalysts. **a** Apparent activation energies ( $E_a$ ) and **b** reaction orders respective to  $\text{H}_2$  ( $n_{H_2}$ ) for methanol synthesis and the RWGS reaction over  $\text{In}_2\text{O}_3$  catalysts as a function of their nickel content. **c** Graphical representation of the structures of  $\text{In}_2\text{O}_3$  and Ni- $\text{In}_2\text{O}_3$  catalysts with low and high nickel loadings and indications where products shall be predominantly formed on them. The rings surrounding the molecules represent the respective product selectivity. Reaction conditions:  $T = 553 \text{ K}$ ,  $P = 5 \text{ MPa}$ ,  $WHSV = 24,000 \text{ cm}_3\text{TP}^{-3} \text{ h}^{-1} \text{ g}_{\text{cat}}^{-1}$ .

extracted from catalytic tests conducted at variable temperature (Supplementary Fig. 12), are significantly lower already upon incorporation of the smallest nickel amount in comparison to pure indium oxide (from 101 to 83 and from 116 to 92  $\text{kJ mol}^{-1}$ , respectively). The smaller difference between activation barriers for methanol and CO synthesis over 1Ni- $\text{In}_2\text{O}_3$  rationalizes its lower methanol selectivity compared to the unpromoted oxide (from 15 to 9  $\text{kJ mol}^{-1}$ ). A further increase of the nickel content has little impact on the activation energies, which reach values of 84 and 80  $\text{kJ mol}^{-1}$  for the RWGS and methanol synthesis for 20Ni- $\text{In}_2\text{O}_3$  respectively. The activation barriers for methanation on the materials active for this reaction (15 and 20Ni- $\text{In}_2\text{O}_3$ ) were determined at ca. 90  $\text{kJ mol}^{-1}$ , in good agreement with literature on pure nickel catalysts (85–94  $\text{kJ mol}^{-1}$ )<sup>35,41,42</sup> and corroborating the feasibility of methane formation on metallic nickel sites in these systems. Based on the weak dependence of the apparent activation energies for methanol and CO formation on the nickel content, the mechanisms leading to these products are likely highly similar throughout the materials. Hence, the progressive decay of methanol selectivity in favor of CO at higher loadings (Fig. 1b) has a kinetic origin. Since DFT calculations pointed to facilitated hydrogen activation as the origin of the promotional effect, apparent reaction orders respective to this reactant were determined from experiments at variable  $\text{H}_2$  concentrations in the feed (Fig. 6b, Supplementary Fig. 13). For methanol synthesis, they decreased by equal amounts for all systems relative to bulk  $\text{In}_2\text{O}_3$ , from 0.8 to 0.5, in line with the stoichiometric coefficient of hydrogen splitting on the  $\text{InNi}_3$  layers ( $\frac{1}{2}\text{H}_2 \rightarrow \text{H}^*$ ). At higher partial pressures of  $\text{H}_2$ , the chemical potential of  $\text{H}^*$  species adsorbed on the alloy layers increases as well, thus promoting  $\text{H}^*$  spillover towards the  $\text{In}_2\text{O}_3$  active site. The 0.5 reaction order suggests that the spillover mechanism dominates over the  $\text{In}_2\text{O}_3$  on-site splitting at working conditions. For the RWGS reaction, the reaction orders increased from  $-0.7$  to  $-0.3$  for 1 and 5Ni- $\text{In}_2\text{O}_3$ , i.e., the systems which contain mainly flat  $\text{InNi}_3$  structures.

On these catalysts, both methanol and CO are produced on unpromoted  $\text{In}_2\text{O}_3$  ensembles with the two paths competing for  $\text{H}^*$  donated by the alloy patches. The negative reaction orders for the RWGS are explained by its first step ( $\text{CO}_2 + \text{H}^* \rightarrow \text{COOH}$ ) being kinetically unfavored compared to the first of methanol production ( $\text{CO}_2 + \text{H}^* \rightarrow \text{HCO}_2$ , Supplementary Fig. 11a). The progressive decrease in apparent activation energy for the RWGS reaction upon increasing Ni content might be explained based on the formation of additional metastable  $\text{Ni}_1$ - $\text{In}_2\text{O}_3$  and  $\text{Ni}_2$ - $\text{In}_2\text{O}_3$  ensembles selective to this competitive reaction (Supplementary Figs. 10 and 11). On  $\text{Ni}_i$ - $\text{In}_2\text{O}_3$  ensembles,  $\text{H}_2$  splitting is barrierless, and thus the net reaction is not controlled by the partial pressure of  $\text{H}_2$ . At Ni contents of 15–20 wt.%, the RWGS reaction shall be mostly performed on these ensembles rather than on those free of nickel, and the reaction order with respect to  $\text{H}_2$  decreases to zero. Overall, the kinetic data are in good agreement with earlier and above-presented investigations. Specifically, when  $\text{H}_2$  is activated on pure  $\text{In}_2\text{O}_3$ , it is split into polarized species ( $\text{In}^{\delta-}$  and  $\text{H}^{\delta+}$ ) which are adsorbed on the  $\text{In}_2\text{O}_3$  ensemble on an  $\text{In}_3^{\delta+}$  substructure and  $\text{O}^{\delta-}$  atom respectively<sup>18</sup>. The subsequent transfer to adsorbed  $\text{CO}_2$  is energetically disfavored due to the strong polar interaction between adsorbed  $\text{H}_2$  and the  $\text{In}_2\text{O}_3$  surface. Neutral hydrogen atoms, provided by the alloy phases, do not have to overcome this energy barrier, thus leading to lower activation energies for methanol synthesis and the RWGS reaction<sup>32</sup>. However, consecutive proton and hydride supply to adsorbed  $\text{CO}_2$  are highly selective towards methanol, whereas uncharged species foster both methanol and CO formation. Consequently, methanol synthesis cannot be enhanced beyond a certain threshold even if more homolytically split hydrogen is provided by more abundant alloy phases. On the contrary, the RWGS reaction is boosted to a greater extent in the presence of high nickel contents, presumably as a consequence of an excessive supply of hydrogen atoms (Fig. 6c).

## Discussion

Herein, the use of nickel as an economically attractive promoter for  $\text{In}_2\text{O}_3$  in the direct hydrogenation of  $\text{CO}_2$  to methanol was studied in fundamental and applied terms. Considering facile synthetic strategies, dry impregnation led to more stable and active catalysts than coprecipitation. Methanol synthesis was boosted along with the RWGS reaction to some extent and no methane was formed below a nickel content of 10 wt.%, despite the known high  $\text{CO}_2$  methanation activity of nickel nanoparticles. In-depth characterization revealed a two-dimensional  $\text{InNi}_3$  phase highly dispersed on  $\text{In}_2\text{O}_3$  in nickel-lean samples, which is accompanied by nanoparticles of the same alloy as well as metallic nickel at progressively higher promoter contents. The formation of layered structures rather than agglomerated particles, due to peculiar wetting properties of nickel on  $\text{In}_2\text{O}_3$  fostering film growth, and their strong anchoring on the oxide via alloying emerged as key contributors to the high catalyst stability. DFT simulations elucidated that indium-modulated nickel layers easily provide homolytically split hydrogen to  $\text{In}_2\text{O}_3$ , enhancing oxygen vacancy formation and contributing to  $\text{CO}_2$  hydrogenation, while barely activating  $\text{CO}_2$  on their own, which overall explains the beneficial effects and the lack of methane generation. Hydrogen radicals spilled from the  $\text{InNi}_3$  phase can concomitantly support methanol and CO formation, while hydrides and protons produced on  $\text{In}_2\text{O}_3$  preferably mediate methanol production. The variable relevance of the former species at distinct contents rationalizes the product distribution and kinetic parameters experimentally determined across all samples. The catalyst comprising 1 wt.% of nickel offers an optimal balance between charged and radical hydrogen atoms, reaching a doubled methanol STY compared to unpromoted indium oxide. Overall, this study identified key structural and electronic features controlling the performance of the classical hydrogenation metal nickel in contact with indium oxide relevant to attain a stable promoted system for a sustainable application. It also highlights that the atomic engineering of a promoter for  $\text{In}_2\text{O}_3$  is strongly metal-specific, even when similarity in behavior is expected for elements belonging to the same group in the periodic table.

## Methods

**Catalyst preparation.** Unpromoted and nickel-promoted (1–2.5 wt.% nickel)  $\text{In}_2\text{O}_3$  catalysts were prepared via a (co)precipitation (CP) synthesis similar to one reported earlier<sup>31</sup>. In addition, 1–20 wt.% and 5 wt.% nickel was added to pure indium oxide and to mixed indium-aluminum oxide supports with variable stoichiometry (0–100 mol% indium), respectively, by a dry impregnation (DI) method. The nickel-containing catalysts are labeled with the amount of promoter in wt.%, separated by a hyphen from the carrier, i.e., 5Ni- $\text{In}_2\text{O}_3$  indicates 5 wt.% nickel on  $\text{In}_2\text{O}_3$ . Details to all syntheses applied are provided in the Supplementary Methods.

**Catalyst characterization.** The metal content in the catalysts was determined by XRF, and porous properties of the catalysts were assessed by  $\text{N}_2$  sorption. Catalyst reducibility was monitored by temperature-programmed reduction in hydrogen ( $\text{H}_2$ -TPR).  $\text{CO}$  adsorption was assessed by diffuse-reflectance Fourier transform infrared spectroscopy (CO-DRIFTS) and temperature-programmed desorption (CO-TPD). Nickel speciation, coordination geometry, and dispersion were assessed via X-ray absorption spectroscopy (XAS), X-ray diffraction in monochromatic light (XRD), STEM-EDX, and HRTEM. The surface area of  $\text{In}_2\text{O}_3$  accessible to reactants was determined using volumetric chemisorption of  $\text{CO}_2$ . Details to all characterization techniques are available in the Supplementary Methods.

**Catalytic evaluation.** The experimental setup used for catalytic testing is described in detail elsewhere<sup>18</sup>. Briefly, all experiments were performed in a high-pressure continuous-flow fixed-bed reactor with an inner diameter of 2.1 mm surrounded by an electric furnace. In a typical experiment the reactor was loaded with 100 mg of catalyst with a particle size of 75–100  $\mu\text{m}$ , which was held in place by a bed of quartz wool and heated from ambient temperature to 553 K ( $5\text{ K min}^{-1}$ ) at 5 MPa under a flow of  $\text{H}_2$  ( $20\text{ cm}^3_{\text{STP}}\text{ min}^{-1}$ ). After 3 h, the gas flow was switched to the reactants mixture ( $40\text{ cm}^3_{\text{STP}}\text{ min}^{-1}$ ) comprising  $\text{H}_2$  and  $\text{CO}_2$  in a molar ratio of 4:1. To determine apparent activation energies, the reaction was initiated at 473 K and the temperature

stepwise increased to 553 K (increments of 20 K). Reaction orders with respect to  $\text{H}_2$  were acquired applying a constant flow of  $\text{CO}_2$  ( $8\text{ cm}^3_{\text{STP}}\text{ min}^{-1}$ ) and increasing the flow of  $\text{H}_2$  (from 20–32  $\text{cm}^3_{\text{STP}}\text{ min}^{-1}$ , increments of 3  $\text{cm}^3_{\text{STP}}\text{ min}^{-1}$ ), while using  $\text{He}$  to balance the total flow to 40  $\text{cm}^3_{\text{STP}}\text{ min}^{-1}$ . Ethane (0.5  $\text{cm}^3_{\text{STP}}\text{ min}^{-1}$ , Messer, >99.9%) was added to the effluent stream to serve as an internal standard before the stream was sampled every 20 min and analyzed by online gas chromatography. The evaluation procedure of gas chromatography data is reported in the Supplementary Methods. Materials were tested for 16 h for performance comparison, catalyst stability was established over 72 h on stream, and, during kinetic tests, data were collected for 3 h at each condition and averaged. The absence of intra- and extraparticle diffusion limitation during kinetic tests were corroborated by the fulfillment of the Weisz-Prater and Carberry criteria.

**Computational methods.** DFT simulations were conducted with the Vienna ab initio simulation package (VASP) using the Perdew-Burke-Ernzerhof (PBE) density functional<sup>43–45</sup>. Core electrons were described by projector augmented-wave pseudopotentials (PAW)<sup>46</sup>, while valence electrons were expanded from a plane-wave basis set with a kinetic energy cutoff of 500 eV and a reciprocal grid size narrower than  $0.025\text{ \AA}^{-1}$ . Bulk metal, intermetallic, and oxide structures relevant to investigate  $\text{In}_2\text{O}_3$  promotion by nickel were modeled from their stable structures at ambient conditions. All bulk structures were fully relaxed and formation energies were obtained taking the bulk elements and gas-phase  $\text{O}_2$  as reference. Spin-polarization was considered for Ni-containing systems.

The most abundant termination of bixbyite  $\text{In}_2\text{O}_3$ , the (111) surface<sup>16,18</sup>, was modeled as a  $p(1 \times 1)$  slab containing five O-In-O trilayers. The two outermost layers were allowed to relax and the three bottommost layers were fixed in their bulk positions. This surface is 14.56  $\text{\AA}$  wide, corrugated, and highly anisotropic. It features a protrusion, which is the active site for  $\text{CO}_2$  hydrogenation to methanol. To represent  $\text{In}_2\text{O}_3$  catalysts with low nickel contents, a nickel atom was adsorbed on the pristine  $\text{In}_2\text{O}_3$  (111) surface between three oxygen atoms of the protrusion at symmetrically inequivalent positions. This process was repeated for low-nuclearity clusters containing 2–4 nickel atoms. Finally, 1–3 oxygen vacancies were created to check the ability of these clusters to favor oxygen abstraction. Besides, different nickel layers were accommodated onto  $\text{In}_2\text{O}_3$  deriving from the  $5 \times 5$ ,  $3\sqrt{3} \times 3\sqrt{3}$ , and  $6 \times 6$  expansions of a Ni(111) monolayer, containing 25, 27, and 36 Ni atoms, respectively. Each layer was placed on  $\text{In}_2\text{O}_3$ (111) surfaces with 0, 1, 2, 3, 6, 9, and 12 vacancies considering three different translations. To describe  $\text{In}_2\text{O}_3$  catalysts with high nickel contents, the  $\text{InNi}_3$ (111) and Ni(111) surfaces were also tested. The mechanism and energetics of  $\text{CO}_2$  hydrogenation were investigated considering the adsorption of relevant species and full reaction paths<sup>18,31</sup>. Transition states were obtained from the climbing image nudged elastic band (CI-NEB)<sup>47</sup> and improved dimer method (IDM)<sup>48</sup>. Details to the calculations specific to surfaces containing low-nuclearity clusters and to metal-support interactions are provided in the Supplementary Methods.

## Data availability

The authors declare that the data supporting the findings of this study are available within the article and its Supplementary Information file. The DFT data are accessible at the ioChem-BD database at <https://doi.org/10.19061/iochem-bd-1-183>. All other relevant source data are available from the corresponding author upon reasonable request.

Received: 11 October 2020; Accepted: 25 February 2021;

Published online: 30 March 2021

## References

1. van Santen, R. A. Chemical basis of metal catalyst promotion. *Surf. Sci.* **251**, 252, 6–11 (1991).
2. Bartholomew, C. H. & Farrauto, R. J. *Fundamentals of Industrial Catalytic Processes*. (Wiley, Hoboken, 2006).
3. Hutchings, G. J. Promotion in heterogeneous catalysis: A topic requiring a new approach? *Catal. Lett.* **75**, 1–12 (2001).
4. Zaera, F. Shape-controlled nanostructures in heterogeneous catalysis. *ChemSusChem* **6**, 1797–1820 (2013).
5. Pérez-Ramírez, J. & López, N. Strategies to break linear scaling relationships. *Nat. Catal.* **2**, 971–976 (2019).
6. Dong, C. et al. Supported metal clusters: Fabrication and application in heterogeneous catalysis. *ACS Catal.* **10**, 11011–11045 (2020).
7. Zhang, Z., Zandkarimi, B. & Alexandrova, A. N. Ensembles of metastable states govern heterogeneous catalysis on dynamic interfaces. *Acc. Chem. Res.* **53**, 447–458 (2020).
8. Kondratenko, E. V., Mül, G., Baltrusaitis, J., Larrazábal, G. O. & Pérez-Ramírez, J. Status and perspectives of  $\text{CO}_2$  conversion into fuels and chemicals by catalytic, photocatalytic and electrocatalytic processes. *Energy Environ. Sci.* **6**, 3112–3135 (2013).

- Alvarez, A. et al. Challenges in the greener production of formates/formic acid, methanol, and DME by heterogeneously catalyzed CO<sub>2</sub> hydrogenation processes. *Chem. Rev.* **117**, 9804–9838 (2017).
- González-Garay, A. et al. Plant-to-planet analysis of CO<sub>2</sub>-based methanol processes. *Energy Environ. Sci.* **12**, 3425–3436 (2019).
- Dias, V. et al. Energy and economic costs of chemical storage. *Front. Mech. Eng.* **6**, 21 (2020).
- Sun, K. et al. Hydrogenation of CO<sub>2</sub> to methanol over In<sub>2</sub>O<sub>3</sub> catalyst. *J. CO<sub>2</sub> Util.* **12**, 1–6 (2015).
- Martin, O. et al. Indium oxide as a superior catalyst for methanol synthesis by CO<sub>2</sub> hydrogenation. *Angew. Chem., Int. Ed.* **55**, 6261–6265 (2016).
- Frei, M. S. et al. Role of zirconia in indium oxide-catalyzed CO<sub>2</sub> hydrogenation to methanol. *ACS Catal.* **10**, 1133–1145 (2020).
- Tsoukalou, A. et al. Operando X-ray absorption spectroscopy identifies a monoclinic ZrO<sub>2</sub>:In solid solution as the active phase for the hydrogenation of CO<sub>2</sub> to methanol. *ACS Catal.* **10**, 10060–10067 (2020).
- Albani, D. et al. Semihydrogenation of acetylene on indium oxide: Proposed single-ensemble catalysis. *Angew. Chem., Int. Ed.* **56**, 10755–10760 (2017).
- Zhang, S. et al. Solid frustrated-lewis-pair catalysts constructed by regulations on surface defects of porous nanorods of CeO<sub>2</sub>. *Nat. Commun.* **8**, 15266 (2017).
- Frei, M. S. et al. Mechanism and microkinetics of methanol synthesis via CO<sub>2</sub> hydrogenation on indium oxide. *J. Catal.* **361**, 313–321 (2018).
- Wang, L. et al. In<sub>2</sub>O<sub>3</sub> nanocrystals for CO<sub>2</sub> fixation: atomic-level insight into the role of grain boundaries. *iScience* **16**, 390–398 (2019).
- Ye, J., Ge, Q. & Liu, C.-J. Effect of PdIn bimetallic particle formation on CO<sub>2</sub> reduction over the Pd-In/SiO<sub>2</sub> catalyst. *Chem. Eng. Sci.* **135**, 193–201 (2015).
- Rui, N. et al. CO<sub>2</sub> hydrogenation to methanol over Pd/In<sub>2</sub>O<sub>3</sub>: Effects of Pd and oxygen vacancy. *Appl. Catal., B* **218**, 488–497 (2017).
- Snider, J. L. et al. Revealing the synergy between oxide and alloy phases on the performance of bimetallic In-Pd catalysts for CO<sub>2</sub> hydrogenation to methanol. *ACS Catal.* **9**, 3399–3412 (2019).
- Bavykina, A. et al. Turning a methanation Co catalyst into an In-Co methanol producer. *ACS Catal.* **9**, 6910–6918 (2019).
- Chou, C. Y. & Lobo, R. F. Direct conversion of CO<sub>2</sub> into methanol over promoted indium oxide-based catalysts. *Appl. Catal., A* **583**, 117144 (2019).
- Han, Z., Tang, C., Wang, J., Li, L. & Li, C. Atomically dispersed Pt<sup>III</sup> species as highly active sites in Pt/In<sub>2</sub>O<sub>3</sub> catalysts for methanol synthesis from CO<sub>2</sub> hydrogenation. *J. Catal.* <https://doi.org/10.1016/j.jcat.2020.06.018> (2020).
- Jia, X., Sun, K., Wang, J., Shen, C. & Liu, C.-J. Selective hydrogenation of CO<sub>2</sub> to methanol over Ni/In<sub>2</sub>O<sub>3</sub> catalyst. *J. Energy Chem.* **50**, 409–415 (2020).
- Sun, K. et al. A highly active Pt/In<sub>2</sub>O<sub>3</sub> catalyst for CO<sub>2</sub> hydrogenation to methanol with enhanced stability. *Green. Chem.* **22**, 5059–5066 (2020).
- Wang, J., Sun, K., Jia, X. & Liu, C.-J. CO<sub>2</sub> hydrogenation to methanol over Rh/In<sub>2</sub>O<sub>3</sub> catalyst. *Catal. Today* <https://doi.org/10.1016/j.cattod.2020.05.020> (2020).
- Rui, N. et al. Hydrogenation of CO<sub>2</sub> to methanol on a Au<sup>III</sup>-In<sub>2</sub>O<sub>3-x</sub> catalyst. *ACS Catal.* **11**, 11307–11317 (2020).
- Li, M. M.-J. et al. Methanol synthesis at a wide range of H<sub>2</sub>/CO<sub>2</sub> ratios over a Rh-In bimetallic catalyst. *Angew. Chem., Int. Ed.* **59**, 16039–16046 (2020).
- Frei, M. S. et al. Atomic-scale engineering of indium oxide promotion by palladium for methanol production via CO<sub>2</sub> hydrogenation. *Nat. Commun.* **10**, 3377 (2019).
- Vogt, C. et al. Unravelling structure sensitivity in CO<sub>2</sub> hydrogenation over nickel. *Nat. Catal.* **1**, 127–134 (2018).
- Hengne, A. M. et al. Ni-Sn-supported ZrO<sub>2</sub> catalysts modified by indium for selective CO<sub>2</sub> hydrogenation to methanol. *ACS Omega* **3**, 3688–3701 (2018).
- Károlyi, J. et al. Carbon dioxide reforming of methane over Ni-In/SiO<sub>2</sub> catalyst without coke formation. *J. Ind. Eng. Chem.* **58**, 189–201 (2018).
- Jalama, K. Carbon dioxide hydrogenation over nickel-, ruthenium-, and copper-based catalysts: review of kinetics and mechanism. *Catal. Rev.* **59**, 95–164 (2017).
- Németh, M., Somodi, F. & Horváth, A. Interaction between CO and a coke-resistant NiIn/SiO<sub>2</sub> methane dry reforming catalyst: a DRIFTS and CO pulse study. *J. Phys. Chem. C* **123**, 27509–27518 (2019).
- Bergwerff, J. A. & Weckhuysen, B. M. in *Handbook of Heterogeneous Catalysis* Vol. 1 (eds. Ertl, G. et al.) 1188–1197 (Wiley-VCH, 2008).
- Baskaran, A. & Smereka, P. Mechanisms of Stranksi-Krastanov growth. *J. Appl. Phys.* **111**, 044321 (2012).
- Ernst, B. Phänomenologische Theorie der Kristallabscheidung an Oberflächen. *Z. Kristallogr.* **110**, 372–394 (1958).
- Göttl, F., Murray, E. A., Tacey, S. A., Rangarajan, S. & Mavrikakis, M. Comparing the performance of density functionals in describing the adsorption of atoms and small molecules on Ni(111). *Surf. Sci.* **700**, 121675 (2020).
- Van Herwijnen, T., Van Doesburg, H. & De Jong, W. A. Kinetics of the methanation of CO and CO<sub>2</sub> on a nickel catalyst. *J. Catal.* **28**, 391–402 (1973).
- Weatherbee, G. D. & Bartholomew, C. H. Hydrogenation of CO<sub>2</sub> on group VIII metals: II. Kinetics and mechanism of CO<sub>2</sub> hydrogenation on nickel. *J. Catal.* **77**, 460–472 (1982).
- Kresse, G. & Furthmüller, J. Efficiency of ab-initio total energy calculations for metals and semiconductors using a plane-wave basis set. *Comput. Mater. Sci.* **6**, 15–50 (1996).
- Kresse, G. & Furthmüller, J. Efficient iterative schemes for ab initio total-energy calculations using a plane-wave basis set. *Phys. Rev. B* **54**, 11169–11186 (1996).
- Perdew, J. P., Burke, K. & Ernzerhof, M. Generalized gradient approximation made simple. *Phys. Rev. Lett.* **77**, 3865–3868 (1996).
- Blöchl, P. E. Projector augmented-wave method. *Phys. Rev. B* **50**, 17953–17979 (1994).
- Henkelman, G., Uberuaga, B. P. & Jónsson, H. A climbing image nudged elastic band method for finding saddle points and minimum energy paths. *J. Chem. Phys.* **113**, 9901–9904 (2000).
- Heyden, A., Bell, A. T. & Keil, F. J. Efficient methods for finding transition states in chemical reactions: comparison of improved dimer method and partitioned rational function optimization method. *J. Chem. Phys.* **123**, 224101 (2005).

#### Acknowledgements

Total Research & Technology Feluy is thanked for sponsoring this project. Dr. S. Mitchell and Dr. F. Krumeich are thanked for the electron microscopy measurements, and the Scientific Center for Optical and Electron Microscopy (ScopeM) at the ETH Zurich for the use of their facilities. We are grateful to Dr. Nicola Casati for performing the in situ XRD analyses. Dr. Marcos Rellán-Piñero is thanked for his input in the theoretical calculations. The Spanish Ministry of Science and Innovation RTI2018-101394-B-I00 project is acknowledged for financial support and the Barcelona Supercomputing Center – MareNostrum (BSC-RES) for providing generous computer resources.

#### Author contributions

J.P.-R. and C.M. conceived and coordinated all stages of this research. M.F. and M.P. prepared and characterized the catalysts and conducted the catalytic tests. O.S. coordinated acquisition and performed the evaluation of X-ray absorption spectroscopy data. R.G.-M., J.M.-V., and N.L. conducted computational studies. J.A.S. and D.C.F. contributed setting industrial targets for the experimental program. All authors contributed to the writing of the manuscript.

#### Competing interests

The authors declare no competing interests.

#### Additional information


**Supplementary information** The online version contains supplementary material available at <https://doi.org/10.1038/s41467-021-22224-x>.

**Correspondence** and requests for materials should be addressed to J.Pér-Rir.

**Peer review information** *Nature Communications* thanks Dequan Xiao, Bert Weckhuysen and the other, anonymous, reviewer(s) for their contribution to the peer review of this work. Peer review reports are available.

**Reprints and permission information** is available at <http://www.nature.com/reprints>

**Publisher's note** Springer Nature remains neutral with regard to jurisdictional claims in published maps and institutional affiliations.

 **Open Access** This article is licensed under a Creative Commons Attribution 4.0 International License, which permits use, sharing, adaptation, distribution and reproduction in any medium or format, as long as you give appropriate credit to the original author(s) and the source, provide a link to the Creative Commons license, and indicate if changes were made. The images or other third party material in this article are included in the article's Creative Commons license, unless indicated otherwise in a credit line to the material. If material is not included in the article's Creative Commons license and your intended use is not permitted by statutory regulation or exceeds the permitted use, you will need to obtain permission directly from the copyright holder. To view a copy of this license, visit <http://creativecommons.org/licenses/by/4.0/>.

© The Author(s) 2021

Heterogeneous Catalysis

How to cite: *Angew. Chem. Int. Ed.* **2023**, e202306563  
doi.org/10.1002/anie.202306563

## Reaction-Induced Metal-Metal Oxide Interactions in Pd-In<sub>2</sub>O<sub>3</sub>/ZrO<sub>2</sub> Catalysts Drive Selective and Stable CO<sub>2</sub> Hydrogenation to Methanol

Thaylan Pinheiro Araújo\*, Jordi Morales-Vidal\*, Georgios Giannakakis, Cecilia Mondelli, Henrik Eliasson, Rolf Erni, Joseph A. Stewart, Sharon Mitchell, Núria López, and Javier Pérez-Ramírez\*

**Abstract:** Ternary Pd-In<sub>2</sub>O<sub>3</sub>/ZrO<sub>2</sub> catalysts exhibit technological potential for CO<sub>2</sub>-based methanol synthesis, but developing scalable systems and comprehending complex dynamic behaviors of the active phase, promoter, and carrier are key for achieving high productivity. Here, we show that the structure of Pd-In<sub>2</sub>O<sub>3</sub>/ZrO<sub>2</sub> systems prepared by wet impregnation evolves under CO<sub>2</sub> hydrogenation conditions into a selective and stable architecture, independent of the order of addition of Pd and In phases on the zirconia carrier. Detailed *operando* characterization and simulations reveal a rapid restructuring driven by the metal-metal oxide interaction energetics. The proximity of InPd<sub>x</sub> alloy particles decorated by InO<sub>x</sub> layers in the resulting architecture prevents performance losses associated with Pd sintering. The findings highlight the crucial role of reaction-induced restructuring in complex CO<sub>2</sub> hydrogenation catalysts and offer insights into the optimal integration of acid-base and redox functions for practical implementation.

### Introduction

In 2016, indium oxide (In<sub>2</sub>O<sub>3</sub>) was identified as a highly selective catalyst for methanol synthesis via carbon dioxide hydrogenation (CO<sub>2</sub> + 3H<sub>2</sub> ⇌ CH<sub>3</sub>OH + H<sub>2</sub>O), a sustainable route to produce this vital commodity and energy carrier.<sup>[1–3]</sup> Detailed mechanistic studies showed that surface oxygen

vacancies formed upon reaction are key to creating a catalytic ensemble that favors methanol formation while suppressing undesired carbon monoxide production through the reverse water-gas shift reaction (RWGS, CO<sub>2</sub> + H<sub>2</sub> ⇌ CO + H<sub>2</sub>O).<sup>[4]</sup> Nonetheless, methanol space-time yield (STY) over In<sub>2</sub>O<sub>3</sub> is limited and therefore many efforts have since been devoted to enhance its overall catalytic performance.<sup>[5–15]</sup> Two effective strategies towards this goal comprise deposition on *monoclinic* zirconia (*m*-ZrO<sub>2</sub>) and palladium promotion as both approaches boost oxygen vacancy generation and also, in the case of the latter, enhances H<sub>2</sub> splitting, which limits the rate of unmodified In<sub>2</sub>O<sub>3</sub>.<sup>[15,7,8,13]</sup> Additionally, the *m*-ZrO<sub>2</sub> support grants improved CO<sub>2</sub> adsorption capacity and indium dispersion.<sup>[11,13,14,16]</sup> Integrating both strategies via flame spray pyrolysis (FSP) yielded a ternary Pd-In<sub>2</sub>O<sub>3</sub>/ZrO<sub>2</sub> catalyst demonstrating *ca.* 2 to 3-fold higher methanol productivity than that of binary counterparts (1 wt% Pd/In<sub>2</sub>O<sub>3</sub> and 5 wt% In<sub>2</sub>O<sub>3</sub>/ZrO<sub>2</sub>), and thus realistic prospects for practical application.<sup>[17]</sup>

While this example demonstrates the potential of Pd-In<sub>2</sub>O<sub>3</sub>/ZrO<sub>2</sub> catalysts for CO<sub>2</sub> hydrogenation, catalytic materials synthesized by FSP generally exhibit unique structures and properties compared to those obtained by commonly practiced wet-chemistry routes, due to intrinsic steps involved in FSP synthesis such as exposure to high temperatures (*i.e.*, 2000–3000 K) and rapid quenching.<sup>[18–20]</sup> Consequently, our understanding of the catalyst architecture and associated reactivity of Pd-In<sub>2</sub>O<sub>3</sub>/ZrO<sub>2</sub> systems synthesized by scalable routes such as impregnation remains limited. Additionally, multicomponent catalysts often experience

\*T. P. Araújo, Dr. G. Giannakakis, Dr. C. Mondelli, Dr. S. Mitchell, Prof. J. Pérez-Ramírez  
Institute of Chemical and Bioengineering, Department of Chemistry and Applied Biosciences, ETH Zurich  
Vladimir-Prelog-Weg 1, 8093 Zurich (Switzerland)  
E-mail: jpr@chem.ethz.ch  
J. Morales-Vidal, Prof. N. López  
Institute of Chemical Research of Catalonia (ICIQ-CERCA), The Barcelona Institute of Science and Technology  
Av. Països Catalans 16, 43007 Tarragona (Spain)  
J. Morales-Vidal\*  
Universitat Rovira i Virgili  
Av. Catalunya 35, 43002 Tarragona (Spain)

H. Eliasson, Prof. R. Erni  
Electron Microscopy Center, Empa, Swiss Federal Laboratories for Materials Science and Technology  
Überlandstrasse 129, 8600 Dübendorf (Switzerland)  
Dr. J. A. Stewart  
TotalEnergies OneTech Belgium  
Zone Industrielle Feluy C, 7181 Senefle (Belgium)

[†] These authors contributed equally to this work.

© 2023 The Authors. Angewandte Chemie International Edition published by Wiley-VCH GmbH. This is an open access article under the terms of the Creative Commons Attribution Non-Commercial License, which permits use, distribution and reproduction in any medium, provided the original work is properly cited and is not used for commercial purposes.



surface reconstruction in response to reactive environments, which directly impacts their catalytic response.<sup>[16,21–23]</sup> Various phenomena have been reported for Pd/In<sub>2</sub>O<sub>3</sub> catalysts attained by impregnation, such as palladium sintering, formation of palladium-indium intermetallic compounds, and encapsulation of metallic nanoparticles by InO<sub>x</sub> overlayers have been reported, leading to diverse outcomes in methanol selectivity.<sup>[5,10,11]</sup> Moreover, while In<sub>2</sub>O<sub>3</sub>/*m*-ZrO<sub>2</sub> systems display stable performance, subnanometric supported In<sub>2</sub>O<sub>3</sub> islands or clusters present in the fresh catalysts were substantially altered after the reaction. Besides, no phase intermixing in the form of a solid solution was observed.<sup>[24]</sup> Based on these observations, it is therefore fundamental to understand the structural evolution of Pd-In<sub>2</sub>O<sub>3</sub>/ZrO<sub>2</sub> catalysts to map the resulting architecture to its function under reaction conditions.

In this study, we uncover that Pd-In<sub>2</sub>O<sub>3</sub>/ZrO<sub>2</sub> catalysts prepared by impregnation evolve into a unique catalyst architecture under CO<sub>2</sub> hydrogenation, resulting in high methanol selectivity and stable performance. Detailed space and time-resolved analyses using microscopy and *operando* X-ray diffraction (XRD) and X-ray absorption spectroscopy (XAS) reveal that the restructuring process occurs rapidly and is governed by the energetics of metal-metal oxide interactions between each component phase. In essence, partially reduced indium oxide species, InO<sub>x</sub>, migrate from the ZrO<sub>2</sub> surface onto palladium nanoparticles (*ca.* 10 nm) present from the catalyst synthesis, inducing the formation of InPd<sub>x</sub> alloy domains decorated by InO<sub>x</sub> layers. Density functional theory (DFT) simulations indicate that the dynamic behavior of In<sub>2</sub>O<sub>3</sub> is directed by its degree of reduction, with InO<sub>x</sub> preferably stabilizing over metallic palladium. Remarkably, although palladium exists as nanoparticles, which is well documented to favor CO formation<sup>[5,7,11,25,26]</sup>, this is curtailed on InPd<sub>x</sub>, which activates H<sub>2</sub> homolytically and its proximity to InO<sub>x</sub> is identified as essential for promoting methanol formation. Overall, this study provides atomic-level understanding of the working state of a prospective industrial catalyst for CO<sub>2</sub>-based methanol synthesis, highlighting that surface reconstruction and *operando* characterization are critical in advancing the design of practically relevant catalytic materials.

## Results and Discussion

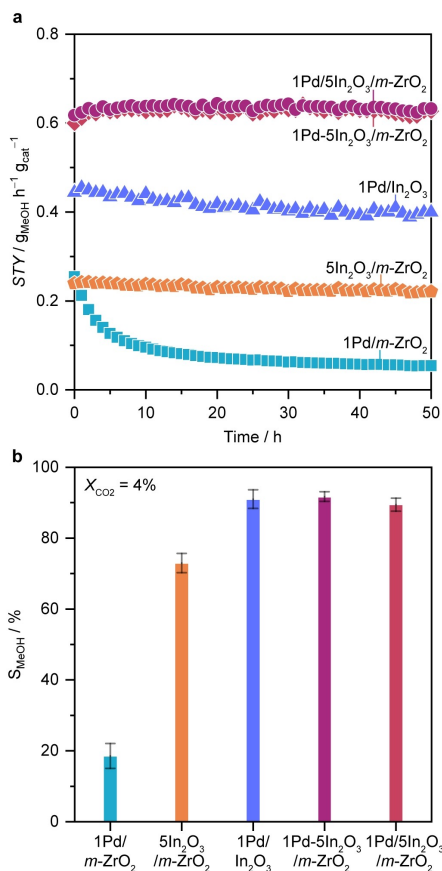
### Catalytic Performance

Ternary catalysts with optimal nominal contents of In<sub>2</sub>O<sub>3</sub> (5 wt %) and palladium (1 wt %)<sup>[5,13,17]</sup> were prepared by *one* or *two-step* impregnation approaches onto *m*-ZrO<sub>2</sub> to produce 1Pd-5In<sub>2</sub>O<sub>3</sub>/*m*-ZrO<sub>2</sub> and 1Pd/5In<sub>2</sub>O<sub>3</sub>/*m*-ZrO<sub>2</sub>, respectively (see full description in the **Experimental Section**, Supporting Information). Binary systems (1Pd/In<sub>2</sub>O<sub>3</sub>, 5In<sub>2</sub>O<sub>3</sub>/*m*-ZrO<sub>2</sub>, and 1Pd/*m*-ZrO<sub>2</sub>) were also synthesized by impregnation for reference (Table S1). All catalysts possessed similar specific surface area (*S*<sub>BET</sub>) and nominal In<sub>2</sub>O<sub>3</sub> and palladium contents closely matched experimental values (Table S2 and S3). Performance assessment at relevant CO<sub>2</sub>

hydrogenation to methanol conditions (5 MPa, 553 K, H<sub>2</sub>/CO<sub>2</sub>=4, and gas-hourly space velocity (*GHSV*=24,000 cm<sup>3</sup> h<sup>-1</sup> g<sub>cat</sub><sup>-1</sup>) revealed that both ternary catalysts display very similar methanol space-time yield (*STY*=*ca.* 0.62 g<sub>MeOH</sub> h<sup>-1</sup> g<sub>cat</sub><sup>-1</sup>), which remains unaltered after 50 h on stream and significantly outperforms that of binary counterparts (Figure 1a). The superior methanol productivity of the ternary catalysts is linked to their higher activity in converting CO<sub>2</sub> (Figure S1a). In addition, comparing methanol selectivity (*S*<sub>MeOH</sub>, Figure 1b) at similar CO<sub>2</sub> conversion levels (*X*<sub>CO<sub>2</sub></sub>=*ca.* 4 %) showed that these materials are generally more selective than 5In<sub>2</sub>O<sub>3</sub>/*m*-ZrO<sub>2</sub> and especially 1Pd/*m*-ZrO<sub>2</sub> (*S*<sub>MeOH</sub>=*ca.* 80 % versus 25 %). Interestingly, while ternary catalysts and 5In<sub>2</sub>O<sub>3</sub>/*m*-ZrO<sub>2</sub> are remarkably stable, the *STY* of 1Pd/In<sub>2</sub>O<sub>3</sub> and especially 1Pd/*m*-ZrO<sub>2</sub> drops significantly during the first 20 h on stream before stabilizing (Figure 1a). This could be attributed to a moderate decrease in *S*<sub>MeOH</sub> (from 80 % to 70 %, Figure S1b) and losses in both *S*<sub>MeOH</sub> (Figure S1b) and particularly *X*<sub>CO<sub>2</sub></sub> (from 12 % to 4 %, Figure S1a) for 1Pd/In<sub>2</sub>O<sub>3</sub> and 1Pd/*m*-ZrO<sub>2</sub>, respectively. In particular, the loss in performance is closely linked to the *S*<sub>BET</sub> of these catalysts drastically diminishing (*ca.* 40 %, Table S3) upon reaction, hinting at palladium and/or indium oxide sintering, while it remained virtually unchanged for ternary systems and 5In<sub>2</sub>O<sub>3</sub>/*m*-ZrO<sub>2</sub>. Analysis by scanning transmission electron microscopy coupled to energy-dispersive X-ray spectroscopy (STEM-EDX, Figures S3a,b) revealed that palladium clusters present on fresh 1Pd/*m*-ZrO<sub>2</sub> sinter into large nanoparticles (*ca.* 10 nm) with progressing time on stream. For 1Pd/In<sub>2</sub>O<sub>3</sub>, considerable agglomeration of palladium into nanoparticles (Figures S5a,b) and In<sub>2</sub>O<sub>3</sub> (from 13 to 22 nm as determined by XRD, Figure S2) is observed. In contrast, In<sub>2</sub>O<sub>3</sub> is equally well dispersed in fresh and used 5In<sub>2</sub>O<sub>3</sub>/*m*-ZrO<sub>2</sub> (Figures S4a,b). Based on these observations, palladium nanoparticles are also expected to be present on ternary systems, but a synergic interplay between the promoter, In<sub>2</sub>O<sub>3</sub>, and *m*-ZrO<sub>2</sub> most likely prevents additional sintering under reaction conditions, and consequent catalyst deactivation. Still, it is striking that the performance of 1Pd-5In<sub>2</sub>O<sub>3</sub>/*m*-ZrO<sub>2</sub> does not deviate from that of 1Pd/5In<sub>2</sub>O<sub>3</sub>/*m*-ZrO<sub>2</sub>. In particular, because palladium is deposited onto In<sub>2</sub>O<sub>3</sub>/*m*-ZrO<sub>2</sub> rather than co-deposited with indium onto *m*-ZrO<sub>2</sub>, and thus could interact less strongly with In<sub>2</sub>O<sub>3</sub> (Figure 1a). This points to their active sites for methanol formation possessing similar structure, and hints at these materials undergoing surface reconstruction upon reaction, which must occur rapidly since no apparent induction time is observed (Figure 1a).

### Reaction-Induced Catalyst Restructuring

Detailed space and time-resolved characterization were conducted to rationalize the highly selective and stable behavior of the ternary catalysts. EDX maps clearly evidenced palladium nanoparticles in fresh 1Pd-5In<sub>2</sub>O<sub>3</sub>/*m*-ZrO<sub>2</sub> and 1Pd/5In<sub>2</sub>O<sub>3</sub>/*m*-ZrO<sub>2</sub> (Figures 2a and S6a, respectively), whereas In<sub>2</sub>O<sub>3</sub> is highly dispersed on the *m*-ZrO<sub>2</sub>



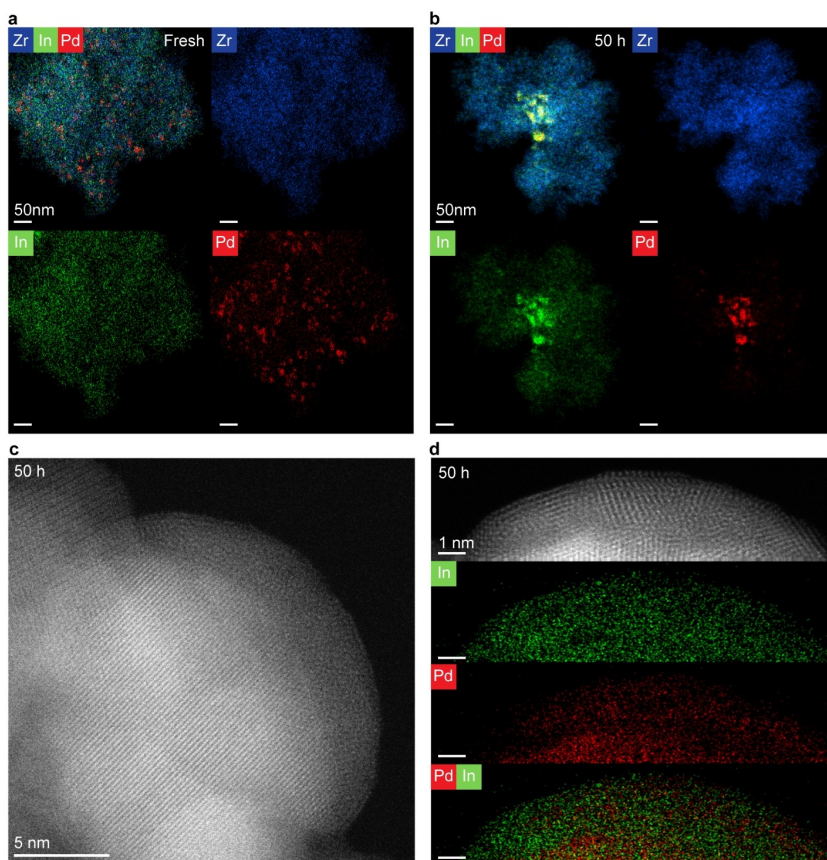
**Figure 1.** (a) Methanol space-time yield, STY and (b) selectivity,  $S_{\text{MeOH}}$  during CO<sub>2</sub> hydrogenation over ternary catalysts prepared by one (1Pd-5In<sub>2</sub>O<sub>3</sub>/m-ZrO<sub>2</sub>) or two-step (1Pd/5In<sub>2</sub>O<sub>3</sub>/m-ZrO<sub>2</sub>) impregnation, with binary systems serving as reference.  $S_{\text{MeOH}}$  was assessed at constant CO<sub>2</sub> conversion (ca. 4%) by adjusting the GHSV (24,000–96,000  $\text{cm}^3 \text{h}^{-1} \text{g}_{\text{cat}}^{-1}$ ), and corresponds to the averaged values measured over 50 h on stream with their corresponding error bars. Numbers preceding Pd or In<sub>2</sub>O<sub>3</sub> in the catalyst codes indicate their nominal content in wt%. Reaction conditions:  $T = 553 \text{ K}$ ,  $P = 5 \text{ MPa}$ ,  $\text{H}_2/\text{CO}_2 = 4$ , and  $\text{GHSV} = 24,000 \text{ cm}^3 \text{h}^{-1} \text{g}_{\text{cat}}^{-1}$ .

surface, particularly in the former sample, forming most likely monolayers. Remarkably, while no significant further agglomeration of palladium is detected in used samples collected after 50 h on stream (Figures 2b, S7, and S6b), we observe clear clustering of indium at the same location

where palladium nanoparticles are present. This suggests a strong interaction between these phases and, more importantly, highlights that both ternary systems restructure and converge to a virtually identical architecture upon reaction, thereby explaining their very similar performance independent on the order of addition of the components (Figure 1a). For this reason, special emphasis was devoted to further investigate 1Pd-5In<sub>2</sub>O<sub>3</sub>/m-ZrO<sub>2</sub>, which is attained by one-step impregnation. Accordingly, EDX mapping of the Pd–In particle shown in Figure 2c reveal that the concentration of palladium and indium varies heterogeneously within the particle regions (Figure 2d), suggesting a complex structure of different interacting phases. High-resolution high-angle annular dark-field STEM (HAADF-STEM) images support this claim as the morphology of the particles appear almost amorphous, while also often exhibiting a more crystalline core (Figure 2c).

*Operando* XAS experiments were conducted under pretreatment in He (1.5 MPa and from 303 to 553 K) and CO<sub>2</sub> hydrogenation conditions (1.5 MPa and 553 K) in the Pd and In *K*-edges to probe their corresponding local environments, while product evolution is evaluated by mass spectrometry (Figure S8). *Operando* XANES reveals that both palladium and indium exist as oxidized phases in the fresh catalyst (Figures 3a,b). Upon thermal treatment under He, however, a gradual reduction is observed for both elements; palladium fully reduces, matching the spectra of the reference material (1Pd/m-ZrO<sub>2</sub>) comprising nanoparticles, while indium maintains partially reduced state (In<sub>2</sub>O<sub>3</sub>). Interestingly, exposure to the reaction mixture for 30 min causes significant changes to the palladium character and deviations with respect to the reference are observed (Figure 3a). This change indicates an interaction of palladium with indium that leads to alloy formation. Indium shows a further reduction, yet still maintaining characteristics of In<sub>2</sub>O<sub>3</sub> phases. This is expected, based on microscopic analysis, as only a fraction of indium is expected to interact with palladium nanoparticles, while its majority is still highly dispersed on the m-ZrO<sub>2</sub> surface. This rapidly evolved architecture is preserved even after 12 h on stream (Figure 3a), accounting for the stable performance of the catalyst (Figure 1a).

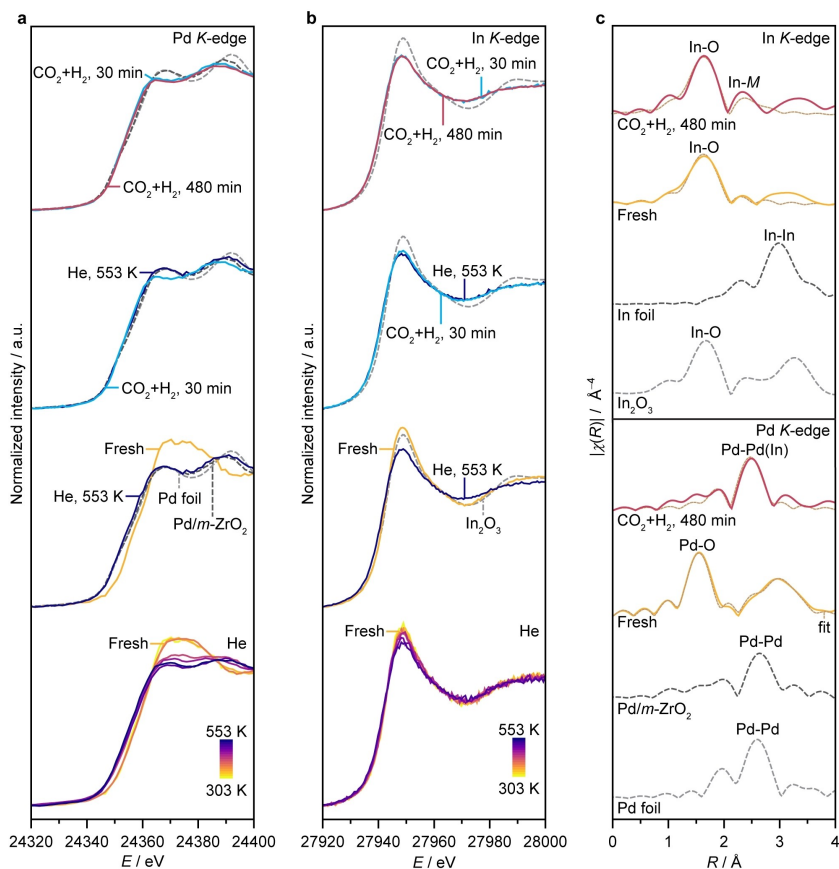
In line with XANES spectra, EXAFS analysis of the fresh catalysts exhibits strong metal-oxygen (M–O) interactions for both 1Pd-5In<sub>2</sub>O<sub>3</sub>/m-ZrO<sub>2</sub> and Pd/m-ZrO<sub>2</sub> (Figure 3c). Under reaction conditions however, a clear difference is observed between the two catalysts. While Pd/m-ZrO<sub>2</sub> shows Pd–Pd contributions, the Pd–M contributions are clearly shifted for 1Pd-5In<sub>2</sub>O<sub>3</sub>/m-ZrO<sub>2</sub>, which could be attributed to either alloying and/or palladium hydride (PdH<sub>x</sub>) formation. However, no signal associated with hydrides is observed via H<sub>2</sub>-TPR on used or activated 1Pd-5In<sub>2</sub>O<sub>3</sub>/m-ZrO<sub>2</sub> (Figure S9b) or bond elongation is evidenced by EXAFS, excluding PdH<sub>x</sub> formation (Table S5). Therefore, the changes in Pd–Pd/In distances are predominantly due to alloying between palladium and indium. Regarding the In *K*-edge EXAFS (Figure 3c), the sample largely exhibits In–O interactions and only a small In–M contribution is observed, which is shifted compared to that



**Figure 2.** EDX maps of the 1Pd-5In<sub>2</sub>O<sub>3</sub>/m-ZrO<sub>2</sub> catalyst in (a) fresh form and (b) after CO<sub>2</sub> hydrogenation for 50 h. (c) STEM-HAADF image and (d) high magnification EDX maps of the 1Pd-5In<sub>2</sub>O<sub>3</sub>/m-ZrO<sub>2</sub> catalyst after CO<sub>2</sub> hydrogenation for 50 h. Reaction conditions:  $T = 553$  K,  $P = 5$  MPa,  $H_2/CO_2 = 4$ , and  $GHSV = 24,000$  cm<sup>3</sup> h<sup>-1</sup> g<sub>cat</sub><sup>-1</sup>.

of the In foil. This can be rationalized on the premise that only a small fraction of indium is alloyed with palladium whereas its majority remains associated with *m*-ZrO<sub>2</sub>. Further pieces of evidence regarding the alloy formation can be gathered by techniques that assess the chemical properties of these materials, such as their ability to bind CO or split H<sub>2</sub>. Indeed, CO chemisorption experiments (Table S4) showed that a significantly lower amount of CO adsorbs on ternary catalysts, indicating a modified palladium surface.<sup>[10,27]</sup> This weakened interaction with CO has been reported for palladium alloys,<sup>[28]</sup> protecting their surfaces

from CO poisoning. In the case of 1Pd-5In<sub>2</sub>O<sub>3</sub>/m-ZrO<sub>2</sub>, modification by indium results in the absence of peaks associated with PdH<sub>2</sub> (Figure S9). These observed changes, supported by standard characterization techniques (H<sub>2</sub>-TPR, CO chemisorption and XAS), indicate significantly different properties between bare and modified palladium nanoparticles. These results explain the significant differences in methanol selectivity and *STY* between 1Pd-5In<sub>2</sub>O<sub>3</sub>/m-ZrO<sub>2</sub> and 1Pd/*m*-ZrO<sub>2</sub>, (Figures 1a, b) as a consequence of palladium-indium alloy formation.



**Figure 3.** Operando (a) Pd and (b) In K-edge XANES spectra of 1Pd-5In<sub>2</sub>O<sub>3</sub>/m-ZrO<sub>2</sub> catalyst during the heating ramp ( $m_{\text{cat}}=0.013$  g,  $F_1=15$  cm<sup>3</sup> min<sup>-1</sup>, heating rate = 5 K min<sup>-1</sup>,  $T=553$  K,  $P=1.5$  MPa, and dwell time = 30 min in He) and under reaction conditions ( $m_{\text{cat}}=0.013$  g,  $F_1=15$  cm<sup>3</sup> min<sup>-1</sup>,  $T=553$  K,  $P=1.5$  MPa, H<sub>2</sub>/CO<sub>2</sub>=4, dwell time = 480 min) with time on stream. (c) Fourier-transformed EXAFS spectra of 1Pd-5In<sub>2</sub>O<sub>3</sub>/m-ZrO<sub>2</sub> catalyst in fresh form and under reaction conditions corresponding to the spectra in a and b. XANES and EXAFS spectra of Pd and In foils, In<sub>2</sub>O<sub>3</sub>, and activated 1Pd/m-ZrO<sub>2</sub> ( $m_{\text{cat}}=0.013$  g,  $F_1=15$  cm<sup>3</sup> min<sup>-1</sup>,  $T=553$  K,  $P=1.5$  MPa, H<sub>2</sub>/CO<sub>2</sub>=4, dwell time = 480 min) are shown as reference.

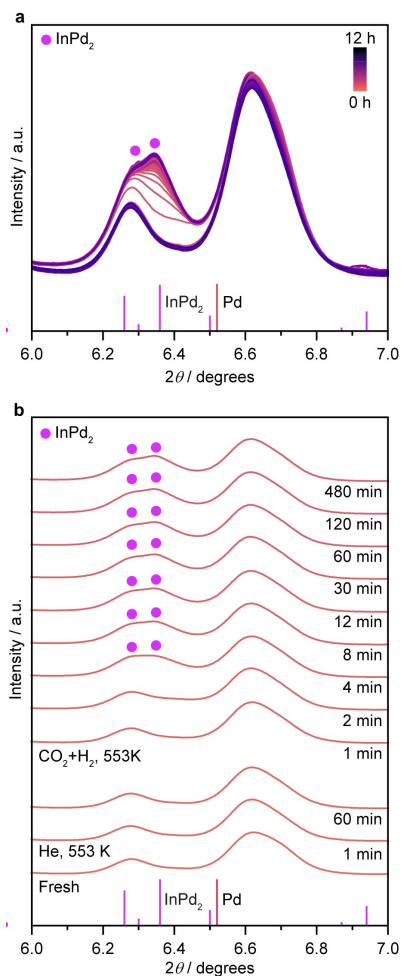
To shed light on the evolution of palladium-indium particles beyond the 5 nm range, a common limitation of XANES and EXAFS analyses,<sup>[21]</sup> we performed *operando* time-resolved XRD experiments. In principle, no characteristic signal of PdO and In<sub>2</sub>O<sub>3</sub> phases can be detected in the fresh catalyst (Figure S10), due to their diffraction features overlapping with that of the *m*-ZrO<sub>2</sub> carrier and high dispersion of indium, respectively, in line with microscopy

findings (Figure 2a). While XANES (Figures 3a,b) showed that palladium and, to a lesser extent, indium already reduce upon heating of the catalyst in He, no apparent structural changes are observed by XRD (Figures 4a,b). Since the main diffraction lines of metallic palladium and InPd, phases do not overlap with that of *m*-ZrO<sub>2</sub>, this indicates that reduced palladium and indium species generated at this stage do not form nanostructures with long-range crystal-

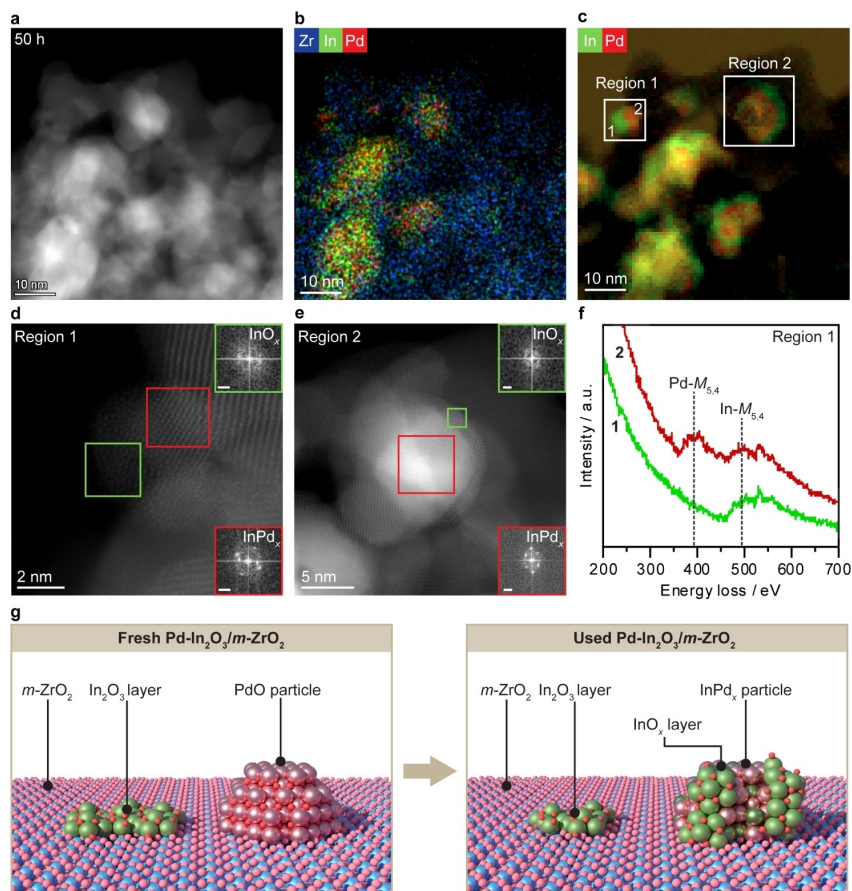
linity, and therefore remain XRD silent. In contrast, diffraction peaks at 6.26 and 6.36  $2\theta$  specific to  $\text{InPd}_2$  alloys appeared with progressing exposure of the catalyst to the  $\text{CO}_2/\text{H}_2$  mixture at 553 K (Figures 4a, b). This confirms that the formation of  $\text{InPd}_2$  nanoparticles occurs under reductive environments. Interestingly, a close look at the reflections at 6.26 and 6.36  $2\theta$  (Figure 4b) revealed that their intensity and width stop evolving within ca. 30 min. It is noteworthy that even anisotropic broadening of the reflections caused by further changes in shape and size of the particles can be easily detected by synchrotron XRD due to its high sensitivity.<sup>[22]</sup> Hence, these findings are strong evidence that the restructuring process of the ternary catalysts occurs rapidly, equilibrating before the first performance data is analyzed by gas chromatography (ca. 30 min), which explains their stable methanol *STY* (Figure 1a) with no apparent induction time.

In addition to the formation of crystalline  $\text{InPd}_2$  nanoparticles confirmed by *operando* HR-XRD, high-resolution STEM-EDX indicates that small (sub)nanometer domains with low degree of ordering are present at the surface of these nanostructures (Figure 2d). Nonetheless, the EDX signal is inherently weak due to detection limitations and thus susceptible to noise by, e.g. spurious X-rays, especially at high magnification and low electron beam current. Therefore, the used catalyst retrieved after 50 h on stream was further investigated by a combination of HAADF-STEM and electron energy-loss spectroscopy (EELS, Figures 5a, c and S11). The latter is well known for its high sensitivity to probe surface changes in atomic structure and chemical properties at metal-oxide interfaces in heterogeneous catalysts.<sup>[29–36]</sup> The EELS maps clearly reveal that the mixed palladium-indium nanoparticles possess a core-shell-like structure (Figures 5c, and S11). Analyzing the corresponding HR-STEM image reveals that the palladium-rich areas overlap well with the crystalline core-regions. By inspecting the EELS spectra in different areas of the particles (Figure 5f and S11), we observe that the  $\text{Pd-}M_{5,4}$  peak disappears in the amorphous shells (Figure 5d, e), suggesting only trace-amounts of palladium in the shell. Together with STEM-EDX and *operando* XRD and XAS findings (Figures 2a, 3a–c, 4a, 4b, and 5b), these results strongly suggest that  $\text{In}_2\text{O}_3$  migrates onto palladium particles upon reaction, forming crystalline  $\text{InPd}_2$  nanostructures in the core that are encapsulated to some extent by amorphous layers comprising partially reduced indium oxide species ( $\text{InO}_x$ ), as illustrated in Figure 5g. Furthermore, *operando* and *ex situ* characterization point to the alloying process being irreversible under reaction and even after exposure to air, underlining the stability of the  $\text{InPd}_2$  phase.

With detailed experimental investigations evidencing the reaction-induced restructuring of the ternary systems, we sought to further rationalize this process by DFT simulations using a thermodynamic model. To illustrate the driving force for the restructuring, we computed the interaction energy ( $E_{\text{int}}$ ) between an  $\text{In}_2\text{O}_3(111)$  monolayer at different degrees of reduction with both *m*- $\text{ZrO}_2(-111)$  and metallic  $\text{Pd}(111)$  surfaces (Figure S14, see detailed description in the Experimental Section, Supporting Information). At low degrees of



**Figure 4.** *Operando* time-resolved HR-XRD patterns of 1Pd-5 $\text{In}_2\text{O}_3$ /*m*- $\text{ZrO}_2$  catalyst during the heating ramp ( $m_{\text{cat}}=0.013$  g,  $F_T=15$   $\text{cm}^3 \text{min}^{-1}$ , heating rate = 5  $\text{K min}^{-1}$ ,  $T=553$  K,  $P=1.5$  MPa, and dwell time = 30 min in He) and under reaction conditions ( $m_{\text{cat}}=0.013$  g,  $F_T=15$   $\text{cm}^3 \text{min}^{-1}$ ,  $T=553$  K,  $P=1.5$  MPa,  $\text{H}_2/\text{CO}_2=4$ , dwell time = 480 min) with (a) continuous and (b) selected time on stream. Diffractograms were acquired every 30 s using monochromatic light ( $\lambda=0.25509$  Å). Vertical lines show reference data ( $\text{InPd}_2$ , ICSD ID 417907).



**Figure 5.** (a) HAADF-STEM image with corresponding (b) EDX and (c) EELS maps of 1Pd-5In<sub>2</sub>O<sub>3</sub>/m-ZrO<sub>2</sub> catalyst after CO<sub>2</sub> hydrogenation for 50 h. (d, e) High magnification STEM images of regions 1 and 2 shown in (c). Insets in (d, e) show fast Fourier transforms of indicated areas, evidencing the presence of both amorphous InO<sub>x</sub> and crystalline InPd<sub>x</sub> phases. (f) Averaged EELS spectra of the green (green curve) and red (red curve) regions shown in d. The palladium peak clearly disappears in the amorphous shell. (g) Schematic representation of the catalyst architecture of fresh and used 1Pd-5In<sub>2</sub>O<sub>3</sub>/m-ZrO<sub>2</sub> catalyst, depicted on the left and right, respectively. Reaction conditions:  $T=553$  K,  $P=5$  MPa,  $H_2/CO_2=4$ , and  $GHSV=24,000$  cm<sup>3</sup> h<sup>-1</sup> g<sub>cat</sub><sup>-1</sup>.

reduction (*i.e.*, 0–17% oxygen loss), In<sub>2</sub>O<sub>3</sub> interacts similarly with the two surfaces (Figure S14). This agrees with the high expected dispersion of this phase over *m*-ZrO<sub>2</sub> in fresh catalysts, as evidenced by microscopy analyses (Figure 2a). For high degrees of reduction (*i.e.*, > 17%, Figure S14), InO<sub>x</sub> prefers to interact with metallic palladium compared to *m*-ZrO<sub>2</sub>. As more O atoms are removed from In<sub>2</sub>O<sub>3</sub>, its surface

energy increases translating into a less favorable wetting of the *m*-ZrO<sub>2</sub> carrier, and thus higher mobility, as previously reported for In<sub>2</sub>O<sub>3</sub>/m-ZrO<sub>2</sub> catalysts under CO<sub>2</sub> hydrogenation conditions.<sup>[24]</sup> Consequently, because oxygen vacancy formation on In<sub>2</sub>O<sub>3</sub> is fostered by thermal treatments in both inert and reductive atmospheres,<sup>[1,17]</sup> the migration and stabilization of InO<sub>x</sub> overlayers onto metallic palladium

nanoparticles experimentally evidenced for Pd-In<sub>2</sub>O<sub>3</sub>/m-ZrO<sub>2</sub> catalysts is driven by these thermodynamic considerations. Interestingly, this suggests that these systems experience a special case of strong metal-support interactions (SMSI) under reaction conditions. Generally, SMSI overlayer formation on metal particles is reported for binary systems, where In<sub>2</sub>O<sub>3</sub> and other reducible oxides serve as supports.<sup>[32,34,37–39]</sup> For ternary Pd-In<sub>2</sub>O<sub>3</sub>/m-ZrO<sub>2</sub> systems, however, the active InO<sub>x</sub> phase rather than the m-ZrO<sub>2</sub> support partially encapsulates the particles of the palladium promoter, which we attribute to its more strongly reducible nature rendering it more mobile under reaction conditions. The reduction of In<sub>2</sub>O<sub>3</sub> is corroborated experimentally, by linear fitting combination (LFC) analysis of spectra shown in Figure 3b using In<sub>2</sub>O<sub>3</sub> and In foil as the reference materials, which indicates that In<sub>2</sub>O<sub>3</sub> is reduced by ca. 35% under reaction conditions. Finally, because indium and palladium are not mixed in the fresh catalyst, we put forward that the restructuring of Pd-In<sub>2</sub>O<sub>3</sub>/m-ZrO<sub>2</sub> catalysts begins with migration of InO<sub>x</sub> onto palladium nanoparticles, followed by alloy formation between part of the oxidic phase and palladium (Figure 5g). Indeed, the computed formation energies of InPd<sub>2</sub> and InPd (−1.51 and −0.97 eV, respectively) indicate a high tendency for the formation InPd<sub>2</sub> alloy phases, in line with *operando* XAS and XRD results (Figures 3a and 4a, b).

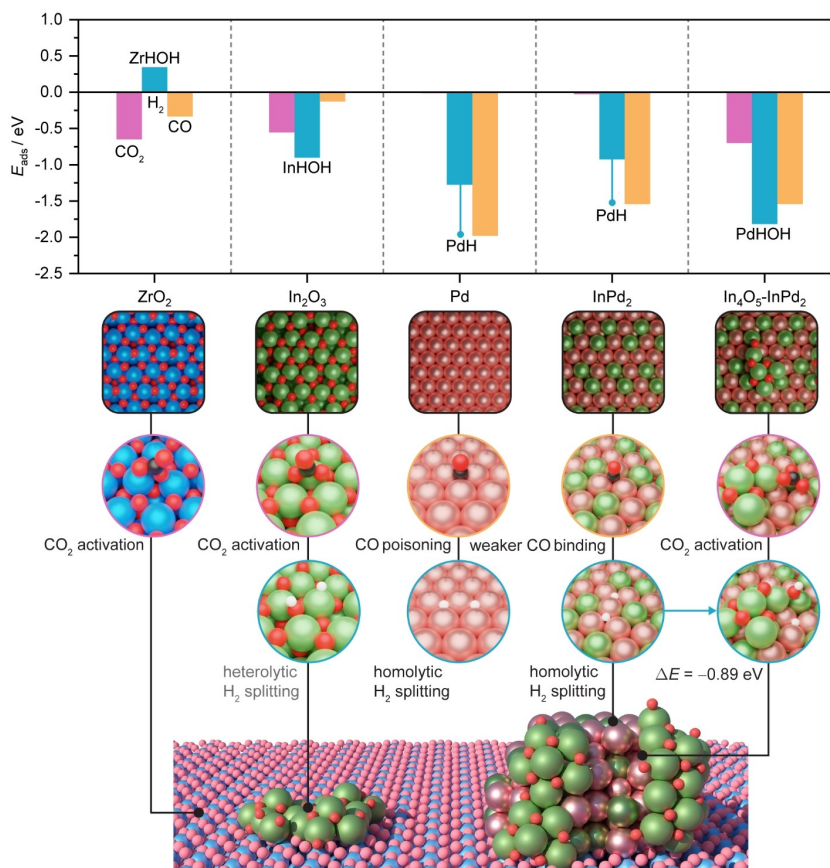
#### Mapping Catalyst Structure to Function

CO<sub>2</sub> hydrogenation to methanol requires the activation of the reactants (CO<sub>2</sub> and H<sub>2</sub>), followed by hydride-proton transfers avoiding the RWGS side reaction, which leads to CO poisoning (Figure S15). For a given catalytic material to be effective in catalyzing this transformation, a combination of acid-base properties (to trap CO<sub>2</sub>) and easy activation of H<sub>2</sub> is needed. In general, metallic centers show poor CO<sub>2</sub> activation properties whereas basic centers on oxides (lattice oxygen atoms) uptake CO<sub>2</sub> effectively. However, oxides possess a limited ability to split H<sub>2</sub>, as this process takes place *via* a heterolytic route generating protons (H<sup>+</sup>) and hydrides (H<sup>−</sup>). In contrast, this can be easily solved by metals since they homolytically activate H<sub>2</sub> in low-energy processes.<sup>[5,40]</sup> To assess the role of the distinct catalytic components in the reaction, various model surfaces were considered based on the experimentally revealed catalyst architecture (see **Modelling of the Catalytic Systems** subsection, Supporting Information). It is worth noting that adsorption studies conducted in ultra-high vacuum do not fully capture the catalyst structure under real operating conditions due to the pressure and associated material gap.<sup>[41–43]</sup> Therefore, we computed adsorption energies ( $E_{\text{ads}}$ ) of CO<sub>2</sub>, dissociated H<sub>2</sub>, and CO on these experimentally-guided model surfaces (see Experimental Section in the Supporting Information). This holistic approach enabled us to bridge the pressure gap, and provides valuable insights to rationalize the catalytic activity and stability of Pd-In<sub>2</sub>O<sub>3</sub>/m-ZrO<sub>2</sub> systems. Figure 6 shows the most relevant and favorable  $E_{\text{ads}}$ , while the values associated with different

adsorption conformations and models can be found in Figures S16–17. CO<sub>2</sub> adsorption is favored on m-ZrO<sub>2</sub> and In<sub>2</sub>O<sub>3</sub> over Pd, while the opposite trend is observed for H<sub>2</sub> dissociation products. These results indicate that in binary catalysts (Pd/In<sub>2</sub>O<sub>3</sub>, Pd/m-ZrO<sub>2</sub>), CO<sub>2</sub> is activated and hydrogenated on the metal oxides and H<sub>2</sub> splitting takes places on Pd (Figure S15). This implies spillover of hydrogen from Pd to the metal oxides, which although it can be long-range, it is a stochastic process and thus ineffective.<sup>[44,45]</sup> In addition, the ability of palladium surfaces to activate H<sub>2</sub> (as H atoms) boosts both methanol and carbon monoxide formation. On the contrary, the computed  $E_{\text{ads-CO}}$  on InPd<sub>2</sub> and InPd (Figure S16) points to CO adsorption being weakened with respect to extended Pd surfaces. This contributes to the ternary catalysts circumventing CO poisoning and controlling the H coverage, which can explain the CO chemisorption and catalytic tests (Table S4 and Figure 1a, b).

For the restructured Pd-In<sub>2</sub>O<sub>3</sub>/m-ZrO<sub>2</sub>, InO<sub>x</sub> overlayers permit an easy CO<sub>2</sub> adsorption at the basic sites on the edge of In<sub>2</sub>O<sub>3</sub> clusters deposited on Pd and InPd<sub>2</sub> surfaces (In<sub>4</sub>O<sub>5</sub>-Pd and In<sub>4</sub>O<sub>5</sub>-InPd<sub>2</sub> models, Figure S16). Concomitantly, H<sub>2</sub> can be homolytically activated in the InPd<sub>2</sub> regions nearby the InO<sub>x</sub> clusters allowing the formation of InO<sub>x</sub>H and InPd<sub>2</sub>H species at the interface ( $\Delta E = -0.89$  eV). This configuration promotes selective CO<sub>2</sub> hydrogenation to methanol by minimizing transport as all active species are confined in close proximity. Overall, the interface between InO<sub>x</sub> clusters and Pd/InPd<sub>2</sub> nanoparticles are the active sites for CO<sub>2</sub> hydrogenation to methanol on the ternary Pd-In<sub>2</sub>O<sub>3</sub>/m-ZrO<sub>2</sub> system (Figure 6). It should be noted however that indium phases that do not associate with palladium but rather remain dispersed on ZrO<sub>2</sub> still contribute to the overall activity, considering the reactivity of In<sub>2</sub>O<sub>3</sub>/m-ZrO<sub>2</sub>.

Our study reveals a remarkable result that two distinct synthetic methods - the wet chemical synthesis employed here and the FSP method demonstrated previously<sup>[17]</sup> - can produce ternary systems with similarly stable and selective behavior, despite exhibiting very different architectures. The essential functions of the catalysts include (i) facilitating reactant activation via acid-base or metal catalysis, (ii) efficiently removing the desired product through acid-base catalysis, and (iii) enabling convenient transport of activated reactants. In the systems prepared by impregnation, the active site is formed by the migration of small InO<sub>x</sub> clusters to the metal surface under reducing conditions, incorporating some of the In atoms as an alloy. Comparatively, the FSP method creates low-nuclearity Pd clusters with sufficient metallic character, surrounded by the In<sub>2</sub>O<sub>3</sub> oxide matrix to form the active ensemble (Figure S18). Similar structural characteristics were also observed for Pd-In<sub>2</sub>O<sub>3</sub> obtained by coprecipitation.<sup>[5]</sup> However, the current study demonstrates a more practical and scalable catalyst with optimal indium content, while achieving similar methanol *STY* and stability. Our work highlights that different active site configurations can perform similar functions and the fact that these structures may appear under reaction conditions. Moreover, our novel architecture obtained using a common synthesis method demonstrates the potential for improving methanol synthesis with high selectivity.



**Figure 6.** Adsorption energies,  $E_{\text{ads}}$ , of reaction species on relevant surfaces representative of the different constituents of ternary Pd-In<sub>2</sub>O<sub>3</sub>/m-ZrO<sub>2</sub> systems attained by impregnation. The adsorption mode for the dissociated hydrogen is indicated for each model. Snapshots of activated CO<sub>2</sub> and H<sub>2</sub> indicate the locations at which these key steps for methanol synthesis are more favored over the catalyst surface. The formation of InO<sub>x</sub>H and InPd<sub>2</sub>H species is favored on In<sub>4</sub>O<sub>5</sub>-InPd<sub>2</sub> after barrierless homolytic H<sub>2</sub> splitting on InPd<sub>2</sub>. Snapshots of CO specify surfaces at which poisoning by this specie is favored. Color code of DFT models: Zr (blue), In (green), Pd (light pink), O (red), C (dark gray), and H (white).

## Conclusion

This study demonstrates that ternary Pd-In<sub>2</sub>O<sub>3</sub>/m-ZrO<sub>2</sub> catalysts produced by scalable wet impregnation routes undergo rapid surface reconstruction during CO<sub>2</sub> hydrogenation. Irrespective of the order of addition of the Pd and In precursors during the synthesis, this results in a stable and selective catalyst architecture with improved methanol productivity compared to binary systems. *Operando* XAS

confirms the autoreduction of palladium nanoparticles to a metallic state prior to reaction, and the partial reduction of In<sub>2</sub>O<sub>3</sub> into InO<sub>x</sub> species that migrate onto the metallic palladium surface. EELS and *operando* HR-XRD analyses reveal that the catalysts further restructure into InPd<sub>x</sub> alloy particles partially encapsulated by InO<sub>x</sub> layers induced by the reductive environment during CO<sub>2</sub> hydrogenation. DFT simulations support that metal-metal oxide interactions govern the structural evolution and reactivity. The InPd<sub>x</sub>



phase activates H<sub>2</sub> homolytically, while the InO<sub>x</sub> overlayer facilitates acid-base steps, enhancing methanol formation. Overall, our study advances the understanding of reaction-induced structural dynamics in In<sub>2</sub>O<sub>3</sub>-based catalytic systems and uncovers a highly effective architecture for CO<sub>2</sub>-based methanol synthesis. It also highlights the potential for surface reconstruction to tailor other reducible oxides in heterogeneous catalysis.

### Supporting Information

Supporting Information is available from the Wiley Online Library or from the author.

### Acknowledgements

TotalEnergies OneTech Belgium is thanked for sponsoring this project. This publication was also supported by NCCR Catalysis (grant number 180544), a National Centre of Competence in Research funded by the Swiss National Science Foundation. The Scientific Center for Optical and Electron Microscopy (ScopeM) at the ETH Zurich is thanked for access to their facilities. Mr. Dario Faust Akl is thanked for acquiring the HAADF-STEM-EDX data. We are grateful to Mr. Tangsheng Zou and Ms. Zaira Ruiz-Bernal for assistance with XAS and XRD measurements. The Spanish Ministry of Science and Innovation is acknowledged for financial support (PRE2019-088791, PID2021-122516GB-I00, and Severo Ochoa Grant MCIN/AEI/10.13039/501100011033 CEX2019-000925-S) and the Barcelona Supercomputing Center-MareNostrum (BSC-RES) for providing generous computer resources. The Swiss Norwegian beamlines (SNBL, ESRF) are acknowledged for provision of beamtime and its staff for invaluable support. H. Eliasson and R. Erni acknowledge financial support by the Swiss National Science Foundation, project number 200021-196381. Open Access funding provided by Eidgenössische Technische Hochschule Zürich.

### Conflict of Interest

The authors declare no conflict of interest.

### Data Availability Statement

The data that support the findings of this study are openly available in Zenodo at <https://doi.org/10.5281/zenodo.7916390>.<sup>[46]</sup> DFT data can be found online in the ioChem-BD repository,<sup>[47,48]</sup> at <https://doi.org/10.19061/iochem-bd-1-275>.

**Keywords:** CO<sub>2</sub> Hydrogenation · Metal-Metal Oxide Interactions · Methanol Synthesis · Operando Analysis · Pd-In<sub>2</sub>O<sub>3</sub>/ZrO<sub>2</sub> Catalyst

- [1] O. Martin, A. J. Martin, C. Mondelli, S. Mitchell, T. F. Segawa, R. Hauert, C. Drouilly, D. Curulla-Ferré, J. Pérez-Ramírez, *Angew. Chem. Int. Ed.* **2016**, *55*, 6261–6265.
- [2] A. González-Garay, M. S. Frei, A. Al-Qahtani, C. Mondelli, G. Guillén-Gosálbez, J. Pérez-Ramírez, *Energy Environ. Sci.* **2019**, *12*, 3425–3436.
- [3] G. A. Olah, *Angew. Chem. Int. Ed.* **2005**, *44*, 2636–2639.
- [4] M. S. Frei, M. Capdevila-Cortada, R. García-Muelas, C. Mondelli, N. López, J. A. Stewart, D. Curulla Ferré, J. Pérez-Ramírez, *J. Catal.* **2018**, *361*, 313–321.
- [5] M. S. Frei, C. Mondelli, R. García-Muelas, K. S. Kley, B. Puértolas, N. López, O. V. Safonova, J. A. Stewart, D. Curulla Ferré, J. Pérez-Ramírez, *Nat. Commun.* **2019**, *10*, 3377.
- [6] S. Dang, B. Qin, Y. Yang, H. Wang, J. Cai, Y. Han, S. Li, P. Gao, Y. Sun, *Sci. Adv.* **2020**, *6*, eaaz2060.
- [7] J. Ye, Q. Ge, C. J. Liu, *Chem. Eng. Sci.* **2015**, *135*, 193–201.
- [8] T. Pinheiro Araújo, J. Morales-Vidal, T. Zou, R. García-Muelas, P. O. Willi, K. M. Engel, O. V. Safonova, D. Faust Akl, F. Krumeich, R. N. Grass, et al., *Adv. Energy Mater.* **2022**, *12*, 2103707.
- [9] T. Y. Chen, C. Cao, T. B. Chen, X. Ding, H. Huang, L. Shen, X. Cao, M. Zhu, J. Xu, J. Gao, et al., *ACS Catal.* **2019**, *9*, 8785–8797.
- [10] J. L. Snider, V. Streibel, M. A. Hubert, T. S. Choksi, E. Valle, D. C. Upham, J. Schumann, M. S. Duyar, A. Gallo, F. Abild-Pedersen, et al., *ACS Catal.* **2019**, *9*, 3399–3412.
- [11] N. Rui, Z. Wang, K. Sun, J. Ye, Q. Ge, C. jun Liu, *Appl. Catal. B* **2017**, *218*, 488–497.
- [12] Z. Han, C. Tang, J. Wang, L. Li, C. Li, *J. Catal.* **2021**, *394*, 236–244.
- [13] M. S. Frei, C. Mondelli, A. Cesarini, F. Krumeich, R. Hauert, J. A. Stewart, D. Curulla Ferré, J. Pérez-Ramírez, *ACS Catal.* **2020**, *10*, 1133–1145.
- [14] C. Yang, C. Pei, R. Luo, S. Liu, Y. Wang, Z. Wang, Z. J. Zhao, J. Gong, *J. Am. Chem. Soc.* **2020**, *142*, 19523–19531.
- [15] N. Rui, F. Zhang, K. Sun, Z. Liu, W. Xu, E. Stavitski, S. D. Senanayake, J. A. Rodríguez, C.-J. Liu, *ACS Catal.* **2020**, *10*, 11307–11317.
- [16] A. Tsoukalou, P. M. Abdala, A. Armutulu, E. Willinger, A. Fedorov, C. R. Müller, *ACS Catal.* **2020**, *10*, 10060–10067.
- [17] T. Pinheiro Araújo, C. Mondelli, M. Agrachev, T. Zou, P. O. Willi, K. M. Engel, R. N. Grass, W. J. Stark, O. V. Safonova, G. Jeschke, et al., *Nat. Commun.* **2022**, *13*, 5610.
- [18] S. Pokhrel, L. Mädlar, *Energy Fuels* **2020**, *34*, 13209–13224.
- [19] S. Ding, H. A. Chen, O. Mekasuwandumrong, M. J. Hüsey, X. Fu, Q. He, J. Panpranot, C. M. Yang, N. Yan, *Appl. Catal. B* **2021**, *281*, 119471.
- [20] R. Koirala, S. E. Pratsinis, A. Baiker, *Chem. Soc. Rev.* **2016**, *45*, 3053.
- [21] A. Beck, M. A. Newton, M. Zabitskiy, P. Rzepka, M. G. Willinger, J. A. van Bokhoven, *Angew. Chem. Int. Ed.* **2022**, *61*, e202200301.
- [22] O. Martin, C. Mondelli, A. Cervellino, D. Ferri, D. Curulla-Ferré, J. Pérez-Ramírez, *Angew. Chem. Int. Ed.* **2016**, *55*, 11031–11036.
- [23] A. Tsoukalou, P. M. Abdala, D. Stoian, X. Huang, M. G. Willinger, A. Fedorov, C. R. Müller, *J. Am. Chem. Soc.* **2019**, *141*, 13497–13505.
- [24] X. Zhang, A. V. Kirilin, S. Rozeveld, J. H. Kang, G. Pollefeyt, D. F. Yancey, A. Chojceki, B. Vanchura, M. Blum, *ACS Catal.* **2022**, *12*, 3868–3880.
- [25] A. Baiker, D. Gasser, *J. Chem. Soc. Faraday Trans. 1* **1989**, *85*, 999–1007.
- [26] Y.-P. Du, A. M. Bahmanpour, L. Milošević, F. Héroguel, M. D. Mensi, O. Kröcher, J. S. Luterbacher, *ACS Catal.* **2020**, *10*, 12058–12070.

- [27] Z. Wu, E. C. Wegener, H.-T. Tseng, J. R. Gallagher, J. W. Harris, R. E. Diaz, Y. Ren, F. H. Ribeiro, J. T. Miller, *Catal. Sci. Technol.* **2016**, *6*, 6965–6976.
- [28] M. T. Darby, E. C. H. Sykes, A. Michaelides, M. Stamatakis, *Top. Catal.* **2018**, *61*, 428–438.
- [29] R. F. Klie, M. M. Disko, N. D. Browning, *J. Catal.* **2002**, *205*, 1–6.
- [30] W. Zhou, I. E. Wachs, C. J. Kiely, *Curr. Opin. Solid State Mater. Sci.* **2012**, *16*, 10–22.
- [31] S. Chenna, P. A. Crozier, *ACS Catal.* **2012**, *2*, 2395–2402.
- [32] Y. Niu, X. Liu, Y. Wang, S. Zhou, Z. Lv, L. Zhang, W. Shi, Y. Li, W. Zhang, D. S. Su, B. Zhang, *Angew. Chem. Int. Ed.* **2019**, *131*, 4276–4281.
- [33] X. Huang, D. Teschner, M. Dimitrakopoulou, A. Fedorov, B. Frank, R. Kraehnert, F. Rosowski, H. Kaiser, S. Schunk, C. Kuretschka, R. Schlögl, M.-G. Willinger, A. Trunschke, *Angew. Chem. Int. Ed.* **2019**, *58*, 8709–8713.
- [34] T. Pu, W. Zhang, M. Zhu, *Angew. Chem. Int. Ed.* **2023**, *62*, e202212278.
- [35] Y. Zhang, J. Liu, K. Qian, A. Jia, D. Li, L. Shi, J. Hu, J. Zhu, W. Huang, *Angew. Chem. Int. Ed.* **2021**, *60*, 12074–12081.
- [36] A. Ruiz Caridad, R. Erni, A. Vogel, M. D. Rossell, *Micron* **2022**, *160*, 103331.
- [37] N. Rui, X. Wang, K. Deng, J. Moncada, R. Rosales, F. Zhang, W. Xu, I. Waluyo, A. Hunt, E. Stavitski, et al., *ACS Catal.* **2023**, *13*, 3187–3200.
- [38] J. C. Matsubu, S. Zhang, L. DeRita, N. S. Marinkovic, J. G. Chen, G. W. Graham, X. Pan, P. Christopher, *Nat. Chem.* **2017**, *9*, 120–127.
- [39] K. J. Sawant, Z. Zeng, J. P. Greeley, *Chem. Sci.* **2023**, *14*, 3206–3214.
- [40] M. S. Frei, C. Mondelli, R. García-Muelas, J. Morales-Vidal, M. Philipp, O. V. Safonova, N. López, J. A. Stewart, D. Curulla Ferré, J. Pérez-Ramírez, *Nat. Commun.* **2021**, *12*, 1960.
- [41] A. Urakawa, *Nat. Catal.* **2021**, *4*, 447–448.
- [42] A. Beck, M. Zabilskiy, M. A. Newton, O. Safonova, M. G. Willinger, J. A. van Bokhoven, *Nat. Catal.* **2021**, *4*, 488–497.
- [43] N. J. Divins, D. Kordus, J. Timoshenko, I. Sinev, I. Zegkinoglou, A. Bergmann, S. W. Chee, S. Widrinna, O. Karshoglu, H. Mistry, M. Lopez Luna, J. Qiang Zhong, A. S. Hoffman, A. Boubnov, J. Anibal Boscoboinik, M. Heggen, R. E. Dunin-Borkowski, S. R. Bare, B. Roldan Cuenya, *Nat. Commun.* **2021**, *12*, 1435.
- [44] R. Prins, *Chem. Rev.* **2012**, *112*, 2714–2738.
- [45] T. Kamada, T. Ueda, S. Fukuura, T. Yumura, S. Hosokawa, T. Tanaka, D. Kan, Y. Shimakawa, *J. Am. Chem. Soc.* **2023**, *145*, 1631–1637.
- [46] T. Pinheiro Araújo, J. Morales-Vidal, G. Giannakakis, C. Mondelli, H. Eliasson, R. Erni, J. A. Stewart, S. Mitchell, N. López, J. Pérez-Ramírez, *Zenodo* **2022**, <https://doi.org/10.5281/zenodo.7916390>.
- [47] M. Álvarez-Moreno, C. de Graaf, N. López, F. Maseras, J. M. Poblet, C. Bo, *J. Chem. Inf. Model.* **2015**, *55*, 95–103.
- [48] C. Bo, F. Maseras, N. López, *Nat. Catal.* **2018**, *1*, 809–810.

Manuscript received: May 10, 2023

Accepted manuscript online: July 3, 2023

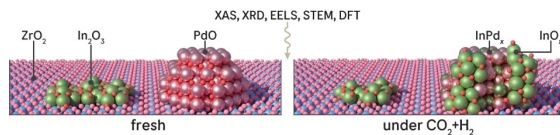
Version of record online: ■■, ■■

## Research Articles

### Heterogeneous Catalysis

T. P. Araújo, J. Morales-Vidal,  
G. Giannakakis, C. Mondelli, H. Eliasson,  
R. Erni, J. A. Stewart, S. Mitchell, N. López,  
J. Pérez-Ramírez\* [e202306563](#)

Reaction-Induced Metal-Metal Oxide Interactions in Pd-In<sub>2</sub>O<sub>3</sub>/ZrO<sub>2</sub> Catalysts Drive Selective and Stable CO<sub>2</sub> Hydrogenation to Methanol



Pd-In<sub>2</sub>O<sub>3</sub>/ZrO<sub>2</sub> catalysts prepared by impregnation evolve into a unique nanostructure under CO<sub>2</sub> hydrogenation conditions, leading to selective and stable methanol production. Space and time-resolved *operando* characterization and

simulations reveal that the rapid restructuring process leads to InPd, alloy particles decorated by In<sub>2</sub>O<sub>3</sub> layers, whose proximity is crucial to avoiding performance losses typically observed when palladium agglomerates.

UNIVERSITAT ROVIRA I VIRGILI  
MODELLING OF CATALYTIC SYSTEMS TOWARDS GREEN FUELS  
Jordi Morales Vidal

UNIVERSITAT ROVIRA I VIRGILI  
MODELLING OF CATALYTIC SYSTEMS TOWARDS GREEN FUELS  
Jordi Morales Vidal

UNIVERSITAT ROVIRA I VIRGILI  
MODELLING OF CATALYTIC SYSTEMS TOWARDS GREEN FUELS  
Jordi Morales Vidal

UNIVERSITAT ROVIRA I VIRGILI  
MODELLING OF CATALYTIC SYSTEMS TOWARDS GREEN FUELS  
Jordi Morales Vidal



UNIVERSITAT  
ROVIRA i VIRGILI